Generalised Braiding of Anyonic Excitations and Topological Quantum Computation

Aaron Conlon

B.Sc.

To my family and friends

Contents

Declaration

I declare that this thesis has not been submitted in whole, or in part, to this or any other university for any other degree and is, except where otherwise stated, the original work of the author.

<div style="text-align: right">

_____

Aaron Conlon, October 6, 2023

</div>

Acknowledgements

and more boring note, I am sincerely grateful for your guidance. Throughout the years you were always there for a chat and advice. In particular during the Majorana project, although I did not appreciate the project at the time (I hid these feelings immaculately), in hindsight I am very grateful I did this project with you, I really learned a lot. Not just about the project itself, but about scientific research in general. Even your advice to test simple cases, which is obvious in retrospect, was not something that I thought of. I have tried to take this advice into every project I've done since.

In many ways, one of my favourite parts of my PhD was my collaboration with Domenico. We've worked on four projects, made four posters, written two papers (edited and proofread many more), travelled to eleven cities (remember San Sebastian?) in five countries, and countless pubs. I'm not sure I would have enjoyed this PhD without these experiences. Probably the best lesson I learned from you was to accept that the first draft of everything will not be good and that's okay, it's better to get it down and improve it. Of course, you may have phrased it slightly different, but the message was clear. You've always been a great collaborator and a great friend, so thank you for all of the ahhhhhh and asking me one.

I have to thank Kevin, we've known each other for about ten years, through three degrees (I can't believe we're getting our own individual PhDs). You're a really great friend and provider of all things distracting. It will be strange not to share an office with you and listen to your in-depth discussion of film (mainly Interstellar). I'm so happy that we both did our PhDs together.

I have to also thank Ian, our chats on physics have really broadened my knowledge and it's a pity we didn't get to work on a full project together. Even outside of physics you have been one of the most supportive friends I've ever been lucky enough to know, you have a heart of pure gold and I appreciate the time you've given me over the years, even if you are an absolute ned.

I would also like to thank my collaborator Tomasz for introducing me to what would be my favourite project and which has brought me so much joy. I've really enjoyed working with you and I'm very proud of what we've produced together.

I would also like to thank Alex, from discussions with you I've really learned to better understand category theory and the abstract structures of topological physics better than I thought I would. I hope we can work through the night in my garage again or discuss politics till the morning on the Liffey.

I am also grateful to everyone in DIAS who made it such a welcoming place to do research, in particular; Shane, Luuk, Denjoe, Brian, Gian, Neetu, Takaki and Elo. Thank you also to everyone in Maynooth; Gert, Babatunde, Aonghus, Darragh, John, Stephen, Paul, Peter, Jiri, Jonivar, Ryan, Monica and Suzie. Also, I would also like to thank Danny Heffernan without whose encouragement, I never would have switched from biomedical science to theoretical physics.

Abstract

This thesis investigates various topological phases of matter in two-dimensional and quasi one-dimensional systems. These exotic states of matter have applications in topological quantum computation; which is an inherently fault-tolerant quantum computation scheme. In these schemes, computations are implemented by braiding anyonic excitations. In this thesis we examine three aspects of braiding: braiding of anyonic excitations on graphs, topological lattice models, and non-adiabatic perturbations of a qubit constructed from Majorana bound states.

In the first part of the thesis we introduce a universal framework to discuss the braiding of anyonic excitations on graphs as a model of a quantum wire network. We show that many features of the planar algebraic theory of anyons may be extended to graphs. In this direction, we introduce graph hexagon equations, a generalisation of the planar hexagon equations and demonstrate that this framework has several similarities and differences from its planar counterpart. Notably, depending on the graph, we find solutions that do not exist in the planar theory. We study this framework on a variety of graphs and tabulate solutions.

In the second part, we investigated non-adiabatic perturbations of a topological memory that consists of two p-wave superconducting wires separated by a non-topological junction. We consider noise in the potential creating the non-trivial topological phase and also the effect of shuttling the Majoranas, a necessary step in braiding. We examine a mechanism for bit and phase flip errors where excitations from one wire tunnel through a junction into another wire, we also outline a scheme that utilises disorder to minimise such situations.

In the final part of the thesis, we construct a modified toric code from Hopf algebra gauge theory. We find that introducing a non-trivial quasitriangular structure on the gauge group changes the identification of braiding statistics in the quantum double, although it is of the same topological order as the toric code. In particular, when the gauge group is $\mathbb{C}\mathbb{Z}_N$ we can interpret this as a form of flux attachment, where under exchange, the electric charges behave as if they have fluxes attached.

Chapter 1

Introduction

Among the notable advancements in recent times, the discovery of anyons and their relevance to topological phases of matter is particularly interesting. Anyons attract considerable interest in modern developments in condensed matter physics, quantum information theory, and mathematical disciplines such as topology and category theory. Topological phases of matter are characterised by topological invariants, that can be calculated from the ground state wavefunction. Generically, the Hamiltonian's describing these systems have an energy gap, separating the high energy states from the ground state manifold. Another interesting property of these systems is that the ground state manifold's dimension depends on the spatial manifold's topology. In these systems, the behaviour of low-energy states is described using topological quantum field theory. Notably, anyons, which are quasiparticle excitations in two spatial dimensions, display unique exchange statistics. This statistical behaviour is known as braid statistics, and extends beyond the usual fermionic and bosonic statistics observed in standard quantum mechanics. These systems can be effectively realised in laboratory conditions by energetically penalising motion in one direction. One of the modern motivations for the study of anyons is their application in a fault-tolerant regime of quantum computation, known as topological quantum computation. In this regime, the logical qubit is encoded within the non-local degenerate ground state manifold. These encoded qubits are manipulated by adiabatically transporting anyons around one another, thereby implementing quantum gates. The remarkable aspect of this approach is that both the qubits and the gates rely solely on the system's topology, rendering them inherently resistant to local error processes that commonly afflict traditional quantum computing architectures. Mathematically topological phases of matter can be understood as a topological quantum field theory (TQFT). These abstract quantum field theories can be modelled axiomatically in category theory and have sparked their own interest. One of the applications of category theory is that it allows a description of the crucial properties of the anyons, which does not depend on specifics of a particular realisation, i.e. microscopic details. Of further interest is the fact that often a TQFT

can be described by a finite set of combinatorial data arising from solving polynomial equations. This means we can describe the collection of anyons, multi-anyon states and their exotic braid statistics in one structure, known as a braided tensor category.

Quantum exchange statistics and anyons

Historically, one of the first papers to formally analyse quantum exchange statistics in different spatial dimensions was the work by Leinaas and Myrheim ([111]). They analysed the topology of the particles' configuration space, in different spatial dimensions. The configuration space is the space of particle positions, and by analysing the space of paths on the configuration space (i.e. the first fundamental group), they studied the possible particle trajectories, including those that arise due to exchanging two or more particles. They showed that in $3 + 1$ dimensions or greater, the unitary operators corresponding to the exchange of two particles transform under irreducible representations of the permutation group. In particular, bosonic exchange corresponds to the trivial representation, and fermionic exchange the alternating representation. Crucially, for either particle, exchanging twice is equivalent to not exchanging the particles at all. However, in $2 + 1$ dimensions, they showed that the unitary operators transform under irreducible representations of the Artin braid group, and hence they are said to have *braid statistics*. This means that under exchange, the wave function can acquire *any* phase factor, hence the name "anyon" ([173]). Crucially, exchanging twice is not necessarily equivalent to not exchanging. This gives a much larger class of possible particle statistics in $2 + 1$ than in $3 + 1$ dimensions.
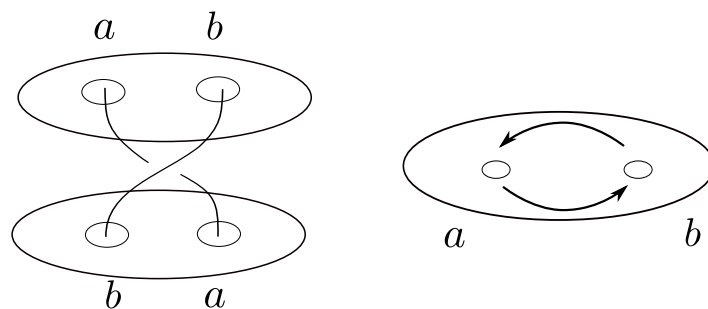
Figure 1.1: A spacetime picture of a braid (left) and a top-down view of the exchange (right)

This was developed further in the 1980s and non-Abelian anyons were introduced. Non-Abelian anyons are a type of anyon possessing non-commutative braiding properties, and when two non-Abelian anyons are combined, there is more than one possible type of anyon that can result. If we denote the unitary operator exchanging the ith anyon with the jth anyon by U_{ij}, then the composition of exchanges, $U_{ij}U_{jk}$, is

in general, not equal to $U_{jk}U_{ij}$. This is very different from bosons or fermions. Originally they were proposed in the context of conformal field theory (126; 127; 128), as well as in the context of Chern-Simons theory (175) and later in quantum field theory (78). The presence of non-Abelian anyons signals the ground state manifold is degenerate on any manifold. This is because when two non-Abelian anyons are combined, there is more than one possible outcome, given by the fusion rules. For example, one anyon model we will frequently encounter is the Ising model, and it has a non-Abelian anyon generally denoted σ. This anyon has fusion rules: $\sigma \times \sigma = 1 + \psi$. This states that if we bring two σ anyons together, they may fuse to a ψ-excitation or a 1-excitation, and 1 is interpreted as the vacuum. Hence this is an example of a non-Abelian anyon. Therefore, if we have a collection of σ-anyons and fix the final anyon, given by fusing all of the anyons, there are still degrees of freedom associated with each in-between fusion outcome. The collection of in-between fusion outcomes is known as the fusion space. The non-Abelian braid statistics and the fusion space form the foundation of topological quantum computation (TQC).

Topological quantum computation
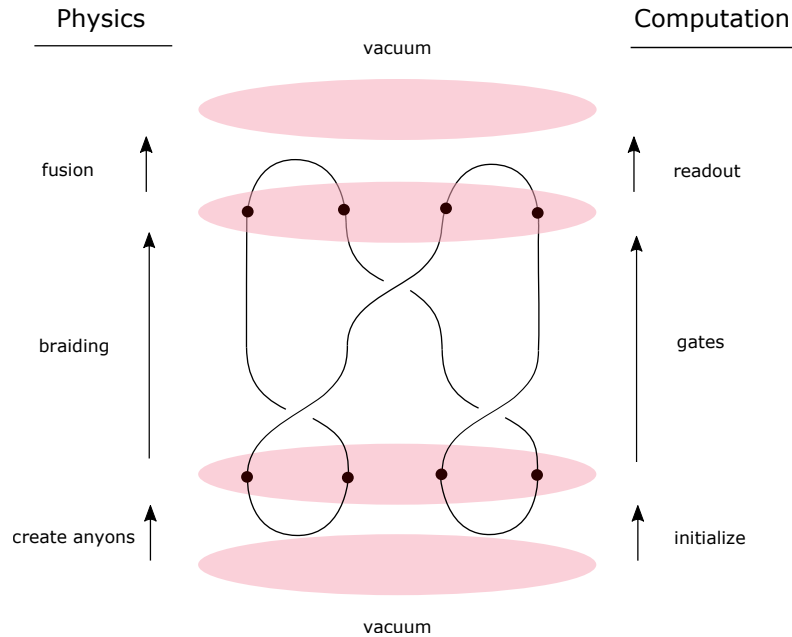
Figure 1.2: The conceptual schematic of how topological quantum computation proceeds.

One of the major challenges in quantum computation is reducing the interaction between the qubits and the environment. Otherwise, this can cause the quantum states of the qubits to undergo uncontrolled phase changes or get entangled with the environment. As a result, the delicate quantum information encoded in the qubits becomes corrupted. In TQC, introduced by Kitaev (102), anyons are harnessed for

their unique properties to perform quantum computations in a fault-tolerant manner. The key idea is to encode quantum information using the non-local fusion space of anyons and to implement the quantum gates by braiding the anyons. Specifically, the logical qubit is not encoded in a local piece of the system, such as the spin or charge of one particular anyon. Instead, it is encoded in the space of fusing outcomes of many different anyons, which can be spatially separated. This makes the qubit inherently resistant to local error processes. Braiding the anyons generates unitary operators acting on the fusion space. Braiding generates gates such as NOT or phase gates for the quantum computer depending on the types of anyons and the types of exchanges. When the braiding is performed adiabatically, i.e. slowly compared to a timescale set by the energy gap, the braiding only leads to rotations within the ground state manifold, corresponding to states in the fusion space. Furthermore, the braiding leads to a non-Abelian Berry phase (geometric phase), which does not depend on the exact geometric details of the trajectory itself, only its topology. Hence the corresponding unitary operator is also topological and therefore, the gate is also topological.

The main candidate systems are the fractional quantum Hall effect discovered by Tsui (167). Several different anyon models we will encounter have been proposed to exist in FQHE systems. One notable example is the $\nu = 5/2$ state, which was first studied in (126). In this model, there are vortices in the electron gas, which can host exotic states, known as *Majorana bound states* (MBS). MBS are zero energy excitations that give rise to a degenerate ground state manifold (57; 144; 137). The MBS can be effectively modelled by the σ anyon in the Ising model we discussed previously. On the experimental side, there is a large body of evidence supporting Abelian anyons in the FQHE, see e.g. (67; 83; 151), and in fact they are essential to the theoretical understanding of the FQHE. However to date, there has been no confirmed measurement of the braiding of non-Abelian anyons. Despite this, there is still a large effort to produce these systems.

Another platform which has been proposed for anyons is topological superconductors. One of the first proposed instances of this was by Read and Green (144). They showed that the MBS we mentioned for the $\nu = 5/2$ FQH state can also arise in a two-dimensional $p + ip$-superconductor. This led to the search for other condensed matter platforms that could host excitations that behave like anyons. One of the most relevant platforms for our present context is MBS arising on one-dimensional nanowires. In (99), Kitaev proposed that a one-dimensional p-wave superconductor could host MBS if there are insulating boundaries on both ends of the wire. The two MBS are at opposite ends of the wire. When they are brought together, they may fuse into a Bogoliubov fermion or annihilate. This is the same fusion rules as the σ anyon we mentioned earlier. Due to the non-local nature of the MBS, this system has been proposed as a way to store information for quantum computation.

Graph braiding

One ingredient that is missing for TQC on nanowires is braiding. Even if we can create excitations in one dimension, which mirrors many of the properties of anyons in two dimensions, we clearly can't braid the excitations. However, by joining nanowires into junctions, we can implement braiding. This was first proposed for MBS in (8). They showed that one can recover non-Abelian braid statistics by forming a simple trijunction and shuttling the MBS. The MBS are bound to the interfaces between the nanowire and the insulating boundaries, so they can be shuttled by tuning the underlying voltage in segments of the nanowire (18; 95). There has already been extensive analysis on the effect of this process on the topological qubit (45; 156). However, this has only been developed for MBS. One may wonder, can only MBS be made on networks of $1d$ wires? This is related to another perspective. As we mentioned, the exchange of anyons in the plane generates unitary operators corresponding to representations of the braid group, but if we're now exchanging anyons by shuttling around networks, does the planar braid group still govern the exchange statistics? In essence, we are now thinking about *braiding on networks*.
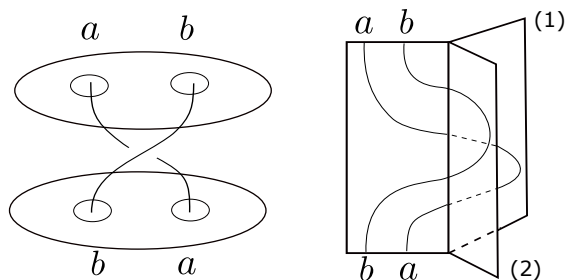
Figure 1.3: A comparison between planar braiding (left) and braiding on a trijunction as an example of a graph braid (right).

For particles moving on networks, there are a variety of exchange groups, known as graph braid groups, the actual structure of the graph braid group depends on the graph in question. These have recently been analysed in some detail in (10; 115; 116), and are the natural tool to study the exchange statistics of particles on wire networks without reference to a two-dimensional medium. Graph braid groups are constructed similarly to how Leinaas and Myrheim arrived at the braid group governing exchanges in $2 + 1$ dimension. One first constructs a space of particle positions on a graph and then studies topologically inequivalent paths in this configuration space, exchanging the particles. For simple junctions, such as the trijunction, graph braid groups are free groups, allowing for arbitrary statistical exchange phases. This suggests that more physical input is needed to pick specific graph braid representations. This poses a rather natural question: for a given set of fusion rules, can we recover the same graph braid statistics as the planar anyon models? This question will be one of the central focuses of this thesis.

1.1 Overview

In Chapter 2, we review the formalism of anyonic excitations and the connection to braided tensor categories. We shall illustrate the connection without an in-depth analysis of category theory itself. Instead, we will focus on the algebraic theory of anyons and the equivalent categorical concepts like; fusion rules, F and R symbols and their origin equations; the pentagon and hexagon equations. We will close the chapter by collecting standard quantities for some of the commonly studied anyon models such as; $\mathbb{Z}_N$, quantum double models, Tambara-Yammagami categories and Fibonacci anyons.

In Chapter 3, we will discuss our adaption of graph braid groups with the anyon formalism developed in the previous chapter. Our main focus will be on explaining how to adapt fusion commuting with braiding to braiding on a graph. The result of this will be the graph hexagon equations, our generalisation of the planar hexagon equations. These equations constrain the possible exchange statistics of anyon-like excitations on a quantum wire network. We shall focus in particular on a trijunction and a tetrajunction. We will discuss solutions for the following fusion categories; $\mathbb{Z}_N$, Ising and Fibonacci anyons. The results in this chapter are based on (50).

In Chapter 4, we will extend the graph anyons models of the previous chapter to more general graphs. In particular, we will introduce graphs containing loops. These graphs introduce new braid moves and we construct further graph hexagon equations for the new moves and discuss compatibility with the moves introduced in the previous chapter. We will also solve the graph hexagon equations on these new graphs for fusion rules such as $\mathbb{Z}_N$, Tambara-Yammagami and Fibonacci anyons. One of the notable graphs introduced here is the circle graph, on which we find coherence of the model at $N = 3$ particles. We will discuss further anyon model quantities that we introduced in Chapter 2, like topological twist. We will also give an anyon-adapted proof that on a theta graph, one recovers the planar anyon models. We close the chapter by discussing a topological qubit constructed from graph braided anyon models. The results in this chapter are based on (114).

In Chapter 5, we will provide background material on quantum nanowires hosting Majorana zero modes. We will discuss the existence of Majorana-bound states on p-wave superconductors. This is a toy model displaying many of the ideal features for topological memories or topological qubits. We will also discuss the exchange statistics of Majorana bound states on a trijunction, originally proposed in (8).

In Chapter 6, we consider the p-wave superconductor from Chapter 5 and focus on the error process that can occur in a topological qubit constructed from Majorana bound states. In particular, we analyse two regimes of non adiabatic perturbation: periodic bound driving and deliberate shuttling of the topological qubit. The first of these error processes is related to the accuracy of controlling the boundaries that define the non-trivial topological phase.

The latter is related to transporting the qubit. This is the first step in braiding excitations on a network of quantum wires, which if done in a finite time, is an inherently non-adiabatic process. The results in this chapter are based on (49).

In Chapter 7, we review the toric code model introduced in (102). In particular we focus on the quantum double structure of excitations, which gives a lattice realisation of anyons in an exactly solvable model. We shall also discuss the generalisation to non-Abelian groups.

In Chapter 8, we discuss our paper (48), on Hopf algebra gauge theory and toric code models. Our work in this area will be studying applications of this formalism to Hopf algebras constructed over finite groups, the closest one could remain to the discrete group lattice gauge theory. We will show that on a lattice, with gauge group $\mathbb{Z}_N$, the braided tensor product from (124), induces a permutation on the particle exchange statistics in the resulting quantum double. The results in this chapter are based on (48).

Finally, in Chapter 9, we discuss conclusions and further directions of work.

The aim of Chapters 2, 5 and 7 is to provide background material for Chapters 3, 4, 6 and 8 respectively.

This thesis is based on the following publications, coauthored by the author of this thesis:

- (48) A. Conlon, D. Pellegrino and J. K. Slingerland, **Modified toric code and flux attachment from Hopf algebra gauge theory**,

- (49) A. Conlon, D. Pellegrino, J. K. Slingerland, S. Dooley and G. Kells, **Error generation and propagation in Majorana-based topological qubits**.

- (50) A. Conlon and J.K. Slingerland, **Compatibility of Braiding and Fusion on Wire Networks**,

- (114) T.Maciążek, A. Conlon, G. Vercleyen and J.K. Slingerland, **Extending the planar theory of anyons to quantum wire networks**,

Chapter 2

Anyons and categories

2.1 Introduction

This chapter will focus on anyons, which are localized quasiparticle excitations in two-dimensional topological phases of matter. They have been proposed to arise as low-energy excitations in several condensed matter systems, most notably the fractional quantum Hall effect (FQHE). The FQHE is a highly interacting electron gas with long-range correlations, making it very difficult to understand. One of the most interesting features is that the low-energy excitations have exchange statistics that are not necessarily fermionic or bosonic and in fact form a representation of the braid group. In particular, they can have "any" $U(1)$ exchange statistics, hence named Abelian "anyons". It has also been proposed that even more exotic anyons may exist, which have non-Abelian exchange statistics. Of course, anyons are not fundamental particles and instead should be thought of as collective behaviour of many fermions, or regions which have fewer electrons, i.e. quasiparticles and quasiholes. As many-body excitations in a condensed matter system, these excitations can be hard to understand. One of the main approaches to understanding these systems is proposing trial wave functions, motivated by simpler situations or good physical principles.

In this chapter, we will focus on an abstract model of anyons, which is deeply connected to category theory. We will essentially abstract the physical system of anyons to three mathematical structures. Furthermore, we will make extensive use of graphical calculus, to convey spacetime processes. This is captured by the language of unitary braided fusion categories (UBFC). This framework allows one to describe the universal properties of the excitations without referring to the microscopic degrees of freedom. Firstly, our particles will be labelled by what is often called a topological charge. This could be some local quantum number, such as a winding number of a vortex, or electrical charge or spin. The exact nature of this quantum number will not be relevant in this present context. Instead, for us, it will be some abstract label.

The collection of these labels in our model will have the structure of a fusion algebra. Secondly, our Hilbert space will be given by outcomes of including composites, or fusing, of the topological charges. In particular, a state in our Hilbert space will be some outcome for fusing two anyons. When we have several anyons present, there are multiple orders in which we could fuse them. The different compositions of fusing order are related by unitary matrices known as F-symbols. Thirdly, and the most interesting structure: braiding. We will encode space-time processes where two or more particles exchange their position into unitary maps relating different states in our fusion Hilbert space. These operators are known as R-symbols.

The material contained in this chapter is a review of known results, see for example the textbooks on this topic (140; 159). We will first build up the mathematical structures and then discuss the equivalent structure in anyon models. At the end of the chapter in Section 2.6 we provide several notable examples of anyon models encountered in this thesis. We aim to explain the core concepts in the "algebraic theory of anyons" (100; 128). In Chapter 3 and Chapter 4, we will extend the algebraic theory of anyons to exchanges on graphs.

In particular, we want a mathematical structure to capture the following crucial aspects;

- distinct types of anyon excitations labelled by their topological charge and these charges satisfy a fusion algebra structure:

$$a \times b = \sum_c N_c^{ab} c \tag{2.1}$$

- general (possibly non-Abelian) exchange statistics

$$R_c^{ab} : a \times b \to b \times a \tag{2.2}$$

where R_c^{ab} is the unitary operator giving the effect of exchanging the locations of anyon a with anyon b, which when fused have a total charge c.

We summarise the connection between UBFCs and anyon models in Table 2.1. We will explain this connection throughout the chapter.

Topological order	UBTC	Anyon model
Algebraic data	$(\mathcal{C}, \oplus, \otimes, 1, \alpha, C)$	$(N_c^{ab}, R_c^{ab}, \left[F_d^{abc}\right]_{ef})$
Anyon types	Isomorphism classes of simple objects	Fusion algebra
Fusion & recoupling rules	monoidal structure & associator	fusion rules & F-symbols
Exchange statistics	Braiding	R-symbols

Table 2.1: This is an example of a Rosetta stone for translating the concepts relevant to this chapter between category theory and anyon models.

2.2 Fusion categories

We shall start with the relevant categorical structure. We will essentially follow the standard definitions which can be found in (69). For a comprehensive treatment of foundational category theory, we recommend the text by Mac Lane (108). The categories that find application in topological phases of matter are particularly concrete, compared to the general algebraic theory, so we will focus only on the relevant structures here and try to justify them on physical grounds. To describe a category we need to discuss the objects, maps between objects (which are referred to as morphisms), and which structures we have on the category. Before giving the formal definition of a fusion category, we will try to motivate some of the features.

Objects

In the categories describing topological phases of matter, we have a finite set of distinct types of excitations, called the set of objects, $\mathcal{C}^0$. We shall denote objects in a category by:

$$A, \quad B, \quad C, \ \ldots. \tag{2.3}$$

We require that the category is semisimple, meaning any object in the category can be written as a direct sum of finitely many simple objects. We further require there is a special simple object, 1, called the unit. This will correspond to the vacuum charge in anyon models. Therefore, requiring the unit object to be a simple object means that on a disk, we can identify this configuration with the absence of anyons.

Morphisms

The collection of morphisms between any two objects is denoted $\mathrm{Hom}(X,Y)$. The morphisms are often represented by strings between vertices, which makes an analogy with anyon models rather fitting. We require that the Hom spaces have the structure of a finite-dimensional $\mathbb{C}$-linear vector space. We will model an anyon by a simple object in the category, so $\mathrm{Hom}(A, A) \simeq \mathbb{C}$. Additionally we can not transform one anyon into another, so $\mathrm{Hom}(A, B) = \delta_{A,B}\,\mathbb{C}$. We also require the fusion category to be unitary, meaning we have a Hermitian adjoint structure on the Hom spaces to allow a positive definite inner product, i.e. this will be our model for the Hilbert space. This is further interpreted as having a structure of duals on the anyons.

Fusion product and associativity

The monoidal product $\otimes$ is the categorical abstraction of the fusion product, which we discuss in detail in Section 2.3. This allows us to consider "combined objects", like $A \otimes B$. The semisimplicity then tells us that we can express the combined object $A \otimes B$ in terms of a finite sum of simple objects, i.e.

$$A \otimes B = \bigoplus_{C \in \mathrm{Irr}(\mathcal{C})} N_C^{AB} \, C \ , \qquad (2.4)$$

where by $\mathrm{Irr}(\mathcal{C})$ we denote the set of isomorphism classes of simple objects in $\mathcal{C}$. For example, when $\mathcal{C}$ is the category of representations of a finite group, then the monoidal product is the familiar tensor product and the simple objects are irreducible representations.

In a fusion category, we do not have associativity of multiplying (combining) exactly. Instead, there is an isomorphism, the associator, relating distinct compositions. In this sense, we can see a category as a weakening of other algebraic structures. For instance, in a group, associativity is an axiom, i.e. $(g_1 \times g_2) \times g_3 = g_1 \times (g_2 \times g_3)$. Here instead this is weakened, we have an isomorphism relating the two compositions. This idea falls under the umbrella of "categorification" (69; 108).

Definition 2.2.1. A fusion category is a finite semisimple tensor category, $(\mathcal{C}, \otimes, \alpha, 1, l, r)$, with simple unit, 1 and the monoidal product $\otimes : \mathcal{C} \times \mathcal{C} \to \mathcal{C}$. By α we denote the associator isomorphism

$$\alpha_{A,B,C} : (A \otimes B) \otimes C \to A \otimes (B \otimes C). \tag{2.5}$$

For $A, B, C, D \in \mathcal{C}^0$ the following pentagon diagram commutes,

$$
\begin{array}{c}
(A \otimes B) \otimes (C \otimes D) \\
\end{array}
$$

$$
\begin{array}{ccc}
& \alpha_{A \otimes B, CD} & \alpha_{A,B,C \otimes D} \\
((A \otimes B) \otimes C) \otimes D & & A \otimes (B \otimes (C \otimes D)) \\
\alpha_{A,B,C} \otimes \mathrm{id}_D & & \mathrm{id}_A \otimes \alpha_{B,C,D} \\
& (A \otimes (B \otimes C)) \otimes D \xrightarrow[\alpha_{A,B \otimes C,D}]{} A \otimes ((B \otimes C) \otimes D) &
\end{array}
$$

$$\tag{2.6}$$

For natural isomorphisms, $l_A : 1 \otimes A \to A$ and $r_A : A \otimes 1 \to A$, called the left and right unit isomorphisms, the following triangle diagram commutes,

$$
\begin{array}{ccc}
(A \otimes 1) \otimes B & \xrightarrow{\alpha_{A,1,B}} & A \otimes (1 \otimes B) \\
& & \\
r_A \otimes \mathrm{id}_B & & \mathrm{id}_A \otimes l_B \\
& A \otimes B &
\end{array}
$$

$$\tag{2.7}$$

As we can see in the pentagon diagram 2.6, each vertex is given by one particular parenthesization of four objects in $\mathcal{C}$. The isomorphism α allows us to recouple the bracketing, which translates to moving between the different vertices. The equating of the upper and lower compositions of the pentagonal diagram is called the associativity constraint. In Section 2.3 we will see this diagram leads to the pentagon equation.

Coherence

If we consider the possible parenthesization of five objects, this would introduce a larger diagram. However, it was proven in (117) that the pentagon axiom is sufficient for consistent reparenthesization of any number of objects. This is known as the Mac Lane Coherence theorem.

Theorem 2.2.2. *Let* $\{A, B, \ldots, C\} \in \mathcal{C}$. *Let* P_1, P_2 *be any two parenthesized product of* $(A, B, \ldots, C)$ *(in this order) with arbitrary insertions of the unit object* 1. *Let* $f, g : P_1 \to P_2$ *be two isomorphisms obtained by composing associativity and unit isomorphisms and their inverses possibility tensored with identity morphisms. Then* $f = g$.

This theorem tells us that for any choice of parenthesization on any number of objects, if we construct a diagram, with two separate paths starting from one parenthesization to another, then the sequence of morphisms corresponding to the two paths are equal, exactly. We will discuss the reparenthesization in the context of anyon models in Section 2.3, and in particular, the pentagon equation for anyon models is given in Equation (2.19).

2.3 Anyon types, fusion rules and F-symbols

To apply the abstract structure we just described to anyon physics, we move to the skeletonisation of the fusion category. This consists of choosing a basis and a representative element in each isomorphism class. This gives us the finite set of anyon types, corresponding to the fusion category's object set. In this view, we are studying the underlying fusion algebra of the category. Further details and definitions can be found in (69). A fusion algebra has a finite set of topological charges $\mathcal{L}^0$,

$$1, \quad a, \quad b, \quad c, \ldots . \tag{2.8}$$

The monoidal product is given in terms of fusion rules

$$a \times b = N_c^{ab} c + N_d^{ab} d + \cdots = \sum_{c \in \mathcal{L}^0} N_c^{ab} c. \tag{2.9}$$

The $\times$ notation indicates fusion, whereas $+$ indicates possible outcomes. We use $\times$ to make a distinction between the fusion of anyons and an abstract monoidal product ($\otimes$) in a category. The coefficients $N_c^{ab} \in \mathbb{Z}_{\geq 0}$ are the dimension of the fusion space V_c^{ab} of ground states with two particles of charges a and b, and with overall charge c. For multiplicity free fusion rules, then each N_{ab}^c is 0 or 1.

The key space involved in the description of anyons is the fusion space denoted V_c^{ab}. This is the anyon notation corresponding to the finite-dimensional $\mathbb{C}$ vector space, $\mathrm{Hom}(A \otimes B, C)$. The choice of orthonormal basis for each nontrivial fusion space V_c^{ab}, introduces a gauge freedom u_c^{ab}, a unitary matrix of dimension N_c^{ab}. In the multiplicity free case, $u_c^{ab} \in U(1)$. There is an equivalent description in terms of splitting spaces, which are the dual vector spaces and often denoted V_{ab}^c. A set of normalised basis vectors for these spaces are often represented graphically as,
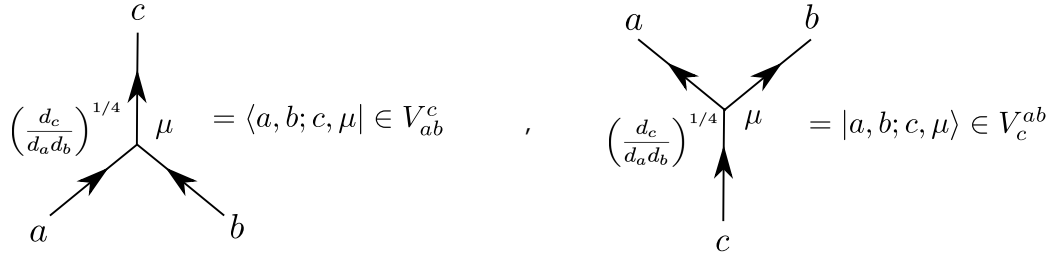
Figure 2.1: A graphical representation of fusion and splitting trees.

where $\mu = 1, \ldots, N_c^{ab}$, labels the basis vector for particular a, b, c. The normalisation of these states is chosen such that we have isotopy invariance (159). Here we can see the duality between the fusion and splitting spaces. We can write these as basis vectors in the Hom spaces in the skeletal category as, $\mathrm{Hom}(c, a \times b)$ and $\mathrm{Hom}(a \times b, c)$.

We note the worldlines (strings) in Figure 2.1 are oriented. Inverting the orientation of a line is equivalent to dualising the charge of the particle. The relation between anyon and "dual" anyon is often graphically represented as

We will generally omit the directional arrows on graphical diagrams, and hence any worldline drawn is oriented upwards. If $a = \bar{a}$, then the anyon is said to be self-dual.

Each fusion algebra contains a unique object called the vacuum charge, generally denoted as 1. Fusion with the vacuum is trivial

$$a \times 1 = 1 \times a = a. \tag{2.10}$$

This implies the following condition on the fusion coefficients

$$N_b^{a1} = N_b^{1a} = \delta_{ab}. \tag{2.11}$$

Physically, we interpret this as the ability to introduce and remove vacuum charges freely.

This is the anyon model analogue of the left and right unit isomorphisms being the identity map. Each anyon has a unique antiparticle $\bar{a}$ such that,

$$a \times \bar{a} = \bar{a} \times a = 1 + \ldots \qquad \forall\, a \in \mathcal{L}^0. \tag{2.12}$$

If an anyon is Abelian, then there will be the unique outcome of the vacuum excitation, 1, on the right-hand side. However when an anyon is non-Abelian there can be more than one outcome on the right-hand side. We have already encountered an example of this, the σ anyon mentioned in the Introduction and we will see more examples in Section 2.6. This implies the following condition on the fusion coefficients,

$$N_1^{a\bar{a}} = N_1^{\bar{a}a} = 1_{\mathbb{C}}. \tag{2.13}$$

We use a subscript on the right-hand side to make a distinction between 1, the vacuum anyon and $1_{\mathbb{C}}$, the number in the complex field $\mathbb{C}$. When the fusion product is commutative, the fusion coefficients satisfy the following relations,

$$N_c^{ab} = N_c^{ba}. \tag{2.14}$$

However, this does not imply that the braiding is Abelian.

For unitary theories, each particle has an associated quantity known as quantum dimension or Frobenius-Perron dimension (69). This is represented graphically as

$$a \; \bigcirc = d_a$$

This means in any arbitrarily complicated spacetime history, we can remove a closed loop from the diagram at the cost of the quantum dimension of the anyon. The collection of quantum dimensions forms a one-dimensional representation of the fusion algebra, so they satisfy the fusion rules of the theory,

$$d_a d_b = \sum_{c \in \mathcal{C}^0} N_c^{ab} d_c \ . \tag{2.15}$$

The total quantum dimension or global dimension is defined as

$$\mathcal{D} = \sqrt{\sum_a (d_a)^2} \ . \tag{2.16}$$

F-symbols and the pentagon equation

In this previous section we defined our basis vectors for the fusion space of two anyons, V_c^{ab}. However, for practical implementations such as topological quantum computation we would like to have more than two anyons. It is mportant to understand the structure of the fusion space in the presence of several anyons. In particular, when there are three or more anyons, we can fuse them to get a fixed total charge in multiple ways. For three anyons, there are two isomorphic ways to fuse, a, b and c to get a total topological charge d.

$$V_d^{abc} \simeq \bigoplus_e V_e^{ab} \otimes V_d^{ec} \simeq \bigoplus_f V_d^{af} \otimes V_f^{bc} \tag{2.17}$$

The F-symbols define a natural isomorphism between these decompositions with respect to a basis for each fusion space,

$$[F_d^{abc}]_{e,f} : \bigoplus_e V_e^{ab} \otimes V_d^{ec} \rightarrow \bigoplus_f V_d^{af} \otimes V_f^{bc}. \tag{2.18}$$

The F-symbols are the coefficients of the associator of the monoidal product with respect to a basis for the vector spaces V_c^{ab}. The action of F-symbols are depicted as,

Figure 2.2: Definition of the F-symbols

The F-symbols are required to satisfy the *pentagon equation* (69; 128; 140). This comes from the pentagon axiom in Section 2.2.

$$\left[F_e^{fcd}\right]_{gl} \left[F_e^{abl}\right]_{fk} = \sum_h \left[F_g^{abc}\right]_{fh} \left[F_e^{ahd}\right]_{gk} \left[F_k^{bcd}\right]_{hl} \tag{2.19}$$

Each of the F-symbols relates different decompositions of V_e^{abcd}. The diagram corresponding to the pentagon equation is depicted in Figure 2.3.

As discussed, we need only solve the pentagon equation for a consistent set of F-symbols (69; 100; 108). Morally, this is a statement of locality. The coherence theorem guarantees that the solution of the equation is sufficient for consistent recoupling rules in any arbitrarily complicated space-time history, containing any number of particles. Or in other words, if we constructed a diagram, similar to the pentagon diagram, except where the states on the vertices consisted of greater than four anyons, fusing in different ways, the corresponding consistency equation
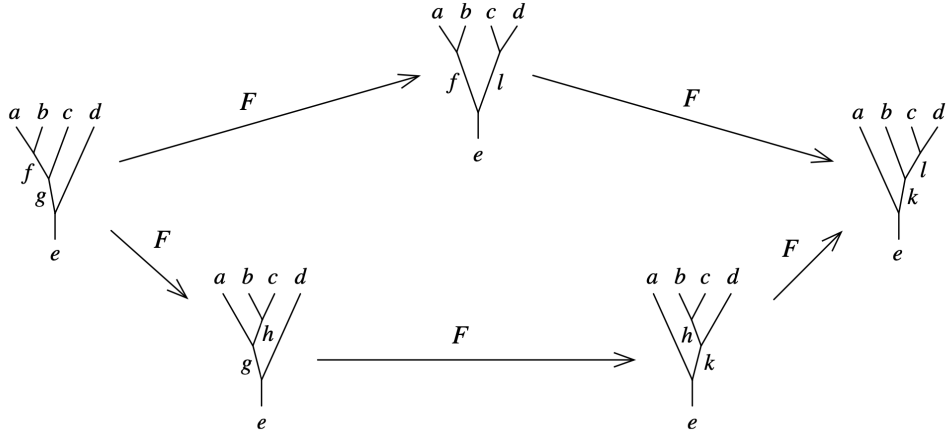
Figure 2.3: Graphical representation of the pentagon axiom with anyon fusion trees. By equating the sequences of F-symbols corresponding to the upper and lower paths, one arrives at the pentagon equation.

would not give any new constraints on the F-symbols. In fact, it would already be guaranteed by the pentagon equation.

When the category /anyon model is unitary, we have the following relations on the F-symbols

$$\left[(F_d^{abc})^\dagger\right]_{fe} = \left[(F_d^{abc})^*\right]_{ef} = \left[(F_d^{abc})^{-1}\right]_{fe}. \tag{2.20}$$

The left and right unit isomorphisms discussed in Section 2.2 can be expressed in F-symbols by the following,

$$l_a = \left[(F_a^{11a})^{-1}\right]_{1a}, \qquad r_a = \left[F_a^{a11}\right]_{a1}. \tag{2.21}$$

In general, one chooses a basis such that if one or more of the superscripts in an F-symbol is the vacuum charge, 1, the F-symbol is unity. This is why the unit isomorphisms in Definition 2.2.1 are generally not addressed in anyon models. The action of gauge transformation or a change fo basis for the fusion space has the following effect on the F-symbols

$$[F_d^{abc}]'_{ef} = \frac{u_d^{af} u_f^{bc}}{u_e^{ab} u_d^{ec}} [F_d^{abc}]_{ef}. \tag{2.22}$$

Another interesting quantity related to F-symbols is the Frobenius Schur indicator of an anyon a, which we denote by ν_a. For the Ising theory in Section 2.6.2, the two inequivalent solutions to the pentagon equation are labelled by ν_σ. See for example (100; 140; 160). This is graphically given by,
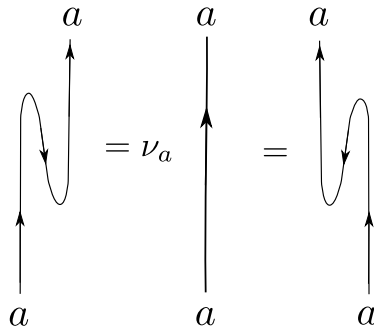
Figure 2.4: The Frobenius-Schur indicator expresses the straightening of the "zig-zag" diagram.

The Frobenius-Schur indicator of an anyon a is $\nu_a = \pm 1$. If an anyon is not self-dual, then ν_a can be fixed to be 1. But if an anyon is self-dual, i.e. $\bar{a} = a$, then ν_a is a gauge invariant quantity. Frobenius-Schur indicators being non-trivial ($\nu_a = -1$) can lead to the diagrammatic calculus not being isotopy invariant, which means it is not a properly topologically invariant algebraic model for a TQFT. A more detailed discussion can be found in (107; 160). This concludes the fusion structure of anyon models now, we move on to braiding structures on categories.

2.4 Braided fusion category

Now that we have discussed the formalism of fusing and splitting of anyons, which is the anyon version of the monoidal structure of the fusion category, we now turn our attention to the *braiding* part of UBFC. This mathematical structure is suitable for modelling the exchange statistics of anyons. We will first discuss the mathematical formalism and then, in the following subsection, discuss how this is applied to anyon models. For further details on the mathematics of braiding, particularly in the context of quasitriangular Hopf algebras, to which much of the formalism can trace its roots, see (96; 118).

Definition 2.4.1. A braiding on a fusion category $(\mathcal{C}, \otimes, 1, \alpha)$ is a family of natural isomorphisms,

$$c_{A,B} : A \otimes B \to B \otimes A \tag{2.23}$$

so that the following hexagon diagrams commute,

$$
\begin{array}{ccc}
& A \otimes (B \otimes C) \xrightarrow{c_{A,B \otimes C}} (B \otimes C) \otimes A & \\
\alpha_{A,B,C} \nearrow & & \searrow \alpha_{B,C,A} \\
(A \otimes B) \otimes C & & B \otimes (C \otimes A) \\
c_{A,B} \otimes \mathrm{id}_C \searrow & & \nearrow \mathrm{id}_B \otimes c_{A,C} \\
& (B \otimes A) \otimes C \xrightarrow[\alpha_{B,A,C}]{} B \otimes (A \otimes C) &
\end{array}
\tag{2.24}
$$

$$
\begin{array}{ccc}
& (A \otimes B) \otimes C \xrightarrow{c_{A \otimes B,C}} C \otimes (A \otimes B) & \\
\alpha_{A,B,C}^{-1} \nearrow & & \searrow \alpha_{C,A,B}^{-1} \\
A \otimes (B \otimes C) & & (C \otimes A) \otimes B \\
\mathrm{id}_A \otimes c_{B,C} \searrow & & \nearrow c_{A,C} \otimes \mathrm{id}_B \\
& A \otimes (C \otimes B) \xrightarrow[\alpha_{A,C,B}^{-1}]{} (A \otimes C) \otimes B &
\end{array}
\tag{2.25}
$$

There are also two diagrams corresponding to the inverse braiding, denoted $c_{A,B}^{-1}$, but they are implied already by these diagrams.

The braiding being a natural isomorphism is part of a larger structure of functors and natural transformations, however, here we take it to mean that braiding is compatible with fusion. By this we mean, if we braid two anyons, $c_{A,B} : A \otimes B \to B \otimes A$, then this process should not change the fusion of A and B. Therefore, this leads to an isomorphism between $A \otimes B$ and $B \otimes A$. We recommend (108), for exact details on natural transformations.

We can see that braiding relates the object $A \otimes B$ to the object $B \otimes A$. Hence, the hexagon axiom is also called a commutativity constraint since braiding is, in essence, a weakening of commutativity (118). This concept can be made more exact by considering the centre of an algebra, which is defined by elements a, b such that $a \times b = b \times a$. We can adapt this concept to categories. In going from a conventional algebraic structure to a category one weakens equalities to say they hold "up to" isomorphism. We see then the close connection between the centre of an algebra

19

and a braided fusion category, as $c_{A,B}$ is an isomorphism relating $A \otimes B$ to $B \otimes A$.

There is a generalisation of the Mac Lane coherence theorem for braided monoidal categories (141). As a result, the description of the braiding of three objects is sufficient for any number of objects, analogous to how the description of fusion of four objects is sufficient for any number of objects. We can make a closer connection with the braid group by considering a strict fusion category.

Definition 2.4.2. A monoidal category $\mathcal{C}$ is strict if for all objects A,B,C, the following is true

$$(A \otimes B) \otimes C = A \otimes (B \otimes C),$$
$$A \otimes 1 = 1 \otimes A = A,$$

which states the associativity isomorphism and the unit isomorphisms are given by

$$\alpha_{A,B,C} = \mathrm{id}_{A \otimes B \otimes C} \qquad r_A = l_A = \mathrm{id}_A . \tag{2.26}$$

In a strict braided category, all morphisms in the hexagon axiom which only involve reparentization become trivial and so, the hexagonal diagrams become triangles. The following diagram can be constructed from the two hexagon axioms

$$\tag{2.27}$$

By starting at $A \otimes B \otimes C$ and traversing the diagram in two different paths to arrive at $C \otimes B \otimes A$, the Yang-Baxter equation can be read off of this diagram,

$$(c_{B,C} \otimes \mathrm{id}_A) \circ (\mathrm{id}_B \otimes c_{A,C}) \circ (c_{A,B} \otimes \mathrm{id}_C) = (\mathrm{id}_C \otimes c_{A,B}) \circ (c_{A,C} \otimes \mathrm{id}_B) \circ (\mathrm{id}_A \otimes c_{B,C}).$$
$$\tag{2.28}$$

In fact, in a braided strict monoidal category, the hexagon diagrams in Definition 2.4.1 can be expressed by the following equations

$$c_{A,B \otimes C} = (\mathrm{id}_B \otimes c_{A,C}) \circ (c_{A,B} \otimes \mathrm{id}_C),$$
$$c_{A \otimes B,C} = (c_{A,C} \otimes \mathrm{id}_C) \circ (\mathrm{id}_A \otimes c_{B,C}). \tag{2.29}$$

These equations express that braiding an object $A \otimes B$ with an object C is the same as braiding the consistent A with C and then the constituent B with C. We can see this is a statement of isotopy in the graphical calculus. This can be interpreted as the naturality of braiding with respect to fusion. We will discuss this in Section 2.5.

Representations of the braid group

One of the uses of BTCs is they naturally provide representations of the Artin braid group in the following sense. Fix an object, $A \in \mathcal{C}^0$ in a strict braided monoidal category and define the following action of a generator of the braid group on automorphisms on n copies of the monoidal product of A:

$$
\begin{aligned}
\rho_{n,A} : B_n &\longrightarrow \operatorname{Aut}_{\mathcal{C}}(A^{\otimes n}) \\
: \sigma_n &\longrightarrow \operatorname{id}_{A^{\otimes(i-1)}} \otimes \; c_{A,A} \; \otimes \operatorname{id}_{A^{\otimes(n-i-1)}}
\end{aligned}
\tag{2.30}
$$

Hence, the braiding on the object A induces a representation of the braid group. We can see in this representation, the Yang Baxter equation in Equation(2.28) becomes the familiar braid relation in the Artin braid group (13; 19).

One further property we need for our algebraic model of anyons is the twist and the resulting ribbon structure. In category theory, the twist is defined as a natural isomorphism of endomorphisms of an object, i.e. isomorphisms of maps from an object to itself.

Definition 2.4.3. The twist, $\theta \in \operatorname{Aut}(\operatorname{id}_{\mathcal{C}})$ satisfies the following

$$
\theta_{A \otimes B} = (\theta_A \otimes \theta_B) \circ c_{B,A} \circ c_{A,B} \quad \forall A, B \in \operatorname{Obj}(\mathcal{C}).
\tag{2.31}
$$

The twist is related to the trace of the braiding natural isomorphism (69). A twist is called a ribbon structure if $(\theta_A)^* = \theta_{A^*}$, where X^* is the dual object and $(\theta)^*$ is the dual morphism, and a vertical string starting and ending on A is identified with id_A. If every object in the BFC has a dual object, which is true in our cases, and the twist satisfies the ribbon structure, then the UBFC is called a unitary ribbon fusion category. This is a rather abstract notion, however the terminology comes from considering one particular example of a braided category, known as the framed tangle category, in which the string diagrams we have drawn are replaced with ribbons, see for example (96), for details. In our present context the twist is related to the spin of an anyon. In fact if we want to keep track of rotations of anyons on their axis, we need to extend the notion of worldlines to "world-ribbons". The terminology of ribbon comes from considering the framing of anyons (146). Then we can make an exact relation with the spin-statistics theorem. See for example (140; 159). We will discuss ribbon structure on anyons in Appendix B, where we will study a half twist of an anyon world-ribbon.

2.5 Braiding in anyon models

Now that we have described the abstract structure of braiding as a morphism relating objects $A \otimes B$ with $B \otimes A$, we can apply these ideas to anyon models. Firstly we need to define the action of the braiding morphism on the anyon fusion space, this is, what is the effect on the states of the system due to exchanging the spatial locations of two anyons.
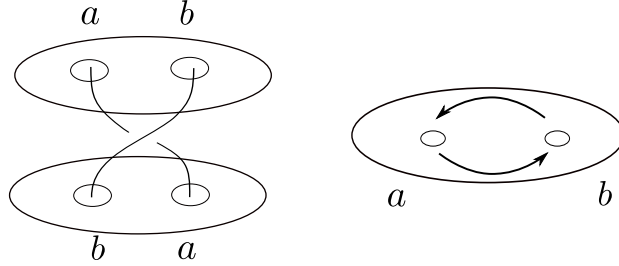
Figure 2.5: A spacetime picture of a braid (left) and a top-down view of the exchange (right)

The description of braiding in anyon models or equivalently skeletonisation of the UBFC is implemented by R-symbols: R_c^{ab}, which relate the fusion spaces V_c^{ab} and V_c^{ba}.
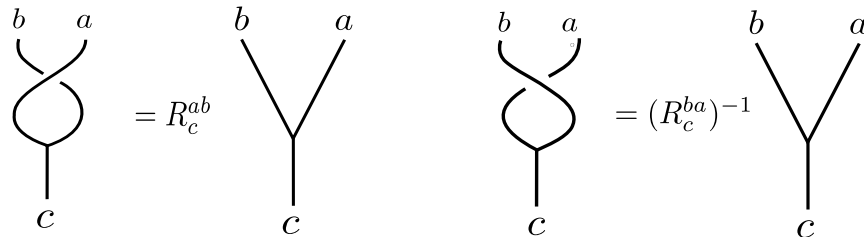
Figure 2.6: Definition of R-symbols and the inverse R-symbols, which are related by the Hermitian adjoint.

In any graphical diagram containing a crossing, we can resolve the crossing using an R-symbol as,

Figure 2.7: Graphical representation of resolving a braiding.

We always enforce that braiding of any anyon a with the vacuum charge is trivial

$$R_a^{a1} = R_a^{1a} = 1. \tag{2.32}$$

We also require that the R symbols are unitary matrices

$$(R_c^{ab})^{-1} = (R_c^{ab})^\dagger = (R_c^{ab})^*. \tag{2.33}$$

The inverse R-symbols correspond to under-crossing rather than over-crossings. As we discussed in Section 2.3, a choice of basis of the fusion space introduces a u_c^{ab} gauge freedom. Under a gauge transformation, the R-symbols transform as

$$[R_e^{ab}]' = \frac{u_e^{ba}}{u_e^{ab}}[R_e^{ab}], \tag{2.34}$$

where again since each $N_c^{ab} \in 0, 1$ then each $u_c^{ab} \in U(1)$.

Now that we have defined the action of the R symbols and discussed some of the constraints on the operators, the next question is how to make braiding compatible with fusion. The compatibility of fusion and braiding is often phrased by saying that *fusion commutes with braiding* or that braiding is *natural* with respect to fusion. In spacetime diagrams, it means that we can slide a braid under or over a fusion or splitting vertex. There are, in total, four possible topologically independent (two choices of fusion vertex and then a choice of over or under crossing), fusion commutes with braiding equalities. We show one example of this in Figure 2.8. However, only two of the four possible equalities lead to independent constraint equations on the R symbols.
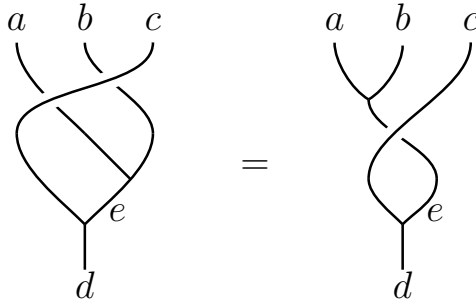
Figure 2.8: Enforcing fusion commuting with braiding leads to equating these states. We read these diagrams as spacetime histories of two different sequences of processes and by equating these histories, we are enforcing an isotopy relation on the graphical calculus which physically means that fusion and braiding are compatible.

Starting from Figure 2.8 and considering using the action of F symbols to recouple the fusion trees to arrive at states which do not contain any braids leads to Figure 2.9.
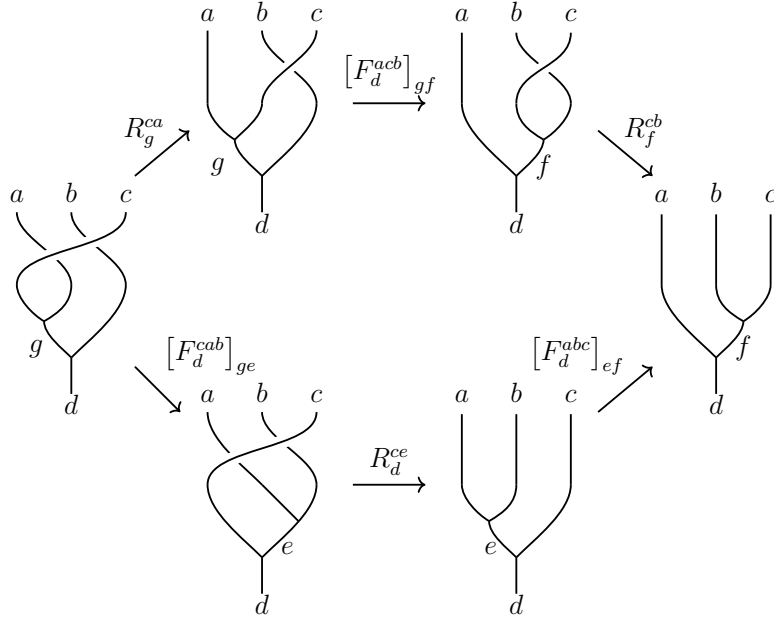
Figure 2.9: The hexagon axiom applied to anyons. Starting from the leftmost state and ending at the furthest right, but taking two different sequences of F and R symbols and equating them produces the hexagon equation. This diagram leads to the first equation in Equation 2.35.

The other independent hexagon diagram is obtained when the worldlines of anyons a and b braid over the worldline of anyon c. One of the most important spacetime histories in Figure 2.9 is the state in the bottom left. This is the state containing the information that fusion commutes with braiding. By taking the lower path around the graphical depiction of the hexagon axiom, we slide the $a \times b$ vertex through the braid with c so that we can remove it with the action of one R-symbol: R_d^{cf}.

The R-symbols are required to satisfy the *hexagon equations*. There are four sets of hexagon equations corresponding to four topologically different ways that fusion can commute with braiding. However, only two of the sets of equations are independent and are written as follows

$$
\begin{aligned}
R_g^{ca} \left[F_d^{acb} \right]_{gf} R_f^{cb} &= \sum_e \left[F_d^{cab} \right]_{ge} R_d^{ce} \left[F_d^{abc} \right]_{ef}, \\
R_g^{ca} \left[(F_d^{bac})^{-1} \right]_{ge} R_e^{ba} &= \sum_f \left[(F_d^{bca})^{-1} \right]_{gf} R_d^{fa} \left[(F_d^{abc})^{-1} \right]_{fe}.
\end{aligned}
\tag{2.35}
$$

The other two equations can be derived by taking the Hermitian adjoint of these equations, which corresponds to considering under-crossing rather than over crossings.

We will extensively use the idea of fusion commuting with braiding in Chapter 3 and Chapter 4 when we introduce the braiding of anyons on graphs.

Any planar braid is a composition of simple braids exchanging pairs of neighbouring anyons. Thus, using the R-symbols one can construct a representation of

the planar braid group. In particular, for $N = 3$ anyons of topological charge a and the total charge c, we get the following representation of $B_3 \to U(d)$ (63; 130; 150),

$$\rho(\sigma_1) = \text{diag}\left(R_{b_1}^{aa}, \ldots, R_{b_d}^{aa}\right), \quad \rho(\sigma_2) = (F_c^{aaa})^{-1} \rho(\sigma_1) F_c^{aaa}, \tag{2.36}$$

where the b_k are the fusion outcomes of $a \times a = b_1 + \cdots + b_d$. The $d \times d$ unitary matrices $\rho(\sigma_1)$ and $\rho(\sigma_2)$ are called the braiding operators. Crucially, the braiding operators satisfy the Yang-Baxter relation, i.e.

$$\rho(\sigma_1)\rho(\sigma_2)\rho(\sigma_1) = \rho(\sigma_2)\rho(\sigma_1)\rho(\sigma_2). \tag{2.37}$$

In other words, the braiding operators form a representation of the Artin braid group (13).

2.5.1 Modular tensor categories

The formalism thus far gives a finite set of data to construct a braided tensor category. However, the F-symbols and R-symbols have gauge freedom, which for the multiplicity free case are given by the action of u_c^{ab} on the fusion basis. This gives freedom in the definition of the R and F symbols. There are only a discrete set of solutions to the pentagon (2.19) and hexagon (2.35) equations (70; 100), up to gauge freedom, which is known as Oceanu rigidity. The fusion coefficients, quantum dimensions and total quantum dimension are natural gauge invariant quantities. So, what about invariant data for the braiding structure? Considering these questions will lead us to modular tensor categories (MTC). Let's first consider the topological twist of an anyon,

$$\theta_a = \theta_{\bar{a}} = \sum_c \frac{d_c}{d_a} R_c^{aa} = \frac{1}{d_a} \underset{a}{\infty} \tag{2.38}$$

The twist of the vacuum charge is trivial since braiding with the vacuum is trivial, so $\theta_1 = 1$. The θ_a are constrained to be roots of unity by Vafa's theorem (168). The R-symbols for a full braid can be expressed in terms of the twist factors using the ribbon property

$$R_c^{ab} R_c^{ba} = \frac{\theta_c}{\theta_a \theta_b}. \tag{2.39}$$
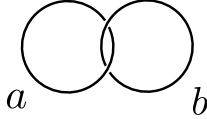
One of the most important features in quantum mechanics is the spin of a particle. This is abstracted to anyon models as the topological spin s_a, which is related to the twist as

$$\theta_a = e^{2\pi i s_a}. \tag{2.40}$$

The topological twists are often collected in the T matrix

$$T_{ab} = \theta_a \delta_{ab}. \tag{2.41}$$

The gauge invariant quantity for braiding is known as the S matrix and is given by the following equation and graphical diagram

$$S^{ab} = \frac{1}{\mathcal{D}} \sum_c R_c^{ba} R_c^{ab} = \frac{1}{\mathcal{D}} \sum_c N_c^{ab} \frac{\theta_c}{\theta_a \theta_b} d_c = \frac{1}{\mathcal{D}} \quad a \bigcirc\!\!\bigcirc \, b \tag{2.42}$$

Together the S and T matrices form a projective representation of the modular group, $\mathrm{SL}(2, \mathbb{C})$. The S and T matrices collectively are called the "modular data". If $\det(S) \neq 0$, i.e. the S matrix is invertible, then the braiding is non-degenerate (100). This means that each anyon can be distinguished by its braiding with the other anyons alone, this is why the braiding is said to be non-degenerate. The braided tensor category then gets the special name of "modular tensor category" (MTC). In an MTC, the fusion coefficients (from Equation 2.9) can be directly related to the S matrix through the Verlinde formula,

$$N_c^{ab} = \sum_e \frac{S_{ae} S_{be} S_{\bar{c}e}}{S_{1e}}. \tag{2.43}$$

In fact, for a UBFC, the R symbols are given, up to gauge freedom, by the modular data (27). Recently, all possible MTCs up to rank five (five distinct anyon types) have been classified (34). We would be remiss if we didn't end this section with one caveat: the modular data is not always sufficient to determine a MTC uniquely (125). Additional data may be needed (25; 27) to classify all MTCs.

2.6 Examples of anyon models

There are many well-known examples of anyon models, so we shall name just a few familiar ones that we intend to reference in this thesis.

2.6.1 Abelian fusion rules

A fusion algebra can be constructed over any finite Abelian group, G. The topological charges are labelled by elements of G and the fusion rules are given by group multiplication. Since group multiplication always has a unique outcome, all of the non-trivial fusion vector spaces are one-dimensional and the indices specifying fusion outcomes such as R_c^{ab} are necessary. The F-symbols are generally denoted as,

$$\left[F_{(abc)}^{a,b,c}\right]_{(ab),(bc)} := w(a,b,c) \tag{2.44}$$

In this notation the pentagon equation given in Equation (2.19) takes the simple form,

$$dw = w(a,b,c)\overline{w(ab,c,d)}w(a,bc,d)\overline{w(a,b,cd)}w(b,c,d) = 1, \tag{2.45}$$

This is the equation for a group cocycle in the third cohomology group of G with $U(1)$ coefficients. The action of gauge transformation on the F-symbols can be recognised as the defining equation of a coboundary du of a 2 cochain denoted by u. For any fusion algebra over an Abelian group, the quantum dimensions of each particle are $d_a = 1$ and the total quantum dimension is given by $\mathcal{D} = \sqrt{|G|}$.

Cyclic group $\mathbb{Z}_M$

In the collection of Abelian theories, there is one subfamily in particular, we shall collect some important quantities for, namely $G = \mathbb{Z}_M$. This anyon model has topological charges, $\mathcal{C}^0 = \{0, 1, 2, 3, \ldots M - 1\}$. The three-cocycles are explicitly given by,

$$w(a,b,c) = \exp(\frac{2\pi i k}{M^2} a\,(bc - [bc]_M)\,), \tag{2.46}$$

where $k = 0, 1, \ldots M - 1$, parameterises the distinct three-cocycles and by $[bc]_M$ we mean multiplication modulo M. Since all of the fusion outcomes are fixed, the R symbols are functions $R(a,b) : \mathbb{Z}_M \times \mathbb{Z}_M \to U(1)$. The hexagon equations are written

$$R(c,a)\,w(a,c,b)\,R(c,b) = w(c,a,b)R(c,ab)\,w(a,b,c),$$
$$R(c,a)\,w^*(b,a,c)\,R(b,a) = w^*(b,c,a)\,R(bc,a)\,w^*(a,b,c). \tag{2.47}$$

If we take the trivial group cocycle, $w(a, b, c) = 1$, then the hexagon equations are written as

$$
\begin{aligned}
R(ab, c) &= R(a, c)R(b, c), \\
R(c, ab) &= R(c, a)R(c, b).
\end{aligned}
\tag{2.48}
$$

One can see that bicharacters give solutions to the hexagon equations. There is only a non-trivial solution to the hexagon equations with non-trivial group cocycle when M is even (28; 69; 81). An explicit solution for any M with trivial $w(a, b, c)$ is given by,

$$
R(a, b) = e^{\frac{2\pi i k}{M}([a]_M [b]_M)}
\tag{2.49}
$$

If M is even, then there are non-trivial solutions for the R symbols with non trivial $w(a, b, c)$ given by $k = M/2$. Explicitly they are written

$$
R(a, b) = e^{\frac{2\pi i (k+\frac{1}{2})}{M}([a]_M [b]_M)}.
\tag{2.50}
$$

The S matrix for trivial cocycle is given as

$$
S_{a,b} = \frac{1}{\sqrt{M}} e^{i\frac{4\pi i k}{M}ab},
\tag{2.51}
$$

and the twist factors are given as

$$
\theta_a = \exp 2\pi i \frac{a^2 k}{M^2}.
\tag{2.52}
$$

The simplest example is the braided fusion category over $\mathbb{Z}_2$. The anyon types are $\mathcal{C}^0 = \{0, 1\}$. There are two solutions to the pentagon equation, $w(1, 1, 1) = \pm 1$, i.e. one with trivial cocycle and one with non-trivial cocycle. This model admits two solutions to the hexagon equations distinguished by ± 1 on the non-trivial R symbol. The non-trivial choice of cocycle and the non-trivial choice of R symbol is known as the semion model. The non-trivial data is,

$$
w(1, 1, 1) = -1 \qquad \mathcal{D} = \sqrt{2}, \qquad R(1, 1) = \pm i, \qquad \theta_1 = i.
\tag{2.53}
$$

Drinfeld double of $\mathbb{Z}_N$

A notable example we shall discuss later is the category of representations of the Drinfeld double of $\mathbb{Z}_N$, often denoted as $D(\mathbb{Z}_N)$. The Drinfeld double or quantum double is a quasi-triangular Hopf algebra. As a vector space the quantum double of $\mathbb{Z}_N$ is isomorphic to the tensor product of the group algebra of $\mathbb{Z}_N$ with functions on $\mathbb{Z}_N$, i.e. $D(\mathbb{Z}_N) \simeq \mathbb{C}\mathbb{Z}_N \otimes (\mathbb{C}\mathbb{Z}_N)^*$. In Chapter 7 we will discuss the corresponding lattice model, known as toric code (102). Here we will focus on the anyon details. The anyons types are denoted,

$$\{(e_i, m_i)\}, \qquad e_i\,,\, m_i \in \mathbb{Z}_N. \tag{2.54}$$

The left entry is generally associated with electric charges, and the right entry with flux or magnetic charges. We note each $(e_i, m_i) \in \mathbb{Z}_N \times \mathbb{Z}_N$. The fusion rules are addition mod N in each entry

$$(e_1, m_1) \times (e_2, m_2) = ([e_1 + e_2]_N,\, [m_1 + m_2]_N). \tag{2.55}$$

Since all of the anyon types are group elements, the quantum dimensions are $d_a = 1$. The F symbols are trivial

$$\left[F^{a,b,c}_{(a+b+c)}\right]_{(a+b),(b+c)} = 1\,. \tag{2.56}$$

The R-symbols and twist factors are,

$$R^{a,b}_{a+b} = e^{\frac{2\pi i}{N}e_1 m_2}, \qquad \theta_a = e^{2\pi i \frac{e_1 m_1}{N}}. \tag{2.57}$$

The S matrix is given by

$$S^{a,b} = \frac{1}{N}e^{\frac{2\pi i}{N}(e_1 m_2 + e_2 m_1)}. \tag{2.58}$$

One notable example in this family is $N = 2$, so the category of representations of $D(\mathbb{Z}_2)$. The fusion rules are $e \times e = m \times m = 0$. The anyon $(1,1)$ is dyonic, which is a combination of an electric charge and a magnetic charge and in Chapter 7 we will denote this anyon as ψ. It has the exchange statistics of a fermion. In Chapter 8 we will study the lattice model of $\mathbb{Z}_N$ toric code and the corresponding anyon model. More generally, one can construct an anyon model from, $\mathrm{Rep}(G)$, the category of representations of $D(G)$, for any finite group (69).

2.6.2 Tambara-Yamagami categories

Another example is the family of Tambara-Yamagami categories (164). These categories are constructed by taking a fusion category over a finite Abelian group G and adding an extra object, denoted σ, whose fusion with itself gives a direct sum of all of the elements of G, i.e.

$$TY(G) := \mathbb{C}G \oplus \mathbb{C}\sigma . \tag{2.59}$$

The objects in the category are given by $\mathcal{C}^0 = \{G, \sigma\}$. The fusion rules are given by,

$$g_i \times g_j = g_i g_j, \qquad \sigma \times g_i = g_i \times \sigma = \sigma, \qquad \sigma \times \sigma = \sum_G g_i, \tag{2.60}$$

where $g_i \in G$. The quantum dimensions are given by,

$$d_g = 1_{\mathbb{C}} \quad \forall g \in G \qquad d_\sigma = \sqrt{|G|} \qquad \mathcal{D} = \sqrt{2|G|}. \tag{2.61}$$

Most F symbols are one, the non-trivial F-symbols are;

$$\left[F_\sigma^{g_i \sigma g_j}\right]_{\sigma\sigma} = \left[F_{g_j}^{\sigma g_i \sigma}\right]_{\sigma\sigma} = \chi(g_i, g_j), \qquad \left[F_\sigma^{\sigma\sigma\sigma}\right]_{g_i g_j} = \nu_\sigma \, \tau \, \chi^{-1}(g_i, g_j), \tag{2.62}$$

where $\tau = (\sqrt{|G|})^{-1}$, χ is a non degenerate symmetric bicharacter and, $\nu_\sigma = \pm 1$, is the Frobenius-Schur indicator of σ. There are no non-trivial solutions to the hexagon equations if G is not a 2 group, by this we mean a group where every element except the identity is of order two (158). Explicitly, when solving the hexagon equations for these fusion rules and F-symbols, one finds that χ must be of order two. In the case G is a 2-group, then σ is referred to as a non-Abelian anyon.

2.6.3 Ising

One notable example in the Tambara-Yamagami family is the Ising MTC, which has $G = \mathbb{Z}_2$. This is anyon model we mentioned in the Introduction 1. Here we have the following topological charges, $\mathcal{C}^0 = \{g_0, g_1, \sigma\} \equiv \{1, \psi, \sigma\}$. We denote by 1 the vacuum charge, ψ is identified with the non-trivial element of $\mathbb{Z}_2$ and has the exchange statistics of a fermion, finally, σ is the non-Abelian anyon. The fusion rules are,

$$\psi \times \psi = 1, \qquad \sigma \times \psi = \sigma \times 1 = \sigma, \qquad \sigma \times \sigma = 1 + \psi. \tag{2.63}$$

We can see from the fusion rules that all of the particles are self-dual. There are two non-equivalent sets of F-symbols, distinguished by the value of the Frobenius-Schur indicator $\nu_\sigma = \pm 1$. Most F-symbols equal 1.

The non-trivial Ising F-symbols are given as,

$$\left[F_\psi^{\sigma\psi\sigma}\right]_{\sigma\sigma} = \left[F_\sigma^{\psi\sigma\psi}\right]_{\sigma\sigma} = -1, \qquad [F_\sigma^{\sigma\sigma\sigma}]_{e,f} = \frac{\nu_\sigma}{\sqrt{2}} \begin{pmatrix} 1 & 1 \\ 1 & -1 \end{pmatrix}. \tag{2.64}$$

The solutions to the hexagon equations are,

$$R_1^{\sigma\sigma} = e^{(2k+1)i\pi/8} \quad R_1^{\sigma\sigma} = \pm i R_\psi^{\sigma\sigma} \quad R_\sigma^{\sigma\psi} = R_\sigma^{\psi\sigma} = (-i)^k \quad R_1^{\psi\psi} = -1_\mathbb{C} \tag{2.65}$$

where $k \in \{0, 1, 2, 3\}$. We note, the cases $k = 0$ and $k = 3$ occur for the set of F-symbols with $\nu_\sigma = 1$, and remaining cases occur for $\nu_\sigma = -1$. The S matrix is given by

$$S = \frac{1}{2} \begin{pmatrix} 1 & \sqrt{2} & 1 \\ \sqrt{2} & 0 & -\sqrt{2} \\ 1 & -\sqrt{2} & 1 \end{pmatrix}. \tag{2.66}$$

There is a mirror solution given by the complex conjugation of the R symbols in Equation (2.65).

This UMTC arises frequently in topological phases of matter. In particular, the Majorana bound states mentioned in Chapter 1, which are zero energy excitations associated with vortices in certain FQHE systems, and also associated with domain walls in topological superconductors are identified with the σ anyon (which we discuss in Chapter 5 and Chapter 6). If two Majorana bound states are brought together, they can fuse to a Dirac fermion or annihilate, we can see this abstracted in the fusion rule: $\sigma \times \sigma = 1 + \psi$.

2.6.4 Fibonacci

Another example of a non-Abelian anyon theory is the Fibonacci MTC. A detailed introduction to this model can be found in (72; 140; 166). The objects are $\mathcal{C}^0 = \{1, \tau\}$. Both of the particles are their own antiparticle. The fusion rules are

$$\tau \times \tau = 1 + \tau, \qquad \tau \times 1 = \tau. \tag{2.67}$$

The quantum dimensions are

$$d_1 = 1, \qquad d_\tau = \phi, \qquad \mathcal{D} = \sqrt{1 + \phi}, \tag{2.68}$$

where ϕ is the golden mean,

$$\phi = \frac{1 + \sqrt{5}}{2}. \tag{2.69}$$

The non-trivial F-symbols are

$$[F_\tau^{\tau\tau\tau}]_{e,f} = \begin{pmatrix} \phi^{-1} & \phi^{-1/2} \\ \phi^{-1/2} & -\phi^{-1} \end{pmatrix}. \tag{2.70}$$

The solutions to the hexagon equations up to complex conjugation (chirality) are,

$$R_1^{\tau\tau} = e^{-4\pi i/5} \qquad R_\tau^{\tau\tau} = e^{3\pi i/5}. \tag{2.71}$$

The twist of the τ particle is $\theta_\tau = e^{4\pi i/5}$. The S matrix for the Fibonacci theory is given by

$$S = \frac{1}{\sqrt{\phi + 2}} \begin{pmatrix} 1 & \phi \\ \phi & -1 \end{pmatrix}. \tag{2.72}$$

The Fibonacci anyon model is one of the most interesting for topological quantum computing because the set of topological quantum gates, i.e. the computations (unitaries) that can be performed by topological operations(braiding) are universal for quantum computation (76; 131). This means any quantum gate for TQC can be implemented by braiding alone. Other anyon models often require the inclusion of some non-topological operations to implement all of the gates for a quantum computer.

As a topological phase of matter, it has been proposed that the Fibonacci anyon model can arise as the low energy excitations in certain fractional quantum Hall effect states known as Read-Rezayi states (145). The Fibonacci anyons arise as low energy excitations modelled by the part (integer spin) representations of $SU(2)_k$ Chern-Simons gauge theory, where k is known as the level and controls the strength of the electron-electron interaction (12; 131).

2.7 Summary

In this chapter we have presented the algebraic theory of anyons. This is an abstraction of many features of anyon excitations in topological physics. Our focus was on showing how many of the ingredients arise from a mathematical object known as a unitary braided fusion category. We presented a dictionary to translate the relevant quantities between the anyon model and categorical structures in Table 2.1. Structurally, throughout the chapter we first discussed the categorical structure and the analgoue in anyon models.

In Section 2.2 we motivated and introduced the fusion category structure. We gave the definition of the monoidal product and the decomposition of an arbitrary object in the category into simple objects. The main idea here was that in a category associativity is given by an isomorphism, α, rather than an equality as in the case of a group or a ring. We also showed the pentagon axiom that α must satisfy. This weakening of an equality to an isomorphism is called categorification. We then moved on to discuss the analogous structures in the context of anyons in Section 2.3. The monoidal product and decomposition into simples are known as the fusion rules and fusion coefficients. The associativity isomorphism is known as F-symbols, which are found by solving the pentagon equation 2.19. We also introduced the states of our anyon Hilbert space and the diagrammatic calculus that we used throughout the chapter.

In Section 2.4 we introduced the naturality of braiding the hexagon axiom. This enforces that braiding and the monoidal product are compatible. We also showed how the Yang-Baxter equation (2.28) arises from BTC when the associator is trivial. Here we can see the connection between BTC and the braid group.

In Section 2.5 we discuss how the braiding of anyons is encoded in the abstract model, by this we mean the unitary operators, known as R-symbols. We showed how the compatibility of braiding and fusion, Figure 2.8 leads to the hexagon equation 2.35.

In Section 2.5.1 we then studied a special type of BTC known as a modular tensor category. The special feature of this category is that the braiding is non-degenerate and every particle type can be detected by braiding with the other particles in the anyon model.

In Section 2.6 we provided some noteworthy examples that we will return to in different chapters. For example, the Drinfeld double anyon model arises as the collection of excitations in the $\mathbb{Z}_N$ toric code we will study in Chapter 8. The Ising category in Section 2.6.3 will arise in our graph anyon formalism in Chapters 3 and 4.

This concludes our discussion of anyon models. In Chapter 3 and Chapter 4 we will use this framework to discuss anyons restricted to exchanges on graphs.

Chapter 3

Graph braiding of anyons

3.1 Introduction

Two decades ago, it was realised that an inherently fault tolerant quantum computation scheme could be implemented using the exchange statistics of anyons. This gave birth to the field of *topological quantum computation* (TQC), (75; 100; 102; 131). Although originally envisioned on two dimensional platforms like the FQHE, it was later realised that one dimensional wires could be engineered to host topological excitations like Majorana zero modes (113; 136). Then in (8), it was proposed that the braiding of Majorana bound states could be performed on networks of one dimensional semiconductor wires joined at junction points. The actual braiding is implemented by tuning gate voltages in the wire to transport the Majorana around the network. However, on a network or graph, exchanges are not governed by the usual braid group but instead by a graph braid group. To this, we introduce *graph braiding of anyons*. This is a framework for adapting the algebraic models of anyons to exchanges coming from graph braid groups rather than the planar braid group. This chapter is based on (50) in collaboration with J.K. Slingerland. We extend the results of this chapter in Chapter 4.

3.2 Quantum exchange statistics and graph braid groups

The exchange statistics of N identical particles are governed by the representations of the fundamental group of the configuration space of the system. This is the space of unordered collections of N distinct particle positions in the relevant geometry (74; 78; 111). For particles on the plane, the fundamental group is the braid group. In three-dimensional space, we obtain the permutation group S_N, leading to the symmetric exchange statistics of bosons and the anti-symmetric exchange statistics of fermions.

However, we obtain graph braid groups for particles moving on graphs, which depend on the actual graph chosen. These have recently been analysed in some detail in (10; 86; 115; 116), and appear to be the natural tool for studying the exchange statistics of particles on wire networks. Let's first refresh the planar braid group and contrast it with graph braid groups. The braid group arises as the fundamental group of the configuration space of particles moving on $\mathbb{R}^2$,

$$\pi_1(C_N(\mathbb{R}^m)) = \begin{cases} 1, & m = 1, \\ \mathcal{B}_n, & m = 2, \\ S_n, & m \geq 3. \end{cases} \tag{3.1}$$

The N strand Artin braid group, $\mathcal{B}_N$ is an infinite order group with $N-1$ generators, we denote by τ_i, which exchanges neighbouring strands labelled i and $i+1$ subject to the following relations, (13);

$$\begin{aligned} \tau_i \, \tau_j &= \tau_j \, \tau_i, & |j - i| \geq 2, \\ \tau_{i+1} \, \tau_i \, \tau_{i+1} &= \tau_i \, \tau_{i+1} \, \tau_i \, . \end{aligned} \tag{3.2}$$

We may call these relations the commutativity (upper) and braiding or Yang-Baxter relations (lower). The construction of the graph braid group proceeds in the same vein as (111). We fix a graph Γ and decorate it with N particles. The configuration space of distinct particle positions is defined as

$$C_N = (\Gamma^{\times N} - \Delta_N)/S_N \tag{3.3}$$

where,
$$\Delta_N = \{(x_1, \ldots, x_N) \in \Gamma^{\times N} \mid x_i = x_j, \text{ for some } i, j\} \tag{3.4}$$

which are configurations corresponding to multiple particles at the same point. In (115), they study the fundamental group of this space,

$$\pi_1(C_N(\Gamma)) = B_N(\Gamma). \tag{3.5}$$

This is the definition of the N-strand graph braid group, $B_N(\Gamma)$. For convenience, we take the base point of the fundamental group so that all particles are located on a single edge of the graph. A graph braid is represented by the spacetime history of a process where the particles start at their positions on this initial edge, are then transported to other edges and finally returned to the initial edge, possibly with the order of some of the particles exchanged. We show an example of such a process in Figure 3.2.
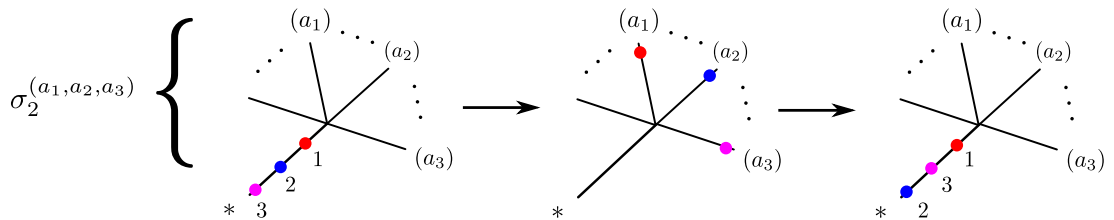
Figure 3.1: A graph braid is given by a composition of shuttling particles onto the edges of a graph and then returning them to the initial edge in a different order. Here we depict a $\sigma_2^{(a_1,a_2,a_3)}$ braid

The left graphical diagram in Figure 3.2 displays an action of τ_1 in the planar braid group, and the right diagram shows an example of a $\sigma_1^{(1,2)}$ graph braid. In (10), an intuitive presentation based on two-particle exchanges is introduced, which we will now explain. The presentation has generators defined as

$$\sigma_j^{(a_1,a_2,a_3...,a_j,a_{j+1})} \tag{3.6}$$

where a_i denotes the edge that the ith particle away from the junction point is moved to during the graph braid. The edges are enumerated clockwise from the junction point. The subscript j denotes the exchange of the j'th particle from the vertex with the $j + 1'$th particle. The inverse of a σ generator is given by switching a_j with a_{j+1}, so that the composition of these generators is isotopic to the trivial graph braid. For general graphs, one makes this unambiguous by first fixing a spanning tree of the graph and choosing the initial edge to be the stem of this tree. This fixes the path taken out to edge a_i. The subscript j denotes that after the action of σ_j the particles return to the initial edge in the same ordering except that particle $j + 1$ returns before particle j, so that these particles end up on the initial edge in reverse order. We can contrast these generators with a presentation of the planar braid group B_N generated by the exchanges τ_i. All the $\sigma_j^{(a_1,a_2,a_3...,a_j,a_{j+1})}$ operators would correspond either to τ_j or to τ_j^{-1} if the particles were free to move in the plane. However, when motion is restricted to the graph, it is necessary to keep track of the edges where the rest of the particles, which are not being exchanged are sent to. As a result graph braid groups have multiple counterpart generators for the τ_j with $j > 1$. In Figure 3.2 we illustrate the sequence of shuttling

In general, graph braid groups are less constrained than the Artin braid group (10; 116). In particular, if the graph has one vertex and d incident edges, the graph braid group is isomorphic to a free group of rank

$$\text{Rank}(B_N(d)) = (d - 2)\binom{N + d - 2}{N - 1} - \binom{N + d - 2}{N} + 1. \tag{3.7}$$

However, the σ presentation of the generators is, in general, over-complete. Although the graph braid group is a free group of some rank, the total number of elements in
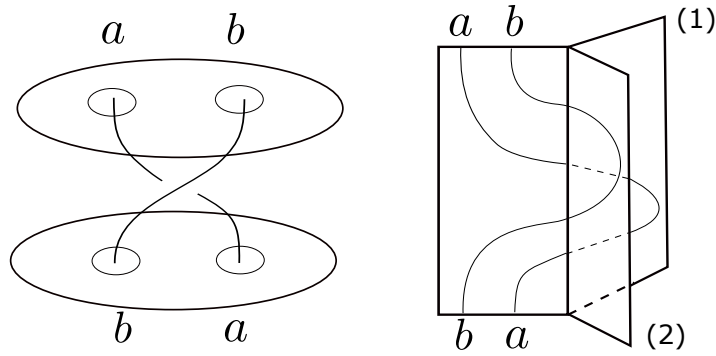
Figure 3.2: The left picture depicts a planar braid. The right picture depicts $\sigma_1^{(1,2)}$, one of the generators of $B_3(\Gamma_3)$. We can see that a graph braid is a process where particles starting from an initial configuration on an edge of the graph are transported to other edges and returned to the initial edge in a different ordering. The edges are enumerated clockwise, the backplane is labelled (1), and the front plane is labelled (2). We can see that $\sigma_1^{(1,2)}$ does not have finite order.

this presentation, $|\sigma|_{N,d}$ is greater than the rank as a free group. In fact, it is given by,

$$|\sigma|_{N,d} = \sum_{i=1}^{N-1} (d-1)^{i-1} \binom{d-1}{2}. \tag{3.8}$$

The overcompleteness of this generating set can be used to construct so-called "pseudo" relations, which come in two types; pseudocommutative and pseudobraid, to match the analogous relations in the Artin braid group (116). On a star graph of any valence decorated by four or more particles ($N \geq 4$), pseudo commutative relations appear between generators that are exchanging particles which are a distance of $j - i \geq 2$ in their initial ordering on the initial edge. These relations in general are given as

$$\sigma_j^{(a_1,...,a_{j+1})} \sigma_i^{(a_1,...,a_{i+1})} = \sigma_i^{(a_1,...,a_{i+1})} \sigma_j^{(a_1,...,a_{i-1}a_{i+1}a_i a_{i+2},...,a_{j+1})}. \tag{3.9}$$
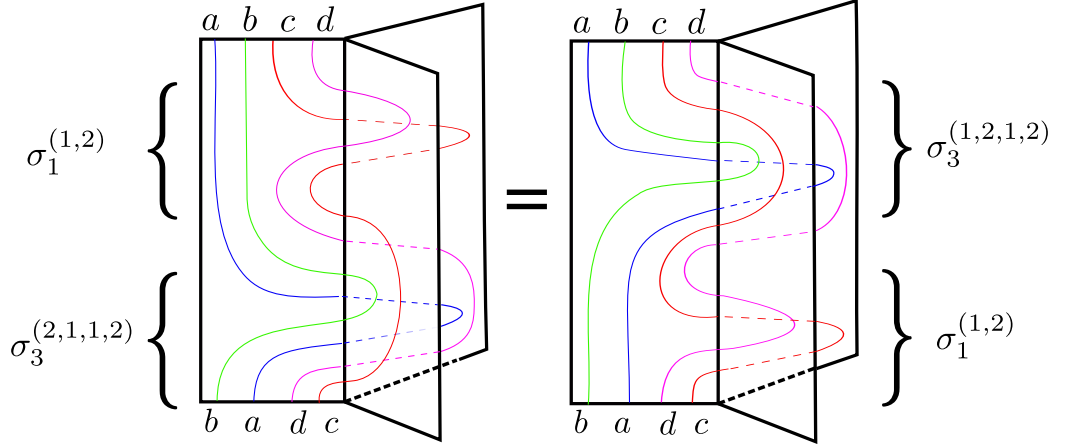
Figure 3.3: The pseudocommutative relation in Equation 3.10.

An example of a pseudo commutative relation on a trijunction, which has $d = 3$, is

$$\sigma_3^{(2,1,1,2)} \, \sigma_1^{(1,2)} = \sigma_1^{(1,2)} \, \sigma_3^{(1,2,1,2)}. \tag{3.10}$$

We graphically show this equation in Figure 3.3. We can see the pseudocommutative relations closely mirror the commutation relation in Equation (3.2) in the Artin braid group; group elements acting on disjoint strands commute. When one considers graphs with a valence greater than three ($d \geq 4$) and $N \geq 3$, pseudo-braid relations appear, for $1 \leq i \leq n-2$,

$$
\begin{aligned}
&\sigma_{i+1}^{(a_1,\ldots,a_{i-1}a_i a_{i+1} a_{i+2})} \, \sigma_i^{(a_1,\ldots,a_{i-1}a_i a_{i+2})} \, \sigma_{i+1}^{(a_1,\ldots,a_{i-1}a_{i+2}a_i a_{i+1})} \\
&= \sigma_i^{(a_1,\ldots,a_{i-1}a_i a_{i+1})} \, \sigma_{i+1}^{(a_1,\ldots,a_{i-1}a_{i+1}a_i a_{i+2})} \, \sigma_i^{(a_1,\ldots,a_{i-1}a_{i+1}a_i a_{i+2})}.
\end{aligned}
\tag{3.11}
$$

An example of a pseudo braid relation on a tetrajunction, which we will examine in Section 3.5 is,

$$\sigma_2^{(1,2,3)} \, \sigma_1^{(1,3)} \, \sigma_2^{(3,1,2)} = \sigma_1^{(1,2)} \, \sigma_2^{(2,1,3)} \, \sigma_1^{(2,3)}. \tag{3.12}$$

We show a graphical depiction of this relation in Figure 3.4. The pseudobraid relation is the graph braiding analogue of a Yang-Baxter equation. By pseudocommutative (pseudobraid) relations, we are referring to the fact the σ generating set is, in general, over complete (10; 116). However, this presentation is particularly suited to the discussion of braiding particles and proceed accordingly.

We shall focus in particular, on a star graph of valence three, more often called a trijunction or T junction. This is one of the most familiar setups for TQC on networks, see for example the following (8; 47; 98; 178). We fix to $N = 3$ particles. The graph braid group is then generated by

$$B_3(\Gamma_3) = \langle \sigma_1^{(1,2)}, \, \sigma_2^{(2,1,2)}, \, \sigma_2^{(1,1,2)} \rangle. \tag{3.13}$$
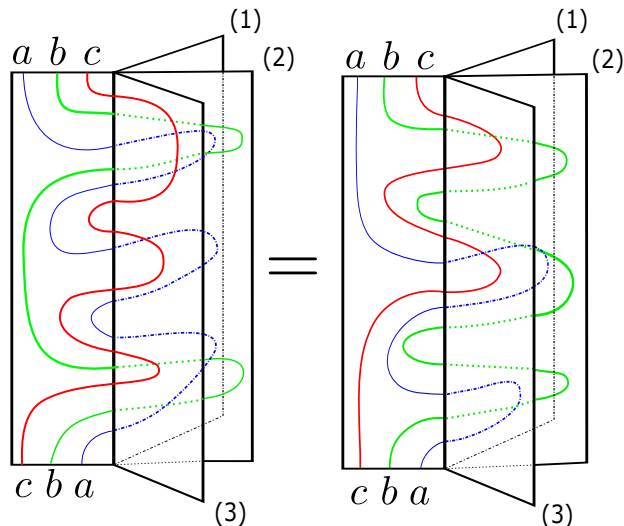
Figure 3.4: The pseudobraid relation on the tetrajunction. The left diagram corresponds to the left hand side of Equation (3.12), with composition in the equation going vertically in the diagram. The edges the particles are assigned stay fixed throughout the composition on both sides of the equality, for example particle b, the green line always goes to edge (2).

The inverses of these generators are given as follows,

$$(\sigma_1^{(1,2)})^{-1} = \sigma_1^{(2,1)}, \quad (\sigma_2^{(2,1,2)})^{-1} = \sigma_2^{(2,2,1)}, \quad (\sigma_2^{(1,1,2)})^{-1} = \sigma_2^{(1,2,1)}. \tag{3.14}$$

We depicted the action of $\sigma_1^{(1,2)}$ in Figure 3.2, and we will show the action of the σ_2 graph braids acting on the anyon fusion space in Figure 3.7. The graph braid group for three particles on a trijunction is isomorphic to a free group on three generators, and there is no overcompleteness of the σ presentation. If we wanted to construct a representation of the graph braid group on a trijunction to examine what exchange statistics are possible, this would seem to create a rather unsatisfactory picture. Since it is just a free group, we could assign any unitary operator to the exchange of any types of particles. However, we will see in Section 3.3 that introducing topological charge and fusion rules reduces this freedom. If the graph contains closed paths, then this introduces additional generators into the graph braid group. However, we delay the treatment of these graphs to Chapter 4. This concludes our overview of the relevant features of graph braid groups for this chapter.

3.3   Graph anyon models

In this section, we will explain our adaptation of the braiding of anyons described in Section 2 to anyons restricted to movement on graphs, focusing on a trijunction. We described the generators of the graph braid group in Equation (3.13). Particles in a graph anyon model carry one of a finite set of topological charges $a, b, c, \dots$.

We define the fusion of topological charges on a graph in the same vein as Chapter 2. Given two particles carrying topological charge a and b, their fusion product is given by

$$a \times b = \sum_c N_c^{ab} c \ . \tag{3.15}$$

The coefficient $N_{ab}^c \in \mathbb{Z}_{\geq 0}$ is the dimension of the fusion space V_c^{ab} of ground states of a system on a single edge, with two particles of charges a and b and with overall charge c. We assume that the fusion rules are the same on the graph as they are in the plane.
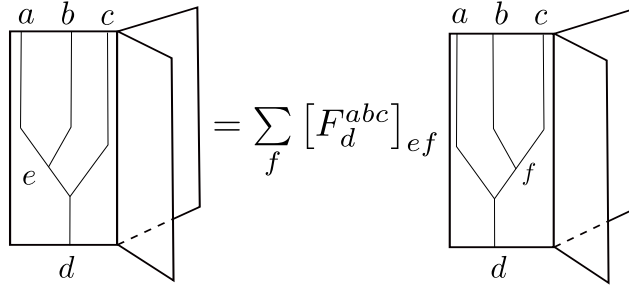
Figure 3.5: The action of F-symbols on a trijunction, though we have drawn the F-symbols acting on one edge, we allow fusion on any edge of the graph.

In Figure 3.5, we display our convention for the action of the F-symbols on a trijunction. On a general graph one first fixes a spanning tree and a root of the graph and then defines the action of the F-symbols with respect to this ordering. We impose that the F-symbols of the theory satisfy the same pentagon in Equation (2.19). We would like to adapt the R-symbols in Section 2.5 and enforce compatibility with fusion. By not modifying the fusion rules or F-symbols, we could equivalently say that we are not modifying the underlying fusion category as discussed in Chapter 2. Instead, we are just adapting the braiding structure to be compatible with a graph braid group.

The compatibility of fusion and braiding is often phrased as fusion *commutes* with braiding or braiding is natural with respect to fusion. In spacetime diagrams, this means that we can slide a particle worldline under or over a fusion or splitting vertex. For braiding on a graph, the usual hexagon equations are not valid. In fact, fusion and braiding do not always commute. However, there are still particular processes where a continuous deformation of the particles' history leads to an exchange of a fusion vertex with braiding in time. See Figure 3.8 for an example. We now define appropriate symbols satisfying graph hexagon equations, which express this remaining consistency of fusion and braiding on a trijunction,

$$\rho(\sigma_1^{(1,2)}) := R, \qquad \rho(\sigma_2^{(1,1,2)}) := P, \qquad \rho(\sigma_2^{(2,1,2)}) := Q. \tag{3.16}$$

We denote by $\rho(\sigma)$ the action of the graph braid generators on the anyon fusion space. We display the action of our graph braid symbols on states in our Hilbert space, V_c^{ab} in Figure 3.6.
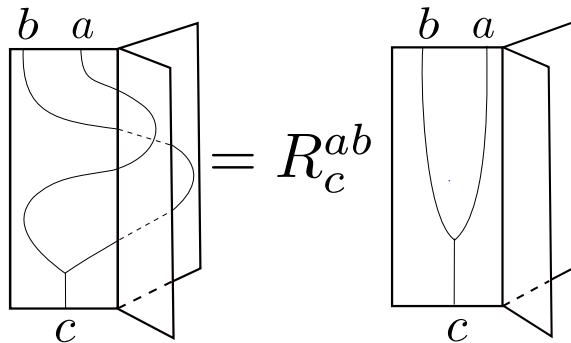
Figure 3.6: We define the action of $\rho(\sigma_1^{(1,2)}) = R_c^{ab}$. The inverse generator $\rho(\sigma_1^{(2,1)}) = \rho(\sigma_1^{(1,2)})^{-1} = (R_c^{ab})^{-1}$ is defined similarly, but the edges which the particles go to are inverted. We use the dotted lines to show that the particle b is going into the back plane, which was labelled (1) in Figure 3.2.

By this action, we are enforcing that the braided state and the unbraided state are related by a phase factor. Even though we denote $\rho(\sigma_1^{(1,2)}) := R$, we do not take solutions to the conventional planar hexagon equations for R, instead in our system, this will be a matrix to be solved for, just like P and Q.

Now we turn our attention to the graph braid generators that act on three particles, $\sigma_2^{(a_1,a_2,a_3)}$. These generators exchange the second and third particles away from the junction. The particle closest to the junction, which goes to the edge labelled a_1, returns to the same place in the ordering on the initial edge, after the action of $\sigma_2^{(a_1,a_2,a_3)}$. We can see from the presentation given in Equation (3.13) there are two such graph braid generators, $\sigma_2^{(1,1,2)}$ and $\sigma_2^{(2,1,2)}$.
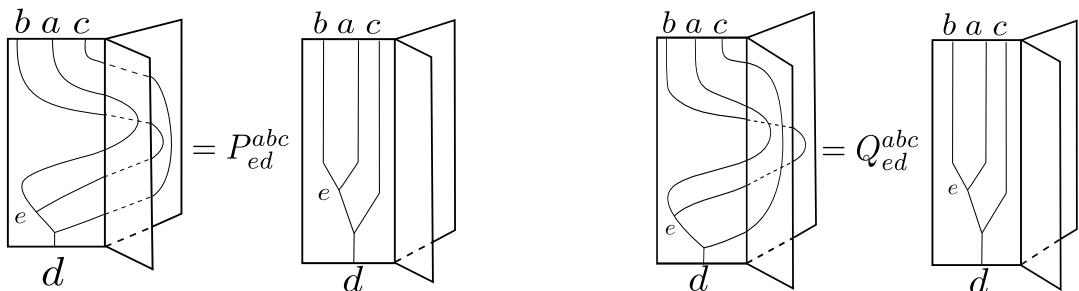
Figure 3.7: In the left diagram we display the action of $\rho(\sigma_2^{(1,1,2)}) = P_{ed}^{abc}$ and in the right graphical diagram we display the action of $\rho(\sigma_2^{(2,1,2)}) = Q_{ed}^{abc}$. We can see that these are two different processes, as the particle c goes to different edges. Because of this, we have decided to include a dependence of anyon c in the graph braid matrices corresponding to P and Q.

Note that these braiding processes necessarily involve all three particles labelled a, b, c and so we have introduced additional labels characterizing the full three-

particle state to label matrix elements of the graph braid matrices. We also want to follow the traditional R-symbols which we describe in Section 2.5, so one can only resolve a crossing in a spacetime diagram if the two particles being braided are joined by a fusion tree. This implies that we must have the left associated fusion tree structure which we can see in either subfigure in Figure 3.7. If we made P or Q depend only on a, b and their fusion outcome, we would always have $P = Q$, since both of these generators involve sending the second particle to edge (1) and the third particle to edge (2). However, P and Q are representations of distinct generators in the graph braid group. Our rectification is to introduce a dependence on c, the particle closest to the junction point and a dependence on the total fusion channel of all three particles, which we denoted by d in Figure 3.7. Since these generators differ by the edge that the particle closest to the junction point goes to during the graph braid. We believe this captures the essence of the graph braid group on a trijunction. We still require that, for a complete choice of anyon labels, the P and Q are complex numbers of unit norm acting on the states of the fusion vector space, which we defined in Equation (2.17). Despite the introduction of the extra labels, the gauge transformations of P and Q have the same structure as the gauge transformation of the planar R-symbols, as we defined in Equation (2.34),

$$[P_{ed}^{abc}]' = \frac{u_e^{ba}}{u_e^{ab}} P_{ed}^{abc}, \qquad [Q_{ed}^{abc}]' = \frac{u_e^{ba}}{u_e^{ab}} Q_{ed}^{abc}. \tag{3.17}$$

Now that we have defined the graph braiding R-symbols, we turn our attention to the compatibility of fusion and graph braiding. We shall start with the premise that performing fusion or splitting should commute with graph braiding and try to adapt the diagrams in Figure 2.8 to a trijunction[1].

If we consider adapting the left diagram in Figure 2.8, which has splitting before braiding, then after splitting, there will be three particles on the trijunction, and we must do two braids in the spacetime diagram. One of the graph braids would correspond to a σ_1, however the second would be a σ_2, since there will be a third particle on the trijunction, c as we have labelled them. So what we want is pairs of σ_1's and σ_2's that can be composed in a compatible manner with the structure of fusion such that we can "slide" a fusion vertex through a graph braid. This implies that, of the three particles involved, two particles must go to the same edge, which we can see in Figure 3.8. If we instead tried to combine a $\sigma_1^{(2,1)}$ and a $\sigma_2^{(1,1,2)}$, we would find it impossible to slide a fusion vertex onto one of the edges through the graph braid since the fusion vertex would get "stuck" on the junction point of the graph.

---

[1]This procedure works on any graph once a spanning tree is fixed.
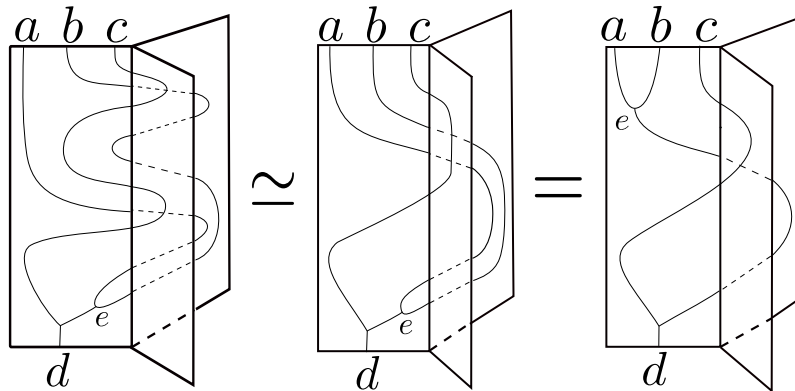
Figure 3.8: Fusion commuting with graph braiding. Reading these diagrams from the bottom up, the furthest right picture displays a process where two particles e and c are exchanged using a $\rho(\sigma_1^{(1,2)})$ graph braid and then afterwards e splits into particles a and b. The middle picture shows a process, where e first splits into a and b and then a $\rho(\sigma_1^{(1,1,2)})$ graph braid switches c and a and then after that a $\rho(\sigma_1^{(1,2)})$ graph braid switches c and b. We consider these processes equal because they are related by sliding the splitting vertex of $e = a \times b$ up through the back edge. This is the graph braiding analogue of the right graphical state in Figure 2.8.

In Figure 3.8 we show the composition of two exchanges such that we can *slide* a fusion vertex through a graph braid. This implies that the two particles with total charge $e = a \times b$ must go to the same edge during the braiding process. If we chose to make the particle closest to the junction move out of the way to an edge other than the one where the second particle moves, the move pushing the splitting vertex upward would be blocked at the graph's vertex and it would not pass under the worldline of charge c. Adapting the notation from the σ presentation, we can write an equation for the diagram identity in Figure 3.8 as follows,

$$\sigma_2^{(1_b, 1_a, 2_c)} \circ \sigma_1^{(1_b, 2_c)} = \sigma_1^{(1_{b \times a}, 2_c)} = \sigma_1^{(1_e, 2_c)}, \tag{3.18}$$

where by 1_b we mean particle b goes to the edge labelled (1), 2_c, states particle c goes to edge (2) during the graph braid, and by $\circ$ we mean multiplication in the graph braid group, which is given by composition. This is an adaption of the notation in the σ algebraic presentation from Section 3.2 in particular Equation (3.6). Here we change the superscript of a σ generator in the following way: instead of enumerating the particles in an increasing order away from the junction point, we label them with a subscript for the topological charge they are carrying.

This procedure can construct consistency equations for graph braiding and fusion: the graph hexagon equations. We note that we can connect the two sides of the identity in Figure 3.8 by a series of F-symbols and resolving exchanges, and we then require this combination of moves to be the identity, exactly analogous to Figure 2.9. This leads to the hexagonal commutative diagram in Figure 3.9. Following this procedure, the graph braiding hexagon equations corresponding to this particular
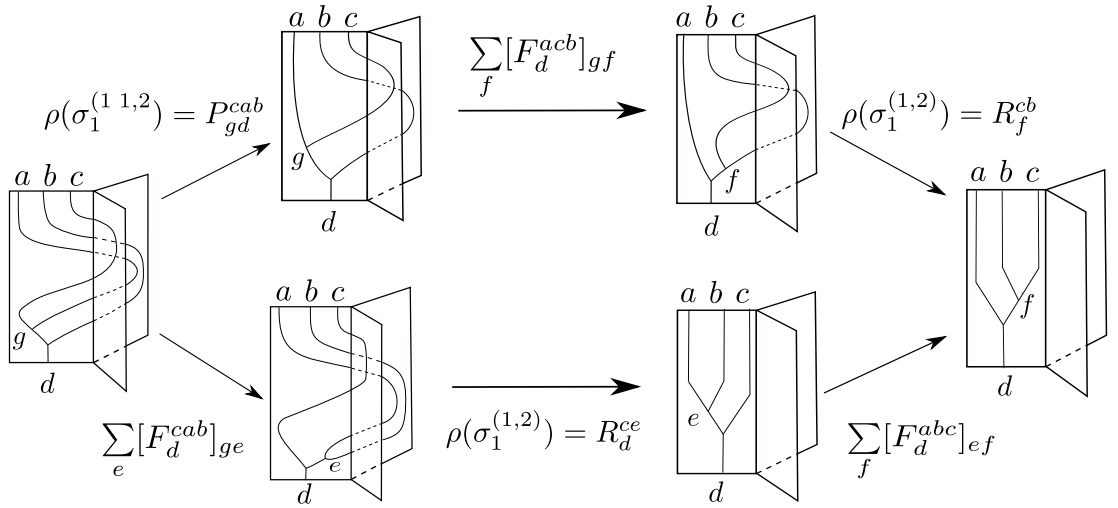
Figure 3.9: A hexagonal commutative diagram enforcing compatibility of fusion and graph braiding. In the bottom left state, we have used the premise that fusion commutes with graph braiding. This allows us to slide the fusion vertex, $a \times b = e$ through the graph braid, which we display explicitly in Figure 3.8. Then the crossing can be resolved with a $\rho(\sigma_1^{(1,2)})$ to arrive at the standard fusion basis. The far left state has the two particles furthest away from the junction point joined into a fusion channel, so the $\rho(\sigma_2^{(1,1,2)})$ crossing can be resolved. We use the dotted lines to show that the particle is going into the backplane.

fusion commutes with graph braiding state in Figure 3.8 are given as,

$$P_{gd}^{cab} \left[F_d^{acb} \right]_{gf} R_f^{cb} = \sum_e \left[F_d^{cab} \right]_{ge} R_d^{ce} \left[F_d^{abc} \right]_{ef}. \tag{3.19}$$

We have used the following convention for the fusion rules, $a \times b = e$, $b \times c = f$, and $a \times c = g$. We can see this is very similar to Figure 2.9. Equivalently, we could say Equation (3.18) can be obtained from Equation (3.19) by imposing that the F-symbols are trivial, we can notice this mirrors quite closely the structure of Equation (2.29). Following this procedure for the other graph braid generators and their representation matrices, the following graph braiding hexagon equations can be similarly deduced,

$$(Q_{gd}^{acb})^* \left[F_d^{acb} \right]_{gf} (R_f^{bc})^* = \sum_e \left[F_d^{cab} \right]_{ge} (R_d^{ec})^* \left[F_d^{abc} \right]_{ef},$$

$$R_g^{ca} \left[(F_d^{bac})^{-1} \right]_{ge} Q_{ed}^{bac} = \sum_f \left[(F_d^{bca})^{-1} \right]_{gf} R_d^{fa} \left[(F_d^{abc})^{-1} \right]_{fe}, \tag{3.20}$$

$$(R_g^{ac})^* \left[(F_d^{bac})^{-1} \right]_{ge} (P_{ed}^{abc})^* = \sum_f \left[(F_d^{bca})^{-1} \right]_{gf} (R_d^{af})^* \left[(F_d^{abc})^{-1} \right]_{fe}.$$

The graph hexagon equations in Equation (3.20) come from the following compatibility of graph braid generators,

$$\sigma_2^{(2_b,2_a,1_c)} \circ \sigma_1^{(2_b,1_c)} = \sigma_1^{(2_e,1_c)} = \sigma_1^{(2_{b\times a},1_c)},$$

$$\sigma_1^{(1_a,2_c)} \circ \sigma_2^{(2_c,1_a,2_b)} = \sigma_1^{(1_a,2_f)} = \sigma_1^{(1_a,2_{b\times c})}, \qquad (3.21)$$

$$\sigma_1^{(2_a,1_c)} \circ \sigma_2^{(1_c,2_a,1_b)} = \sigma_1^{(2_a,1_f)} = \sigma_1^{(2_a,1_{b\times c})}.$$

We can observe that the first equation in Equation (3.21) is the inverse process of equation (3.18). Hence their corresponding graph hexagon equations are not independent. So, similar to the planar hexagon equations, there are only two independent graph braiding hexagon equations, the equations for P^{-1} and Q^{-1} can be deduced by taking the Hermitian adjoint of the hexagon equations for P- and Q- symbols respectively. Before we proceed with solutions, we can check that the equations are consistent with simple physical requirements. If we set the second or third particle away from the junction equal to the vacuum charge, we find that the value of the P- and Q- graph braid symbols are trivial. This is consistent with what one would physically expect since this would be braiding a particle with a vacuum charge, which is trivial,

$$P_{ae}^{1ab} = Q_{ae}^{1ab} = P_{ae}^{a1b} = Q_{ae}^{a1b} = 1_{\mathbb{C}}. \qquad (3.22)$$

If the particle closest to the junction is the vacuum charge, the P and Q matrices reduce to $R_e^{ab} = \rho(\sigma_1^{(1,2)})$. This is what one would expect, since if the particle closest to the junction is trivial then there is no particle in the way that must be moved. Therefore, the particles are exchanged with a σ_1 graph braid,

$$P_{ee}^{ab1} = Q_{ee}^{ab1} = R_e^{ab}. \qquad (3.23)$$

Since the graph braid matrices and F symbols are invertible, we can use the graph hexagon equations to express the P and Q symbols in terms of the R symbols and F-symbols. So we can express the $\rho(\sigma_2)$ generators in terms of $\rho(\sigma_1)$ generators and F symbols. This is not possible in the graph braid group, but the introduction of fusion and naturality of graph braiding allows us to. From the graph hexagon equations (3.19) and (3.20), we have, using unitarity of F, given in 2.20 and R,

$$P_{gd}^{cab} = \sum_e \left[F_d^{cab}\right]_{ge} R_d^{ce} \left[F_d^{abc}\right]_{ef} (R_f^{cb})^* / \left[F_d^{acb}\right]_{gf} \qquad (3.24)$$

$$Q_{ed}^{bac} = \sum_f \left[F_d^{bca}\right]_{fg}^* R_d^{fa} \left[F_d^{abc}\right]_{ef}^* (R_g^{ca})^* / \left[F_d^{bac}\right]_{eg}^* \qquad (3.25)$$

We can deduce similar equations for P^{-1} and Q^{-1}. This means we only need to supply the F-symbols and find the R_e^{ab} to fix all symbols. Examining this equation,

we observe that the right hand side equation is dependent on the label f. However P_{gd}^{cab} does not depend on f. This is because we have made P depend on all three particles, but it does not depend on the fusion channel of the two particles closest to the junction since it does not act on the right associated fusion tree. Therefore, for any assignment of f, we must get the same value for P_{gd}^{cab}. For theories with non-Abelian braidings, such as Tambara-Yamagami and Fibonacci, this is an important observation needed to solve the system, as it allows us to equate the right hand side of Equation (3.24) for different choices of f to get expressions purely for the R graph braid matrices. We will see an example of this in Section 3.4.3.

As a final remark, we note there is no a priori reason that describing the graph braiding of three particles is sufficient to describe it for any number of particles. As we introduce more particles to the system, new graph braid generators are introduced, e.g. $\sigma_3^{(1,1,1,2)}$, etc. We will return to this later in Section 4.2 and Section A. This is in contrast to the planar theory of anyons in which the solution of the hexagon equations for three particles is sufficient for any number of particles (102).

3.4 Solutions of the trijunction graph hexagon equations

Now we will proceed with solving the graph hexagon equations on a trijunction. First of all, we note that when $P_{ed}^{abc} = Q_{ed}^{abc} = R_e^{ab}$, for all a, b, c, d, e, the graph hexagons reduce to the usual hexagon equations for planar systems. The corresponding graph braid group representations are representations of $\mathcal{B}_N$, the planar braid group. Hence any planar anyon model immediately provides solutions to these equations, although often further solutions exist. We now consider some simple fusion models to illustrate what else is possible.

3.4.1 Abelian fusion rules

We start with a fusion model constructed over an Abelian group, G as we described in Section 2.6.1. In this case, the label f in Equation (3.24) is fixed as the unique fusion channel of b and c since group multiplication always has a unique outcome. Hence a choice of $R_{a \times b}^{ab}$ just fixes the P and Q symbols. There are no requirements on R, apart from $R_c^{ab} \in U(1)$ and $R_a^{a1} = R_a^{1a} = 1$. The graph braiding hexagon equations reduce to the simpler form,

$$P_{gd}^{cab} \, w(a, c, b) \, R_f^{cb} = w(c, a, b) R_d^{c,ab} \, w(a, b, c),$$
$$R_g^{c,a} \, w^*(b, a, c) \, Q_{ed}^{bac} = w^*(b, c, a) \, R_d^{bc,a} \, w^*(a, b, c) \,.$$

This gives us many examples which do not satisfy the planar hexagon equations. For example, when $G = (\mathbb{Z}_M, +)$, the cyclic group written with the additive product.

We can use the group cocycle defined in Equation (2.46), which is symmetric in the last two inputs, to simplify the graph hexagon equations. We find the graph hexagon equations are written as,

$$P_{gd}^{cab} = (R_f^{cb})^* \, R_d^{c,a+b} \, w(c,a,b)$$
$$Q_{ed}^{bac} = (R_g^{ca})^* \, R_d^{b+c,a} \, w^*(a,b,c). \tag{3.26}$$

We can tabulate solutions. Let $M = 2$, then there is one non trivial configuration with $a = b = c = d = 1$, the non trivial element in $\mathbb{Z}_2$,

$$P_{01}^{111} = (R_0^{11})^* \, w(1,1,1) = (R_0^{11})^* e^{\pi i k},$$
$$Q_{01}^{111} = (R_0^{11})^* \, w^*(1,1,1) = (R_0^{11})^* e^{-\pi i k}, \tag{3.27}$$

where k is the parameter labelling the three cocycle. We find that R_0^{11} is a free parameter, so there is a continuous family of solutions. In contrast, for the planar hexagon equations, there is only a finite family of solutions (70; 100). If we consider $\mathbb{Z}_3^{\omega}$, where ω is a non trivial cocycle and let $\alpha := e^{-2\pi i/3}$ we find,

$$
\begin{array}{ll}
P_{10}^{222} = R_0^{21}(R_0^{22})^* \alpha & Q_{10}^{222} = (R_1^{22})^* R_0^{12} \alpha^* \\
P_{12}^{221} = (R_0^{21})^* \alpha & Q_{10}^{221} = (R_0^{12})^* \alpha^* \\
P_{02}^{212} = (R_1^{22})^* \alpha & Q_{02}^{212} = (R_0^{21})^* R_2^{11} \alpha^* \\
P_{02}^{122} = (R_0^{12})^* R_2^{11} \alpha & Q_{02}^{122} = (R_1^{22})^* \alpha^* \\
P_{21}^{112} = (R_0^{12})^* \alpha & Q_{21}^{112} = (R_0^{21})^* \alpha^* \\
P_{01}^{121} = (R_2^{11})^* \alpha & Q_{01}^{121} = (R_0^{12})^* R_1^{22} \alpha^* \\
P_{01}^{211} = (R_0^{21})^* R_1^{22} & Q_{01}^{211} = (R_2^{11})^* \\
P_{20}^{111} = (R_2^{11})^* R_0^{12} & Q_{20}^{111} = R_0^{21}(R_2^{11})^*
\end{array}
\tag{3.28}
$$

So $R_2^{11}, R_0^{12}, R_0^{21}$ and R_1^{22} are independent free parameters. If we impose $P = Q$ and focus in particular on $P_{20}^{111} = Q_{20}^{111}$ and $P_{21}^{112} = Q_{21}^{112}$, we find no solution to the graph hexagon equations with non trivial cocycle. The solutions R_c^{ab} to the planar hexagon equations for $\mathbb{Z}_M^{\omega}$ with trivial $\omega = 1$ are required to form a symmetric bicharacter (69), but no such requirement is needed on a graph. Perhaps more interestingly, there is often no nontrivial solution to the planar hexagon equations. This occurs e.g. when M is odd and $\omega(a,b,c)$ is cohomologically non-trivial (28; 69; 81). Nevertheless, there is a solution for any choice of the $R_{a\times b}^{a,b}$ on the trijunction, and so we can graph braid particles that do not allow for planar braiding.

Overall, for any Abelian group G, we obtain a $(|G| - 1)^2$ parameter family of solutions for any fixed choice of F-symbols. Not all of these solutions are physically distinct, as some are related by the gauge freedom given in Equation (3.17). However, since the exchange $R_{a\times a}^{aa}$ and the products $R_{a\times b}^{ab} R_{b\times a}^{ba}$ are independent and

gauge invariant for all $a, b \neq 1$, we always have $|G|(|G| - 1)/2$ parameters up to gauge freedom. Now one may wonder could we make gauge invariant quantities from the new graph braid symbols; P or Q, such as P^{aab} and $P^{abc} \times P^{bac}$. However, we could use the hexagon equations to express either of these in terms of R and F symbols, so they are not independent gauge invariant quantities.

3.4.2 Fibonacci

The next model we will examine is the Fibonacci anyon theory. We discussed the planar Fibonacci model in Section 2.6.4. Since there is an f intermediate anyon degree of freedom in determining P_{ed}^{abc} and a g anyon degree of freedom in Q_{ed}^{abc}, there will be two expressions for each value of P and Q.

We shall begin with $a = b = c = \tau$ and total topological charge, $d = 1$, then the graph hexagon equations are written as,

$$P_{\tau 1}^{\tau\tau\tau} \left[F_1^{\tau\tau\tau}\right]_{\tau\tau} R_\tau^{\tau\tau} = \left[F_1^{\tau\tau\tau}\right]_{\tau\tau} R_\tau^{\tau\tau} \left[F_1^{\tau\tau\tau}\right]_{\tau\tau},$$
$$R_\tau^{\tau\tau} \left[(F_1^{\tau\tau\tau})^{-1}\right]_{\tau\tau} Q_{\tau 1}^{\tau\tau\tau} = \left[(F_1^{\tau\tau\tau})^{-1}\right]_{\tau\tau} R_1^{\tau\tau} \left[(F_1^{\tau\tau\tau})^{-1}\right]_{\tau\tau}.$$

$$(3.29)$$

Then from Chapter 2 we know all of the F-symbols are equal to $1_\mathbb{C}$ and Equation 3.29 simplify to

$$P_{\tau 1}^{\tau\tau\tau} = (R_\tau^{\tau\tau})^* R_1^{\tau\tau}$$
$$Q_{\tau 1}^{\tau\tau\tau} = R_1^{\tau\tau}(R_\tau^{\tau\tau})^*.$$

$$(3.30)$$

We can observe that $P_{\tau 1}^{\tau\tau\tau} = Q_{\tau 1}^{\tau\tau\tau}$. The next configuration is $a = b = c = d = \tau$. The graph hexagon equations are written as follows

$$P_{g\tau}^{\tau\tau\tau} \left[F_\tau^{\tau\tau\tau}\right]_{gf} R_f^{\tau\tau} = \sum_e \left[F_\tau^{\tau\tau\tau}\right]_{ge} R_\tau^{\tau e} \left[F_\tau^{\tau\tau\tau}\right]_{ef}$$
$$R_g^{\tau\tau} \left[(F_\tau^{\tau\tau\tau})^{-1}\right]_{ge} Q_{e\tau}^{\tau\tau\tau} = \sum_f \left[(F_\tau^{\tau\tau\tau})^{-1}\right]_{gf} R_\tau^{f\tau} \left[(F_\tau^{\tau\tau\tau})^{-1}\right]_{fe}.$$

$$(3.31)$$

The possible intermediate labels are,

$$e = 1/\tau, \qquad f = 1/\tau, \qquad g = 1/\tau. \qquad (3.32)$$

We can express the P- and Q- symbols in terms of the F symbols and the R symbols, as mentioned previously, for each P there will be two expressions, given by different values of f, similar for Q except with the label g. We shall express the two expressions for P with the left equality given by the value, $f = 1$ for the intermediate anyon and the right equality given by the value, $f = \tau$,

$$P_{1\tau}^{\tau\tau\tau} = (R_1^{\tau\tau})^*(\phi^{-1} + R_\tau^{\tau\tau}) = (R_\tau^{\tau\tau})^*\phi^{-1}(1 - R_\tau^{\tau\tau})$$
$$P_{\tau\tau}^{\tau\tau\tau} = (R_1^{\tau\tau})^*\phi^{-1}(1 - R_\tau^{\tau\tau}) = -(R_\tau^{\tau\tau})^*(1 + \phi^{-1}R_\tau^{\tau\tau}).$$

$$(3.33)$$

The expressions for Q in terms of R and F-symbols are similar. To proceed further with the solution we first take the Hermitian adjoint of Equation (3.31) to get an expression for $(P_{1\tau}^{\tau\tau})^{-1}$ and then imposing $P_{1\tau}^{\tau\tau} \times (P_{1\tau}^{\tau\tau})^{-1} = 1$ with $f = 1$ we get

$$(R_1^{\tau\tau})^*(\phi^{-1} + R_\tau^{\tau\tau})R_1^{\tau\tau}(\phi^{-1} + (R_\tau^{\tau\tau})^*) = 1,$$
$$\implies \phi^{-1}(R_\tau^{\tau\tau} + (R_\tau^{\tau\tau})^*) = -\phi^{-2} \tag{3.34}$$
$$\implies R_\tau^{\tau\tau} + (R_\tau^{\tau\tau})^* = -\phi^{-1}.$$

But we know that $R_\tau^{\tau\tau} \in U(1)$ and we are adding a complex number to its complex conjugate, so this equation implies

$$2\operatorname{Re}(R_\tau^{\tau\tau}) = -\phi^{-1}.$$
$$\implies \operatorname{Re}(R_\tau^{\tau\tau}) = \frac{-1 + \sqrt{5}}{4} \tag{3.35}$$

On the unit circle, there are two values that $R_\tau^{\tau\tau}$ can have;

$$R_\tau^{\tau\tau} = e^{\frac{3\pi i}{5}} \text{ or } e^{\frac{-3\pi i}{5}}. \tag{3.36}$$

Now we proceed by equating the expressions for $P_{1\tau}^{\tau\tau\tau}$ with $f = 1$ to that with $f = \tau$ to get,

$$(R_1^{\tau\tau})^*(\phi^{-1} + R_\tau^{\tau\tau}) = (R_\tau^{\tau\tau})^*\phi^{-1}(1 - R_\tau^{\tau\tau}) \tag{3.37}$$

This gives the solutions

$$R_\tau^{\tau\tau} = e^{\frac{3\pi i}{5}} \implies R_1^{\tau\tau} = e^{\frac{-4\pi i}{5}}$$
$$R_\tau^{\tau\tau} = e^{\frac{-3\pi i}{5}} \implies R_1^{\tau\tau} = e^{\frac{4\pi i}{5}}. \tag{3.38}$$

For $N = 3$ particles on a trijunction, we have recovered the planar solution exactly. This is an instance of a model which has,

$$P_{ed}^{abc} = Q_{ed}^{abc} = R_e^{ab}. \tag{3.39}$$

As we discussed, this is the limit in which the graph braiding hexagon equations are exactly equivalent to the planar braiding hexagon equations.

3.4.3 Ising

In this section, we will solve the graph hexagon equations for the Ising fusion rules on a trijunction. There are two non-equivalent sets of F-symbols, distinguished by the value of the Frobenius-Schur indicator, $\nu_\sigma = \pm 1$ (100). We first consider Equation (3.19) with $a = b = c = d = \sigma$.

Focusing on the equation for $P_{1\sigma}^{\sigma\sigma\sigma}$ and substituting the F-symbols we find that

$$P_{1\sigma}^{\sigma\sigma\sigma} = \frac{\nu}{\sqrt{2}} (R_f^{\sigma\sigma})^* [(F_\sigma^{\sigma\sigma\sigma})^*]_{1f} \sum_e [F_\sigma^{\sigma\sigma\sigma}]_{1e} R_\sigma^{\sigma e} [F_\sigma^{\sigma\sigma\sigma}]_{ef}. \tag{3.40}$$

We note that f on the right hand side of this expression can be equal to 1 or ψ, this leads to the following two expressions for $P_{1\sigma}^{\sigma\sigma\sigma}$

$$\begin{aligned}
P_{1\sigma}^{\sigma\sigma\sigma} &= \frac{\nu}{\sqrt{2}} (R_1^{\sigma\sigma})^* \left(R_\sigma^{\sigma 1} + R_\sigma^{\sigma\psi} \right) \\
&= \frac{\nu}{\sqrt{2}} (R_\psi^{\sigma\sigma})^* \left(R_\sigma^{\sigma 1} - R_\sigma^{\sigma\psi} \right).
\end{aligned} \tag{3.41}$$

We note Equation (3.41) gives two equivalent expressions for $P_{1\sigma}^{\sigma\sigma\sigma}$, given by the choices $f = 1$ and $f = \psi$. However, since $P_{1\sigma}^{\sigma\sigma\sigma}$ does not depend on the choice of f, we can equate the expressions for each choice and arrive at an expression purely for the R symbols. This is given by

$$(R_1^{\sigma\sigma})^* \left(1 + R_\sigma^{\sigma\psi} \right) = (R_\psi^{\sigma\sigma})^* \left(1 - R_\sigma^{\sigma\psi} \right). \tag{3.42}$$

This gives us an expression constraining the R symbols directly. Notice that this equation does not depend on ν, and neither do other equations for the R symbols, so the solutions for R will not detect the dependence on the Frobenius-Schur indicator. Additionally, we can take the Hermitian adjoint of Equation (3.40) to get an expression for $(P_{1\sigma}^{\sigma\sigma\sigma})^{-1}$ and then imposing $P_{1\sigma}^{\sigma\sigma\sigma} \times (P_{1\sigma}^{\sigma\sigma\sigma})^{-1} = 1$ with $f = 1$ we get,

$$\begin{aligned}
1 &= \frac{\nu^2}{2} (R_1^{\sigma\sigma})^* (1 + R_\sigma^{\sigma\psi}) R_1^{\sigma\sigma} (1 + (R_\sigma^{\sigma\psi})^*) \\
&= 1 + \frac{1}{2} \left(R_\sigma^{\sigma\psi} + (R_\sigma^{\sigma\psi})^* \right)
\end{aligned} \tag{3.43}$$

and hence $(R_\sigma^{\sigma\psi})^* = -R_\sigma^{\sigma\psi}$, which yields $R_\sigma^{\sigma\psi} = \pm i$.
Substituting this back into Equation (3.42), we find that

$$R_1^{\sigma\sigma} = R_\sigma^{\sigma\psi} R_\psi^{\sigma\sigma} = \pm i R_\psi^{\sigma\sigma}. \tag{3.44}$$

By equating the expressions for $Q_{1\sigma}^{\sigma\sigma\sigma}$ with $f = 1$ and $f = \psi$ we find

$$(R_1^{\sigma\sigma})^*(1 + R_\sigma^{\psi\sigma}) = (R_\psi^{\sigma\sigma})^*(1 - R_\sigma^{\psi\sigma}). \tag{3.45}$$

Comparing Equation (3.45) with Equation (3.42) implies $R_\sigma^{\sigma\psi} = R_\sigma^{\psi\sigma}$.
We can tabulate the resulting values for P and Q.
The value for $a = b = c = d = \psi$;

$$P_{1\psi}^{\psi\psi\psi} = Q_{1\psi}^{\psi\psi\psi} = (R_1^{\psi\psi})^*. \tag{3.46}$$

Two particles are ψ and one particle is σ;

$$
\begin{aligned}
P^{\sigma\psi\psi}_{\sigma\sigma} &= Q^{\psi\sigma\psi}_{\sigma\sigma} = \pm i, \\
P^{\psi\sigma\psi}_{\sigma\sigma} &= -Q^{\sigma\psi\psi}_{\sigma\sigma} = \pm i \, (R^{\psi\psi}_1)^*, \\
P^{\psi\psi\sigma}_{1\sigma} &= Q^{\psi\psi\sigma}_{1\sigma} = -1.
\end{aligned}
\tag{3.47}
$$

Two particles are σ, one particle is ψ and the total topological charge $d = \psi$;

$$
\begin{aligned}
P^{\psi\sigma\sigma}_{\sigma\psi} &= Q^{\psi\sigma\sigma}_{\sigma\psi} = \pm i, \\
P^{\sigma\sigma\psi}_{1\psi} &= Q^{\sigma\sigma\psi}_{1\psi} = R^{\sigma\sigma}_1, \\
P^{\sigma\psi\sigma}_{\sigma\psi} &= Q^{\sigma\psi\sigma}_{\sigma\psi} = \pm i.
\end{aligned}
\tag{3.48}
$$

Two particles are σ, one particle is ψ and the total topological charge $d = 1$;

$$
\begin{aligned}
P^{\psi\sigma\sigma}_{\sigma 1} &= Q^{\sigma\psi\sigma}_{\sigma 1} = \mp i R^{\psi\psi}_1, \\
P^{\sigma\psi\sigma}_{\sigma 1} &= Q^{\psi\sigma\sigma}_{\sigma 1} = \pm i, \\
P^{\sigma\sigma\psi}_{\psi 1} &= Q^{\sigma\sigma\psi}_{\psi 1} = \mp i R^{\sigma\sigma}_1.
\end{aligned}
\tag{3.49}
$$

The final configuration has $a = b = c = d = \sigma$;

$$
\begin{aligned}
P^{\sigma\sigma\sigma}_{1\sigma} &= Q^{\sigma\sigma\sigma}_{1\sigma} = \nu \, e^{\frac{\pm\pi i}{4}} \, (R^{\sigma\sigma}_1)^*, \\
P^{\sigma\sigma\sigma}_{\psi\sigma} &= Q^{\sigma\sigma\sigma}_{\psi\sigma} = \nu \, e^{\frac{\mp\pi i}{4}} \, (R^{\sigma\sigma}_1)^*.
\end{aligned}
\tag{3.50}
$$

The corresponding values for Q^{-1} and P^{-1} are given by the Hermitian adjoints of the relevant equations for Q and P. By direct verification, all graph braid hexagon equations are now satisfied for any choice of $R^{\sigma\sigma}_1$ and $R^{\psi\psi}_1$ in $U(1)$ and for both choices of ν and of the signs. It is interesting to observe that we have $P \neq Q$ whenever $R^{\psi\psi}_1 \neq -1$. In other words, $P \neq Q$ unless ψ is a fermion. Nevertheless, even if $R^{\psi\psi}_1 = -1$, the solution is usually not planar, as $R^{\sigma\sigma}_1$ is still a $U(1)$-free parameter. In Chapter 4 we will discuss new constraint equations that arise from considering more particles on a graph. When we take these into account we will find exactly $R^{\psi\psi}_1 = -1$.

3.5 Tetrajunction

The tetrajunction Γ_4 is one of the simplest graphs for which the graph braid group contains a pseudobraid relation, as discussed in Section 3.2. Additionally $B_3(\Gamma_4)$ contains three sub-trijunctions. To see this consider first assigning particles to an edge, then to exchange two particles they must go to distinct edges, of which there are then three choices of pairs of edges. So explicitly, we can exchange using edges; (1,2), edges (2,3) or edges (1,3) for the exchange. The graph braid group $B_3(\Gamma_4)$ is a

free group of rank eleven, but there are twelve elements in the σ presentation. One of these can be eliminated by utilising the pseudobraid relation (10). The graph braid matrices representing the generators of $B_3(\Gamma_4)$ can be written;

$$
\begin{aligned}
\rho(\sigma_1^{(1,2)}) &:= X, & \rho(\sigma_2^{(a_1,1,2)}) &= X_{a_1}, \\
\rho(\sigma_1^{(2,3)}) &:= Y, & \rho(\sigma_2^{(a_1,2,3)}) &= Y_{a_1}, \\
\rho(\sigma_1^{(1,3)}) &:= Z, & \rho(\sigma_2^{(a_1,1,3)}) &= Z_{a_1},
\end{aligned}
\tag{3.51}
$$

where $a_1 \in \{1, 2, 3\}$ labels the edge that the particle closest to the junction point goes to during the graph braid. This notation highlights the trijunction subgroups. Referring to the notation used for the trijunction in Equation (3.16), we see that the R-matrices (given by exchanging the two particles closest to the junction point) for each sub-trijunction occur in the first column above and are now labelled X, Y and Z for the three sub trijunctions. The P and Q graph braid matrices appear in the second column, and for example, the trijunction which utilises edges (1) and (2) has $R \equiv X$, $P \equiv X_1$ and $Q \equiv X_2$. Similarly (Y, Y_2, Y_3) and (Z, Z_1, Z_3) also generate trijunction subgroups. As an example, the graph hexagon equations for the Z sub-trijunction are written as;

$$
\begin{aligned}
Z_1{}_{gd}^{cab} \left[F_d^{acb}\right]_{gf} Z_f^{cb} &= \sum_e \left[F_d^{cab}\right]_{ge} Z_d^{ce} \left[F_d^{abc}\right]_{ef}, \\
Z_g^{ca} \left[(F_d^{bac})^{-1}\right]_{ge} Z_3{}_{ed}^{bac} &= \sum_f \left[(F_d^{bca})^{-1}\right]_{gf} Z_d^{fa} \left[(F_d^{abc})^{-1}\right]_{fe}.
\end{aligned}
\tag{3.52}
$$

The generators X_3, Y_1 and Z_2 utilise all edges and have no counterpart on a trijunction. Consistency of braiding and fusion now comes down to graph hexagon equations similar to Equation (3.19) and (3.20) on each sub-trijunction, yielding six independent sets of equations. No hexagon equations exist for the generators that involve all three edges. In particular, if one tries to commute a fusion vertex through a graph braid involving one of these generators, the fusion vertex will get blocked on the junction point.

Since we have three independent copies of the graph hexagon equations for the trijunction, they can be solved as before. However, one can make independent choices of solutions for each set of trijunction hexagon equations. E.g. in the case of the Ising fusion rules, one could have $X_\sigma^{\sigma\psi} = +i$ and $Y_\sigma^{\sigma\psi} = Z_\sigma^{\sigma\psi} = -i$. Similarly, for the Fibonacci model, which only allows the usual planar solutions on the trijunction, we can now choose solutions of different chirality on the subjunctions, which yields non-planar solutions for this model on the tetrajunction. The generators X_3, Y_1 and Z_2, which use all edges, occur in the pseudobraid relation,

$$
\sigma_2^{(1,2,3)} \sigma_1^{(1,3)} \sigma_2^{(3,1,2)} = \sigma_1^{(1,2)} \sigma_2^{(2,1,3)} \sigma_1^{(2,3)}.
\tag{3.53}
$$

This is a graph braiding analogue of a Yang-Baxter equation (10; 116). One may write 6 such relations for different permutations of $(1, 2, 3)$, but only one is independent. We can write the pseudobraid relation in terms of the X, Y and Z symbols by introducing fusion trees at the bottom of the diagrams in Figure 3.4. The equality then induces a dodecagonal commutative diagram of F-moves and exchanges, similar to how the equality expressing the compatibility of fusion and braiding induced the graph braiding hexagon equations in Figure 3.9. This gives the following equations,

$$
\begin{aligned}
&Y_{1\,fd}^{cba} \sum_{e,g} \left[F_d^{bca}\right]_{fg} Z_g^{ca} \left[(F_d^{bac})^{-1}\right]_{ge} X_{3\,ed}^{bac} \left[F_d^{abc}\right]_{ef} \\
&= Y_f^{cb} \sum_{e,g} \left[F_d^{cba}\right]_{fe} X_e^{ba} \left[(F_d^{cab})^{-1}\right]_{eg} Z_{2\,gd}^{cab} \left[F_d^{acb}\right]_{gf}
\end{aligned}
\tag{3.54}
$$

Let's examine some trivial cases of this expression involving vacuum charge 1,

$$
\begin{aligned}
a = 1 &\implies Y_{1\,ff}^{cb1} = Y_f^{cb} \\
b = 1 &\implies Z_{2\,gg}^{ca1} = Z_g^{ca} \\
c = 1 &\implies P_{3\,ee}^{ba1} = X_e^{ba}.
\end{aligned}
\tag{3.55}
$$

This expresses that since the edge assignment is fixed throughout the pseudobraid relation, if one of the particles is a vacuum charge, the pseudobraid relation does not involve that edge and, in fact, it is just a σ_1 braid involving the two edges the other two particles are sent. This equation allows us to fix the Y_1 symbols in terms of the other symbols. There is never a conflict with the graph hexagons for the trijunctions, as they never involve Y_1. Of course, by choosing a different pseudobraid relation, we could choose to eliminate the X_3 or Z_2 symbols if we prefer. Note that, although we can always eliminate one of the families of symbols that involve all three edges, the other two families are free parameters, as they are not constrained by any further equations. For example, for Abelian fusion rules governed by a group G, we have an extra $2(|G-1|)^3$ free parameters in addition to the $3(|G|-1)^2$ parameters coming from the trijunctions. The situation is similar for non-Abelian models – we have free parameters for all of these, although the actual parameter counting is a little more complicated. For example, in the Fibonacci model, we have the following summary of generators,

$$
\begin{aligned}
&W_c^{ab}; \quad W_1^{\tau\tau} \quad W_\tau^{\tau\tau}, \\
&W_{a_1\,ed}^{\ \ abc}; \quad W_{a_1\tau\tau}^{\ \tau\tau\tau} \quad W_{a_1\tau 1}^{\ \tau\tau\tau} \quad W_{a_1 1\tau}^{\ \tau\tau\tau},
\end{aligned}
\tag{3.56}
$$

where $W \in \{X, Y, Z\}, a_1 \in \{1, 2, 3\}$. There are $2 \times |\sigma_1| = 2 \times 3 = 6$, Fibonacci variables of σ_1 generators and there are $3 \times |\sigma_2| = 3 \times 9 = 27$ variables corresponding to σ_2 generators. Using the pseudobraid relation, we then know there are three free

X_3 symbols and 3 free Z_2 symbols, even though there are no free parameters on the trijunction, see Section 3.4.2.

Equation (3.54) simplifies for Abelian fusion rules. For these, $\left[F_{a \times b \times c}^{abc}\right]_{a \times b, b \times c} = \omega(a, b, c)$, where ω is a $U(1)$ valued group 3-cocycle, which we discussed in Section 2.6.1. We can write the pseudobraid relation in this case as

$$Y_{1fd}^{cba} \, c_a(b, c) \, X_{3ed}^{bac} \, Z_g^{ca} \;=\; Y_f^{cb} \, c_a(c, b) \, X_e^{ba} \, Z_{2gd}^{cab}, \tag{3.57}$$

where $c_a(b, c)$ is the Slant product (60),

$$c_a(b, c) := (i_a \omega)(b, c) = \frac{\omega(a, b, c)\omega(b, c, a)}{\omega(b, a, c)}. \tag{3.58}$$

Often, we can take $c_a(b, c) = c_a(c, b)$, this happens for example for all $\mathbb{Z}_M^\omega$ anyon models. In that case, the Abelian pseudobraid equation does not depend on the F-symbols. So the implication is that one of the σ_2 generators can be expressed in terms of the others. Therefore it is not independent, which we already know from $B_3(\Gamma_4)$. So then each sub trijunction has $(M - 1)^2$ free $U(1)$ parameters. There are three graph braid generators involving all three edges, so there are $3(M - 1)^3$ possible graph braid matrices for these for $\mathbb{Z}_M^\omega$. The pseudobraid relation then gives that $(M - 1)^3$ of these variables can be removed, so there are

$$3(M - 1)^2 + 3(M - 1)^3 - (M - 1)^3 = 3(M - 1)^2 + 2(M - 1)^3$$

free $U(1)$-parameters for $\mathbb{Z}_M$ fusion rules on a tetra junction.

Finally, we note that we also have new gauge invariant parameters on a tetrajunction - for example, the gauge invariant quantities $W^{ab}(W')^{ba}$, where $W = \{X, Y, Z\}$ and $W \neq W'$, appear in addition to the parameters W^{aa} and $W^{ab}W^{ba}$ which come from the sub-trijunctions.

3.6 Hopping model for graph braiding on a trijunction

In this section, we will introduce a local model of quasiparticles exchanging at a trijunction to model solutions of the graph braiding hexagon equations presented in Section 3.3 in particular, Section 3.4.1. Our construction in this chapter so far has involved extending the planar algebraic theory of anyons to anyons exchanging on a graph, however, there are other approaches to finding anyon exchange statistics. One example we will study in Chapter 7 is the toric code. In this model we will use local operators to move particles around a 2D lattice to deduce the braiding operators. It is this type of concept we would like try to adapt to a graph. In particular, we would like to understand under what conditions could a microscopic model of particle

hopping along a trijunction lattice under the action of local operators, produce the non-planar solutions we have found.

We have quasiparticles labelled by $\mathbb{Z}_2$, written additively, i.e. the presence of a quasiparticle is identified with 1, the non-trivial element of $\mathbb{Z}_2$ and fusion rules $1 \times 1 = 0$. We identify states in the Hilbert space with the positions of quasiparticles along the wires. We will construct unitary operators hopping the quasiparticles along the wires to implement the exchanges. The composition of these local operators will satisfy the solution to the graph hexagon equations for $\mathbb{Z}_2$ fusion rules and trivial F symbols.

The graph hexagon equations for $\mathbb{Z}_M$ fusion rules with trivial group cocycle (F-symbols) are written as,

$$P_{gd}^{cab} R_f^{cb} = R_d^{ce}, \qquad\qquad R_g^{ca} Q_{ed}^{bac} = R_d^{fa}. \qquad (3.59)$$

These equations can be derived starting from the graph braiding hexagon equations in Section 3.4. For $M = 2$, the case we are interested in, there is only one non-trivial constraint and it is given by,

$$P_{01}^{111} = Q_{01}^{111} = (R_0^{11})^*. \qquad (3.60)$$

There are no further constraints on R_0^{11}, apart from $R_0^{11} \in U(1)$ and $R_1^{10} = R_1^{01} = 1$. In contrast, there are two discrete solutions to the planar hexagon equations with trivial cocycle, given by $\tilde{R}_0^{11} = 1$ or $\tilde{R}_0^{11} = -1$, (28). Furthermore, as we discussed in Section 3.3, to recover the planar hexagon equations (2.35), from the graph braiding hexagon equations (3.19) and (3.20), is to impose $P = Q = R$. Therefore we would see $P = Q = R$ as the planar solution and Equation 3.60 as a graph braid solution.
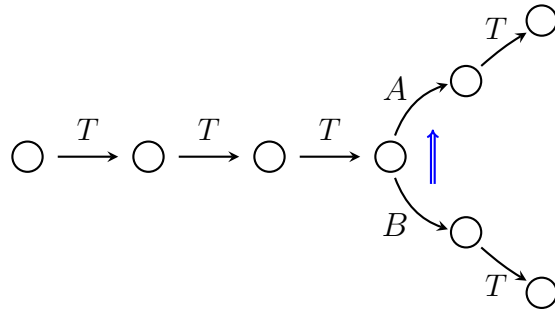
Figure 3.10: Here, we display a graphical representation of our hopping model. Each circular dot represents a region in the wire which may contain a quasiparticle excitation. We use the blue arrow to denote the ancillary degree of freedom. We also display the lattice sites where our unitary operators act.

To model this, we introduce an ancillary degree of freedom, displayed as a blue arrow in Figure 3.10. The purpose of this is to keep track of how many particles have passed through the junction. As each particle passes the junction, the spin flips 180 degrees, so two particles passing through the junction returns the ancillary

to its initial configuration. Accordingly, we label the resulting phase acquired by the states in our Hilbert space. We define the action of the T operator, which shuttles particles to the junction point to be,

$$T\left|\bullet \circ \Uparrow {\circ \atop \circ}\right\rangle = \left|\circ \bullet \Uparrow {\circ \atop \circ}\right\rangle. \tag{3.61}$$

We have chosen this action to isolate the effect of exchanging the particles at the junction rather than the dynamical effects of shuttling particles along a quantum wire. One could introduce phases under the action of the T operator. However since we are always returning to the initial configuration, the resulting phases will cancel. We define the following actions of hopping across the junction onto the diagonal edges,

$$A\left|\bullet \Uparrow {\circ \atop \circ}\right\rangle = \theta_u \left|\circ \Downarrow {\bullet \atop \circ}\right\rangle, \qquad A\left|\bullet \Downarrow {\circ \atop \circ}\right\rangle = \theta_d \left|\circ \Uparrow {\bullet \atop \circ}\right\rangle,$$

$$B\left|\bullet \Uparrow {\circ \atop \circ}\right\rangle = \psi_u \left|\circ \Downarrow {\circ \atop \bullet}\right\rangle, \qquad B\left|\bullet \Downarrow {\circ \atop \circ}\right\rangle = \psi_d \left|\circ \Uparrow {\circ \atop \bullet}\right\rangle. \tag{3.62}$$

The inverse actions of A and B are defined such that they are both unitary operators on the Hilbert space. We can see that the phase accumulated from hopping a particle onto a diagonal edge depends on the junction point's configuration. We have introduced a subscript label on the phases to keep track of the orientation of the ancilla. To begin the exchange, we initially place all particles on the horizontal edge of the system. We denote this state by $|\Omega\rangle$, i.e

$$\left|\Omega\right\rangle = \left|\bullet \bullet \bullet \Uparrow {\circ \atop \circ}\right\rangle. \tag{3.63}$$

Although we display the particles on neighbouring sites, in reality, they would be well separated to adhere to adiabatic time evolution. The action of R_0^{11} is then given by the following sequence of hopping operations,

$$R|\Omega\rangle = B^{-1}T^{-1}A^{-1}BTA|\Omega\rangle. \tag{3.64}$$

We have decomposed the R symbol into a sequence of hopping moves. This sequence of operators hops a particle onto the upper edge, then brings a particle along the horizontal edge to the junction point and onto the lower edge. Finally, it brings them back to the initial edge in the opposite order. We can see this action is equivalent to the $\sigma_1^{(1,2)}$ graph braid generator depicted in Figure 3.2. The total phase accumulated by this sequence of hopping moves is,

$$R|\Omega\rangle = \theta_u \psi_d \theta_d^{-1} \psi_u^{-1}|\Omega\rangle. \tag{3.65}$$

The sequence of hopping operators that correspond to P_{01}^{111} is given by,

$$P_{01}^{111}|\Omega\rangle = A^{-1}T^{-1}T^{-1}B^{-1}T^{-1}T^{-1}A^{-1}BTATTTA|\Omega\rangle. \qquad (3.66)$$

The total phase accumulated by the sequence of hopping moves corresponding to P is,

$$P_{01}^{111}|\Omega\rangle = \theta_d\psi_u\theta_u^{-1}\psi_d^{-1}|\Omega\rangle. \qquad (3.67)$$

Similar to P_{01}^{111}, we can write Q_{01}^{111} as the following sequence of hopping operators,

$$Q_{01}^{111}|\Omega\rangle = B^{-1}T^{-1}T^{-1}B^{-1}T^{-1}T^{-1}A^{-1}BTATTTB|\Omega\rangle. \qquad (3.68)$$

The total phase accumulated by the sequence of hopping moves corresponding to Q is,

$$Q_{01}^{111}|\Omega\rangle = \theta_d\psi_u\theta_u^{-1}\psi_d^{-1}|\Omega\rangle. \qquad (3.69)$$

So we can see that in terms of the phases we have,

$$P_{01}^{111}|\Omega\rangle = Q_{01}^{111}|\Omega\rangle = \theta_d\psi_u\theta_u^{-1}\psi_d^{-1}|\Omega\rangle. \qquad (3.70)$$

If we compare the phases accumulated from the P_{01}^{111} and the Q_{01}^{111} exchanges with the R_0^{11} exchange, we can observe this exactly agrees with Equation 3.60. We can recover the planar exchange statistics as a limiting case of this, if $\theta_u = \theta_d$ and $\psi_u = \psi_d$, then we recover $P = Q = R$. We can observe that since we come back to the initial state of identical particles in the Hilbert space, this sequence of unitary operators is tracing out a closed path in the configuration space. As a result, the total phase accumulated during the exchanges can not be gauged away. Therefore we can see what allowed us to reproduce the graph hexagon equation from our local hopping model is the ancilla degree of freedom at the vertex. We used the orientation of the ancilla to label the phases corresponding to hopping a particle across the junction point. If we did not have the ancilla degree of freedom, or the phases in Equation 3.62 did not depend on the orientation of the ancilla, then we would only produce the planar solution; $P = Q = R$.

In essence, one can interpret this process as a discrete analogue of a Berry phase calculation. Of course, in practise, the exchanges would have to be carried out within the adiabatic limit. This has already been discussed in (23; 176) in the context of the Kitaev honeycomb model and in (8; 47), for Majorana bound states exchanging at a trijunction. Our ancilla, modelled as a spin flip, is a placeholder for some external degree of freedom, such as Jordan-Wigner strings for fermions in 1d or control over the gate voltages at the junction point.

3.7 Summary

In this chapter we introduced graph anyon models. This is an adaption of the algebraic theory of anyons we discussed in Chapter 2. On the physical side this is motivated by recent proposals for engineering anyon like excitations on wire networks, which may used for fault-tolerant quantum computation. Therefore, it is important to understand what are the similarities and differences between braiding anyons on the plane and braiding anyons on a graph. As we showed in Equation 2.36, planar anyon models generate representations of the planar braid group, hence we would like our graph anyon models to generate representations of the graph braid group.

In Section 3.2 we began with a comparison of the planar braid group and graph braid groups. Just as the planar braid group arises for identical particles arises from the configuration space 3.1, the graph group arises in an analogous construction for particles on graphs. We also introduced the σ presentation which we make extensive use of throughout the chapter and illustrated it with Figure 3.1.

In Section 3.3 we introduced the foundations of our graph anyon models. We first define the fusion rules and the action of F symbols on a graph. We then proceed to define how the three generators of $B_3(\Gamma_3)$ act on the anyon fusion space, see Figure 3.6 and Figure 3.7. From here we introduced probably the most crucial idea in the entire chapter, namely how to implement fusion commuting with graph braiding. In Section 2.5 we saw how fusion commuting with planar braiding led to the planar hexagon equations, see Equation 2.35. A solution of these equations gives a consistent set of braiding operators. We adapted this to a trijunction in Figure 3.8 and produced the hexagon diagram in Figure 3.9. By equating the sequences of maps on the upper and lower path we produced the first graph braiding hexagon equation, given in Equation 3.19. By considering other compatible generators we produced another three hexagon equations, see Equation 3.20. We then discussed the connection between our graph braiding hexagon equations and the planar hexagon equations. Interestingly we could observe that the planar hexagon equations arise as a limiting case of our graph braiding hexagon equations: $P = Q = R$.

In Section 3.4 we showed some simple solutions to the graph braiding hexagon equations to some notable anyon models: Abelian fusion rules, Fibonacci and Ising. We noted some interesting features. For example for the Fibonacci theory, we only found the planar solution, in comparison for Ising we found a two $U(1)$-parameter family of solutions, in striking contrast to the planar solutions, which have only discrete freedom.

In Section 3.5 we studied the next simplest graph beyond the trijunction, namely a tetrajunction. This is the first appearance of a pseudobraid relation, however the interesting result here is how the fusion commutes with graph braiding works. The tetrajunction contains three trijunction subgraphs, given by a choice of a pair

of edges to exchange particles. We can see this in our definition of the generators and their corresponding symbols in Equation 3.52. In particular we identified exchanges involving edges (2,3) by "Y" symbols. Then on each sub-trijunction there will be hexagon equations. However there is no hexagon equation involving distinct sub-trjunctions, i.e. mixing say Y-symbols and X-symbols. This result is more significant than it appears at first sight. It appears the solutions for $X = \rho(\sigma_1^{(1,2)})$, $Y = \rho(\sigma_1^{(2,3)})$ and $Z = \rho(\sigma_1^{(1,3)})$ are all independent. We find this to be a rather surprising result. The only equation involving generators from distinct subtrijunctions is the pseudobraid relation in Equation 3.53. However for the anyon models we studied, Ising, Fibonacci and $\mathbb{Z}_M$, this equation does not impose significant constraints to enforce something like $X = Y = Z$, as one may expect, physically.

In Section 3.6 we introduced a microscopic model of graph braiding. In particular we reproduced solutions of the graph hexagon equations using a sequence of local unitary hoppings. As we explained, the important ingredient to produce the graph braid solution to the hexagon equation was the introduction of an ancilla degree of freedom which we modelled at the vertex. See Figure 3.10. We defined the action of hopping particles across the junction to depend on the orientation of the ancilla, see Equation 3.62. With these definitions we were able to encode the topological braids e.g. Equation 3.66. From here we were able to reproduce the $\mathbb{Z}_2$ solution to the graph braiding hexagon equation; $P = Q = R^*$.

In Chapter 4 we will generalise this framework to more particles and a variety of graphs. Crucial to the next chapter will be our construction of the trijunction hexagon equations using fusion commuting with graph braiding.

Chapter 4

Graph braiding of anyons on networks

4.1 Introduction

In this chapter, we are concerned with extending the formalism of Chapter 3 beyond a graph consisting of a single vertex. We will study a variety of graphs and construct consistency equations on each of them. Part of the motivation stems from recent results (10; 116) on bi-, and tri-connected networks. These are graphs where between any distinct pairs of vertices there are 2, or 3, topologically distinct paths, respectively. In particular, it was shown that the graph braid group of a theta graph, which consists of two vertices joined by three distinct edges, is equivalent to the planar braid group. We will extend this result to case of anyons exchanging on graphs in Section 4.7. We discussed in Chapter 3 several notable differences between planar anyons and graph braided anyons. We showed that several notable families have continuous free parameters, in contrast to the discrete planar solutions. In addition to this we do not have coherence of the graph hexagon equations at $N = 3$ particles. This naturally motivates studying the graph anyon model on graphs of intermediate complexity between a single junction and the tri-connected graphs. We will show that the structure of the graph anyon models strongly depends on the graph-theoretic connectivity of a given network.

In this chapter we introduce a large variety of graph braid generators and consider their action on the anyon fusion space. We refer to the generators under this action as "graph-symbols", following F and R symbols from the planar algebraic theory of anyons. We tabulate a glossary of these symbols in Table 4.4.

This chapter is based on (114) in collaboration with Dr. Tomasz Maciążek and Gert Vercleyen. In particular, the tables in Section 4.6 were produced by Gert Vercleyen using Mathematica packages developed for the solution of pentagon and hexagon equations. In the paper, we also provide explicit solutions on the circle, lollipop and the trijunction for the Ising model, $D(\mathbb{Z}_2)$ and $TY(\mathbb{Z}_3)$.

4.2 Greater particle number on a trijunction

In this section, we will discuss graph braided anyon models with four or more particles. For planar braided anyon models, this situation is covered by Mac Lane coherence theorem (117), and the braided coherence theorem (141). The implication of these theorems is that the solutions of the pentagon and hexagon equations are sufficient for the description of any number of anyons. Explicitly, if one constructed some braiding polygon for $N > 3$ particles, one could use the pentagon and hexagon equations iteratively to satisfy this polygon and find no new constraint equations on the R and F symbols of the theory. However on a graph, since there are multiple topologically inequivalent choices for σ_j with $j > 1$ (as we discussed earlier), satisfying the 3-particle P- and Q-hexagons does not guarantee that we have a full description for any number of particles. In this section we will focus on a trijunction, the simplest graph permitting particle exchange and discuss later how the analysis translates to higher valence graphs. In the following we will work with the following convention for fusion labels for four particles

$$a \times b = f, \qquad a \times c = n, \qquad a \times d = m, \qquad a \times b \times c = g, \qquad a \times b \times d = j,$$
$$b \times c = h, \qquad b \times d = y, \qquad c \times d = l, \qquad a \times c \times d = r, \qquad b \times c \times d = k. \tag{4.1}$$

The new generators of the graph braid group for $N = 4$ (see Appendix A of (114) for an exhaustive definition of the generators) and their corresponding symbols are

$$\rho(\sigma_3^{(1,1,1,2)}) = X, \quad \rho(\sigma_3^{(2,2,1,2)}) = Y, \quad \rho(\sigma_3^{(2,1,1,2)}) = B, \quad \rho(\sigma_3^{(1,2,1,2)}) = A. \tag{4.2}$$

Note these X- and Y- symbols are unrelated to the family of X and Y symbols we introduced on the tetrajunction in Section 3.5. By $\rho(\sigma)$ we mean the action of a graph braid generator on the anyon Hilbert space see Section 2.5 and 2.3 for the case of the planar braid group generators. The first step is to resolve how the σ_3-graph braids from (4.2) act on the fusion space of four anyons V_e^{abcd}. For the σ_2-braids represented on a three-particle fusion space this is unambiguous – the two particles being exchanged are joined by a fusion vertex (as we can see in Figure 3.7). Thus, the respective braiding exchange operators are necessarily diagonal in the left-fused basis where the second and third particle away from the junction point are joined by a common fusion channel. However, for the σ_3-braids acting on the fusion space of four anyons, the choice of the appropriate fusion tree is not clear at the first sight. Clearly, the two particles being exchanged must be joined by a common fusion vertex. This leaves two choices for the fusion tree structure of the other two particles – the fully left associated (left-fused) basis or the pairwise associated basis.

Crucially, there are important physical arguments that dictate the correct choice of the fusion tree. Namely, if a braiding exchange operator is diagonal in a certain basis, then all the anyon charges appearing in the chosen fusion tree have to be conserved throughout the corresponding braiding exchange process. The total charge of a set of anyons is conserved if one can bound this set of anyons by a disk which remains sufficiently separated from the anyons outside the disk throughout the entire exchange process. These disks are associated with the choice of the fusion tree. For instance, the fusion tree with anyons a, b, c, d being fused pairwise implies two separate disks containing the pairs a, b and c, d respectively and one disk containing all the anyons a, b, c, d (note that the disks cannot leave the graph as this is the actual space where the anyons move) – see Figure 4.1a. Importantly, the pairwise-associated fusion tree is not a correct basis for representing the braid $\sigma_3^{(1_d, 2_c, 1_b, 2_a)}$ diagonally as anyons b and a will necessarily enter the disk containing anyons d and c during the exchange, hence the total charge of c and d may not be conserved. This is shown in Figure 4.1(b).
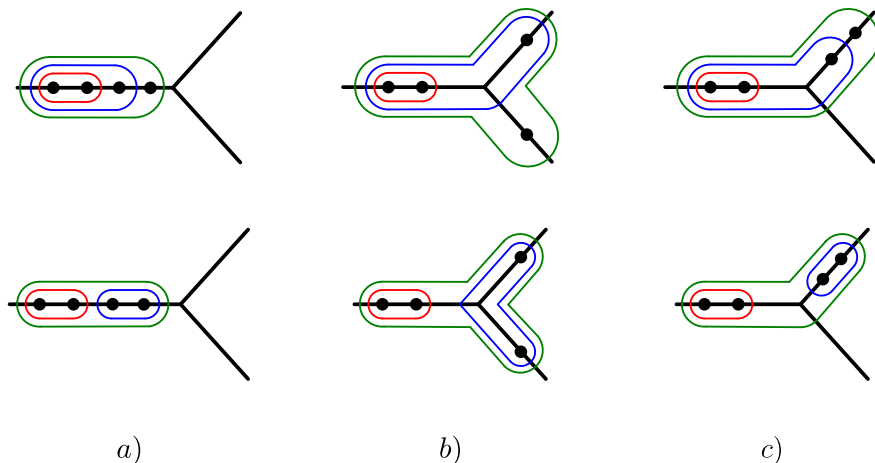
Figure 4.1: a) The disks associated with the left-fused basis (top panel) and the pairwise-fused basis (bottom panel). b) The configuration of particles during the $\sigma_3^{(2,1,1,2)}$-exchange right before the particles bounded by the red disk exchange. The disks in the left-fused basis remain separated during the exchange (top panel) whereas in the pairwise-fused basis (bottom panel) the red disk has to necessarily intersect the blue disk because the blue disk is stretched across the junction. c) A configuration of particles during the $\sigma_3^{(1,1,1,2)}$-exchange right before the particles bounded by the red disk exchange. The disks in both bases remain separated throughout the entire exchange.

Figure 4.1 also explains that the left-fused basis is a good basis for representing diagonally any σ_3-braid. However, the braids $\sigma_3^{(1_d, 1_c, 1_b, 2_a)}$ and $\sigma_3^{(2_d, 2_c, 1_b, 2_a)}$ must be represented diagonally both in the left-fused basis and the pairwise-fused basis. This is because anyons d and c visit the same edge during the exchange and thus can also be bounded by a well-separated disk (see Figure 4.1c). The braid $\sigma_3^{(1,1,1,2)}$ is represented in the left-fused basis by the X-symbols as shown in Figure 4.2.
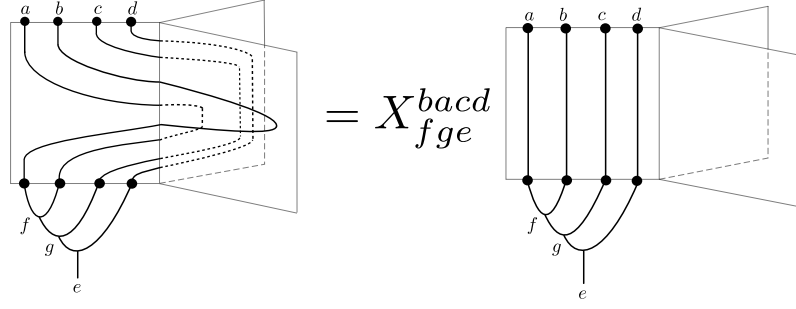
Figure 4.2: The symbol X^{bacd}_{fge} resolving the graph braid $\sigma_3^{(1,1,1,2)}$ on a trijunction.

The $\sigma_3^{(a_1,a_2,a_3,a_4)}$ generators can of course be expressed in the pairwise associated basis, given by conjugation by the appropriate F-symbols;

$$\left[\tilde{W}^{bacd}_{fe}\right]_{l,l'} = \sum_g \left[(F_e^{fcd})^{-1}\right]_{lg} W^{bacd}_{fge} \left[F_e^{fcd}\right]_{gl'} , \qquad W \in \{X, Y, A, B\}, \qquad (4.3)$$

where f is the total charge of a and b, g is the total charge of a, b, c and l, l' are the total charges of c, d. It is generally not guaranteed that a graph braiding exchange operator which is diagonal in the left associated basis is diagonal in the pairwise associated basis (the total charge of the anyons c and d may change), hence we use matrix notation for the $\tilde{W}$ symbols acting in the pairwise associated basis.

Let us next proceed with an analysis of the equations involving the four particle symbols. The $\sigma_3^{(1,1,1,2)}$ sends the two particles closest to the junction to the back plane as displayed in Figure 4.2. Using the F-moves to join the two particles c and d closest to the junction by a fusion vertex, we can slide the $c \times d = l$, fusion vertex through the graph braid. Thus, in the pairwise associated basis the braiding exchange operator corresponding to $\sigma_3^{(1,1,1,2)}$ is effectively represented via $\rho(\sigma_2^{(1_l,1_a,2_b)}) = P^{bal}_{ed}$, i.e. a P-symbol. We display the corresponding commutative square for X and P in Figure 4.3. This leads to the following equations,

$$X^{bacd}_{fge}\delta_{g,g'} = \sum_l \left[F_e^{fcd}\right]_{gl} P^{bal}_{fd} \left[(F_e^{fcd})^{-1}\right]_{lg'} , \qquad (4.4)$$

where we are explicitly imposing the diagonality of the relevant braiding exchange operator in the left fused basis. We can apply analogous reasoning the second the second generator in Equation (4.2) and express any Y-symbol as a combination of F-and Q- symbols.

$$Y^{bacd}_{fge}\delta_{gg'} = \sum_l^r \left[F_e^{fcd}\right]_{gl} Q^{bal}_{fe} \left[(F_e^{fcd})^{-1}\right]_{lg'} . \qquad (4.5)$$

Even though these are two new four particle generators in the graph braid group, the introduction of fusion and naturality of graph braiding allows us to express them
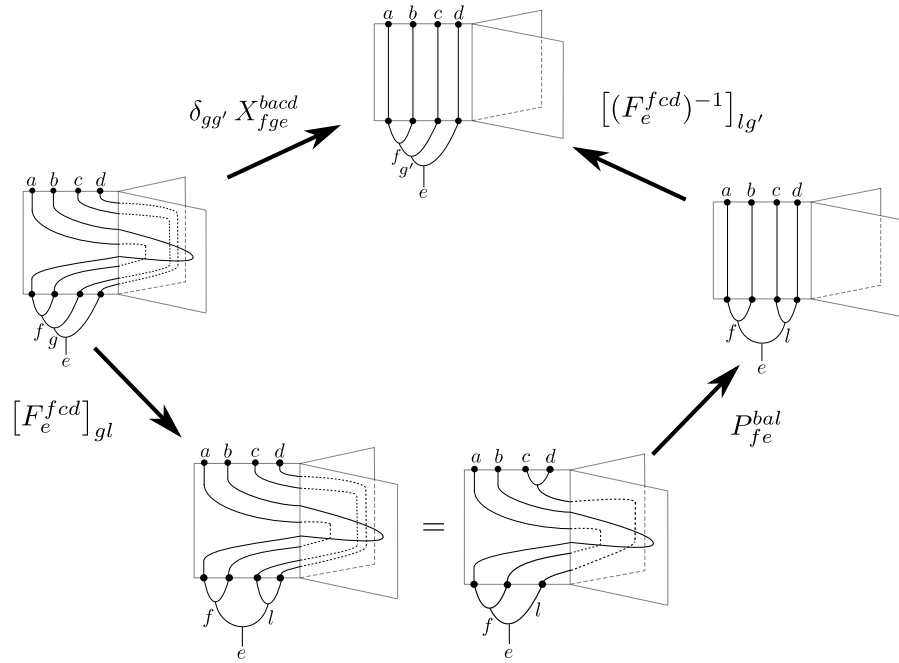
Figure 4.3: The polygon diagram shows how to reduce an X-symbol to a P- symbol using fusion commuting with graph braiding. One can make an analogous figure for the $Y-$ symbol to reduce it to a $Q-$ symbol. The relevant diagram is essentially the same, except the first two particles go to edge 2 (the front plane) instead of edge 1.

via three particle generators [1] . As such, in any equation utilising an $X-$ or $Y-$ symbol, we can express these symbols in terms of an equation for the $P-$ and $Q-$ symbols respectively.

Consider next the two rightmost generators in Equation (4.2), $\sigma_3^{(1,2,1,2)}$ and $\sigma_3^{(2,1,1,2)}$. Note that the particles not being exchanged (the two closest to the junction) go to different edges. Thus, the reasoning presented in Figure 4.3 cannot be applied to the A- and B-symbols in order to reduce them, to either of the P- or Q- symbols. However, one can make one further simplification. Namely, the two generators are related by the pseudocommutative relation (10) in the graph braid group,

$$\sigma_3^{(1,2,1,2)} \, \sigma_1^{(1,2)} = \sigma_1^{(1,2)} \, \sigma_3^{(2,1,1,2)}. \tag{4.6}$$

We can adapt this relation to our graph braiding anyon models by considering the left fused fusion tree to get the following equation which comes from an *octagon diagram*,

$$A_{fje}^{badc} \, \left[F_e^{fdc}\right]_{jl} R_l^{dc} = \sum_{g,l'} \left[F_e^{fdc}\right]_{jl'} R_{l'}^{dc} \left[(F_e^{fcd})^{-1}\right]_{l'g} B_{fge}^{bacd} \left[F_e^{fcd}\right]_{gl'}. \tag{4.7}$$

This allows us to express the A-symbols via the B-symbols. To summarise, there

---

[1]By a three particle generator we mean a generator of the graph braid group exchanging the second and third particles away from the junction.

are a total of 7 generators in the four-strand braid group of the trijunction, however, any anyon model can be described with only four independent sets of symbols: R-, P-, Q- and A-symbols.

Now that we have defined the action of the generators in different bases and discussed relations amongst them, we next proceed with constructing further $N = 4$ equations expressing the compatibility of graph braiding with anyon fusion. We would like to adapt the three-particle diagram in Figure 3.8 where fusion commutes with graph braiding to four particles. Recall that for $N = 3$ the relevant relations which led to the P- and Q-hexagons read

$$\sigma_1^{(1_a, 2_c)} \sigma_2^{(2_c, 1_a, 2_b)} = \sigma_1^{(1_a, 2_{b \times c})}, \quad \sigma_2^{(1_b, 1_a, 2_c)} \sigma_1^{(1_b, 2_c)} = \sigma_1^{(1_{a \times b}, 2_c)}. \tag{4.8}$$

We can raise the above relations to $N = 4$ by conjugating both sides of the equation by a move [2] taking anyon d (closest to the junction) to edge labelled x where $x = 1, 2$. This leads to the relations

$$\sigma_2^{(x_d, 1_a, 2_c)} \sigma_3^{(x_d, 2_c, 1_a, 2_b)} = \sigma_2^{(x_d, 1_a, 2_{b \times c})}, \quad \sigma_3^{(x_d, 1_b, 1_a, 2_c)} \sigma_2^{(x_d, 1_b, 2_c)} = \sigma_2^{(x_d, 1_{a \times b}, 2_c)}. \tag{4.9}$$

We discuss this operation further in Section A and Note that in Equations (4.9) we have applied to the convention for four anyon labels given in (4.1). By putting $x = 1$ (which labels the edge that particle d is sent to) in Equation (4.9) we obtain two relations that allow us to express the A-symbols via P-symbols (the left relation) and the X-symbols via P-symbols (right relation). Similarly, by putting $x = 2$ we obtain two relations that allow us to express the Y-symbols via Q-symbols (the left relation) and the B-symbols via Q-symbols (right relation). One can show by a straightforward but tedious calculation that the resulting equations lead to only one independent consistency equation involving B- and Q-symbols (see also Appendix E (114)) which comes from putting $x = 2$ in the left equation of (4.9) and considering the resulting octagon diagram. The resulting consistency relation reads as follows.

$$\delta_{nn'} \delta_{gg'} B_{nge}^{cabd} = \sum_{f,h,k}^{r} \left[F_g^{cab} \right]_{nf} Q_{ge}^{cfd} \left[F_g^{abc} \right]_{fh} \left[F_e^{ahd} \right]_{gk} (Q_{hk}^{cbd})^{-1} \times$$
$$\times \left[(F_e^{ahd})^{-1} \right]_{kg'} \left[(F_{g'}^{acb})^{-1} \right]_{hn'}. \tag{4.10}$$

There is another way of realising the property of fusion commuting with braiding, namely, one can consider a σ_1-braid exchanging two composite anyons. For $N = 4$ anyons, the possible options for braiding one or two composite anyons via the simple braid $\sigma_1^{(1,2)}$ are as follows;

$$\sigma_1^{(1_{a \times b \times c}, 2_d)}, \qquad \sigma_1^{(1_{a \times b}, 2_{c \times d})}, \qquad \sigma_1^{(1_a, 2_{b \times c \times d})}. \tag{4.11}$$

---

[2]In (114) we denote these moves by β.

Starting from each of these braided states we can pull back the fusion vertices, similar to going from the rightmost state to the leftmost state in Figure 3.8. We can then resolve the resulting graph braids (i.e. expand them to obtain a concatenation of simple braids which involves the constituent factors of the composite anyons), in different ways, analogous to the planar, and graph hexagon equations. For instance, the braid in the rightmost panel from Figure 4.4 is the concatenation of the simple braids

$$\sigma_1^{(1_{a \times b}, 2_{d \times c})} = \sigma_2^{(1_b, 1_a, 2_d)} \, \sigma_1^{(1_b, 2_d)} \, \sigma_3^{(2_d, 1_b, 1_a, 2_c)} \, \sigma_2^{(2_d, 1_b, 2_c)} \ . \tag{4.12}$$

The relation (4.12) can be derived by iteratively applying the relations (4.9) and (4.8). What is more, the polygon equations obtained this way do not yield any new constraints for the relevant symbols as they readily follow from the equations obtained from the relations (4.9), (4.8) and the squares (4.4) and (4.5). We have checked that the same fact holds for all the relations stemming from braiding composite anyons using σ_1- and σ_2- graph braids. This suggests that the polygon equations (4.4), (4.5), (4.7) and (4.10) are all the consistency relations which are needed for the compatibility of fusion and graph braiding of four anyons on a trijunction. However, we do not have a rigorous proof of this fact.
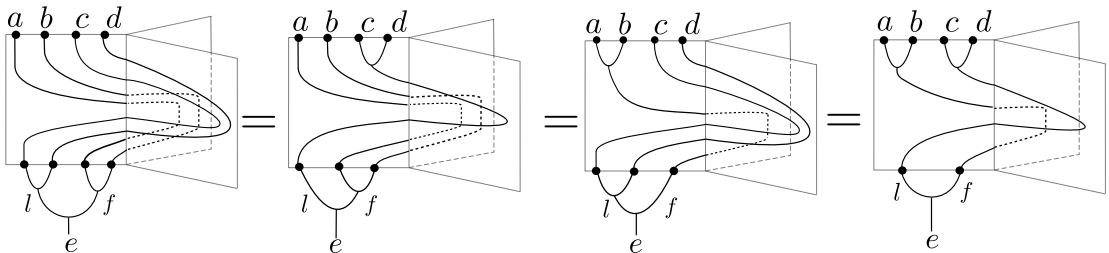
Figure 4.4: The fusion vertices of anyons (a, b) and (c, d) can be pulled through the simple braid $\sigma_1^{(1_{a \times b}, \ 2_{d \times c})}$ involving two composite anyons. The diagram on the furthest left expresses the composition; $\sigma_2^{(1_b, 1_a, 2_d)} \sigma_1^{(1_b, 2_d)} \sigma_3^{(2_d, 1_b, 1_a, 2_c)} \sigma_2^{(2_d, 1_b, 2_c)}$ of graph braids. This is in analogy to the relation from Figure 3.8 which allowed us to derive the P-hexagon equations.

Another important property of the graph braided anyon models is that any symbol representing a σ_j graph braid with $j > 1$ can be expressed as a sum of products of F-symbols and R-symbols. This is because one can reduce any σ_3-braid to a product of σ_2-braids (involving composite anyons) by using the relations (4.9). The resulting σ_2-braids can be in turn reduced to products of σ_1-braids involving composite anyons by applying relations (4.8). As the final result, we obtain that any σ_3-braid is a product of σ_1-braids which involve appropriate exchanges of composite anyons. Thus, translating this relation to the braiding exchange operators acting on the left-fused basis we obtain expressions for A-, B-, X- and Y- symbols involving sums of products of R-symbols and F- symbols.

In Section 4.6 we have applied the $N = 4$ polygon equations (4.4), (4.5), (4.7) and

(4.10) to chosen anyon models of low rank. Importantly, we have found numerous examples of Abelian and non-Abelian anyon models that satisfy all the above polygon equations and differ from planar braiding models. Examples include Abelian $\mathbb{Z}_n$ anyons, the Ising anyons, Tambara-Yamagami anyons with $G = \mathbb{Z}_2 \times \mathbb{Z}_2$, and also $D(\mathbb{Z}_2)$, the quantum double of $\mathbb{Z}_2$.

A natural question follows: does this procedure ever end? Namely, do we have to consider higher and higher particle numbers leading to more complicated fusion diagrams which may further constrain our anyon model? By considering the pseudo-commutative relations for $N > 4$ in Ref.(10) and Section 3.2, one can see that any graph braid of the type σ_j can be expressed by F-, R-, P-, Q- and A-symbols. Thus, no new symbols are introduced for $N > 4$. However, there still may be some new relations appearing in $N > 4$ systems. In Appendix A we take steps toward resolving this issue by conjecturing and providing evidence that it is enough to consider the polygon equations derived from braiding diagrams of $N = 5$ particles on a trijunction. In other words, we conjecture that the graph-braided anyon models will be coherent for $N > 5$ particles. Moreover, we conjecture that on top of the $N = 4$ polygon consistency relations introduced in this section, the only new relations appearing for $N = 5$ systems come from imposing diagonality of certain braiding exchange operators in appropriate bases (relations analogous to the square equations (4.4), (4.5)).

4.2.1 Four particle solutions for Ising

We examined the solutions of the graph hexagon equations for the Ising theory in Section 3.4.3. We have the following solutions

$$R_\psi^{\sigma\sigma} = \mp i R_1^{\sigma\sigma}, \qquad R_\sigma^{\sigma\psi} = R_\sigma^{\psi\sigma} = \varepsilon i, \qquad R_1^{\psi\psi} = z_1, R_1^{\sigma\sigma} = z_2, \qquad (4.13)$$

where $z_1, z_2 \in U(1)$. For four particles, the trijunction equations can only be satisfied if $R_1^{\psi,\psi} = z_1 = -1$ and therefore the solutions have the property that $P \equiv Q$. Note that this does not necessarily imply that $P \equiv R$, i.e. that the solutions are planar.

The solutions are described by adding the values of the A, B, X, and Y symbols which we will describe here. All symbols with a 1 as the third or fourth top label are P, Q, or R symbols and will therefore not be listed.

For the Ising model it turns out that all symbols with the same labels are equal to each other. We can thus write the solutions in terms of the symbol M, where M could be any of A, B, X, Y. The solutions then read

$$M_{fge}^{\psi\psi cd} \equiv -1 \tag{4.14}$$

$$M_{fge}^{\sigma\psi cd} \equiv M_{fge}^{\psi\sigma cd} \equiv \varepsilon i \tag{4.15}$$

$$M_{fge}^{\sigma\sigma cd} = \begin{cases} z_2 & \text{if } c = d \text{ and } f = 1 \\ \varepsilon i z_2 & \text{if } c = d \text{ and } f = \psi \\ \frac{\nu_\sigma}{z_2} \exp\left(\frac{-\varepsilon i \pi}{4}\right) & \text{if } c \neq d \text{ and } f = 1 \\ \frac{\nu_\sigma}{z_2} \exp\left(\frac{\varepsilon i \pi}{4}\right) & \text{if } c \neq d \text{ and } f = \psi \end{cases} \tag{4.16}$$

where $c, d \in \{\psi, \sigma\}$, $f, g, e \in \{1, \psi, \sigma\}$, $\epsilon \in \{-1, 1\}$, ν_σ is the Frobenius Schur indicator of σ. We can see by including the $N = 4$ consistency equations we now only have one a $U(1)$ parameter family of solutions.

4.2.2 Anyon models with simplified symbols

In general, it is a computationally complex problem to determine the braiding exchange operator that corresponds to an arbitrary σ_j graph braid. However, there exists an important simplification which resolves this issue and still leads to graph-braided anyon models that are not planar and which (conjecturally) become coherent already for $N > 4$. These are the models where the braiding exchange symbols depend only on at most four labels, namely on i) the charges of the exchanging anyons – a and b, ii) the total charge of a and b – c, iii) the total charge of a, b and all the anyons standing between b and the junction point – d. In other words, if we have N anyons exchanging on a trijunction and the anyon types are given by the sequence $a_N, \ldots, a_{N-j-1}, a, b, a_{j-1}, \ldots, a_1$ (where a and b are the anyons that exchange), then $c = a \times b$ and $d = a_{j-1} \times \cdots \times a_1$. We define the simplified symbols of the theory by dropping certain labels as follows

$$R_c^{ba}, \quad P_{cd}^{ba}, \quad Q_{cd}^{ba}, \quad A_{cd}^{ba}.$$

See Appendix A for more explanation. The models with such simplified symbols have the property that all the σ_j graph braids are described by the same symbol, regardless of the edges that are visited by the anyons $a_1, \ldots, a_{j-1}$ and independently of the fusion tree of the anyons $a_1, \ldots, a_{j-1}$. In particular, if the anyons $a_1, \ldots, a_{j-1}$ visit edge 1, then the braid $\sigma_j^{(1,\ldots,1,1,2)}$ is always resolved by a P-symbol. Similarly, the braid $\sigma_j^{(2,\ldots,2,1,2)}$ is always resolved by a Q-symbol. If at least two of the anyons $a_1, \ldots, a_{j-1}$ visit two different edges, then the corresponding σ_j graph braid is always resolved by an A-symbol. Importantly, both the Ising anyon model and the Tambara-Yamagami $\mathbb{Z}_2 \times \mathbb{Z}_2$ anyon model which for $N = 4$ have solutions different

than planar, turn out to realise such a graph braided model with the simplified symbols. We further conjecture that for the simplified anyon models the coherence is attained already for $N = 5$, i.e. no new constraints appear for $N > 4$. This conjecture implies in particular that the graph-braided Ising anyon model has the free parameter $R_1^{\sigma\sigma}$ for any N.

4.3   Tree graphs

Now that we have discussed graph anyons models on a trijunction, we will move on to consider a simple network consisting of two trijunctions joined along one edge. The resulting graph is called the H graph, denoted Γ_H. The features of anyon braiding models which we describe in this section also extend in a natural way to any tree graph. The H-graph is displayed in Figure 4.5. The two junction points are denoted by v and w with v being the junction which is the closest to the initial position of anyons. The three-strand graph braid group $B_3(\Gamma_H)$ is freely generated by the following simple braids

$$\sigma_1^{v;(1,2)}, \quad \sigma_2^{v;(2,1,2)}, \quad \sigma_2^{v;(1,1,2)}, \quad \sigma_1^{w;(1,2)}, \quad \sigma_2^{w;(2,1,2)}, \quad \sigma_2^{w;(1,1,2)}. \tag{4.17}$$

In other words, each junction point permits an exchange of particles and exchanges at different junctions are topologically inequivalent. As a result, the exchanges at v will be represented by different symbols than the exchanges at w. Namely,

$$\rho\left(\sigma_1^{v;(1,2)}\right) = R, \quad \rho\left(\sigma_1^{v;(1,1,2)}\right) = P, \quad \rho\left(\sigma_1^{v;(2,1,2)}\right) = Q,$$
$$\rho\left(\sigma_1^{w;(1,2)}\right) = \tilde{R}, \quad \rho\left(\sigma_1^{w;(1,1,2)}\right) = \tilde{P}, \quad \rho\left(\sigma_1^{w;(2,1,2)}\right) = \tilde{Q}.$$

What is more, we have two different sets of hexagon equations with each set of hexagons coming from embedding a trijunction at v or w respectively. There is one P-hexagon involving P-symbols and R-symbols and one P-hexagon involving $\tilde{P}$-symbols and $\tilde{R}$-symbols. Similarly, we have one Q-hexagon involving Q-symbols and R-symbols and one Q-hexagon involving $\tilde{Q}$-symbols and $\tilde{R}$-symbols.
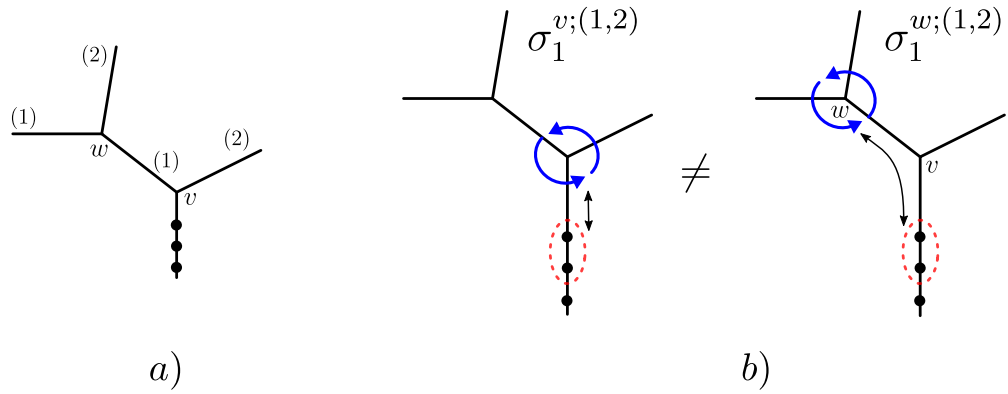
Figure 4.5: a) The H-graph. It contains two junction points denoted by v and w. The branches of each junction are enumerated by (1) and (2) relative to the orientation of the junction with respect to the initial configuration of the anyons (black dots). b) The exchanges at junction v are topologically independent from the exchanges at junction w.

We can observe that the graph braid group of Γ_H with $N = 3$ particles is essentially two copies (formally speaking, the free product) of the trijunction graph braid group, generated by exchanges at the junctions v and w. A natural question presents itself – could one construct a new independent equation involving braids at v and w? The answer is no, which we will now explain. As discussed previously and in (50), to introduce fusion commuting with graph braiding, two of the three particles must go to the same edge and they must be joined by a fusion vertex throughout the entire exchange, so that we can "slide" the fusion vertex through the graph braid diagram. We can see an example of this in Figure 3.8.

Consider next a similar reasoning for the H-graph. Assume that the labels of the anyons in Figure 4.5 are a, b, c with anyon c being the closest to the junction and anyon a being the furthest from the junction. In order to look for possible new relations, we need to consider all the possible exchange processes where a pair of anyons stays joined by a common fusion channel so that the fusion vertex can be pulled through the worldline diagram of the entire process. If this is the case, one obtains a new relation by comparing the effective two-particle exchange process (where the two anyons stay joined by a common fusion channel) with the original three-particle exchange process.

There are two possible options for joining the neighbouring anyons by a common fusion channel. Namely, anyons b and c are joined together into anyon f or anyons a and b are joined together into anyon e. This leads to the following four distinct options for exchanging a pair of anyons joined by a common fusion channel with the other anyon on the H-graph.

Below, we analyse in detail the case when a and b are joined into e. The case where b and c are joined into f follows in an analogous way.

- Anyon c travels through the branch (1) at v and possibly visits the junction at w. In order to initiate an exchange of $e = a \times b$ with c, anyons a and b must travel together to the branch (2) at v. After that, anyon c comes back to the edge where it was initiated which is followed by anyons a and b returning from the branch (2) at v. By deforming the worldline of anyon c, such an exchange can always be continuously deformed to $\sigma_1^{v;(1_c,2_e)}$ where anyon c simply stays near junction v and the entire process is localised only within the trijunction at v. This way, we reproduce the P-hexagon at v involving P-symbols and R-symbols.

- Anyon c travels through the branch (2) at v. In order to initiate an exchange of $e = a \times b$ with c, is that anyons a and b must travel together to the branch (1) at v (and possibly visit vertex w). Two possibilities follow. i) After travelling to branch (1) at v anyons a and b do not exchange at vertex w. Then, anyon c comes back to the edge where it was initiated which is followed by anyons a and b returning together to the edge where they were initiated. Such an exchange is topologically equivalent to $\sigma_1^{v;(2_c,1_e)}$ where anyon e stays near the junction v and the entire process is localised only within the trijunction at v. This way, we reproduce the Q-hexagon at v involving Q-symbols and R-symbols. ii) After travelling to branch (1) at v anyons a and b do exchange at vertex w. After that, anyon c comes back to the edge where it was initiated which is followed by anyons a and b returning together to the edge where they were initiated. One can show that such an exchange process is equivalent to the composition

$$\sigma_1^{v;(2_c,1_e)}\sigma_1^{w;(1_b,2_a)}\sigma_1^{v;(1_e,2_c)},$$

whose corresponding braiding exchange operator is simply $\tilde{R}_e^{ba}$. Thus, such an exchange process does not lead to any new equations.

Summing up, all the possible exchanges with two anyons fused together only lead to hexagon equations which concern exchanges that are fully localised on one of the junctions. This implies that one can treat the hexagon solutions at different trijunctions of the H-graph as independent. For instance, if we chose an anyon model whose trijunction hexagon solutions have free parameters (e.g. Ising fusion rules where the R-symbol $R_1^{\sigma\sigma}$ is a free parameter, see Equation 4.13), then these parameters remain free on the H-graph. In fact, there will also be another set of free parameters for exchanges at w since braids at v and w are topologically inequivalent. If we joined more and more trijunctions, then we could make further independent choices for the free parameters at each junction point.

4.4 Braiding and fusion on the circle

Having revisited the graph anyon models on the simplest building block of networks, i.e. the trijunction, we proceed to define an analogous construction for another simple building block which is the circle. Following this, we will study the interplay between both of these situations by moving to a lollipop graph which consists of a single trijunction and a single loop. On a circle, we first arrange particles next to each other at a particular place on the circle (which is equivalent to fixing the basepoint for the generator of the braid group $B_N(S^1)$). We can then change the ordering by cycling particles around the loop, given by the move δ. In other words, the braid group of the circle is a free group on one generator which we denote by δ. It is uniquely defined by picking an orientation of the circle. Here, we assume the orientation to be counterclockwise. The action of δ moves one of the outermost particles around the circle according to the circle's orientation as shown in Figure 4.6.
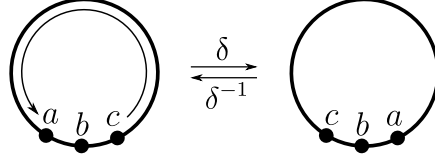
Figure 4.6: The δ-move.

With the δ- move we associate the D-symbols, i.e. $\rho(\delta) = D$, that depend on three anyon labels as shown in Figure 4.7. The gauge transformations of the D-symbols
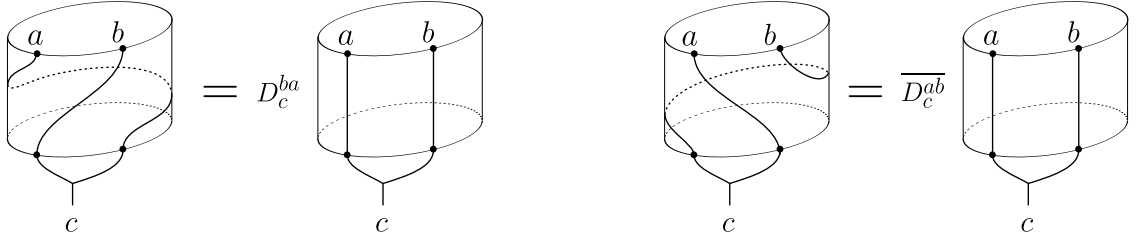
Figure 4.7: The braiding exchange operator associated with the δ-braid is described via D-symbols. The definition extends in a natural way to the δ-move involving $N > 2$ anyons by fusing together the $N-1$ anyons which do not travel around the circle and by sliding their fusion vertex, effectively obtaining the δ-move acting on two anyons only. Note that with the above convention we necessarily have $D_b^{b1} = 1$ and $\overline{D_a^{a1}} = 1$ (the trivial anyon going around the circle), but D_a^{1a} and $\overline{D_b^{1b}}$ are generally different from one.

have the same structure as the gauge transformations of the planar R-symbols given in Eq. 2.34. Requiring the fusion to commute with the δ-braid leads to two families of hexagon equations shown in Figure 4.8 and Figure 4.9. The second set of hexagon equations comes from demanding the δ^{-1}-move to be compatible with fusion.
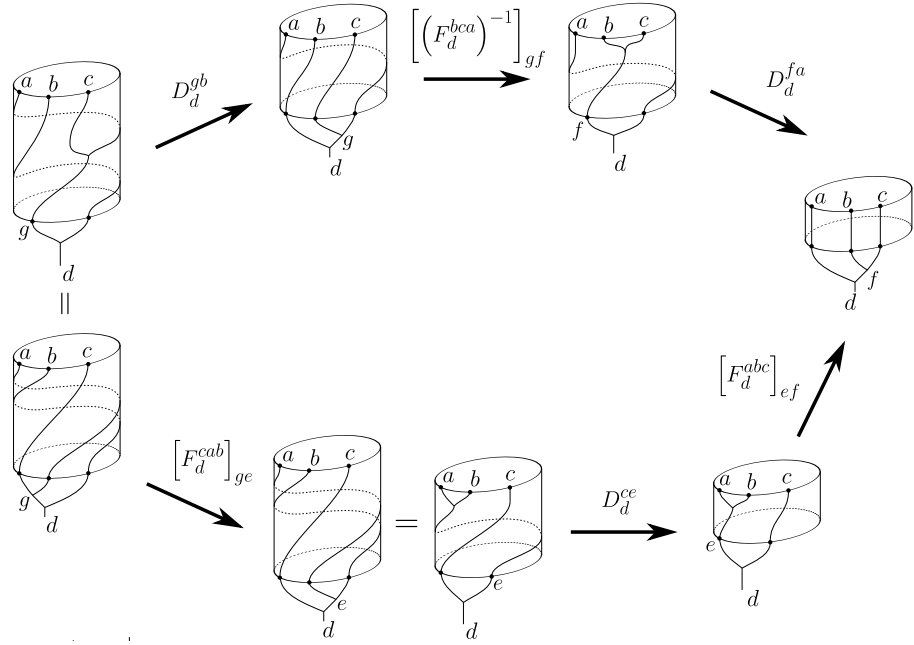
Figure 4.8: The naturality condition for δ showing that fusion commutes with the δ-braid for $N = 3$. Equating the upper and lower path leads to Eq. (4.18).
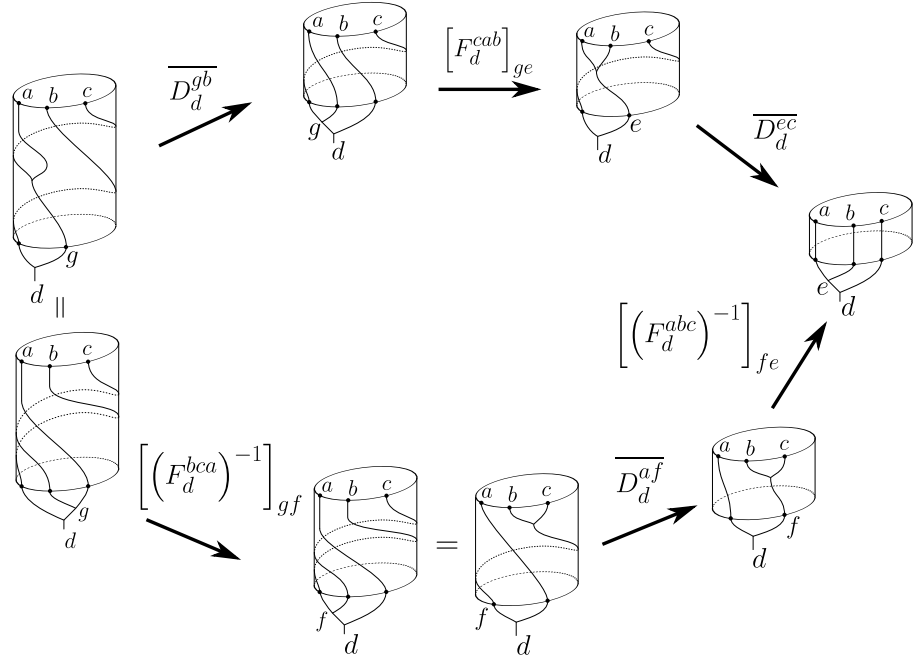
Figure 4.9: The naturality condition for δ^{-1} showing that fusion commutes with the δ^{-1}-braid for $N = 3$. This leads to another set of hexagon equations given in Equation (4.19).

$$D_d^{gb} \left[(F_d^{bca})^{-1} \right]_{gf} D_d^{fa} = \sum_e \left[F_d^{cab} \right]_{ge} D_d^{ce} \left[F_d^{abc} \right]_{ef} \tag{4.18}$$

$$\overline{D_d^{gb}} \left[F_d^{cab} \right]_{ge} \overline{D_d^{ec}} = \sum_f \left[(F_d^{bca})^{-1} \right]_{gf} \overline{D_d^{af}} \left[(F_d^{abc})^{-1} \right]_{fe}. \tag{4.19}$$

In fact, hexagons (4.19) follow from the hexagons (4.18). To see that, put $c = 1$ in

(4.18) to obtain

$$D_e^{ab} D_e^{ba} = D_e^{1e}. \tag{4.20}$$

Then, apply the above identity to the RHS of (4.19) as $\overline{D_d^{af}} = D_d^{fa}\overline{D_d^{1d}}$ and insert $1 = D_d^{gb}\overline{D_d^{gb}}$ to obtain

$$\sum_f \left[\left(F_d^{bca}\right)^{-1}\right]_{gf} \overline{D_d^{af}} \left[\left(F_d^{abc}\right)^{-1}\right]_{fe} = \overline{D_d^{gb}} \sum_f D_d^{gb} \left[\left(F_d^{bca}\right)^{-1}\right]_{gf} D_d^{fa}\overline{D_d^{1d}} \left[\left(F_d^{abc}\right)^{-1}\right]_{fe}.$$

Next, under the above sum, we recognise the LHS of (4.18), thus we can rewrite it as the double sum which we subsequently sum over f

$$\overline{D_d^{gb}D_d^{1d}} \sum_{f,e'} \left[F_d^{cab}\right]_{ge'} D_d^{ce'} \left[F_d^{abc}\right]_{e'f} \left[\left(F_d^{abc}\right)^{-1}\right]_{fe} = \overline{D_d^{gb}D_d^{1d}} \sum_{e'} \delta_{ee'} \left[F_d^{cab}\right]_{ge'} D_d^{ce'} =$$

$$= \overline{D_d^{gb}} \left[F_d^{cab}\right]_{ge} D_d^{ce}\overline{D_d^{1d}}.$$

Finally, we use (4.20) again to obtain $D_d^{ce}\overline{D_d^{1d}} = \overline{D_d^{ec}}$ and the above expression becomes the LHS of (4.19).

As a final comment to this section, we note the connection of the D-symbols D_a^{1a} to the twist factors. The symbol D_a^{1a} is associated with the δ-move taking just a single anyon a around the circle. This is exactly the move which in the $2D$ anyon theory corresponds to the topological twist, which is given by

$$\theta_a = \theta_{\bar{a}} = \sum_c \frac{d_c}{d_a} R_c^{aa}, \tag{4.21}$$

Indeed, for every anyon model, the solutions to the D-hexagons (4.18) always contain the topological twist θ_a expressed in terms of the planar R-symbols in Equation (4.21) as a special case. However, for our graph anyon models, we do not have the relation (4.21) and thus we *define* the generalised topological twist as

$$\theta_a := D_a^{1a}. \tag{4.22}$$

So-defined topological twists typically can have more possible values than their counterparts known from the $2D$ theory. We provide an explicit example of this for the $TY(\mathbb{Z}_3)$ fusion category in Appendix I in Ref. (114).

Importantly, the above defined anyon theory on the circle is readily coherent, i.e. the D-hexagon (4.18) implies the compatibility of anyon fusion with the δ-braid for any $N > 3$. see Section 4.4.1 for the proof.

We present a tabulate of the number of solutions of the D-hexagons for low-rank anyon models in Section 4.6. In (114) we also present solutions for $D(\mathbb{Z}_2)$ and $TY(\mathbb{Z}_3)$. We have found that all the tested models have a finite number of solutions with no free parameters left.

Ising Circle solutions

In this section we will show the solutions to Equation 4.18 for the Ising theory we discussed in Section 2.6.3. There are sixteen solutions to the circle equations for each set of F-symbols. They can be written as follows

$$D_\psi^{1\psi} = -1, \quad D_\sigma^{1\sigma} = \exp\left(i\pi\frac{-2 - \nu_1 + 4\,\nu_2 - 2\,\nu_\sigma}{8}\right), \quad (4.23)$$

$$D_\sigma^{\psi\sigma} = -\nu_1 \exp\left(i\pi\frac{2 - \nu_1 + 4\,\nu_2 - 2\,\nu_\sigma}{8}\right), \quad (4.24)$$

$$D_\sigma^{\sigma\psi} = \nu_1\,i, \quad D_1^{\sigma\sigma} = \nu_3, \quad D_\psi^{\sigma\sigma} = \nu_4\,i, \quad (4.25)$$

where the $\nu_i \in \{-1, 1\}$ and ν_σ, the Frobenius-Schur indicator of the σ anyon is fixed by the choice of F-symbols. In particular, we find that, per set of F-symbols, there are four possible values for the generalized topological spins. These coincide with the values of the topological spins for planar Ising anyons.

4.4.1 Coherence for graph anyon models on the circle

In this section we will discuss the graph anyon model on a circle for $N > 3$ particles. In particular, we provide strong evidence that such a model has the coherence property mentioned in Section 2. Our aim is to show that the consistency equations for four particles are already guaranteed by the solution of the circle hexagon equation for three particles given in Equation (4.18). In other words, no new constraints for the D symbols appear for $N > 3$. This is in contrast to the simple braids at junctions, in which the addition of new particles introduces new, topologically inequivalent generators (up to when the number of particles is at least one greater than the valence of the junction), as discussed in Section 4.2 and Appendix A.

We start with considering the action of the D- symbols given in Equation (4.7). We defined their action to be such that one particle cycles around the circle and the remaining particles are joined by fusion. The D- symbol depends on the topological charge of the particle cycling around the circle and the total topological charge of the remaining particles. See, for instance, the action of D_d^{fa} in the upper path of Figure 4.8. Similarly, if there are N particles on the circle, then anyon f is the total charge of a set of $N - 1$ anyons and the action of the D_d^{fa}- symbol only depends on the total topological charge of the $N - 1$ particle group.

To construct a consistency equation, we consider a diagram where fusion commutes with braiding of four particles and then look at all the possible ways to resolve the braids. This strategy has been employed to derive the D-hexagons in Figure 4.8 (see Figure 3.8 for a similar treatment of the trijunction). Equivalently, we can view this methodology as expressing a braid involving a composite anyon in terms of the composition of simple braids of its constituents.
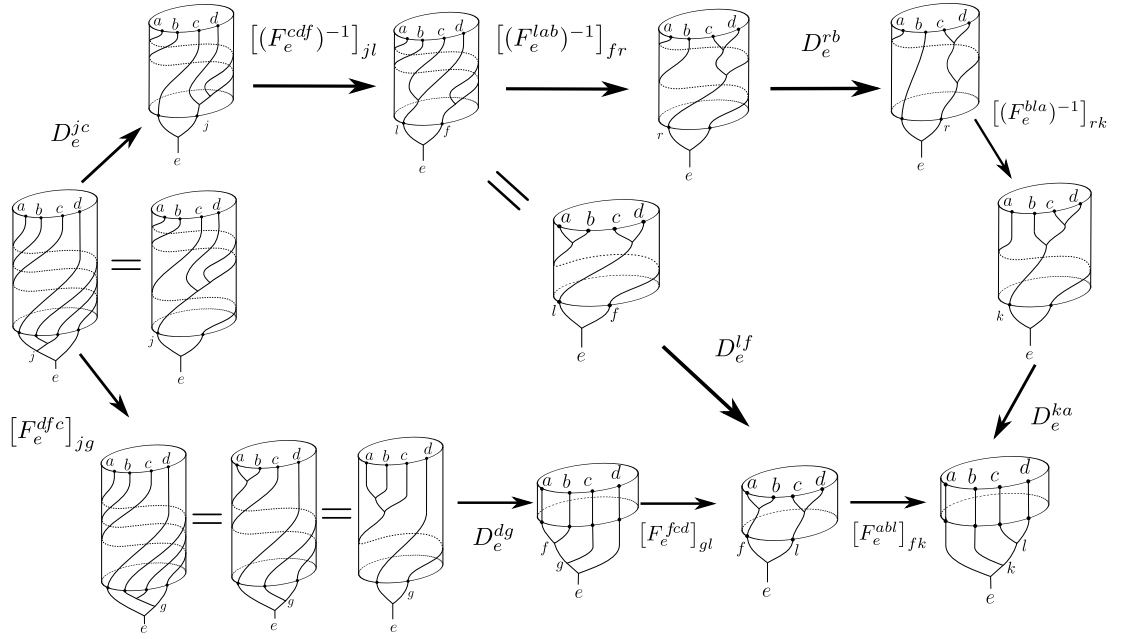
Figure 4.10: Four-particle consistency diagram for particles cycling around the circle graph. In the bottom left we display the fusion commuting with graph braiding states, which are related by sliding a fusion vertex through a δ-braid. The middle diagonal path is what informs us this is will not lead to new constraints on the D-symbols, as it can already be tessellated by the hexagon diagrams.

Explicitly, for four particles we would like to impose the following relations on our anyon model (we use the labelling convention from Equation (4.1));

$$\delta(k,a)\,\delta(r,b)\,\delta(j,c) = \delta(l,f)\,\delta(j,c) = \delta(d,g), \tag{4.26}$$

where the right entry of δ labels the topological charge of the particle cycling around the graph and the left entry labels the total topological charge of the remaining particles. This is analogous to Equation 4.8 for a junction.

The resulting diagram is shown in Figure 4.10. Note that in the bottom left of Figure 4.10 we have equated three states using the fact that fusion commutes with braiding several times. From these states, we can construct consistency equations, stemming from applying appropriate D-symbols and F-symbols to make the diagram commutative. In other words, every loop in the diagram in Figure 4.10 represents a consistency relation. However, the crucial observation is that the large outer loop (decagon diagram) is a composition of two smaller loops, each containing six states (hexagon diagrams). Thus, satisfying the consistency equations corresponding to the two inner hexagonal diagrams will imply that the consistency equations corresponding to the outer decagonal diagram will be satisfied as well.

Let us next take a closer look at the leftmost hexagon diagram in Figure 4.10. Note first that in the resulting equations the constituents of the composite anyon $f = a \times b$ will not appear, as the particles a and b are always connected by a common fusion channel. Thus, this diagram is effectively a three-particle diagram involving

particles f, c and d. Comparing the two paths starting from the leftmost state and ending at the pairwise associated state at the bottom of the diagonal path we obtain the following consistency equation

$$\sum_g \left[(F_e^{dfc})\right]_{jg} D_e^{dg} \left[F_e^{fcd}\right]_{gl} = D_e^{jc} \left[(F_e^{cdf})^{-1}\right] D_e^{lf}. \tag{4.27}$$

Importantly, Equation (4.27) becomes identical to the D-hexagon from Equation (4.18) after appropriate relabelling of anyons. Similarly, the rightmost sub-hexagon diagram in Figure 4.10 leads to effective three-particle equations involving anyons a, b and $l = c \times d$

$$\sum_f \left[F_e^{lab}\right]_{rf} D_e^{lf} \left[F^{abl}\right]_{fk} = D_e^{rb} \left[(F_e^{bla})^{-1}\right]_{rk} D_e^{ka} \tag{4.28}$$

which can also be identified as D-hexagon equations after relabelling.

To summarise, we started with the four particle fusion commuting with graph braiding states which could have led to new constraints on the D- symbols. However, we were able to recognise that this diagram was in fact just given by the three-particle hexagon diagrams. Therefore, when solving these equations for a given fusion model this will add no new constraints. By inducting over the number of particles, one can see similar reasoning shows that we can always do this on a circle, and as we add more and more particles this will lead to no new constraints.

To phrase this more formally, starting from the definition that fusion commutes with graph braiding for three particles (Figures 4.8 and 4.9), which led to the circle hexagon equations (4.18) and (4.19), we then showed that the four particle consistency equations were already satisfied. We did this by constructing the corresponding diagram 4.10 and showing it was already guaranteed by a solution to the three-particle hexagon equations. Hence, the circle graph satisfies the coherence property, analogous to the planar case, where the solution of the three-particle planar hexagon equation is sufficient for any number of particles. For the planar case, the construction of any diagram involving a great number of particles braiding in the plane is guaranteed by the planar hexagon diagram (100). This section provides strong evidence that the circle graph anyon model also has this property. However fully formalising this statement, analogous to the proof of the braided coherence theorem (141), which is done using higher category theory, is beyond the scope of this current work.

4.5 The lollipop graph

The next step is to incorporate loops and junctions into a single graph. The simplest possible configuration is the lollipop graph, Γ_L, shown in Figure 4.11.
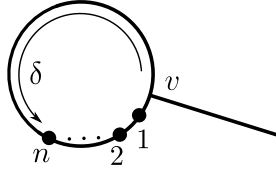
Figure 4.11: The lollipop graph with the root $*$, which determines an embedding of the trijunction graph into the lollipop. We also show the base configuration of anyons corresponding to our choice of the rooted spanning tree and the δ-move coming from embedding the circle-subgraph into the lollipop.

The lollipop graph contains one loop, with which we associate a δ-move and, one essential vertex v, with which we associate the simple graph braids via the embedding of the trijunction graph shown in Figure 4.11a (and presented in more detail in Appendix A in (114)). In other words, the graph braid group $B_3(\Gamma_L)$ is generated by

$$\delta, \qquad \sigma_1^{(1,2)}, \qquad \sigma_2^{(1,1,2)}, \qquad \sigma_2^{(2,1,2)}. \tag{4.29}$$

The above generators are subject to one relation which connects the δ-braid with the simple graph braids. Namely, we have (see also Figure 4.12)

$$\delta\sigma_1^{(1,2)} = \sigma_2^{(1,1,2)}\delta. \tag{4.30}$$
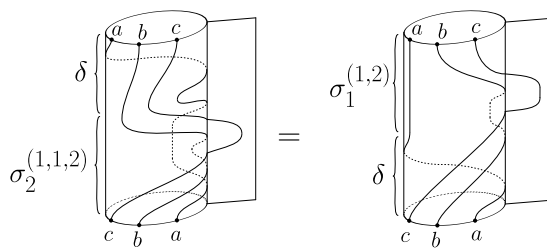
Figure 4.12: A pictorial proof of the lollipop relation (4.30).

This leads to the square diagram shown in Figure 4.13.
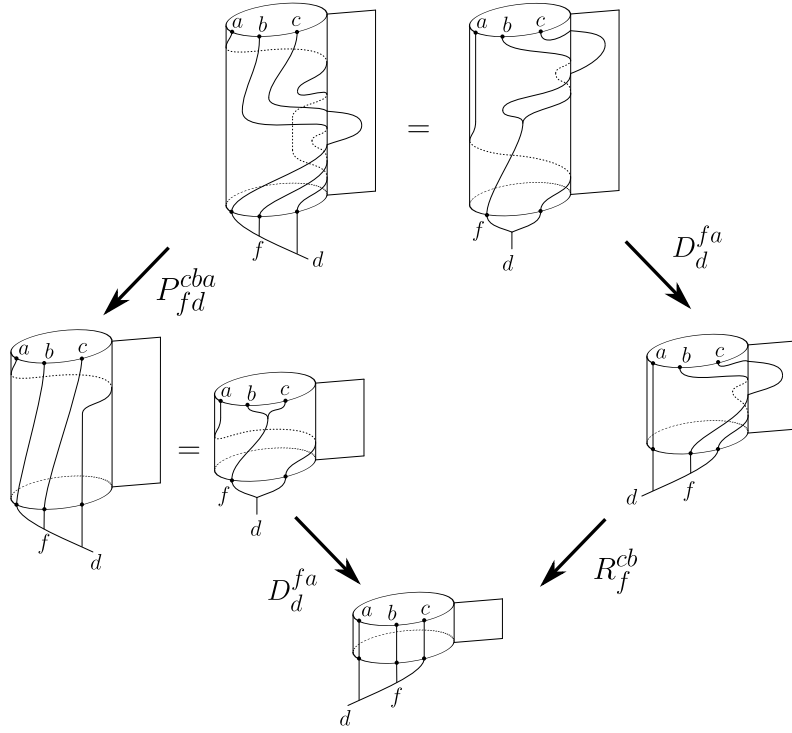
Figure 4.13: The square diagram corresponding to (4.30). The homotopy relation from Figure 4.12 has been used in the top panel of the diagram. The two right-most arrows represent the braiding exchange operators corresponding to the δ-move followed by the simple braid $\sigma_1^{(1,2)}$. The two leftmost arrows represent the braiding exchange operators corresponding to the simple braid $\sigma_2^{(1,1,2)}$ followed by the δ-move.

The resulting equation reads

$$D_d^{fa} P_{fd}^{cba} = R_f^{cb} D_d^{fa}, \tag{4.31}$$

Notably, the diagram 4.13 does not use any F-moves. Using the fact that the D-symbols $D_d^{fa} \in U(1)$, Equation 4.31 reduces to

$$P_{fd}^{cba} = R_f^{cb}. \tag{4.32}$$

On top of the condition (4.32) the P- and Q- hexagons (3.19) and (3.20) are also valid equations for the lollipop as they describe the simple graph braids at the junction of the lollipop. Note that putting $P = R$ in the P-hexagons readily reproduces one set of the hexagon equations from the planar anyon theory (2.35). In other words, creating a lollipop from a trijunction by creating a single loop makes the graph braided anyon model more similar to the planar braided anyon model. As we will see in Section 4.7, one can continue this line of thought to make a complete transition to the planar anyon theory by considering the graph braided anyon theory on the theta-graph and more generally, on the family of tri-connected graphs.
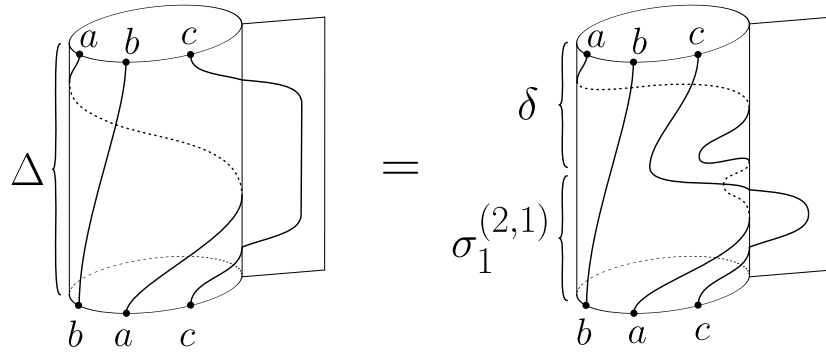
Figure 4.14: The braid Δ. Note that if $c = 1$ (the trivial anyon), then Δ reduces to δ.

4.5.1 The Δ-move

In this section we will introduce an auxiliary braid on the lollipop which we will extensively use on the theta graph in Section 4.7. It is the braid Δ defined in Figure 4.14 which takes into account the possibility of an anyon occupying the lollipop's stick while the remaining two anyons do a δ-like-move. It is expressed by the standard generators as

$$\Delta = \sigma_1^{(2,1)} \delta, \tag{4.33}$$

where $\sigma_1^{(2,1)}$ is the inverse of the simple braid $\sigma_1^{(1,2)}$. The braid Δ will be represented by the G-symbols as shown in Figure 4.15.
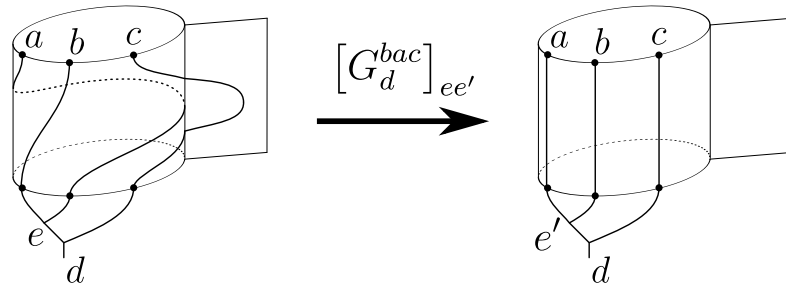
Figure 4.15: The definition of the G-symbols. The anyon c moves out of the way of anyon a so that a can exchange with b utilising the circle of the lollipop.

We use matrix notation for the $[G]$- symbols as the topological charge corresponding to $e = a \times b$ is not necessarily preserved under the action of this braid on the anyon vector space. We illustrate this in Figure 4.16. We can see in the final stage of the braid bringing the anyon c back onto the loop of the lollipop enters the red disk corresponding to $a \times b$.
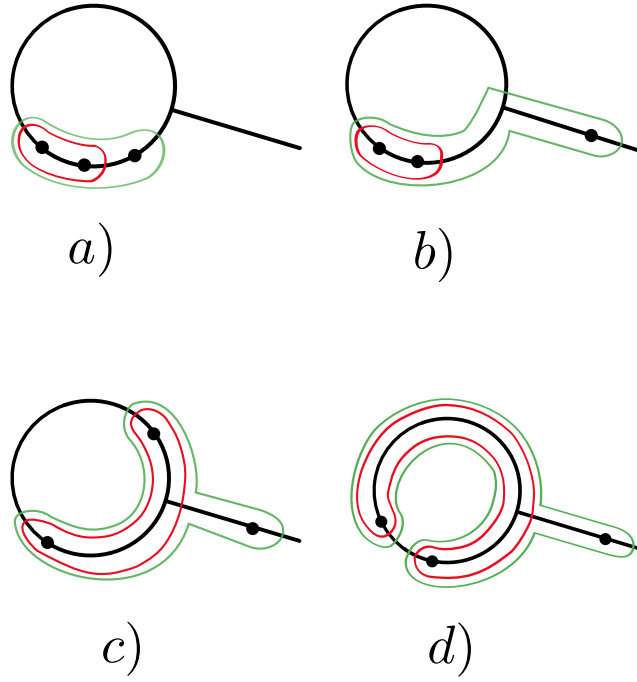
Figure 4.16: Top down view of the stages of a $[G]$- symbol. We can see the $[G]$-symbols do not preserve the topological charge of the fusion of $a \times b$, indicated by the red ellipse. In the final stage of the braid, the c anyon when brought back to the loop of the lollipop will puncture to the red ellipse corresponding to $a \times b$.

The relation (4.33) leads to the hexagon diagram from Figure 4.17 which connects G-, D- and R-symbols.
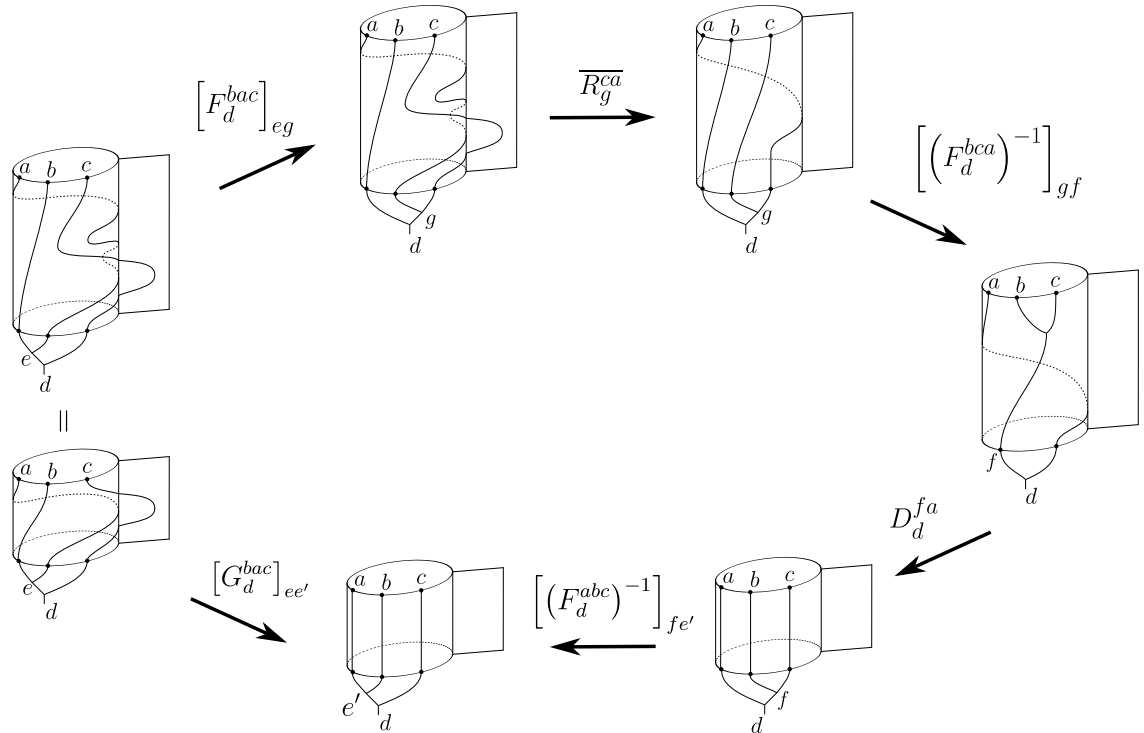
Figure 4.17: The hexagon following from the relation (4.33).

$$\left[G_d^{bac}\right]_{ee'} = \sum_{g,f} \left[F_d^{bac}\right]_{eg} \overline{R_g^{ca}} \left[\left(F_d^{bca}\right)^{-1}\right]_{gf} D_d^{fa} \left[\left(F_d^{abc}\right)^{-1}\right]_{fe'}. \tag{4.34}$$

In particular, if $b = 1$ we obtain the relation

$$\left[G_{ag}^{1ac}\right]_{aa'} = D_g^{ca} \overline{R_g^{ca}} \delta_{aa'}. \tag{4.35}$$

Furthermore,

$$G_{bf}^{b1c} = 1, \quad G_{ee}^{ba1} = D_e^{ba}.$$

Just as in the case of the D-symbols there is a completely analogous naturality for the G-symbols, which follows from the hexagon in Figure 4.17.

Note that the planar anyon theory is retrieved from the graph braided anyon theory on the lollipop by imposing that G_d^{bac}-symbols are independent of c in which case the G-hexagons imply

$$\left[G_d^{bac}\right]_{ee'} = D_e^{ba} \delta_{ee'} \tag{4.36}$$

and become equivalent to the condition $Q = R$. This is because substituting in the hexagon diagram 4.17 i) the G-symbols with the D-symbols according to Equation (4.36) and ii) D-symbols D_g^{ca} with $\overline{R_g^{ca}\theta_a}$ (recall $\theta_a := D_a^{1a}$) according to Equation (4.35) makes the hexagon diagram 4.17 equivalent to the Q-hexagons with $Q = R$. Thus, we have that $Q = P = R$, so under these assumptions, the simple braids on the lollipop are represented by the same R-symbols as the ones coming from the planar anyon theory. What is more, the symbols G_g^{1ac} then acquire the interpretation as the twist factors, i.e.

$$G_g^{1ac} = \theta_a = D_a^{1a}.$$

Interestingly, the so-defined twist factor can still differ from the planar twist factor (defined in equation (4.21)).

4.6 Solutions to the graph braiding equations

In (114), we solved the graph braiding equations for the circle, the trijunction (with three and four particles), and the lollipop graph for a variety of anyon models. We studied several Abelian models: $\mathbb{Z}_2$, $(\mathbb{Z}_2 \times \mathbb{Z}_2)$, $\mathbb{Z}_3$ and $\mathbb{Z}_4$, we defined this family of models in Section 2.6.1. We also considered quantum groups at level k: $\mathrm{SU}(2)_3$, Fibonacci, which is the integer spin part of $\mathrm{SU}(2)_3$, also $\mathrm{SU}(2)_4$ and $\mathrm{PSU}(2)_5$, see Ref. (12) for further details on the representation theory of quantum groups in the context of anyons and the FQHE. We also consider two examples of Tambara-Yamagami categories (see Section 2.6.2 or Ref. (164)); Ising, and TY($\mathbb{Z}_3$). Finally, we also considered two anyon models constructed from the category of representations of the dihedral groups, Rep(D_3) and Rep(D_4), see Refs.(24; 61; 104) for details on these anyon models and how they arise from discrete group gauge theory.

In this section, we present results for a subset of these models which also occur elsewhere in this thesis. The results are summarised in Tables 4.1, 4.2 and 4.3.

Some of these anyon models have different properties when braiding is confined to a graph rather than the plane. There exist, in particular, several fusion categories that never admit planar braiding, despite having solutions for the graph-braid equations. For the anyon models we studied, we observed the following:

- The equations (4.18) for anyons on a circle, like the planar hexagon equations, lead to discrete sets of solutions. There are always at least as many solutions as the planar hexagons allow. Interestingly, the equations for a circle sometimes admit solutions when there is no solution to the planar hexagon equation for the fusion rules and F-symbols. The $\text{TY}(\mathbb{Z}_3)$ fusion model (see Appendix I in Ref.(114) for the solutions) is such an example.

- As explained in Chapter 3, solutions to the trijunction equations for three particles sometimes contain undetermined $U(1)$ parameters. If we add the equations for four particles, then, depending on the model, this freedom either remains unaltered (e.g. for Abelian anyons), gets partially restricted (e.g. Ising anyons), or disappears completely (e.g. $\text{Rep}(D_3)$ anyons). For the models we investigated, we found that if a model has solutions for the three particle equations, it also has solutions to the four particle equations. Specific results on the number of free variables and solutions to the trijunction equations can be found in table 4.1.

- The equations for the lollipop graph consist of (a) the trijunction equations (3.19) and (3.20), (b) equations demanding equality between the P and R symbols (4.32), and (c) equations for anyons on a circle (4.18). We will call the combined set of (a) and (b) the lollipop trijunction equations. The lollipop trijunction equations are sufficient to fix all degrees of freedom in the standard trijunction solutions. Since the equations on a circle give rise to a discrete set of solutions, all investigated models have a discrete set of solutions to the full lollipop equations. Let n_c, n_t, n_l denote the number of gauge-inequivalent solutions to the circle equations, lollipop trijunction equations, and full lollipop equations, respectively. Although the equations for a circle graph are independent of the lollipop trijunction equations, n_l need not be equal to $n_c n_t$. This happens when there is still some gauge freedom left after fixing the values of the F-symbols. In this case, the number of solutions to each set of equations gets reduced by the same factor. This implies that the number of gauge-independent solutions to the combined set of equations will be greater than the product of the number of solutions of the individual equations. For the cases studied only the $\mathbb{Z}_2 \times \mathbb{Z}_2$ model has remaining gauge symmetry. More information on the number of solutions to the planar hexagon equations, the

circle equations, lollipop trijunction equations, and full lollipop equations can be found in tables 4.2 and 4.3.

If all the anyons are Abelian (i.e. the fusion algebra is a group algebra), then:

- The trijunction equations are trivially fulfilled for 3 and 4 particles. All non-trivial R- symbols are thus free variables for trijunction. In particular, each set of trijunction equations admits an infinite set of solutions. This is not the case for the planar hexagon equations. For, e.g., $\mathbb{Z}_3$ anyons only the trivial F-symbols admit a braided structure and for $\mathbb{Z}_2$ and $\mathbb{Z}_2 \times \mathbb{Z}_2$ only half of the sets of F-symbols admit a braided structure.

- For the circle, lollipop trijunction, and full lollipop equations, we find that, for a fixed anyon model, each set of F-symbols gives rise to the same number of solutions. If the F-symbols allow solutions to the planar hexagon equations, then some of the solutions to the lollipop equations are also planar. The number of planar solutions to the lollipop equations is always greater than the number of solutions to the hexagon equations. For more information on the number of solutions to the lollipop equations for Abelian anyons, see table 4.3.

If some of the anyons are not Abelian then:

- The solutions to the trijunction equations without free variables are always planar, and the solutions with free variables are planar for a discrete set of values of the free variables.

- All solutions to the lollipop equations are planar. The number of planar solutions to the lollipop equations is always greater than the number of solutions to the hexagon equations.

For more information on how we solved these equations, see Appendix E in (114).

Fusion Algebra	Solutions to the trijunction hexagon equations				
	$N = 3$		$N = 4$		
	# Soln.	# Free Var.	# Soln.	# Free Var.	Planar?
Fibonacci	2	None	2	None	Always
Ising	2	2	2	1	UCC
$\mathrm{Rep}(D_3)$	1**	2**	3**	0**	Always
$\mathrm{SU}(2)_4$	2*	2	2	1	UCC
$\mathrm{TY}(\mathbb{Z}_3)$	0				
$\mathrm{Rep}(D_4)$	4	10	4	1	UCC

Table 4.1: Here we present the number of solutions of the trijunction hexagon equations per set of unitary F-symbols. Generic properties of solutions to the trijunction equations for three and four particles for various non-Abelian anyon models. Here UCC means that under certain conditions on the free R-symbols the solutions are planar. All solutions listed are gauge-inequivalent. Note that the number of solutions corresponds to the number of gauge-inequivalent families of solutions, possibly parametrized by some free variables. *For these models we only obtained solutions for 1 set of unitary F-symbols per model. **For $\mathrm{Rep}(D_3)$ it looks like there are more solutions to the equations for $N = 4$, but this is only due to the fact that for $N = 4$ all free parameters are fixed and thus instead of 2 infinite families of solutions we find 3 solutions without freedom.

Fusion Algebra	Amount of solutions per type of equations (3 particles) per set of unitary F-symbols			
	Planar Hexagon	Circle	Lollipop Trijunction	Full Lollipop
Fibonacci	2	2	2	2^2
Ising	2^2	2^4	2^2	2^6
$PSU(2)_5$	2^*	2^2	2	2^3
$Rep(D_3)$	$3, 0, 0$	$3, 3, 3$	$3, 0, 0$	$3^2, 0, 0$
$TY(\mathbb{Z}_3)$	0	3	0	0
$SU(2)_4$	2^*	2^8	2	2^9
$Rep(D_4)$	2^3	2^7	2^3	2^{10}

Table 4.2: Number of gauge inequivalent solutions to the consistency equations for various non-Abelian anyon models. Except for the planar hexagon equations all equations were constructed for systems with only three anyons. All of the solutions to the lollipop trijunction equations in this table are planar, i.e. $P = Q = R$. For $Rep(D_3)$ a different amount of solutions was found for the different solutions to the pentagon equations and so we used a notation where the ith number in each column corresponds to data regarding the ith solution to the pentagon equations. *For these models we only obtained solutions for 1 set of unitary F-symbols per case.

Fusion Algebra	Number of solutions per type of equations (3 particles) per set of equivalent F-symbols				
	Planar Hexagon	Circle	Lollipop Trijunction	Full Lollipop	Lollipop but non-planar
$\mathbb{Z}_2$	2	2^2	2	2^3	0
$\mathbb{Z}_3$	3	3^3	3^2	3^5	$\left(\frac{2}{3}\right) 3^5$
	0	3^3	3^2	3^5	3^5
$\mathbb{Z}_2 \times \mathbb{Z}_2$	2^3	2^7	2^5	2^{13}	$\left(\frac{3}{4}\right) 2^{13}$
	0	2^7	2^5	2^{13}	2^{13}
$\mathbb{Z}_4$	2^2	2^8	2^6	2^{14}	$\left(\frac{15}{4}\right) 2^{14}$
	0	2^8	2^6	2^{14}	2^{14}

Table 4.3: Number of gauge inequivalent solutions to the consistency equations for various Abelian anyon models. Here we say two sets of F-symbols are equivalent if they both have solvable planar hexagon equations or not. We chose to do this because, within each equivalence class, all members give rise to identical rows.

4.7   Θ-graph yields effective planar anyon models

The Θ-graph shown in Figure 4.18a) has two independent loops and two essential vertices of degree three.
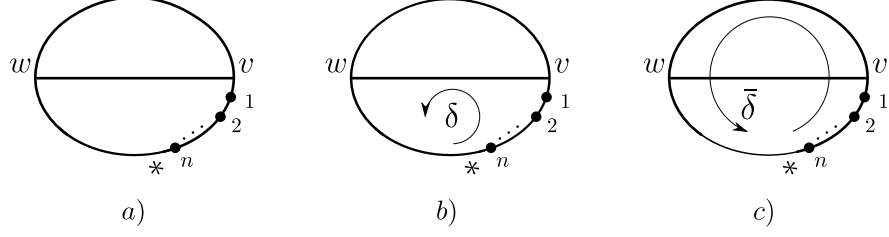
Figure 4.18: a) The Θ-graph Γ_Θ with the root $*$ and the initial position of anyons. b) and c) The choice of the spanning tree uniquely defines the circular moves δ and $\bar{\delta}$ of $B_n(\Gamma_\Theta)$.

Using the universal generators of graph braid groups from (10), we have that $B_3(\Gamma_\Theta)$ is generated by the respective simple braids at vertices v and w

$$\sigma_1^{v;(1,2)}, \quad \sigma_2^{v;(1,1,2)}, \quad \sigma_2^{v;(2,1,2)}, \quad \sigma_1^{w;(1,2)}, \quad \sigma_2^{w;(1,1,2)}, \quad \sigma_2^{w;(2,1,2)}$$

and the two circular moves δ and $\bar{\delta}$. The above generators are defined relative to a choice of the spanning tree of the graph Θ which is shown in Figure 4.18. However, there are many relations between these generators which allow one to present the group $B_3(\Gamma_\Theta)$ using only three independent generators $\sigma_1^{v;(1,2)}$, δ and $\bar{\delta}$ (in fact, the same holds for $B_n(\Gamma_\Theta)$ with any $n \geq 2$ (10)). What is more, by taking the quotient of $B_n(\Gamma_\Theta)$ which identifies all the circular moves with each other, the graph braid group $B_n(\Gamma_\Theta)$ becomes the standard Artin braid group describing anyons in the plane. In the following, we will look into these relations in detail and study their consequences for the graph anyon model on the Θ-graph. In particular, we will show that by assuming that the circular moves δ and $\bar{\delta}$ on the Θ-graph are represented by the same D-symbols, the relations between the generators of $B_3(\Gamma_\Theta)$ imply

$$P_{ed}^{bac} = Q_{ed}^{bac} = R_e^{ba}, \tag{4.37}$$

$$\tilde{P}_{ed}^{bac} = \tilde{Q}_{ed}^{bac} = \tilde{R}_e^{ba}, \tag{4.38}$$

and

$$R_e^{ba} = \tilde{R}_e^{ba}, \tag{4.39}$$

where the symbols in (4.37) refer to the simple exchanges at the vertex v and the symbols in (4.38) refer to the simple exchanges at the vertex w. By Theorem 1 in (10) (and Proposition 5 therein), our results apply not only to the Θ- graph, but also to the more general family of tri-connected graphs.
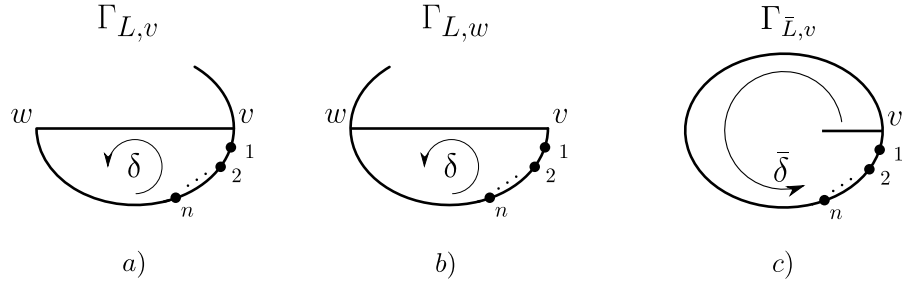
Figure 4.19: The relevant three different embeddings of the lollipop graph into the Θ-graph.

Let us start with Equalities (4.37). These equalities follow immediately from the lollipop relations for the lollipop subgraphs $\Gamma_{L,v}$ and $\Gamma_{\bar{L},v}$ from Figure 4.19a) and c).

To see this, apply the diagram from Figure 4.13 to the respective lollipop relations

$$\sigma_2^{v;(1,1,2)}\,\delta = \delta\,\sigma_1^{v;(1,2)}, \quad \sigma_2^{v;(2,1,2)}\,\bar{\delta} = \bar{\delta}\,\sigma_1^{v;(1,2)}.$$

The first diagram yields $P_{ed}^{bac} = R_e^{ba}$ and the second diagram yields $Q_{ed}^{bac} = R_e^{ba}$, exactly as we derived Equation (4.32). Similarly, the lollipop relation for the subgraph $\Gamma_{L,w}$ from Figure 4.19b) gives

$$\sigma_2^{w;(1,1,2)}\,\delta = \delta\,\sigma_1^{w;(1,2)},$$

thus $\tilde{P}_{ed}^{bac} = \tilde{R}_e^{ba}$.

The derivation of the remaining equalities $R_e^{ba} = \tilde{R}_e^{ba}$ and $\tilde{Q}_{ed}^{bac} = \tilde{R}_e^{ba}$ is considerably more complicated and technical. Importantly, it requires considering the anyon worldlines as world-ribbons and introducing ribbon half-twists. Due to the technical and complicated nature of the proof, we postpone it to Appendix B where we also describe the world-ribbon half-twists on graphs in more detail.

To summarise, we have shown that on the Θ-graph, any graph-braided anyon model is equivalent to the planar anyon model if all the circular moves δ are represented by the same D-symbol. This can be viewed as a mathematical justification for translating results known from the anyon theory in $2D$ to the network-based setting. For instance, it is known that the Majorana zero modes which were initially proposed in two-dimensional FQHE systems (91; 126), and later proposed in one-dimensional networks (113; 136), can host the same exchange statistics in both settings (see (8; 47; 85) for explicit models for the Majorana zero mode exchange on the trijunction). However, our approach here is different from the previous work, because it is independent of the microscopic model.

4.8 Consequences for the quantum circuit depth using topological gates

In the standard paradigm of topological quantum computing schemes, the quantum gates acting on a finite set of qudits come from the unitary matrices $\rho(\sigma_i) \in U(d)$. The representation ρ depends on the anyon model at hand and on the chosen topological Hilbert space $\mathcal{H}_{top}$ which is also associated with the particular way of encoding qudits in $\mathcal{H}_{top}$. It is well-known that a minimal requirement to realise a universal quantum computer is to have i) a set of universal single-qudit gates and ii) at least one entangling two-qudit gate. More formally, for a finite set of single qudit gates $\mathcal{S} \subset U(d)$ we denote the group generated by the matrices from $\mathcal{S}$ by $\langle \mathcal{S} \rangle$. The elements of the group $\langle \mathcal{S} \rangle$ are all the possible unitary matrices obtained by sequentially composing gates from $\mathcal{S}$. The set of gates $\mathcal{S}$ is universal if and only if all the unitary matrices from $\langle \mathcal{S} \rangle$ fill in the group $U(d)$ densely. In other words, any matrix $U \in U(d)$ can be approximated by a sequence of gates from a universal set $\mathcal{S}$ with arbitrary precision ϵ. However, the circuit depth, i.e. the length of the sequence of gates necessary to approximate (compile) a given U increases when the required precision grows, see the celebrated Solovay-Kitaev algorithm (1; 59). In this section, we argue that topological quantum gates coming from the graph braided anyon models can reduce the circuit depth when compared to quantum gates coming from the 2D braided anyon models.

In short, the reason why graph braided anyon models can lead to lower-depth quantum circuits is that the simple braids realised at different junctions of the graph can be topologically inequivalent, i.e. cannot be transformed one into another via isotopies of their corresponding world-lines. This allows us to associate different sets of the R-, P- Q-symbols (and their higher-particle number counterparts) with the junctions which yield topologically inequivalent braids. Such a phenomenon occurs, for instance, in the H-graph as discussed in Section 4.3. Another example of a network architecture where this phenomenon occurs is the stadium graph or, more generally, a bi-connected modular network that consists of a chain of tri-connected modules that are connected by bridges consisting of two edges (10; 116), see Figure 4.20. In the context of Abelian exchange statistics on graphs this has been also pointed out in (86).
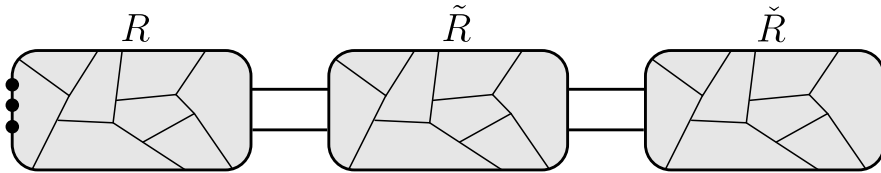
Figure 4.20: A schematic representation of a modular biconnected network composed of three triconnected modules (represented by grey boxes). The base configuration of anyons is on an external edge of the leftmost module. The simple graph braids realised in different modules are topologically independent. By the results of Section 4.7, the braiding within each module is effectively governed by an independent set of R-symbols which constitute a solution to the hexagon equations from the corresponding $2D$ anyon theory. Thus, such a network architecture allows for simultaneous coexistence and mixing of different sets of R-symbols.

For concreteness, let us focus on the stadium graph. As shown in Figure 4.21, there are two ways of embedding a Θ-graph into the stadium graph where the embedded Θ-graph contains either the opposite pairs of essential vertices v and v' or w and w'.
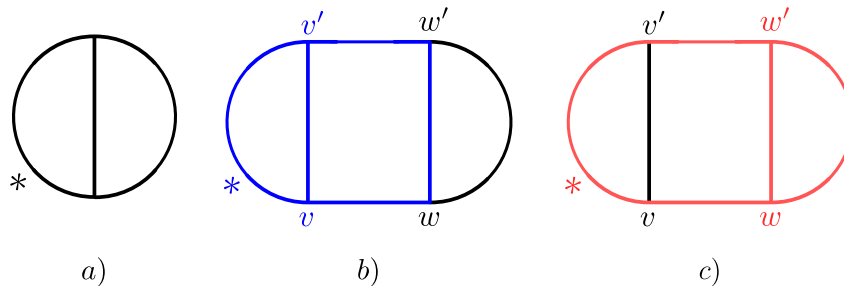
Figure 4.21: a) The Θ-graph together with the choice of the rooted spanning tree. b) and c) Two different embeddings of the Θ-graph into the stadium graph (marked by red and blue) which by the results of Section 4.7 imply that the simple braids at v and v' are equivalent to the braiding in $2D$ and are represented by the same set of R-symbols. Similarly, the simple braids at w and w' are represented by another set of R-symbols coming from the $2D$ anyon theory.

Thus, by the results of Section 4.7 any graph braided anyon model on the stadium graph will admit two independent sets of the planar R-symbols. Namely, the simple braids at v or v' will be represented by one set of R-symbols coming from the 2D braided anyon model and the simple braids at w or w' will be represented by another, *a priori* different, set of R-symbols coming from the 2D braided anyon model. Let us reiterate the crucial fact that the simple braids at w and w' are topologically independent from the simple braids at v or v', thus it is *a priori* possible to represent them by different sets of R-symbols. This in turn can increase the number of the available topological single-qudit quantum gates which constitute the set $\mathcal{S}$. Having access to a larger set of topological gates $\mathcal{S}$ gives one more flexibility when compiling the target quantum algorithm and thus increases the efficiency of the given quantum circuit by lowering the circuit depth.

90

The potential advantage of using the stadium graph architecture and its generalisations is also evident when considering certain non-universal anyon models. For instance, consider the Tambara-Yamagami model over $\mathbb{Z}_2 \times \mathbb{Z}_2$. We defined this anyon model in Section 2.6.2. Denote by σ the anyon with the property

$$\sigma \times \sigma = \bigoplus_{g \in G} g, \quad G = \mathbb{Z}_2 \times \mathbb{Z}_2.$$

The topological Hilbert space of the three σ-anyons of the total charge σ is given by

$$\mathcal{H}_{top} = \text{Span}\left\{|\sigma, \sigma \to g\rangle |g, \sigma \to \sigma\rangle : \quad g \in G\right\} \cong \mathbb{C}^4.$$

In such a setting, the braiding operators are single-ququart topological quantum gates. In the stadium-graph geometry the simple braids $\sigma_1^{v;(2,1)}$ and $\sigma_1^{v';(2,1)}$ are represented by the same braiding exchange operator R which is a diagonal 4×4 matrix whose diagonal entries are the R-symbols $R_g^{\sigma\sigma}$, $g \in G$, which are solutions to the hexagon equations in Equation 2.35, for the anyon model in $2D$. The simple braids $\sigma_1^{w;(2,1)}$ and $\sigma_1^{w';(2,1)}$ are represented by the matrix $\tilde{R}$ constructed from another set of solutions to the hexagon equations for the anyon model in $2D$. For concreteness, let us choose the following solutions to the planar hexagon equations,

$$R = \begin{pmatrix} e^{i\pi/4} & 0 & 0 & 0 \\ 0 & e^{i3\pi/4} & 0 & 0 \\ 0 & 0 & e^{i3\pi/4} & 0 \\ 0 & 0 & 0 & e^{-i3\pi/4} \end{pmatrix}, \quad \tilde{R} = \begin{pmatrix} -i & 0 & 0 & 0 \\ 0 & 1 & 0 & 0 \\ 0 & 0 & -1 & 0 \\ 0 & 0 & 0 & -i \end{pmatrix}.$$

The relevant σ_2-braids $\sigma_2^{v;(112)}$, $\sigma_2^{v;(212)}$, $\sigma_2^{v';(212)}$ and $\sigma_2^{v';(212)}$ are represented by the matrix $B = (F_\sigma^{\sigma\sigma})^\dagger \, R \, F_\sigma^{\sigma\sigma}$ while $\sigma_2^{w;(112)}$, $\sigma_2^{w;(212)}$, $\sigma_2^{w';(212)}$ and $\sigma_2^{w';(212)}$ are represented by the matrix $\tilde{B} = (F_\sigma^{\sigma\sigma})^\dagger \, \tilde{R} \, F_\sigma^{\sigma\sigma}$. Here, the relevant F-matrix reads

$$F_\sigma^{\sigma\sigma} = \frac{1}{2} \begin{pmatrix} -1 & -1 & -1 & -1 \\ -1 & 1 & -1 & 1 \\ -1 & -1 & 1 & 1 \\ -1 & 1 & 1 & -1 \end{pmatrix}.$$

The F-matrix can be found by solving the pentagon equation in Equation 2.19 with the fusion rules defined in Section 2.6.2 for $G = \mathbb{Z}_2 \times \mathbb{Z}_2$.

Let us next consider the (finite) groups generated by the sets $\mathcal{S} := \{R, B\}$ and $\tilde{\mathcal{S}} := \{\tilde{R}, \tilde{B}\}$. We will focus on how the resulting quantum gates act on a single

ququart, i.e. a four level system, which means that we neglect the global phase factors. In other words, we look at the resulting groups projectively by projecting every element to the group $PSU(4)$. It can be verified in a straightforward way that the groups $\langle \mathcal{S} \rangle \subset PSU(4)$ and $\langle \tilde{\mathcal{S}} \rangle \subset PSU(4)$ are different and both are isomorphic to S_4, the permutation group of four elements

$$\langle \mathcal{S} \rangle \neq \langle \tilde{\mathcal{S}} \rangle, \quad \langle \mathcal{S} \rangle \cong \langle \tilde{\mathcal{S}} \rangle \cong S_4 \subset PSU(4).$$

Furthermore, by considering combinations of exchanges on the two Θ-subgraphs of the stadium graph we can generate the group $\langle \mathcal{S} \cup \tilde{\mathcal{S}} \rangle \subset PSU(4)$ which is a finite group of rank 96 and strictly contains the groups $\langle \mathcal{S} \rangle$ and $\langle \tilde{\mathcal{S}} \rangle$. Thus, by combining braids at different junctions of the stadium graph we are able to generate a bigger (although still finite) subgroup of $PSU(4)$ which means that we have increased the computational power when compared to the standard $2D$ setting.

The crucial feature of the above calculation was that the subgroups of $PSU(d)$ generated by the braiding exchange operators R, B and $\tilde{R}$, $\tilde{B}$ were different. A necessary condition for this to happen is that the braiding exchange operator R is different than $e^{i\phi}\tilde{R}$ for every $\phi \in [0, 2\pi]$. Finding such operators R and $\tilde{R}$ is not possible for every model. For instance, in the Ising model (Tambara-Yamagami with $G = \mathbb{Z}_2$) all the braiding exchange operators corresponding to different hexagon solutions are related via multiplication by such a global phase factor. The Tambara-Yamagami model over $\mathbb{Z}_2 \times \mathbb{Z}_2$ is the simplest model which we could find where some of the braiding exchange operators R are not related by a global phase factor.

4.9 Summary

In this chapter we studied anyons exchanging on a variety of graphs. We laid the foundations for this framework in Chapter 3, where we adapted the algebraic theory of anyons from Chapter 2 to include exchanges on a graph which are governed by the graph braid group. In that chapter we focused on three particles on a trijunction and tetrajunction. One of the notable limitations was that the hexagon equations (Equations (3.19) and (3.20)) we derived were for only three particles. In Section 4.2 we first revisited the trijunction and extended our analysis beyond three particles. We introduced the new generators in the graph braid group for four particles and discussed how they must act on the fusion space, see Figure 4.1. Naively this would introduce four new generators, given in Equation (4.2). However as we showed in Figure 4.3, depending on the edges the particles are sent to under the action of a generator, we can often reduce a four-particle generator to a three-particle generator. This is an important insight when we want to understand how the graph anyon model is changed as we consider an arbitrary number of anyons. This falls under the umbrella of coherence. We discuss this in more technical detail in Appendix A.

In Section 4.3 we extended our results for the trijunction to tree graphs, graphs which consist of multiple vertices, with one edge between them, and no loops. Each vertex of the graph affords the ability to exchange anyons, and hence there are graph hexagon equations at each vertex. The main result of this section is that the exchanges at distinct vertices are independent. This is a surprising result, as naively one would expect the addition of extra vertices to constrain the hexagon equations. However we showed that this is not the case, the topological independence of the graph braid generators at each vertex is still true when acting on the anyon fusion space, i.e. by including fusion commuting with graph braiding, and hence the hexagon equations are independent.

In Section 4.4 we studied the simplest graph containing a loop, which is the circle graph. We exchange particles on a circle by cycling them around the graph to arrive at a fixed point of the graph in a different order is given by the δ graph braid, see Figure 4.6. We constructed consistency equations for particles exchanging under the δ graph braid, which we called the D-hexagon, given in Equation (4.18). We illustrated the solutions to this equation for the Ising anyon theory in Section 4.4. One of the most interesting features of the graph anyon model on a circle graph is that the model possesses the coherence property discussed in Appendix A and Ref. (100) for a trijunction. We showed this in Section 4.4.1 by constructing a consistency diagram and equation corresponding to four particles exchanging on a circle and showing that a solution is already guaranteed by a solution to the three-particle consistency equation. Also we observed there are only discrete solutions to our D-hexagon equations, instead of the continuous $U(1)$ parameter families of solutions we found for the junction hexagon equations.

In Section 4.5 we studied a lollipop graph, which contains both a circle subgraph and trijunction subgraph. This is the simplest graph to combine our results in Section 4.2 and Section 4.4. We gave the presentation for the lollipop graph braid group in Equation (4.29). This presentation is subject to one relation in Equation (4.30), which relates the exchanges at the vertex and exchanges on the circle. Encoding this relation into our graph anyon models leads to Figure 4.13. From here we showed this led to Equation (4.31). Incorporating this constraint into the graph hexagon equation, (3.19) leads to first of the two planar hexagon equations in (2.35). Therefore, the graph anyon model on a lollipop is closer to the planar anyon model. However, there is still one graph hexagon equation, corresponding to the Q-symbol, so this graph anyon model is not necessarily planar. We also went on to show another new method to exchange the anyons on a lollipop graph, namely the Δ move in Figure 4.14 and the associated G symbols. This exchange involves shuttling one particle through the junction to the stick of the lollipop while another particle cycles around the loop. This is in some sense a generalisation of the δ move and D-symbols we studied in Section 4.4. The interesting feature of the Δ move

is that the topological charge of the two particles which stay on the loop is not necessarily preserved. We display this in Figure 4.16.

We studied the solutions to our graph consistency equations for a variety of graphs and tabulated some general features we observed in Section 4.6. In Table 4.1 we solved the trijunction hexagon equations and $N = 4$ consistency equations on a trijunction for a variety of anyon models hosting non-Abelian anyons. As a general feature, we noticed including the $N = 4$ consistency equations reduces the amount of continuous $U(1)$ parameters in the model. Crucially we observed even with the inclusion of the $N = 4$ consistency equations many models remain non-planar, i.e. they do not necessarily satisfy $P = Q = R$. Our analysis in Appendix A provides evidence that the free parameters which remain after including the $N = 4$ equations may be a permanent feature of the model. In Table 4.2 we compared the number of solutions per type of consistency equation we studied.

In Section 4.7 and Appendix D, we proved that the graph anyon model on a theta graph is equivalent to the planar anyon model. This result was already proven at the level of the graph braid groups, i.e. $B_n(\Gamma_\theta) \simeq B_n(\mathbb{R}^2)$. However we extended this proof to the level of anyon models. By including the structure of the fusion space and F-symbols, our proof is then essentially an equivalence of the abstract anyon model on the plane and the abstract graph anyon model on the theta graph. More generally this could be phrased as an equivalence of categories. In order to do this we proved that $P = Q = R$ for the exchanges at v and $\tilde{P} = \tilde{Q} = \tilde{R}$ for the exchanges at w. This proves the exchanges at v and w are planar. Finally we proved that $R = \tilde{R}$, implying the exchanges at v and w are equivalent. Therefore, anyons exchanging on a theta graph are equivalent to anyons exchanging in the plane.

In Section 4.8 we studied one application of our graph anyon models to topological quantum computation. Building on the results in Section 4.7, we studied a graph which contains two theta sub-graphs, known as a stadium graph. The exchanges on each of these sub-graphs permit a solution to the planar hexagon equation as we proved in Section 4.7. However the solutions on each of these sub-graphs are independent. Therefore we are free to make independent choices for the solution of the planar hexagon equations. We showed an example where this can have physical consequences. We chose an anyon model with a non-Abelian anyon, which is not universal for quantum computation and showed that by making independent choices for the braiding operators on each theta-subgroup, one could generate a higher, but still finite, braid group image.

In this chapter we have studied a large variety of method to exchange anyons on wire networks. In Section 3.2 we introduced graph braid groups and further information on these groups can be found in Appendix A in (114). We collect a summary of the generators and where they were studied in Table 4.4.

Braid symbol	Graph braid generator	Graphs	Studied
R	$\sigma_1^{(1,2)}$	Γ	sections; 3.3,4.2
P	$\sigma_2^{(1,1,2)}$	Γ	sections; 3.3,4.2
Q	$\sigma_2^{(2,1,2)}$	Γ	sections; 3.3,4.2
A	$\sigma_3^{(1,2,1,2)}$	Γ	sections; 4.2
B	$\sigma_3^{(2,1,1,2)}$	Γ	sections; 4.2
X	$\sigma_3^{(1,1,1,2)}$	Γ	sections; 4.2,A
Y	$\sigma_3^{(2,2,1,2)}$	Γ	sections; 4.2,A
D	δ	circle, lollipop, theta	sections; 4.4,4.5,4.7
G	$\Delta = \sigma_1^{(2,1)}\delta$	lollipop, theta	sections; 4.4,4.5,4.7

Table 4.4: A collection of the graph braid symbols, their corresponding graph braid generators, the graphs where they arise and the sections where they were studied. By Γ we mean all graphs (star, tree, lollipop and theta) except for the circle graph.

Chapter 5

Majorana nanowires

5.1 Introduction

In this chapter, we will turn our attention to one particular non-Abelian anyon, namely the Majorana bound state (MBS), also known as a Majorana zero mode. Majorana fermions were originally proposed in high-energy physics as a particle which is its own anti-particle as a solution to the Dirac equation (122). The quasi-particles we will discuss are zero energy modes whose creation operators are Hermitian, i.e. $\gamma^\dagger = \gamma$. One of the first proposals for MBS in condensed matter physics came in the context of the fractional quantum Hall effect at filling fraction $\nu = 5/2$. The filling fraction gives the ratio of the number of electrons to the number of magnetic flux quanta in the material. This state is often known as the Moore-Read state (126). The low energy excitations in this system are described by the Ising theory, we discussed this anyon model in Chapter 2. The MBS are exotic quantum states bound to vortices (169). The vortices themselves are a local effective degree of freedom consisting of magnetic flux quanta. When two of these vortices are brought together they can annihilate or fuse to a fermion (144). In the algebraic theory of anyons, this is abstracted by the following fusion rule: $\sigma \times \sigma = 1 + \psi$, where by σ we denote the vortex, and by $1/\psi$ we denote the annihilation/fermion. See e.g. (148), for a review of the topic. The MBS themselves are zero-energy modes and are therefore related to ground state degeneracy, in fact for $2n$ isolated MBS this leads to a 2^n-fold degeneracy (137; 144). One of the most interesting features of MBS is their non-commutative exchange statistics (91; 126).

In this chapter, we will focus on one-dimensional implementations of MBS. This brings us to the topic of topological superconductors (21). This is a special class of BCS superconductor in which properties of the edge states can be classified by and described by topological invariants of the band theory of the bulk, see (87) for a review on this topic. In fact, based on symmetries and invariants of the bulk theory, such models have been classified (9; 101), and hence have become known as "Symmetry Protected Topological Phases", (SPT). This is in fact a weaker form

of topological protection than the original topological order (80), in the following sense. SPT means that in order for properties like ground state degeneracy to remain invariant under smooth deformations of the parameters of the Hamiltonian, we must do so, *while* preserving the symmetry of the system as well (148). If the system is perturbed without protecting the symmetry, then the topological order is lost. The model that will focus on in this chapter is in class BDI, which means the model has particle-hole symmetry and time reversal symmetry. Examining the Atland-Zirnaburer classification of free fermion systems this implies there is a $\mathbb{Z}$-classification of topological phases (163).

In particular, we will discuss the model introduced in 2001 in Ref.(99). This consists of a topological superconductor with no spin degrees of freedom, *p*-wave pairing, possessing a gapped excitation spectrum and open boundary conditions. Our focus here will be on demonstrating that in this model the conditions are met to host MBS.

Before delving in into the description of the model let's schematically discuss why this might be the right physical system to host such states. As a superconductor, the quasiparticle excitations involve superpositions of electrons and holes. Since the operators creating Majorana bound states must be Hermitian, the quasiparticle created by it must be its own "anti-quasiparticle", so the excitation must be equal parts electron and hole. If the electron or hole had internal spin degrees of freedom then taking the Hermitian adjoint of such an operator would spoil the duality. Therefore, we restrict to *p*-wave pairing, so that there are only one species of electron, i.e. the material is spin-less (7). Despite the idealised nature of the toy model, it has been proposed that particular quantum wire networks, such as a semiconductor on an *s*-wave superconductor could be fine-tuned to host MBS (113; 136). This has led to much work analysing the viability of constructing wire networks that could host MBS (154). However, to implement TQC in the standard paradigm, one needs to be able to braid the particles in order to enact quantum gates. The unitary operators that result from braiding the excitations implement the gates for the quantum computer. This can not be performed in one dimension. However, if multiple wires are connected then the braiding can be done using exchanges at junctions (8; 47; 116; 154). We will discuss this in Section 5.6. We have also discussed an abstraction of exchanging anyons at junctions in Chapter 3. This highlights the importance of understanding the effect of transport on the fidelity of a topological qubit constructed from MBS. This will be the basis of the question Chapter 6 aims to address.

Firstly we will discuss the MBS in the superconductor. From there we will progress to discuss how to transport MBS and finally how to exchange (braid) them on a trijunction. More detailed discussions of MBS can be found in (7; 21; 163).

5.2   Majorana bound states in one dimension

In (99), Kitaev proposed that four MBS could be used to encode the information for a quantum computer within the degenerate ground state manifold. Furthermore, this information is robust and protected against local perturbations by the topological nature of the MBS, as long as they are well separated and we do not allow perturbations that would break fermion parity. We shall analyse the Hamiltonian of such a model, which is a spinless or fully spin-polarized p-wave superconductor in one dimension with N lattice sites

$$H = -\tilde{\mu} \sum_{j=1}^{N} \left[(c_j^\dagger c_j - 1/2) - w \sum_{j=1}^{N-1} (c_j^\dagger c_{j+1} + c_{j+1}^\dagger c_j) \right] + \tilde{\Delta} \sum_{j=1}^{N-1} (c_j^\dagger c_{j+1}^\dagger + c_{j+1} c_j), \quad (5.1)$$

where c_j is a fermionic annihilation operator at the j'th lattice site. The fermionic operators satisfy the canonical anti commutation relations; $\{c_i, c_j\} = 0$ and $\{c_i^\dagger, c_j\} = \delta_{ij}$. The on-site lattice chemical potential is denoted by $\tilde{\mu}$, which determines the Fermi energy of the system. The probability amplitude, $w > 0$ represents the hopping strength between neighbouring lattice sites, which gives kinetic energy to the fermions. The final term in the Hamiltonian captures, at a mean-field level, superconductivity induced in the wire. In practice this is often done by placing the wire on top of another material (21; 113; 165; 136). When $\tilde{\Delta} \neq 0$, this leads to a superconducting gap. This term is also known as the Cooper pairing term (21). Fermion number is not a conserved quantity in this model, namely the operator,

$$\hat{N}_F = \sum_{j}^{N} c_j^\dagger c_j, \quad (5.2)$$

which counts the occupancy of each lattice site, does not commute with the Hamiltonian. In fact, there is only a $\mathbb{Z}_2$ particle conservation, since the hopping term can increase or decrease the total fermion number by two.

The continuum limit is obtained by taking the number of lattice sites, $N \to \infty$ and simultaneously, the lattice spacing $a \to 0$, with the length of the wire $N = La$, kept constant. In this limit, the lattice Hamiltonian (5.1) becomes a low-energy effective Hamiltonian

$$H = \int_0^L dx\, \Phi^\dagger(x)\, [(-\partial_x^2/2m - \mu(x)\,)\sigma_z + \Delta \partial_x \sigma_x\,]\, \Phi(x) \quad (5.3)$$

where $\Phi^\dagger(x) = (\, c^\dagger(x)\ c(x)\,)$. The lattice parameters are related to the continuum limit parameters under the following:

$$w = 1/(2ma^2), \qquad \mu = \tilde{\mu} + 2w, \qquad \Delta = 2a\tilde{\Delta}, \quad (5.4)$$

where m is the effective mass of the electron. Using the continuum parameters, it is useful to define the Fermi momentum $k_F = \sqrt{2m\mu}$, the Fermi velocity $v_F = k_F/m$ and the energy gap, $E_{\text{gap}} = \Delta k_F$, with $\hbar = 1$. In the remainder of this chapter we will work with the lattice constant $a = 1$, so $N = L$. Following (99), we define the following $2N$ Majorana operators where j labels the lattice site,

$$\gamma_{2j-1} = c_j + c_j^\dagger, \qquad \gamma_{2j} = \frac{c_j - c_j^\dagger}{i}. \tag{5.5}$$

The γ operators satisfy the following Clifford algebraic relations:

$$\gamma^\dagger = \gamma, \qquad \{\gamma_i\, \gamma_j\} = 2\delta_{i,j}. \tag{5.6}$$

It is often stated that this transformation is splitting the complex fermion into real and imaginary Majorana constituents (148). Of course, this could be done in any fermionic lattice model, however we will see applications of this throughout this chapter. In Figure 5.2 we show the splitting of a fermion operator at a lattice site into Majorana operator constituents. We can rewrite the Hamiltonian in the following "Majorana representation",

$$H = \frac{-i\tilde{\mu}}{2} \sum_{j=1}^{N} \left[\, \gamma_{2j-1}\gamma_{2j} + (w + \tilde{\Delta})\gamma_{2j}\gamma_{2j+1} + (-w + \tilde{\Delta})\gamma_{2j-1}\gamma_{2j+2} \,\right]. \tag{5.7}$$

Now let's examine some particular limits of this Hamiltonian to order to understand the non-trivial topological properties of this model.

Topologically trivial limit.

We set $w = |\tilde{\Delta}| = 0$ and $\tilde{\mu} < 0$, to obtain the following Hamiltonian,

$$H = -\tilde{\mu} \sum_{j=1}^{N} (c_j^\dagger c_j - \frac{1}{2}) = -\frac{i\tilde{\mu}}{2} \sum_{j=1}^{N} \gamma_{2j+1} \gamma_{2j}. \tag{5.8}$$

This is a topologically trivial phase in the following sense. There is no hopping between lattice sites and there is no Cooper pairing in the model. The ground state is simply given by pairing Majorana operators on the same lattice site to have fermion occupation number $n_i = 0$. This limit has a unique ground state and no unpaired MBS. We display the couplings of the terms in the Hamiltonian of this limit in Figure 5.1.
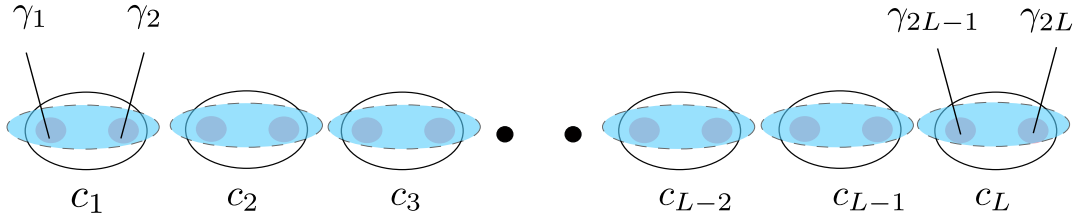

Figure 5.1: We show the coupling terms of the Hamiltonian in Equation (5.8), which leads to a topologically trivial model. We indicate how the terms in the Hamiltonian couple neighbouring sites by blue ellipses and the fermionic lattice sites by black circles.

Topologically non-trivial limit

We set $\tilde{\mu} = 0, |\tilde{\Delta}| = w > 0$, then the Hamiltonian is

$$H = iw \sum_{j=1}^{N-1} \gamma_{2j-1}\,\gamma_{2j}\,. \tag{5.9}$$

We have fixed the system to the centre of the band ($\tilde{\mu} = 0$). There is hopping between neighbouring sites, and we are now only pairing Majorana operators at different sites. With open boundary conditions, we can see two unpaired operators γ_1 and γ_{2L}, which do not enter the Hamiltonian and therefore, commute with the Hamiltonian. We show an example of the couplings of the Hamiltonian between different lattice sites in this limit in Figure 5.2.
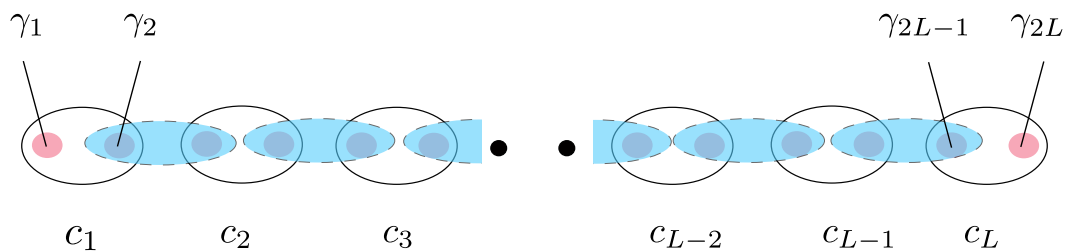
Figure 5.2: The coupling terms between fermionic lattices corresponding to the Hamiltonian in Equation (5.9) are shown. We can see two unpaired Majorana modes at the edges of the system in this limit.

If we introduce a further change of basis to fermionic quasiparticle operators; $\beta_j = \frac{1}{2}(\gamma_{2j} + i\gamma_{2j+1})$, the Hamiltonian takes a simple form;

$$H = 2w \sum_{j=1}^{N-1} (\beta_j^\dagger \beta_j - \frac{1}{2}). \tag{5.10}$$

This is an exactly solvable, free model in the β fermionic quasiparticle operators. If we consider the Dirac fermion constructed from the two unpaired Majorana operators,

$$\beta_0 = \frac{1}{2}(\gamma_1 + i\gamma_{2L}), \tag{5.11}$$

then we can see this fermion mode is not localised to one physical site since it is a bound state of Majorana operators located at opposite ends of the chain.

The existence of this operator has interesting consquences for the states in the quasiparticle Fock space. The many body ground state of this quasiparticle Hamiltonian (5.10), denoted $|\Phi_0\rangle$, can be considered the quasiparticle vacuum (138). We can relate $|\Phi_0\rangle$ to the $c^\dagger$ fermionic vacuum of the Fock space $|0\rangle$ by

$$|\Phi_0\rangle = \prod_{j=1}^{N} \beta_j |0\rangle. \tag{5.12}$$

Furthermore, since β_0 does not enter Equation 5.10, it commutes with the Hamiltonian, therefore making the spectrum two-fold degenerate. This mode is known as a "Dirac zero mode" (7). Therefore, $|\Phi_0\rangle$ and $\beta_0^\dagger|\Phi_0\rangle$ are two orthogonal degenerate ground states. We can observe that these two ground states have different eigenvalues with respect to the fermion parity operator,

$$Q = \prod_j (-i\gamma_{2j-1}\,\gamma_{2j}). \tag{5.13}$$

In fact, $|\Phi_0\rangle$ has even fermion parity whereas $\beta_0^\dagger|\Phi_0\rangle$ has odd fermion parity. This gives us an operator acting on the Fock space of the system with discrete eigenvalues, and since there is no continuous way to change fermion parity, a hint that something topologically interesting may be going on. Furthermore, this implies that if the fermion parity is preserved then the degenerate ground state space is protected by perturbations.

To summarise: on a one-dimensional wire with two boundary points, we found two unpaired Majorana operators. But if we chose periodic boundary conditions, these operators would pair up. Furthermore, since the Dirac fermion zero-energy mode, β_0 is constructed from the unpaired Majorana operators at the two ends of the wire, the resulting fermionic operator is non-local (7; 99).

5.3 Bulk properties of Kitaev chain

Now we will examine the bulk properties of the Kitaev chain and derive the dispersion relation. We start with Equation (5.1), and impose periodic boundary conditions ($c_1 = c_{N+1}$). Then we have translational invariance and momentum is a good quantum number, which we will denote by k. To study the band structure of the Hamiltonian in Equation (5.1), we introduce a discrete Fourier mode basis as follows,

$$c_k = \frac{1}{\sqrt{N}}\sum_{j=1}^{N-1} c_j\,e^{ikj}, \qquad c_k^\dagger = \frac{1}{\sqrt{N}}\sum_{j=1}^{N-1} c_j^\dagger\,e^{-ikj}, \tag{5.14}$$

where $k = 2\pi n/N$ and N denotes the total number of sites with the lattice constant a equal to one. This basis satisfies the canonical anti-commutation algebra. The Hamiltonian is written as

$$H = \sum_k (-w\cos(k) - \mu)c_k^\dagger c_k + \Delta \sum_k \left(e^{ik}c_k c_{-k} + e^{-ik}c_{-k}^\dagger c_k^\dagger\right). \tag{5.15}$$

To simplify the exposition, let's organise this vector space into single particle k subspaces. We do this by introducing a two-component vector;

$$C_k = \begin{pmatrix} c_k \\ c_{-k}^\dagger \end{pmatrix}. \tag{5.16}$$

We can interpret this change of basis as pairing a particle at momentum k and a hole at $-k$. Then the Hamiltonian is written as

$$H = \frac{1}{2} \sum_k C_k^\dagger \mathcal{H}_k C_k + \tilde{\mu} L, \qquad \mathcal{H}_k = \begin{pmatrix} -2w\cos(k) - \mu & -2i\Delta\sin(k) \\ 2i\Delta\sin(k) & 2w\cos(k) + \mu \end{pmatrix}. \tag{5.17}$$

From here we can obtain the dispersion relation, which tells us about the excitation spectrum. We know there will be two bands at each k since $\mathcal{H}_k$ is a 2×2 matrix. The dispersion relation is given by,

$$\epsilon_k = \pm\sqrt{(-2\,w\cos(k) - \mu)^2 + 4\Delta^2\,\sin^2(k)} \tag{5.18}$$

The ground state of the model is given by filling up all single particle states with $\epsilon < 0$. From here we can examine the effect of the different parameters in the model. First, let's examine the dispersion with $\mu = 0$, which is at exactly half-filling. In Figure 5.3 we show how the band structure changes with $\Delta = 0$ and $\Delta \neq 0$.
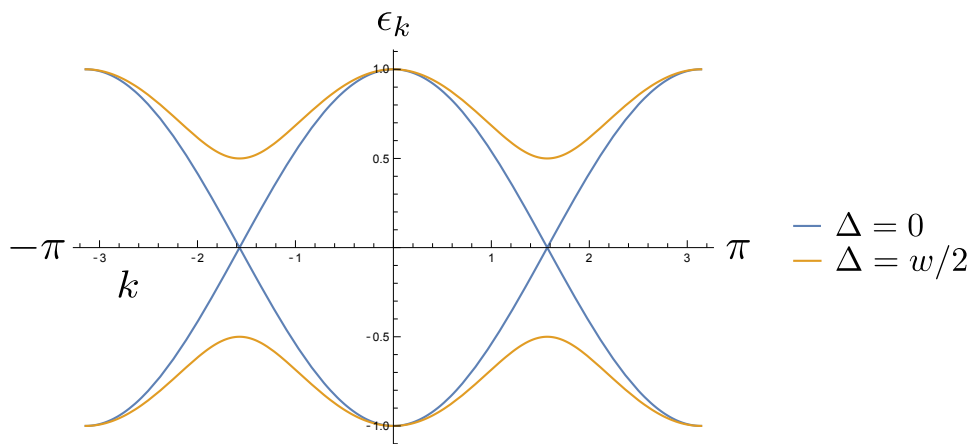
Figure 5.3: We can see that when $\Delta = 0$ the bands touch and therefore, the model is gapless, when $\Delta \neq 0$ there is a finite energy gap in the model given by $E_{\mathrm{gap}} = \Delta k_{\mathrm{F}}$. We fix $w = 0.5$ and $\mu = 0$.

We can see $\Delta \neq 0$ opens a finite energy gap in the model. We can get further insight into the model by fixing to $\Delta \neq 0$ and varying μ. This is important as the underlying gate voltage in any physical implementation of this system affects the

onsite chemical potential.

We plot Equation (5.18) for different values of μ in Figure 5.4.
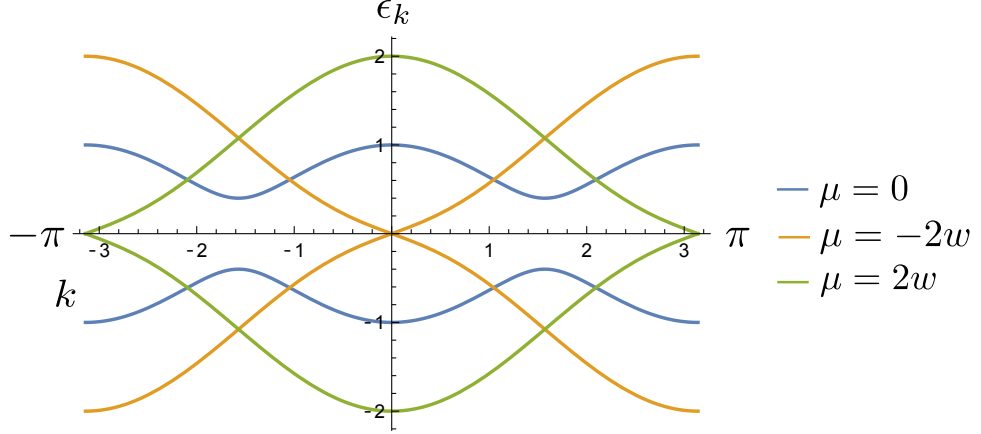
Figure 5.4: We plot the dispersion relation $\pm\epsilon_k$ for $\Delta = 0.2$. We can see the gap closing with $\mu = -2w$ at $k = 0$ and the gap closes at $k = \pi$ for $\mu = 2w$.

We can see the excitation spectrum is gapped almost everywhere except when $k = \pm k_F$, the Fermi wave vector, which is defined by

$$2w\cos(k_F) = \mu\,. \tag{5.19}$$

So the system is gapless if $k_F = 0$ or $\pm\pi$. This corresponds to the limit we can see for the chemical potential, i.e. the gap closes when $\mu = -2w$, corresponding to $k_F = 0$, and at the point $\mu = +2w$, which corresponds to $k_F = \pm\pi$. We can see this in Figure 5.4. This is the point where the two bands touch, meaning we can freely make excitations in the system, so the electrons in the valence band (below k-axis) can excite freely to the conduction band (above k-axis). Therefore the system is in a conducting phase. We can use the continuum limit of the Hamiltonian in Equation (5.17) to write a functional form for the Majorana wave function. In particular, we are looking for states at zero energy in the presence of a finite gap induced by $\Delta \neq 0$. The BdG Hamiltonian is written as

$$\mathcal{H}_k = \begin{pmatrix} \varepsilon & \Delta k \\ \Delta^* k & -\varepsilon \end{pmatrix} \tag{5.20}$$

where we have defined $\varepsilon = k^2/2m - \mu$. The corresponding dispersion relation is $E_k = \pm\sqrt{\varepsilon^2 + \Delta^2 k^2}$.

In order to find a wave function for the MBS, we seek to solve: $[\mathcal{H}_k][\phi] = [0]\phi$, where $\phi = (\psi, \sigma\psi)^{\mathrm{T}}$ and $\sigma = \pm i$. The functional form of the MBS wave function is then given as

$$\psi(x) \propto e^{-x/\xi} e^{i\sqrt{k_F^2 - 1/\xi^2}x}, \tag{5.21}$$

where we have defined the Fermi momentum $k_F = \sqrt{2m\mu}$ and the decay length $\xi = 1/m\Delta$ with $\hbar = 1$. The MBS wave function decays into the superconductor from the edge of the system and hence is approximately localised to the edge of the system, away from the edge the MBS wave function decays exponentially. The degree of the localisation is determined by Δ.

Before we proceed there is one feature that we will make extensive use of in Chapter 6. Namely, one could generalise the Hamiltonian given in Equation (5.1) to have a spatially varying μ, i.e. $\mu(x)$. This then allows the modelling of multiple topologically non-trivial regions along the same wire, by alternating the chemical potential between topologically trivial and topologically non trivial. The MBS will then be bound to domain walls between these phases, this allows the same wire to host multiple MBS. We will use this idea in Section 5.5 when we discuss a topological qubit.

5.4   Topological quantum numbers

In this section, we will discuss another perspective on the topological nature of the Kitaev chain. Our aim is to show the presence of discrete topological invariants classifying the phases of the model. We start again with the Hamiltonian,

$$H = \frac{1}{2}\sum_k C_k^\dagger \mathcal{H}_k C_k, \qquad \mathcal{H}_k = \begin{pmatrix} d_z & -id_y \\ id_y & -d_z \end{pmatrix}, \tag{5.22}$$

where we have defined the following,

$$d_z(k) = -2w\cos(k) - \mu, \qquad d_y(k) = 2\Delta\sin(k). \tag{5.23}$$

For each fixed k, the Hamiltonian density $\mathcal{H}$ is a 2×2 matrix, so we can express it in a basis given by the Pauli matrices;

$$\mathcal{H}_k = d_z(k)\sigma^z + d_y(k)\sigma^y, \tag{5.24}$$

or more succinctly as $\mathcal{H}_k = \vec{d}(k) \cdot \vec{\sigma}$ with $d_x(k) = 0$ (7; 163). First, we analyse the symmetries of the Hamiltonian to find our what symmetry class it belongs to (163). The BdG Hamiltonian is particle-hole symmetric and since it consists of spinless-fermions it is also time reversal symmetric, therefore it belongs to class BDI.

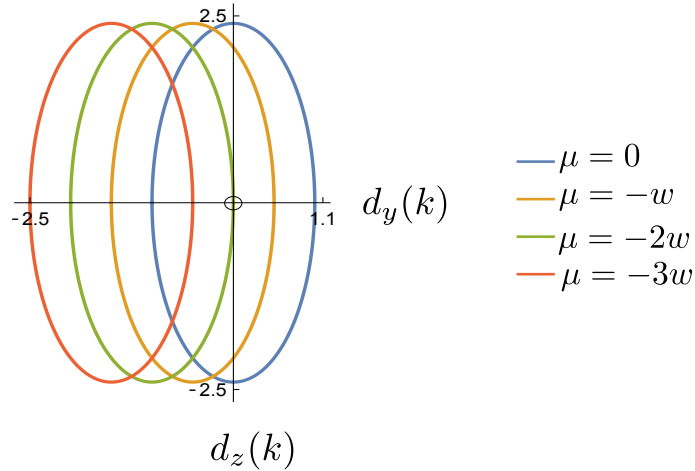Next we will examine the topological features of this $\vec{d}$ space.

Figure 5.5: We plot the $\vec{d}$ given in Equation (5.23). This plot has two distinct regimes depending on whether $\vec{d}$ encircles the origin. At $\vec{d} = 0$ the Hamiltonian is zero, so the system is gapless. The curves encircling $\vec{d} = 0$ cannot be continuously deformed into the curves not encircling the origin without a phase transition signalled by the gap closing.

For this, we focus on Figure 5.5. Firstly, at the point, $\vec{d} = 0$, the Hamiltonian is zero, and the system is gapless. This happens when $\mu = 2w$. We indicate this point by marking the origin with a circle. From here, there are essentially two limits to consider.

When $-2w < \mu < 2w$, this is the topologically non-trivial phase. To see this, note the blue ($\mu = 0$) curve encircles $\vec{d} = 0$. Therefore it can not be continuously deformed into the red curve ($\mu = -3w$), without closing the gap. In essence, the topology of the $\vec{d}$ space, preserving the energy gap, is given by $\mathbb{R}^2 - (0,0)$, which is non-trivial.

If we set $\mu < -2w$ or $\mu > 2w$, this is the topologically-trivial phase as we can adiabatically connect the system to the vacuum ($\mu \to \pm\infty$). Both of these limits in the topologically trivial phase are related by a particle-hole transformation (21; 163). The plots for $\mu > 2w$ are similar but the ellipses will be off to the right of the origin.

More generally, this is characterised by the winding number of the map $k \to \vec{d}(k)$. This is denoted ν and is a $\mathbb{Z}$ topological invariant (163). We first define $q(k) = (d_z - id_y)/|\vec{d}|$, which is a unit vector on the Brillouin zone. Then, the winding number in the continuum is given by

$$\nu = \frac{i}{\pi} \int_{-\pi}^{\pi} dk q^{-1}(k) \frac{d}{dk} q(k) = \frac{-1}{\pi} \int_{-\pi}^{\pi} \frac{\Delta(2w + \mu\cos(k))}{(\mu + 2w\cos(k))^2 + 4\Delta^2\sin^2(k)}. \qquad (5.25)$$

This is the computation of a Chern number on the Brillouin zone. If the integral gives a trivial result, the system can be continuously deformed into a topologically

trivial model. There are two limits of this integral. If $|\mu| > 2w$, then we find $\nu = 0$. If $|\mu| < 2w$, then we find $\nu = \pm 1$. So we can see the topologically trivial phase has $\nu = 0$ and the topologically non-trivial phase has $\nu = \pm 1$ (21; 163). The application of topological invariants has a rich history in topological insulators and superconductors. In fact, based on symmetry considerations, such models have been classified based on topological invariants such as we have just discussed (9).

We note that the p-wave superconductor consists of spinless fermions. In a physical implementation of this system, one would consider the model spin-polarized. This would be implemented by applying a magnetic field. In this sense the model would not be time-reversal invariant and would be considered in class D. This is also discussed in (163).

5.5 Topological qubit

In this section, we will discuss the construction of a topological qubit built from Majorana bound states. If the modes are sufficiently well separated, they are also called Majorana zero modes. If they are not sufficiently well separated then there will be an energy splitting, $E_{\text{split}} \propto \exp(-L/\xi)$, where ξ is the coherence length of the MBS. For the purpose of this section and the following we will assume they always are. The qubit is constructed using the fermion parity operator; however the fermions in question will be the non-local fermions constructed from the linear combination of the unpaired MBS. For a single logical qubit, we will show that we need in fact two Dirac fermion zero modes, which are constructed from four MBS (99). As we saw in Section 5.3, there is a phase transition in the p-wave superconductor at $|\mu| = 2w$, with the topologically non-trivial region being defined by $|\mu| < 2w$ and topologically trivial otherwise. We also saw in Section 5.2, that if the system is defined with open boundary conditions there can be MBS localised at the edge. We can do this equivalently by having the boundary defined by $|\mu| > 2w$ in some region of the wire. Then the MBS are pinned to the domain wall separating the two phases.

We schematically plot the system we have in mind in Figure 5.6. We also indicate the domain walls separating the two phases by σ for reasons we will now explain. Firstly, in two-dimensional implementations of the Ising theory, such as the $p + ip$ superconductor or the $\nu = 5/2$ FQHE, the MBS are zero energy-bound states pinned to vortices. Then bringing two vortices together the MBS can annihilate or fuse to a fermion. This is often written $\sigma \times \sigma = 1 + \psi$, where the $+$ sign on the right-hand side is read as "or". By analogy with the 2d situation, this is why we labelled the domain wall by σ. So, if we have four domain walls we have four σ's and we initialise each topological phase pairwise, also called germinating from the vacuum (8).
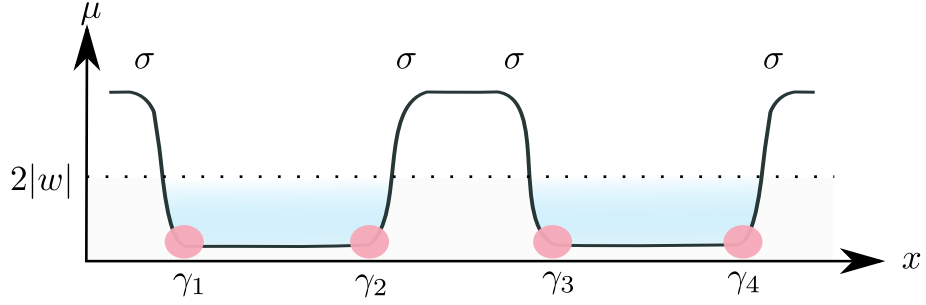
Figure 5.6: A schematic of the minimum setup of a topological qubit consisting of two non-trivial topological phases bounded by four domain walls labelled by σ, which host MBS, labelled by γ_i. We indicate the topological phase transition at $\mu = 2|w|$ by a dotted horizontal line.

This is equivalent to our basis for the fusion space being given in the pairwise associated fusion tree; $(\sigma \times \sigma) \times (\sigma \times \sigma)$. Thus, if we denote the total topological charge (measurement) to be e, then for a fixed total topological charge equal to the vacuum, the fusion space is two-dimensional. This is the foundation for the topological qubit, as expected from our identification of the computational space via fixed fermion parity

Let's denote the relevant Dirac zero mode operators, as we did in Equation (5.11) as follows;

$$
\begin{aligned}
\beta_0^\dagger &= \frac{1}{2}(\gamma_1 - i\gamma_2), & \beta_1^\dagger &= \frac{1}{2}(\gamma_3 - i\gamma_4), \\
\beta_0 &= \frac{1}{2}(\gamma_1 + i\gamma_2), & \beta_1 &= \frac{1}{2}(\gamma_3 + i\gamma_4),
\end{aligned}
\tag{5.26}
$$

where $\beta_i^\dagger$ creates a (delocalized) fermion across the wire. The Hilbert space for a single fermionic mode is two-dimensional, given by whether the mode is occupied or empty. Therefore, the states in this Hilbert space can be distinguished by the eigenvalue of the number operators; $n_i = \beta_i^\dagger \beta_i$. We recall that the Hamiltonian given in Equation (5.1) only conserves fermion number modulo two, so the number operator is clearly not an ideal measure for our topological qubit. However, the Hamiltonian is invariant under conjugation by the total fermion parity operator, so fermion parity is a conserved quantity of the low-energy subspace. The fermion parity is given by

$$
\mathcal{Q} = (-1)^{N_F}
\tag{5.27}
$$

where N_F is the summation of n_i over the lattice. We can adapt the fermion parity to the Majorana operators;

$$
\mathcal{Q} = \prod_i 1 - 2n_i = -i \prod_i \gamma_i \gamma_{i+1},
\tag{5.28}
$$

which gives us a Hermitian operator. We can use this operator to label and distinguish states in the degenerate ground state manifold. We define $|n_1 n_2\rangle$ to be given by $n_i = 0/1$, if the fermion zero mode, β_i is empty/occupied. So if we have four MBS, denoted $\{\gamma_1, \gamma_2, \gamma_3, \gamma_4\}$ localised at the edges of two distinct topologically non-trivial phases then these can combine into two delocalised fermions and we have the total fermion parity number

$$\mathcal{Q}_{\text{tot}} = (i\gamma_1\gamma_2)(i\gamma_3\gamma_4). \tag{5.29}$$

So we can label our qubit space, which is the ground state manifold by the occupation numbers of these fermionic modes;

$$|00\rangle, \qquad |01\rangle, \qquad |10\rangle, \qquad |11\rangle. \tag{5.30}$$

which gives us a four-fold degenerate ground state manifold, the minimum necessary set-up for a topological qubit.

If we restrict to a fixed parity subspace a topological qubit needs at least four MBS, and hence two topological regions in the wire, separated by a non-topological region. The qubit space is then encoded in either the global even or odd parity subspace of the associated 4-fold degenerate ground state space So by fixing to even fermion parity we can write our logical qubit $|\Psi\rangle$ as

$$|\Psi\rangle = \lambda_1|00\rangle + \lambda_2|11\rangle, \quad |\lambda_1|^2 + |\lambda_2|^2 = 1. \tag{5.31}$$

5.6   Braiding of Majorana bound states

In Section 5.5 we discussed how four MBS, if well separated can be used to store information for a quantum computer, as discussed in (99): such a system may be used as a "reliable quantum memory". However, for topological quantum computation, we also need to be able to implement quantum gates. In the two-dimensional paradigm of TQC, the quantum gates are implemented by exchanging anyons, which leads to the braiding of their worldlines in time (102). One of the most interesting features of MBS is their non-Abelian exchange statistics. This was first proposed in two-dimensional systems in (91; 144) and later realised to also hold for MBS in superconductors (8). Before we delve into the details, let's discuss the underlying assumptions for this section.

1. We will focus only on the ground state behaviour, so the unitary operator which enacts the exchange of MBS, will involve only the γ operators and since we are ignoring dynamical errors, the adiabatic exchange operator will act as a rotation within the ground state manifold. Then the entire operation is essentially determining U_{ij}, the operator which exchanges MBS γ_i with γ_j.

Therefore, we assume we can enact the exchange operations sufficiently slowly so that the changing of parameters in the Hamiltonian is slow enough to obey the adiabatic theorem,

2. Another necessary assumption is that the system is closed, so the total fermion parity, $\mathcal{Q}_{\text{tot}}$ is a conserved quantity, before and after the exchange. This means; $[H(0), \mathcal{Q}_{\text{tot}}] = [H(T), \mathcal{Q}_{\text{tot}}] = [U, \mathcal{Q}_{\text{tot}}] = 0$.

3. Thirdly, the exchange of γ_1 and γ_2 has no effect on γ_k, with $k \neq 1$ and $k \neq 2$. This is in essence a statement of the locality of the exchange.

There are further technical points that we are ignoring, such as focusing on the idealised model as opposed to a more realistic model and the stability of the actual qubit under transport. We will turn to the latter of these limitations in Chapter 6.

The unitary exchange operator which satisfies the assumptions of this section is given by

$$U_{ij} = \exp(\alpha\gamma_i\gamma_j) \tag{5.32}$$

where α is a real number which we will next determine. This description is up to an overall phase, which is described as "non-universal" in (8; 131). We start by expanding Equation 5.32 in a Taylor series in terms of β;

$$U_{ij} = \sum_{n=1}^{\infty} \frac{1}{n!}(\alpha\gamma_i\gamma_j)^n = \mathbb{I} + \alpha\gamma_i\gamma_j + \frac{\alpha^2}{2}\gamma_i\gamma_j\gamma_i\gamma_j + \frac{\alpha^3}{3!}\gamma_i\gamma_j\gamma_i\gamma_j\gamma_i\gamma_j + \ldots. \tag{5.33}$$

Now, we can use the γ-operator algebra to simplify this series. Firstly, using, $\gamma_i\gamma_j = -\gamma_j\gamma_i$ to reorder the MBS operators in the third term we get,

$$\frac{\alpha^2}{2}\gamma_i\gamma_j\gamma_i\gamma_j = -\frac{\alpha^2}{2}\gamma_j\gamma_i\gamma_i\gamma_j = -\frac{\alpha^2}{2}\mathbb{I} \tag{5.34}$$

since $\gamma_i^2 = \mathbb{I}$. Further, we can notice that any term corresponding to an even power of α can be reduced to $\alpha^n/n!$, and any term corresponding to an odd power of α can be written in terms of $-\alpha^n\gamma_i\gamma_j/n!$. As a result, we can rewrite the series as,

$$U_{ij} = \mathbb{I} - \frac{\alpha^2}{2} + \ldots + \gamma_i\gamma_j(\alpha - \frac{\alpha^3}{3!} + \ldots). \tag{5.35}$$

We can then recognise the series can be written as

$$U_{ij} = \cos(\alpha)\mathbb{I} + \sin(\alpha)\gamma_i\gamma_i. \tag{5.36}$$

To constrain α, we consider the evolution of the Majorana operators in the Heisenberg picture of quantum mechanics;

$$\gamma_i \to U\,\gamma_i\,U^\dagger,$$
$$\gamma_i \to U\,\gamma_j\,U^\dagger. \tag{5.37}$$

Inserting our ansatz from Equation (5.36), we find

$$\gamma_i \to \cos(2\alpha)\gamma_i - \sin(2\alpha)\gamma_j,$$
$$\gamma_j \to \cos(2\alpha)\gamma_j + \sin(2\alpha)\gamma_i\,. \tag{5.38}$$

Now let's analyse the effect on the γ operators. After the exchange, we must still have Hermitian Majorana operators. We denote γ_i after the exchange by $\gamma_i^{'}$. We can schematically write the action as $\gamma_i^{'} = s\,\gamma_i$. with $s = \pm 1$. Finally, after the exchange, γ_i will now be at the location where γ_j was before the exchange, and therefore we must have;

$$\gamma_1 \to \ \gamma_2,$$
$$\gamma_2 \to -\,\gamma_1. \tag{5.39}$$

This action is denoted T_i in (91). The minus sign in (5.39) is due to the vortices in the $p + ip$ fluid introducing a branch cut in the wave functions, wherein the superconducting phase advances by 2π, when an MBS crosses a branch cut. This is also shown to occur due to the exchange of MBS at a junction in (8). By considering Equation (5.38), we can see we must have $\alpha = \pm\pi/4$, where the $\pm$ sign in α is interpreted as exchanging clockwise or anticlockwise. In the language of Chapter 2, the choice of $\pm\alpha$ corresponds to an R-symbol or an R^{-1}-symbol respectively.

For equivalent derivations of this result, see (8; 30; 47; 88; 152). This result has also been obtained for the chiral two-dimensional p-wave superconductor in (91), and also similarly obtained from conformal field theory in (132).

Putting all of this together we have the following form for the braiding operator

$$U_{ij} = \exp(\pm\frac{\pi}{4}\gamma_i\gamma_j) = \frac{1}{\sqrt{2}}(\mathbb{I} + \gamma_i\gamma_j). \tag{5.40}$$

Now let's consider the action of these braiding operators on the qubit space. Recall the MBS operators can be expressed in terms of the fermion parity operator as

$$\mathcal{Q}_i = i\gamma_i\gamma_{i+1} = 1 - 2\beta_i^\dagger\beta_i = 1 - 2n_i. \tag{5.41}$$

Since Equation (5.40) contains an even number of fermion operators it will preserve the total fermion parity. Furthermore in the qubit basis, which we denote by $|n_1 n_2\rangle$, n_1/n_2 refers to the occupation of the first/ second Dirac zero-energy modes

in Equation 5.26. We can see that

$$i\gamma_1\gamma_2|0\,n_2\rangle = 1\,|0\,n_2\rangle,$$
$$i\gamma_1\gamma_2|1\,n_2\rangle = -1\,|1\,n_2\rangle.$$

(5.42)

Similarly for $i\gamma_3\gamma_4$ except this operator acts on the second entry of $|n_1 n_2\rangle$. The eigenvalues of the operators $i\gamma_i\gamma_j = \pm 1$ correspond to whether the relevant fermionic mode is occupied. We can cast this in the language of Chapter 2, the eigenvalue of $i\gamma_i\gamma_j$ depends on whether the fusion of γ_i with γ_j annihilates or produces a fermion, i.e. it is a 1 or a ψ (131). We can recognise then that as a matrix, both $i\gamma_1\gamma_2$ and $i\gamma_3\gamma_4$ act like the Pauli matrix; σ^z. Next, we turn to the operator $i\gamma_2\gamma_3$, which exchanges the MBS belonging to two different topological phases. To consider the action on the occupation of the fermion zero modes it is useful to rewrite the operator as,

$$i\gamma_2\gamma_3 = i(-i(\beta_0^\dagger - d_0))(\beta_1^\dagger + \beta_1) = \beta_0^\dagger\beta_1^\dagger + \beta_1^\dagger\beta_0 - \beta_0\beta_1^\dagger - \beta_0\beta_1.$$

(5.43)

We can then act with this operator on the fixed fermion parity subspaces to see the action is given by;

$$i\gamma_2\gamma_3 = -\sigma^x.$$

(5.44)

So to summarise, the braiding operators generated by the exchanging four MBS are given by;

$$U_{12} = U_{34} = e^{\frac{\pm i\pi}{4}\sigma^z} = \frac{1}{\sqrt{2}}(\mathbb{I} \pm i\sigma^z),$$
$$U_{23} = e^{\frac{\pm i\pi}{4}\sigma^x} = \frac{1}{\sqrt{2}}(\mathbb{I} \pm i\sigma^x).$$

(5.45)

The non-commutative exchange statistics of MBS can now be readily seen in the non-commuting nature of these matrices, i.e.;

$$[U_{ij}, U_{jk}] = s_{ij}s_{jk}\gamma_i\gamma_k \neq 0, \qquad i \neq k.$$

(5.46)

Furthermore, since all MBS are indistinguishable particles, this generates, in particular, a projective representation of B_4, the Artin braid group on four strands (13).

We can also see that if we initialise the system in $|\Psi(t=0)\rangle = |00\rangle$ and then we perform a U_{23} braiding action, the final state will be given by

$$|\Psi(T)\rangle = \frac{1}{\sqrt{2}}(|00\rangle - i|11\rangle).$$

(5.47)

It should be noted that a quantum computer built from MBS (Ising anyons) is not universal for quantum computation (76; 77). In particular, if we consider n qubits constructed analogously to the single qubit we just discussed, then the collection of unitary operators generates the normalizer of the Clifford group acting on the
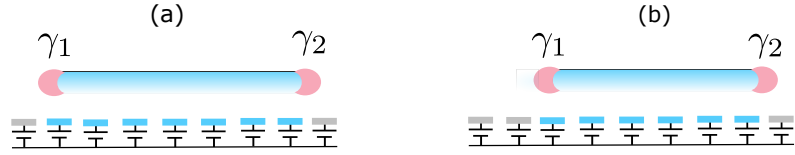
Figure 5.7: By tuning the underlying gate voltage we can shuttle an MBS, denoted γ_1 across a wire. The blue cylinder denotes the topologically non-trivial phase, i.e. $-2w < \tilde{\mu} < 2w$. Since γ_1 is bound to the domain wall between the topologically trivial and topologically non-trivial phase, as the gate voltage is changed, shrinking the topological phase, the associated MBS is shuttled to the right.

Pauli group (133). However, as a group, these quantum gates are not universal for quantum computation. In particular, the phase shift gate, also known as the $\pi/8$ phase gate, is absent. There have been proposals for how to extend the Majorana representations to make them universal (26; 30). In both of these non-topological operations are introduced such as bringing the MBS in sufficient proximity to allow some small splitting of the degenerate space to generate a phase shift. If we did not have degenerate energy levels, then under the action of an adiabatic evolution (braiding), which traces out a closed path in the configuration space, we would find $|\Psi\rangle \rightarrow e^{i\theta}|\Psi\rangle$, i.e. a one-dimensional representation of the braid group. However, since the states created by the Majorana operators are degenerate, we can have a higher representation dimensional representation of the braid group (174).

Now one may wonder how one can actually implement braiding operators like Equation 5.45. This was first proposed in the context of MBS on quantum wires in (8) and further developed in (2; 47). First and foremost we consider a network geometry consisting of p-wave superconductors joined into a network forming trivalent junctions. Then by varying the underlying gate voltage (defining μ), we can shuttle the MBS around the network (18; 94).

We show in Figure 5.7 an example of such a shuttling move, as proposed in (8), we indicate the topological phase by blue and the MBS by the pink circles. This is an example of a U_{12} braiding action.
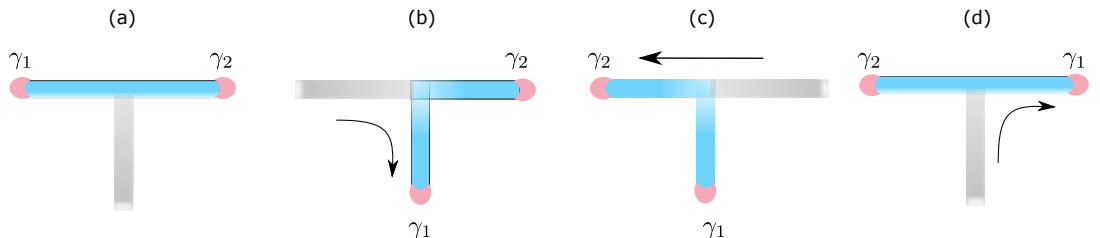

Figure 5.8: A simple exchange of γ_1 and γ_2 following (8). This is an implementation of U_{12} in Equation (5.45).

There have been further generalisations of (8) to allow the junction to not be perfectly in the plane (85). However, to implement this experimentally or to study

the effect of such an evolution we need to generalise the unitary evolution operator to a functional form;

$$U = \mathcal{T}\exp[-i \int_0^t dt' H(t')] \tag{5.48}$$

where $\mathcal{T}$ is the time ordering operator and where $H(t)$ is the time-dependent Hamiltonian. This is a generalisation of Equation (5.40) in the following sense. By considering just the action within the ground state manifold, i.e. processes like $\gamma_i \rightarrow \gamma_j$, we are essentially focusing only on the kinematic Hilbert space. However, in reality, an exchange process such as we have been discussing is a dynamical evolution.

If we move a domain wall in a finite time, then this is changing the system in a non-adiabatic regime and will inevitably create excitations in the system. The actual shuttling of MBS must be done by adiabatically varying the locations of the domain walls. The effect of shuttling the MBS around the network will then enact the unitary braiding operators (47). Of course, if one wants to actually build a topological quantum computer from shuttling MBS around a network, then it is desirable to implement the quantum gates in a finite time. This is a non-adiabatic process that can induce errors (95; 156). We will discuss the effect of such an evolution in Chapter 6, where we study the dynamical evolution of a topological qubit as we have just described.

5.7 Experimental realisation

We will close this chapter with a discussion on the actual experimental realisation of MBS. Although our focus in this chapter and in Chapter 6 is on the theoretical models we shall discuss some of the salient features and notable experimental progress on the signatures of MBS. Firstly, the Kitaev model in Section 5.2 is a toy model, in that there are many effects which we did not consider, such as; interaction terms between the electrons (51), noise in the confining potentials, (157), problems due to finite temperature (14; 15) and the inevitable interaction with the environment (41; 143), to name but a few. The more realistic class of model that may host MBS falls under the umbrella of proximity-coupled nanowires (79; 113; 136). In these systems, a semiconductor wire is situated near a superconducting material. Then superconductivity is induced in the semiconductor via Cooper pairs tunnelling. This is known as proximity-induced superconductivity (21). There are many properties needed to emulate the topologically non-trivial phase, e.g.; effectively spinless fermions, which can be implemented by spin-orbit coupling, breaking time-reversal symmetry and introducing Zeeman splitting in the bands, (via magnetic fields). These properties can effectively make the semiconductor wire behave like a p-wave superconductor (6; 7).

There are two main possible signatures of MBS; the 4π- Josephson effect and zero-bias conductance peaks. We shall discuss the zero bias conductance, for details on

the 4π- Josephson effect, we refer the reader to (7; 135), for a theoretical treatment of the phenomenon and (110) for a recent experimental signature.

One of the most promising signatures is that of a peak in the tunnelling conductance at zero voltage bias, existing at the junction between a metal and a superconducting material (7; 135). This is an indicator of the presence of states within the gap as there is current tunnelling mediated by states within the energy gap. This zero bias conductance is mediated by the MBS at the edge of the material as if they are there, then there is a local density of states which can mediate transport. The first proposed measurement came in 2012 (129). However, this is clouded by the possibility of other states within the gap, such as Andreev-bound states. These states inside the superconducting gap may mimic the zero bias conductance peaks (112; 155). These results were then developed with a follow-up experiment in 2018. However, there were problems in the experiment, which led to the paper being retracted (33). Another problem can occur if the confining potential at the ends of the wire is too smooth, in which case states near zero energy fermionic states can contribute to the zero bias conductance peak (97).

However, the possibility of MBS is such a tantalising prospect for implementing topological quantum computation that experiments have continued since. In fact, in July 2022, there was a new experimental measurement of signatures of the topological gap and the presence of MBS. This result was published by Microsoft Quantum (3). In their setup, they measure zero-bias local conductance peaks at both edges of the nanowire. Although conclusive proof of the existence of MBS is still a delicate and difficult question to answer, we believe the theoretical framework underlying this model merits investigation.

5.8   Summary

In this chapter, we focused on a p-wave superconductor and the associated Majorana bound states. This model hosts Majorana bound states, which may be used to encode a topological qubit (99). The states of the qubit are encoded in the non-local zero energy fermionic mode constructed out of the unpaired Majorana operators. The presence of these modes indicates the ground state is degenerate, and it was proven that this degeneracy is robust against perturbations in (99). In Section 5.2, we showed how to derive the unpaired Majorana operators. We started with the Hamiltonian for a p-wave superconductor in Equation 5.1, and showed how in certain limits of the coefficients, one finds unpaired Majorana operators on the edges of the system. In Figure 5.1 we display how the terms of the Hamiltonian couple differ fermion lattice sites.

In Section 5.3, we focused on the bulk spectrum and how the different terms in the Hamiltonian affect the excitation spectrum. For example, we showed in Figure 5.3

that the superconducting term in Equation 5.15 opens up a finite energy gap. We then fixed to $\Delta \neq 0$ and varied the onsite chemical potential in Figure 5.4. We showed that the spectrum becomes gapless when $\mu = |2w|$, otherwise the spectrum is gapped otherwise. This gives us a region of the parameter space in which the system is gapped. We then developed these ideas further in Section 5.4.

We showed that in the region of the parameter space corresponding to the gapped spectrum, one finds a topologically non-trivial invariant of the system, namely a winding number integrated over the Brillouin zone. We also showed that this topological invariant is trivial in the region of parameter space where the system is gapless. Hence the distinct phase of the system can be classified by this invariant.

In Section 5.5 and Section 5.6 we summarised the features of this model that are relevant for topological quantum computation. In particular, we explained how the qubit is constructed using four Majorana operators, which combine into two fermion zero modes, given in Equation 5.26. We then discussed how MBS can be braided, which implements gates for the quantum computer. In Equation 5.45 we showed the operators that act on the qubit space, resulting from exchanging pairs of MBS. The non-Abelian nature of the MBS exchange follows from the non-commutative nature of the matrices corresponding to the braiding operators.

In Section 5.7, we discussed the current experimental status of Majorana measurements and the idealised nature of the model we studied in this chapter. We briefly explained one of the main experimental signatures of the existence of MBS, namely a zero bias conductance peak.

Chapter 6

Error processes in Majorana-based topological qubits

6.1   Introduction

In this chapter we will analyse sources of qubit error that can be generated by the dynamical evolution of a topological memory, consisting of two non-trivial topological phases in a p-wave superconducting wire. In Chapter 5, we discussed this model and outlined how the topological qubit is constructed. We will focus on two regimes of dynamical evolution: deliberate transport of the qubit and periodic oscillation in the boundary potential. In order to implement TQC on networks, one needs to transport the MBS around the network to implement braiding (8; 154). However transporting a topological qubit around a network in a finite time is inherently a non-adiabatic process (95; 156), which seems to create tension with braiding in TQC. Hence this raises the importance of understanding what effect this has on the qubit and how to mitigate the errors caused by such a process. We also consider periodic driving in the confining potential of the non-trivial phase as a model for error or uncertainty in the control of such a system. Finally, we also demonstrate how such error processes can be minimised by disordering central regions of both wires; this is analysed as a scheme of error prevention.

This chapter is based on (49) in collaboration with Domenico Pellegrino, Shane Dooley, J.K. Slingerland and Graham Kells.

6.2 The model

We start with a p-wave superconductor with two non-trivial topological phases separated by a topologically trivial phase between them. The Hamiltonian for the Kitaev model of a p-wave superconductor is

$$H = -\sum_{j=1}^{N} \tilde{\mu}_j (c_j^\dagger c_j - 1/2) - w \sum_{j=1}^{N-1} (c_j^\dagger c_{j+1} + h.c.) + \tilde{\Delta} \sum_{j=1}^{N-1} (c_j^\dagger c_{j+1}^\dagger + h.c.) - \sum_{j=1}^{N} \lambda_j c_j^\dagger c_j.$$

(6.1)

We have discussed the parameters of this model in Chapter 5. However, in this chapter, our chemical potential $\tilde{\mu}_j$ will become time-dependent, as we will be considering dynamically evolving the boundary potentials. Later in the chapter we will also introduce disorder in the chemical potential using a Gaussian random variable λ_j, which has zero mean and variance α,

$$\langle \lambda_j \rangle = 0, \qquad \langle \lambda_i \lambda_j \rangle = \alpha \, \delta_{ij}/a \,.$$

(6.2)

We will discuss disorder as a means to reduce undetectable qubit errors in Section 6.4.2. The presence of disorder sets a finite localization length $l = v_F^2/\alpha$ of the Majorana bound states (32; 170). The chemical potential $\tilde{\mu}_j$ can vary across the wire and will be used to control the boundaries between topological regions (where $|\tilde{\mu}_j| < 2|w|$) and topologically trivial regions (where $|\tilde{\mu}_j| > 2|w|$) (21; 99). The use of boundary control to transport MBS has been studied in (8; 18) and is often called "piano key" dynamics. In this formalism, one tunes the underlying gate potential in finite regions to transport the boundaries of the topological and non-topological regions and as such, the MBS localised at the boundary. We model a boundary wall separating a topological and a non-topological region at a position x_{wall} along the wire by a sigmoid function for the chemical potential (see Figure 6.1 for an illustration showing several boundary walls). We take the following parameterisation,

$$\mu(x) = \mu_- + \frac{\mu_+ - \mu_-}{1 + e^{-(x-x_{\text{wall}})/\sigma}}$$

(6.3)

where x_{wall} labels the position of the wall, σ characterises the steepness of the wall, and $\mu_\pm$ is the chemical potential in the limit $x - x_{\text{wall}} \to \pm\infty$. For convenience, in Equation 6.3 we use the continuous label x instead of the discrete label j [i.e., $\tilde{\mu}_j \to \mu(x)$], although the lattice sites always appear at the discrete positions $x = ja$, where a is the lattice spacing and $j = 1, ..., N$ is an integer. Multiple walls along the wire are modelled by adding sigmoid functions at various positions ($x_{\text{wall}}^{(2)}, x_{\text{wall}}^{(3)}$, etc.) along the wire, with an appropriate normalisation, to give the desired chemical potential between any two walls. In the two-wire scenario described in Figure 6.1,
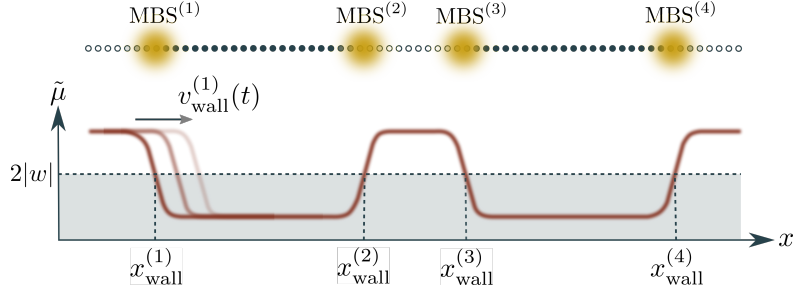
Figure 6.1: Top: A schematic illustration of the Kitaev chain used to encode a single topological qubit. MBS are localised at the boundaries between topological and non-topological regions. Bottom: The chain is in a topological phase in regions where $|\tilde{\mu}| < 2|w|$ (the shaded area) and in a non-topological phase in regions where $|\tilde{\mu}| > 2|w|$.

we choose the normalisation such that the chemical potential at the outer boundary walls is $\mu = 20w$, and at the middle wall is $\mu = 2.5w$ (unless otherwise stated). We can use both of these values for μ to create a boundary between the topological and non-topological regions. To move a boundary wall we allow the wall position $x_{\text{wall}}(t)$ to be time-dependent. Equivalently, we can specify a time-dependent wall velocity $v_{\text{wall}}(t) = dx_{\text{wall}}(t)/dt$. This results in a time-dependent chemical potential $\tilde{\mu}_j(t)$, and hence a time-dependent Hamiltonian, as given in Equation 6.1.

6.2.1 Dynamical time evolution of a topological qubit

To analyse the system, we rewrite our Hamiltonian in Equation 6.1 in the BdG formalism discussed in Appendix G. The Hamiltonian is written as

$$H(t) = \sum_{n=1}^{N} \epsilon_n(t)[\beta_n^\dagger(t)\beta_n(t) - 1/2], \tag{6.4}$$

using the time dependent Bogoliubov transformations:

$$\beta_n(t) = \sum_j U_{j,n}(t)c_j + V_{j,n}^*(t)c_j^\dagger,$$
$$\beta_n^\dagger(t) = \sum_j U_{j,n}^*(t)c_j^\dagger + V_{j,n}(t)c_j, \tag{6.5}$$

where $U_{j,n}(t)$, $V_{j,n}(t)$ are the coefficients of the unitary matrix that diagonalizes the Bogoliubov-De Gennes (BdG) Hamiltonian associated with $H(t)$. We assume that the spectrum is labelled in increasing order $\epsilon_0 \leq ... \leq \epsilon_{N-1}$. Pairs of Majorana bound states, if well separated, are associated with zero energy modes ($\epsilon_0 \approx 0$, $\epsilon_1 \approx 0$,... etc.). If there are m such zero modes $\{\beta_j\}_{j=0}^m$, then there are 2^m degenerate ground states $(\beta_0^\dagger)^{l_0}...(\beta_m^\dagger)^{l_m}|\text{GS}\rangle$, where $l_j \in \{0, 1\}$ and $|\text{GS}\rangle$ is the BCS ground state. If there are two topological phases in the system separated by a non-topological region. we will have 4 degenerate ground states or more generally, 2^N, where N labels

the number of topological regions. We follow Section 5.5 and choose our logical qubit to be spanned by the ground states of the even-parity sector $|\bar{0}\rangle \equiv |GS\rangle$ and $|\bar{1}\rangle \equiv \beta_0^\dagger \beta_1^\dagger |GS\rangle$. Since we are changing the positions of the boundary walls in time by changing $\tilde{\mu}(t)$, our Hamiltonian $H(t)$ is time-dependent, and hence the spectrum $\epsilon_n(t)$, the normal mode operators $\beta_n(t)$, and the degenerate ground states $\{|\bar{0}(t)\rangle, |\bar{1}(t)\rangle\}$ will also be time-dependent. To investigate either of the two regimes we mentioned in the introduction of the chapter, we need to study the time evolution of the qubit. We suppose at an initial time, the system is in the state,

$$|\psi(t_{\text{init}})\rangle = \alpha_0 |\bar{0}(t_{\text{init}})\rangle + \alpha_1 |\bar{1}(t_{\text{init}})\rangle \tag{6.6}$$

where $|\bar{0}(t_{\text{init}})\rangle$ and $|\bar{1}(t_{\text{init}})\rangle$ are ground states of the Hamiltonian $H(t_{\text{init}})$ at that time. At a later time t, the system has evolved to the state

$$|\psi(t)\rangle = \mathcal{U}(t, t_{\text{init}}) |\psi(t_{\text{init}})\rangle, \tag{6.7}$$

where the time evolution operator is given by

$$\mathcal{U}(t, t_{\text{init}}) = \mathcal{T} e^{-i \int_{t_{\text{init}}}^{t} H(t')dt'}. \tag{6.8}$$

If the change of boundary potential locations and as such the change of the Hamiltonian is sufficiently slow then by the adiabatic theorem in an ideal case, the system will stay in a superposition of the ground states of the system,

$$|\psi_{\text{ideal}}(t)\rangle = \alpha_0 |\bar{0}(t)\rangle + \alpha_1 |\bar{1}(t)\rangle, \tag{6.9}$$

with the same amplitudes as the initial state up to some global $U(1)$ phase. We regard $|\psi_{\text{ideal}}(t)\rangle$ as the ideal, error-free evolution. However, the reality is in order for TQC to be feasibly implemented in a finite time in a real-life system, time evolution will affect the qubit space, such as qubit loss, bit flip error and phase error. Any derivations from adiabaticity or ideal time evolution will lead to excitation of the bulk modes, corresponding to qubit loss. We quantify the qubit-loss by the probability P_{loss} that the system is not in one of the instantaneous qubit states:

$$P_{\text{loss}}(t) = 1 - |\langle\psi(t)|\bar{0}(t)\rangle|^2 - |\langle\psi(t)|\bar{1}(t)\rangle|^2. \tag{6.10}$$

So $P_{\text{loss}} = 0$ if there is no qubit-loss and $P_{\text{loss}} = 1$ if the qubit is completely lost. However, as dire as this may appear to be, since qubit loss corresponds to energy excitations, qubit-loss errors can, in principle, be detected by projective measurements of energy (133). Conversely we label bit flip and phase errors as undetectable qubit errors. These error channels occur when some bulk excitation returns to the ground state space. A bit-flip error occurs if the system returns to the qubit space

in the state

$$|\psi_{\text{bit}}(t)\rangle = \alpha_0\,|\bar{1}(t)\rangle + \alpha_1\,|\bar{0}(t)\rangle \tag{6.11}$$

(i.e., with the qubit basis states exchanged $|\bar{1}(t)\rangle \leftrightarrow |\bar{0}(t)\rangle$). We quantify the bit-flip error with the probability:

$$P_{\text{bit}}(t) = |\langle\psi(t)|\psi_{\text{bit}}(t)\rangle|^2. \tag{6.12}$$

In the following study of bit-flip error we will choose $|\psi(0)\rangle = |\bar{0}\rangle$ as our initial state and thus the bit-flip error is simply given as $P_{\text{bit}} = |\langle\psi(t)\rangle\,\bar{1}(t)|^2$. We refer to the relative phase of the qubit basis states by a phase error. A phase-flip error occurs if the system after time evolution is given by,

$$|\psi_{\text{phase}}(t)\rangle = \alpha_0\,|\bar{0}(t)\rangle - \alpha_1\,|\bar{1}(t)\rangle\,. \tag{6.13}$$

This occurs with probability:

$$P_{\text{phase}}(t) = |\langle\psi(t)|\psi_{\text{phase}}(t)\rangle|^2. \tag{6.14}$$

In the following discussions of phase error, we will choose,

$$|\psi(0)\rangle = |\psi_+(0)\rangle \equiv \frac{1}{\sqrt{2}}(|\bar{0}\rangle + |\bar{1}\rangle), \tag{6.15}$$

as our initial ideal state and the state which has undergone a phase error as,

$$|\psi_{\text{phase}}(t)\rangle = |\psi_-(t)\rangle \equiv \frac{1}{\sqrt{2}}(|\bar{0}(t)\rangle - |\bar{1}(t)\rangle) \tag{6.16}$$

To calculate the probabilities of any of these error channels we use the Onishi formula (134; 138):

$$|\langle\psi(t)|\psi'(t)\rangle|^2 = \det\big(U(t)^*U'(t) + V(t)^*V'(t)\big), \tag{6.17}$$

where U' and V' are defined as:

$$\begin{pmatrix} U'(t) \\ V'(t) \end{pmatrix} = \mathcal{U}_{\text{BdG}}(t) \begin{pmatrix} U(0) \\ V(0) \end{pmatrix}, \tag{6.18}$$

and the BdG time evolution operator is given by,

$$\mathcal{U}_{\text{BdG}}(t) = \mathcal{T}\exp\left(\int_0^t dt'\, H_{\text{BdG}}(t')\right). \tag{6.19}$$

The process of time evolution corresponds to: changing the Hamiltonian, construct-
ing the unitary time evolution operator and then acting with this operator on the
eigenstates of the previous iteration to deduce the change's effect on the system.

6.3   Qubit loss

The first error to study is qubit loss since the undetectable errors require the qubit
loss error channel to already be open. We will turn our attention first to the move-
ment of just one wall in our system. The movement of boundary walls generates
excitations in the model. We shall consider the two regimes we mentioned at the
start of the chapter, namely oscillating boundary wall and transport of Majorana
bound states. The first of these regimes is a simple model for error in the control of
the boundary potential. This has been studied previously, see for example (14; 157).
The latter of these regimes is necessary in order to implement braiding of MBS on
a network (8). There is an interesting feature of non-adiabatic evolution of this
system, namely, it is known that there is a critical velocity beyond which the system
suffers heavy qubit loss, which we will now take a mild detour to discuss.

Critical velocity and propagating excitations

In this model the existence of a critical velocity v_{crit} was first pointed out in (156) and
later studied in (95). It is best understood in the continuum limit after transforming
to a moving frame of reference that moves at the velocity $v(t)$ of the boundary wall.
The transformation is implemented by the unitary operator,

$$\mathcal{W}(t) = \exp\{-i\hat{P} \int_0^t v(t')dt'\} \tag{6.20}$$

where $\hat{P}$ is the momentum operator, which expressed in terms of the usual fermionic
creation and annihilation operators is written as,

$$\hat{P} = i \sum_j \frac{c_j^\dagger c_{j+1} - c_{j+1}^\dagger c_j}{2a}, \tag{6.21}$$

where a is the lattice parameter. The fermionic creation and annihilation operators
are related to the quasi-particle operators by,

$$c_j^\dagger = \sum_k U_{jl}^* \beta_k^\dagger + V_{jk}\beta_j, \qquad c_j = \sum_k U_{jl}\beta_k + V_{jk}^*\beta_k^\dagger. \tag{6.22}$$

We can use this transformation to express the momentum operator in the quasi particle basis as, $\hat{P}' = W\hat{P}W^\dagger$ or explicitly after some rearranging,

$$\hat{P}' = i \sum_{k,m} \sum_j \frac{U^*_{j,k}}{2a}(V^*_{j+1,m} - V^*_{j-1,m})\beta^\dagger_k \beta^\dagger_m, \tag{6.23}$$

where m, k label coordinates in k space. The Hamiltonian in the moving frame is written as,

$$H'(t) = \mathcal{W}(t)H(t)\mathcal{W}(t)^\dagger + i\frac{d\mathcal{W}(t)}{dt}\mathcal{W}^\dagger(t) = H(0) + \hat{P}v(t). \tag{6.24}$$

This transformation can also be found in (95). We can separate the Hamiltonian at $t = 0$ because the time dependency in the Hamiltonian enters through the translation in the boundary walls, which are static at $t = 0$.
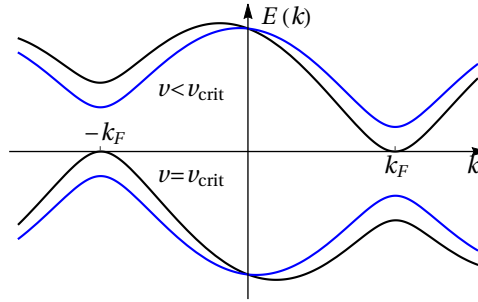

Figure 6.2: Bulk single particle energies of the instantaneous Hamiltonian in k space in the "moving frame" for $v < v_{crit}$ and $v = v_{crit}$, where the gap is closed.

For a translationally invariant system with periodic boundary conditions, [1] the excitation spectrum (plotted in Figure 6.2) can be given as:

$$\epsilon'(k)_\pm = \pm\sqrt{(k^2/2m - \mu)^2 + \Delta^2 k^2} + v(t)\,k. \tag{6.25}$$

This equation shows that for $v < |\Delta|$ the spectrum is gapped (so long as $\mu \neq 0$ and $\Delta \neq 0$). However, when $v \geq |\Delta|$ the spectrum is gapless at approximately either the positive or negative Fermi momentum $\pm k_F = \pm\sqrt{2m\mu}$. If the system is gapless we can create excitations freely, so the ground state manifold is no longer topologically protected. This argument suggests that there is a critical velocity at $v_{crit} = |\Delta|$. In (95), this critical velocity is connected to an apparent "speed of light" in the topological superconductor. Considering the system in the moving frame allows us to understand intuitively why the excitations produced by the wall movement should move with momentum which is peaked at approximately around k_F. The ground state consists of all the one particle states with $E < 0$ occupied. From Figure 6.2 we see that for a sub-critical velocity $v < v_{crit}$, the occupied one particle state

---

[1] So in the absence of boundary walls, or equivalently we can imagine the ring is sufficiently long that can be considered this analysis in a small local part away from the boundary walls.

with the highest energy is at $k = -k_F$. The lowest energy unoccupied one particle state is at $k := k_F$. The smallest energy excitation between states, therefore, has a momentum of $2k_F$. The excitations are composed of quasi-particles and quasi-holes that travel with opposite velocities, This accounts for the excitations travelling with group velocity approximately peaked around v_F. We can also estimate this in Figure 6.8. For example, at the critical velocity, $v = v_{\text{crit}}$ this excitation costs zero energy, since the spectrum is gapless and over time the topological qubit is completely lost to excitations in the wire, which are travelling with Fermi momentum k_F. We will return to the propagating excitations in Section 6.4.1.

6.3.1 Qubit loss due to an oscillating wall

The first regime of qubit loss we shall consider is periodic driving in the position of the edge wall. So in our time evolution the wall at position $x_{\text{wall}}^{(1)}$, is oscillating with a velocity profile of the form:

$$v_{\text{wall}}^{(1)}(t) = v_{\text{max}} \sin(\omega t). \tag{6.26}$$

Since the wall is continuously moving, it is appropriate to calculate the time-averaged rate of qubit-loss over a time interval $t'' - t' = 2n\pi/\omega$ spanning some periods of the oscillation,

$$\langle dP_{\text{loss}}/dt \rangle = \frac{1}{t''-t'} \int_{t'}^{t''} dt (dP_{\text{loss}}(t)/dt) \tag{6.27}$$

The colour map in Figure 6.3(a) shows $\langle dP_{\text{loss}}/dt \rangle$ as a function of the wall motion parameters ω and v_{max}. We can identify several features. First, when $v_{\text{max}} = 0$ or when $\omega = 0$ the qubit-loss rate is zero, as expected, since the wall is static in this case. For small values of v_{max} the qubit-loss rate is small irrespective of the value of ω. This is the adiabatic regime where the wavefunction of the system closely follows the ground state of the instantaneous Hamiltonian and so the system is insensitive to the oscillating wall. Equivalently, the instantaneous qubit states are essentially equal to the time evolved qubit states at each timestep. However, for velocities larger than the critical velocity $v_{\text{crit}} = |\Delta|$ the qubit-loss rate is large, even for small frequencies ω. This makes sense as we discussed in Section 6.3, when the velocity of the wall movement is greater than the critical velocity the excitation spectrum becomes gapless. This is consistent with the results of Refs. (95; 156). In Figure 6.3(a) we see that the rate of qubit-loss is highest when the wall oscillation frequency ω is close to the gap energy $E_{\text{gap}} = \Delta k_F$, which we indicate by the black horizontal arrow at the bottom of the figure. This is verified in Figure 6.3(b), where we plot a cross-section of Figure 6.3(a) at a fixed sub-critical value of $v_{\text{max}} = 0.02$ for different values of the superconducting gap Δ. By considering different values of Δ, we are also considering different values of the energy gap in the model, since they are related; $E_{\text{gap}} = \Delta k_F$. In figure 6.3(b) also shows that for $\omega \gg E_{\text{gap}}$, the qubit-loss

rate decreases quickly. This is somewhat counterintuitive, naively one would expect that increasing the oscillation frequency would make the qubit loss worse; however, there seems to be a resonant frequency in the model beyond which the topological protection is enhanced. This has been analysed further in (52). Examining the right tail of Figure 6.3(b), we see that all of the curves for different values of Δ converge to the same rate of qubit loss. We find numerically that this drop off is proportional to $1/\omega^4$. While the frequency ω_{max}, at which we have maximum
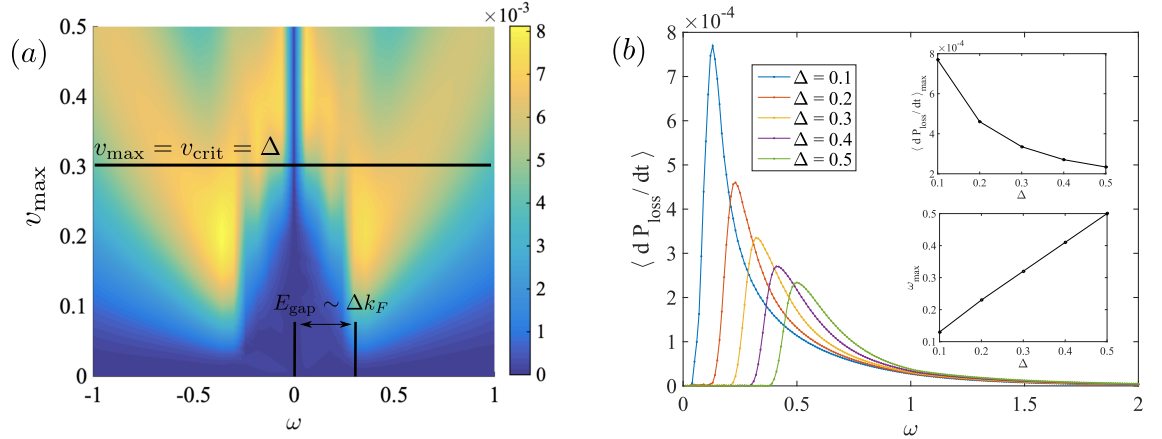

Figure 6.3: (a) The time-averaged qubit-loss, as a function of the wall velocity parameters v_{max} and ω. The horizontal black line shows the critical velocity $v_{\text{crit}} = |\Delta| = 0.3$. To generate this figure we used $L = 200, a = 1, m = 0.5, v(t) = v_{\text{max}} \sin(\omega t)$, and $\mu = 0.5$. The boundary potentials in this case were set to be essentially infinite ($\mu_{\text{boundary}} = -2000$) and the wall gradient with $\sigma = 1$. (b) A cross-section of (a) at $v_{\text{max}} = 0.02$. We see that the maximum qubit-loss rate occurs when the frequency is close to E_{gap}, but where the maximum value decays as $1/E_{\text{gap}}$. The low frequency regime corresponds to the super-adiabatic limit, so we typically see very low rates of qubit loss error. For higher frequencies, we see that the error rate drops off as $1/\omega^4$. Crucially, because the maximum resonant frequency scales with E_{gap}, in the high-frequency regime, increasing the topological order parameter can make the system more susceptible to errors.

qubit-loss rate, grows with Δ, the actual qubit-loss rate $\langle dP_{\text{loss}}/dt \rangle_{\text{max}}$ decreases [see insets of Figure 6.3(b)]. This decrease can be partially put down to the fact that the overall rate of qubit loss depends on the oscillation amplitude. For the choice of parameterisation given in Equation (6.26) we have,

$$x_{\text{wall}}^{(1)}(t) = x_{\text{wall}}^{(1)}(0) + v_{\text{max}}[1 - \cos(\omega t)]/\omega, \tag{6.28}$$

and thus for a fixed maximum velocity, we have a smaller oscillation amplitude at higher frequencies. In similar calculations where the wall movement is parameterised as,

$$x(t) = x_0 + x_{\text{max}} \cos(\omega t) \tag{6.29}$$

i.e., with a fixed amplitude x_{max}, we see the drop-off in qubit-loss rate for $\omega \gg E_{\text{gap}}$ scale as $1/\omega^2$. For fixed frequencies larger than the gap [see e.g., $\omega \approx 0.6$ in Figure

6.3(b)] we see that the rate of qubit-loss increases as Δ is increased. This is in contrast to the situation in the low-frequency adiabatic regime, where increasing Δ (hence increasing the gap E_{gap}) decreases the rate of qubit-loss. Thus while it makes sense to try to maximise the topological gap to counteract low-frequency noise and/or errors associated with the deliberate motion of the topological boundary, the situation is more complicated if the range of perturbing frequencies extends above the frequency corresponding to the bulk gap.

6.3.2 Qubit loss from MBS transport

In (8) it was proposed that braiding could be implemented on networks, so it is important to analyse the effect on the qubit of transporting MBS. On the question of Majorana bound state transport, significant progress has been made previously by Refs. (18; 45; 95; 156) where it was shown that MBS can be transported without incurring any significant qubit loss, provided that the acceleration is sufficiently slow and the maximum velocity is less than a critical value. To model transport, we consider a velocity profile of the form:

$$v_{\text{wall}}^{(1)}(t) = \begin{cases} v_{\text{max}} \frac{1-\cos(\omega t)}{2} & 0 \leq t \leq \frac{\pi}{\omega} \\ v_{\text{max}} & \frac{\pi}{\omega} \leq t \leq \frac{\pi}{\omega} + T \\ v_{\text{max}} \frac{1-\cos(\omega t - \omega T)}{2} & \frac{\pi}{\omega} + T \leq t \leq \frac{2\pi}{\omega} + T \\ 0 & \text{otherwise.} \end{cases} \tag{6.30}$$

This results in an acceleration from zero velocity to a maximum velocity v_{max}, followed by a period T at constant velocity, and finally a deceleration back to zero velocity [see Figure 6.4(a), top panels]. A small frequency ω corresponds to a slow acceleration of the wall, while a large value corresponds to sudden acceleration. In (53), the effect of other velocity profiles is tested, e.g. the bang-bang protocol. We note that in the $v < v_{\text{crit}}$ regime, the motion is by no means adiabatic (except at very low velocity) and there is considerable qubit loss during the wall's motion in the acceleration phase. However, the system returns to the ground state manifold as the wall is slowed down again. This means the wall can be moved far faster than what would be naively considered adiabatic, without permanent qubit loss. This has also been noted in earlier works on this subject (95; 156) and it is linked to the notion of super-adiabaticity, where the motion can be considered adiabatic in a moving frame (see e.g Ref. (22)).

We explore this further in Section 6.3.3 where we note that it is possible to think of the instantaneous energy increase as a kinetic energy of the boundary wall. The final excess energy after the wall has stopped is a small correction to this behaviour, vanishing exponentially with increasing Δ and τ.
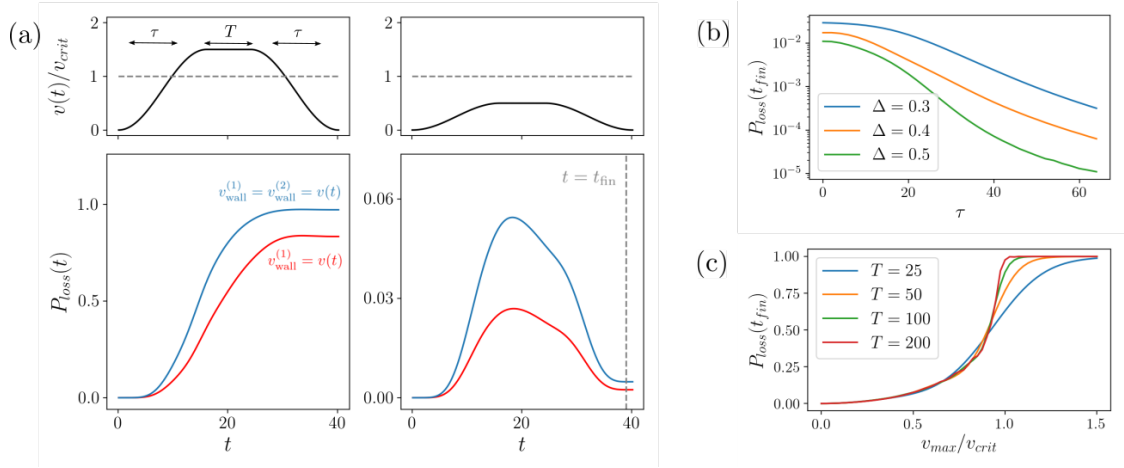
Figure 6.4: (a) Qubit-loss for $v_{\mathrm{max}} > v_{\mathrm{crit}}$ (left panel) and $v_{\mathrm{max}} < v_{\mathrm{crit}}$ (right panel). The corresponding wall velocity profiles are plotted above. We see that the final qubit loss is larger for two moving walls than for a single moving wall (blue lines vs. red lines) (Plotted for $\Delta = 0.4$). (b) The final qubit-loss at some time t_{fin} after the walls have come to rest, plotted as a function of $\tau = 1/\omega$ (for $v_{\mathrm{max}} = 0.1$ and $T = 30$). (c) The final qubit-loss in the limit of sudden wall acceleration ($\tau \to 0$). As T gets large we see a sharp distinction emerge between the $v_{\mathrm{max}} > v_{\mathrm{crit}}$ and $v_{\mathrm{max}} < v_{\mathrm{crit}}$ regimes (here, $v_{\mathrm{crit}} = |\Delta| = 0.2$). [Other parameters: in all figures, $a = 0.5$, $m = 0.5$, $L = 200$, $\mu = 1.0$ (in the topological region).]

6.3.3 Correlated qubit movement and effective wall mass

We also consider the motion of two boundary walls (the two leftmost walls at $x_{\mathrm{wall}}^{(1)}$ and $x_{\mathrm{wall}}^{(2)}$), both by identical velocity profiles $v_{\mathrm{wall}}^{(1)}(t) = v_{\mathrm{wall}}^{(2)}(t)$ given by Equation 6.30, so that the two walls are moving in sync and the length of the wire remains constant, see e.g. Ref. (156).

The numerical results shown in Figure 6.4(a) show that there is no advantage to coordinated wall movement, compared to a single moving wall. Indeed in the right panel of Figure 6.4(a), we see that for $v_{\mathrm{max}} < v_{\mathrm{crit}}$ the qubit-loss is approximately a factor of two higher in this case than for a single moving boundary wall, and that this factor of two persists throughout the movement protocol. Instead of qubit-loss, we examine the energy above the instantaneous ground state. We find that up to small exponential corrections due to changes in velocity, the energy increase scales as $\frac{1}{2}Mv^2$ where the effective mass scales as $M \propto p_F^2/E_{\mathrm{gap}}$. At the end of a movement protocol, the accumulated deviations from super-adiabaticity result in a final resting energy above that of the ground state. However, this result is only evident once the system has come to a complete stop. During a super-adiabatic protocol the instantaneous energy loss can be related to a kinetic energy with an effective mass $M \propto k_F^2/E_{\mathrm{gap}} = k_F/\Delta$.
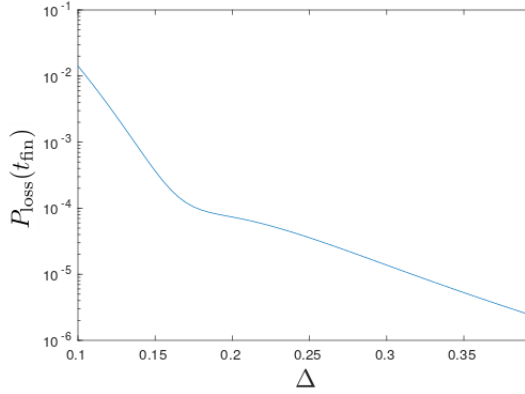
Figure 6.5: Final qubit loss P_{loss} as a function of the superconducting order parameter Δ. We keep the time the wall is accelerating fixed to $\tau = 8$. We can see past $\Delta \sim 0.2$, the qubit loss,P_{loss} behaves nearly exponentially. This data is produced with $\mu = 1$, $m = 0.5$, a system of length $L = 100$ and the lattice constant $a = 0.5$.

To confirm this in the hard-wall limit we work in a position space moving frame picture and estimate the energy increase with respect to the static ground-state energy as:

$$E(t) = \frac{1}{2}\text{Tr}_+(W_{v(t)}^\dagger H_0 W_{v(t)} - W_0^\dagger H_0 W_0) \tag{6.31}$$

where the subscript $+$ on the trace means we only use positive energy modes $[U^T, V^T]^T$ and W is defined by,

$$W(t) = \begin{pmatrix} U(t) & V^*(t) \\ V(t) & U^*(t) \end{pmatrix}, \tag{6.32}$$

In general we find that if the motion is super-adiabatic, as in e.g. (22; 84; 156), then

$$E(t) \approx \frac{M}{2}\gamma(t)v(t)^2. \tag{6.33}$$

where

$$\gamma(t) = 1/\sqrt{1 - v(t)^2/\Delta^2}. \tag{6.34}$$

The effective mass is plotted as a function of Δ and μ in Figure 6.7. The scaling allows us to relate the topological gap $E_{\text{gap}} \propto k_F^2/2M$. In Figure 6.6 we show a comparative plot between $E(t)$ and $\frac{M}{2}\gamma(t)v(t)^2$. The value of the effective mass is obtained by fitting methods.
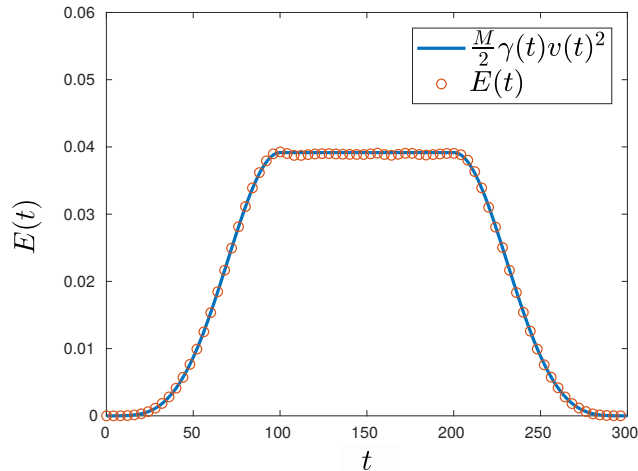
Figure 6.6: The solid line represents the curve $\frac{M}{2}\gamma(t)v(t)^2$. The empty circles represent the value of $E(t)$ obtained through (6.31). The value of $M \approx 1.69$ was obtained by fitting the two curves. The simulations were obtained using $L = 100$, $\Delta = 0.4$, $\mu = 1$, $a = 0.5$ and $m = 0.5$. The velocity profile was chosen as in (6.30), with $\tau = \omega^{-1} = 50$, $T = 100$ and $v_{\max} = 0.2$.
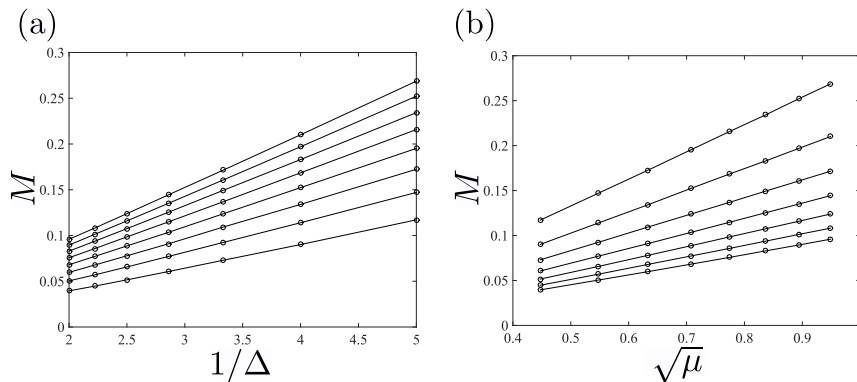

Figure 6.7: The effective mass scales as (a) $M \propto 1/\Delta$ and (b) $M \propto \sqrt{\mu} \propto k_F$. This allows us to relate the topological gap (the energy gap between the ground state and the first excited state) and the effective wall mass as $E_{\mathrm{gap}} \propto k_F^2/2M$.

6.4 Undetectable qubit errors

This section will describe the induced bit flip error due to non-adiabaticity. We call this an undetectable qubit error because the ground states are degenerate; a bit flip error can not be detected by projective energy measurement.

6.4.1 Bit flip errors

In the previous section, we saw that the movement of the boundary wall can lead to qubit-loss that can be recovered, to some extent, when $v < v_{\mathrm{crit}}$. This raises the question: can the system return to the qubit space with an error? In this section, we will show that bit-flip errors can indeed occur, and we will explore how they are related to excitations produced during the wall movement. First, we note that, in general, wall movement generates local excitations because of the local nature of
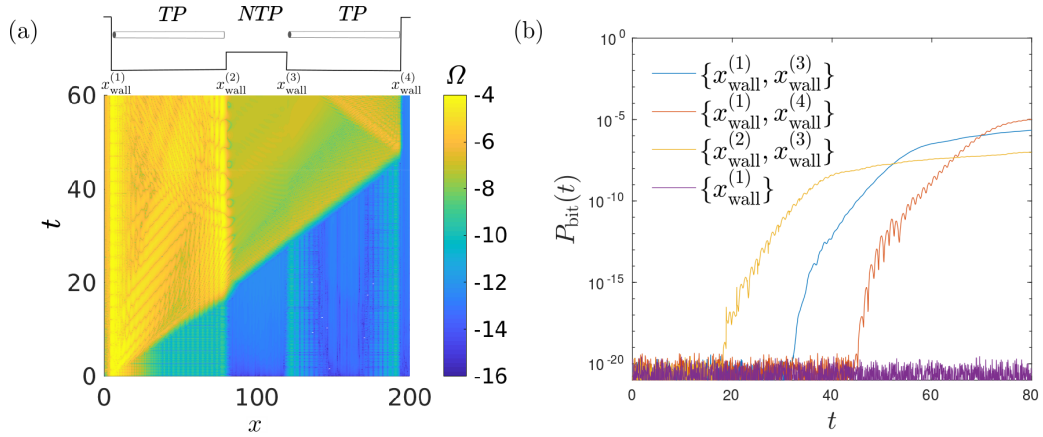
Figure 6.8: (a) The density wave packet generated by a *single* moving wall at $x_{\text{wall}}^{(1)}$ travels at a velocity approximately equal to v_F. We can see the wave tunnelling through the non-topological barrier separating the topological phases (barrier height $\mu_{\text{barrier}} = -2.5$). Here, $v_{\max} = 0.3$, and $\omega = 3$. (b) The bit-flip error P_{bit} increases suddenly as the excitation produced by the movement of one wall hits another moving wall (legend shows which walls are in motion). The time at which the error begins to increase can be estimated as approximately $t \approx |x_{\text{wall}}^{(i)} - x_{\text{wall}}^{(j)}|/v_F$ where $|x_{\text{wall}}^{(i)} - x_{\text{wall}}^{(j)}|$ is the distance between the two moving walls. [Other parameters for both figures: $m = 0.5$, $a = 0.5$, $\Delta = 0.4$, $L = 200$, and $\mu = 1.0$ (in the topological region).]

the perturbation. These local excitations can then propagate through the wire over time. To investigate this, we consider a single wall (at the position $x_{\text{wall}}^{(1)}$) oscillating sinusoidally as in Equation (6.26) [although similar results can be obtained with the shuttling movement protocol given by Equation (6.30)]. In Figure 6.8(a) we plot the deviations from the ideal particle density:

$$\Omega_j(t) = \langle \psi(t)| c_j^\dagger c_j |\psi(t)\rangle - \langle \psi_{\text{ideal}}(t)| c_j^\dagger c_j |\psi_{\text{ideal}}(t)\rangle, \qquad (6.35)$$

as a function of time t and the position $x = ja$ along the wire, due to the motion of the boundary wall. Figure 6.8 shows a quasiparticle density wave that propagates across the wire. The velocity of the propagating wave can be read off from the plot and is found to be approximately equal to the Fermi velocity v_F. This value for the velocity is essentially due to the fact that if we consider the system in the moving frame, excitations, made out of quasiparticle and quasiholes with relative momentum $2k_F$, are energetically favoured (see Section 6.3 for more details). We can now understand a mechanism for the occurrence of bit-flip errors. The excitations generated at a moving wall can travel across the wire, and tunnel through non-topological regions in the wire, carrying information between different MBS. The resulting interaction between MBS can, in principle, induce bit-flip errors in the topological qubit. This mechanism is illustrated schematically in Figure 6.9. It is important to note that, in order for the MBS to interact with the incoming density wave packet, one of the walls on the other side of the system must also be in motion.
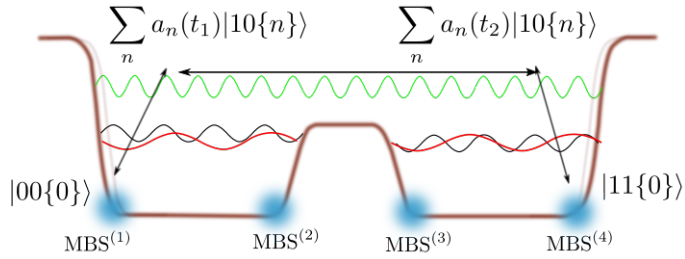
130

Figure 6.9: Schematic showing how excitations originating at the outer walls can dynamically evolve through the system and cause a bit-flip error $|\bar{0}\rangle \leftrightarrow |\bar{1}\rangle$).

If this is not the case, the density wave packet will not be able to dissipate at the wall: it will simply be reflected or transmitted without any chance for the excitation to decay back into the degenerate ground state. This is verified numerically in Figure 6.8(b), where we show the bit-flip error P_{bit} due to the oscillation of boundary walls (the walls that are moving are indicated in curly brackets in the legend). We see that there is no bit-flip error if a single wall is moved and all other walls remain static. However, if two walls are moved, bit-flip errors P_{bit} appear abruptly after some delay. The times at which the bit-flip errors begin to appear can be estimated as the time taken for the propagating wave to reach the other moving wall, i.e., as $t \approx |x_{\text{wall}}^{(i)} - x_{\text{wall}}^{(j)}|/v_F$ where $|x_{\text{wall}}^{(i)} - x_{\text{wall}}^{(j)}|$ is the distance between the two moving walls. This provides strong evidence that the stray excitations propagating along the wire are responsible for the measured bit-flip error.

6.4.2 Disorder induced protection

In this section we will discuss one possible minimization scheme for this problem, utilising Anderson localization (11). The central result of Section 6.4.1 is that bit-flip error can occur in a two-wire setup if there is a process whereby a quasi-particle is excited in one wire, tunnels through the barrier to the other wire, and then decays back to the ground state manifold. See Figure 6.9 (a) for a visual explanation. In order to avoid such a process, one straightforward approach would be to increase the barrier between the wires to prevent inter-wire tunnelling. However, within the schemes to manipulate quantum information using wire networks, see for example Ref. (8), one often needs to bring neighbouring Majorana modes together, a process which would render the barrier more transparent and which would potentially also excite more propagating quasi-particles. In this section, we show that another solution to prevent quasi-particle propagation is to introduce some disorder into the non-trivial topological phases of the wires themselves. Naively, we might introduce disorder throughout the wire. However, there are downsides to doing this. Firstly, in static scenarios, disorder decreases the gap between the ground state and the bulk excitation spectrum, increasing the bound-state decay length (32; 62; 170). This results in a topological space that is less resilient to qubit-loss. Moreover, it has been

shown (95), that moving the confining potential over a disordered region results in a dramatically lower critical velocity, thus severely hampering the rate at which gates can be mechanically performed.
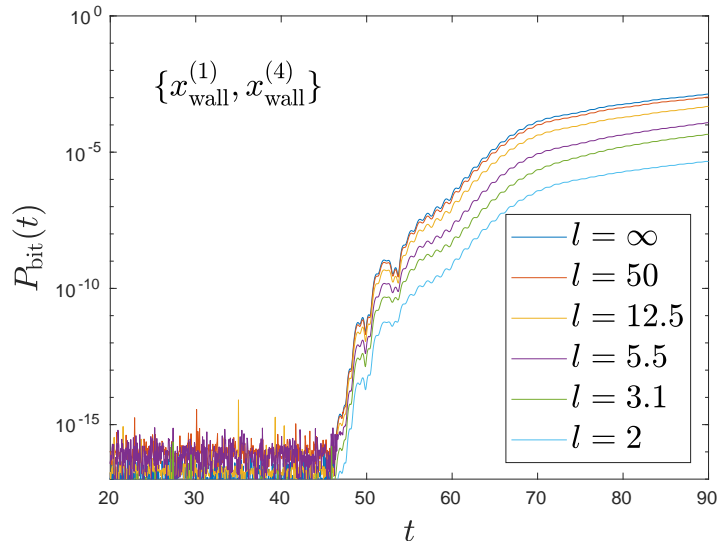

Figure 6.10: Bit-flip error is suppressed by adding disorder in the middle of the left-hand wire. Here, the disordered region is of length ~ 40, and a shorter localisation length l corresponds to increased disorder. We use $v_{\max}/v_{\mathrm{crit}} = 0.75$, the middle barrier height is $\mu_{\mathrm{barrier}} = -2.5$, $\sigma = 2$ and the data is averaged over 20 disorder realizations. [Other parameters used for the figure: $m = 0.5$, $a = 0.5$, $\Delta = 0.4$, $L = 200$, and $\mu = 1.0$ (in the topological region).]

An effective compromise is to deliberately disorder only the central wire regions. This allows for an effective critical velocity of the wire ends that is equal to the p-wave order parameter Δ while also providing a region where bulk excitations are prevented from propagating, reducing the probability that the excitations originating at one wall can tunnel to another wire. This approach still allows for low barrier transparency and so the original schemes (8) for braiding and rotating Majorana pairs can be performed as usual. In Figure 6.10 we present the results of our numerical simulations, where disorder has been introduced in the central regions of both wires. As earlier, we simulate a scenario where there is an oscillation of two walls $x_{\mathrm{wall}}^{(1)}$ and $x_{\mathrm{wall}}^{(4)}$ which are associated with two different non-trivial topological phases. The figure shows the decrease in the probability of bit-flip error as we decrease the localization length l in the disordered region. This indicates that as the disorder is increased, the wave associated with excitations accrued at the boundaries cannot propagate through the wire, and hence the junction, to induce a bit-flip error.

6.5 Summary

In this chapter we discussed our results on error processes in a qubit constructed using Majorana bound states in a p-wave superconductor architecture. This is one of the most well-studied models in topological physics, as it may be used as a qubit for a topological quantum computer. We reviewed the foundational concepts of MBS in the context of a p-wave superconductor in Chapter 5. The topological qubit is constructed using MBS, which are bound to the interface between topologically non-trivial and topologically trivial domains. See Section 5.3 and Section 5.5 for details. In Section 5.6 we discussed how the gates for the quantum computer can be implemented by exchanging the MBS at a junction, following (8). However, in order for this schema to be practical, the gates must be implementable in a finite time. This is a non-adiabatic dynamical evolution. These two situations merit an investigation into the stability of a p-wave superconductor under non-adiabatic evolution.

In particular, we studied the dynamical evolution of a topological qubit that consists of two p-wave superconducting wires separated by a non-topological junction. We studied two regimes of possibly non-adiabatic perturbations to the system: periodic driving in the boundary potentials and shuttling of the Majorana bound states. In Section 6.2.1, we explained how to implement dynamical evolution and we defined the error processes we studied: qubit loss and bit-flip error.

In Section 6.3, we outlined one feature which plays a recurring role in our analysis: a critical velocity of movement, beyond which the protection of the qubit is lost. It has been proposed, and we observed, that this critical velocity equals the superconducting order parameter: $v_{\mathrm{crit}} = \Delta$. In Section 6.3.1 we focused on the regime of periodic driving of the boundary potential. We summarised our results in Figure 6.3. Notably, we found if the velocity of the driving is above v_{crit}, the qubit is more susceptible to qubit loss. We also observed that for $v < v_{\mathrm{crit}}$, the loss is relatively insensitive to the frequency of the wall oscillation. However we did observe that for higher values of Δ, which increases the energy gap, i.e. $E_{\mathrm{gap}} = \Delta k_F$, the qubit can be more susceptible to loss. This is somewhat surprising, as intuitively one would assume that increasing the energy gap always increases the protection of the qubit. However, our results indicate the rate of qubit loss increases.

In Section 6.3.2, we focused on the second regime of dynamical evolution, namely the deliberate shuttling of the MBS. As discussed, in order to implement braiding of MBS, it is crucial to understand what effect this has on the qubit. We observed the aforementioned dramatic change in behaviour depending on whether the qubit is shuttled faster than v_{crit}. It was previously proposed that moving both domain walls of a topological phase would result in less qubit loss than moving one wall. However, we found that moving both domain walls resulted in approximately twice the qubit loss. We display this in Figure 6.4.

In Section 6.4.1 we studied bit flip errors that arise due to excitations tunnelling from one non-topological phase through a barrier into the second topological phase. We studied this in the regime of periodic driving of the domain wall. In Figure 6.8(a) we plot the time evolution of a density wave of excitations produced by the driving of $x_{\mathrm{wall}^{(1)}}$. Most of the excitations remain in one topological phase oscillating between the two domain walls. However, when the excitations tunnel through the barrier they interact with the MBS in the second topological phase and induce a bit flip. We can attribute this process to the excitations by examining Figure 6.8(b) and estimating the time it takes for the excitations to traverse the wire, which is given by $t \approx |x_{\mathrm{wall}}^{(i)} - x_{\mathrm{wall}}^{(j)}|/v_F$. In Section 6.3, we outlined why the excitations travel with group velocity peaked around v_F. Notably, when only one wall in the system is oscillating the error process we just outlined does not occur. In Figure 6.8(b) we can see that P_{bit} only increases when more than one wall is dynamically evolving. Therefore, this error process only occurs if there is dynamical evolution of walls belonging to both of the topological phases. Finally, in Section 6.4.2 we outlined one method to reduce the error process we discussed in Section 6.4.1. Introducing disorder into central regions of the topological phases reduces the propagation of the density wave via localisation, therefore reducing the possibility for this error channel to occur.

Chapter 7

Topological lattice models

7.1 Introduction

In this chapter we will review the toric code introduced in (102). This paper proposed that anyonic excitations could be utilised to implement quantum computation in a fault-tolerant manner. We will show that the code space is identified with states which are invariant, i.e. stabilised under the action of two operators, hence this is an example of a stabiliser code (38). This model is essentially discrete gauge theory, based on a finite group G, where gauge invariance is encoded through an energy penalty for gauge violations, so that the ground states are gauge invariant. Excited states can have electric charges, in which case they transform non-trivially under gauge transformations. Detailed discussions of discrete gauge theories can be found in (61; 149; 171).

The toric code model can almost be considered the canonical example of topological order, in that many of the quintessential features of topological physics appear. The model exhibits ground state degeneracy, i.e. when defined on a surface of genus g, there are 4^g ground states. These states can be used to encode qubits for topological quantum computation and are described by a Turaev-Viro TQFT (16; 103). The excitations exhibit anyonic exchange statistics and can be used to enact quantum gates. In recent years there has been further interest in these models with the advent of quantum simulators (109; 139). In fact, there have recently been experimental measurements of anyonic braiding statistics in systems hosting the toric code ground state (153; 162).

On the mathematical side, these models have many interesting features. The distinct types of excitations are labelled by irreducible representations of $D(G)$, the Drinfeld double of the gauge symmetry G (61). We have discussed the abstract anyon model in Section 2.6.1. This chapter can then be viewed as a lattice realisation of that abstract model. There are many expositions of the toric code, e.g. (54; 140; 159), for further details. This chapter will lay the foundations for Chapter 8, where we discuss a toric code model constructed from Hopf algebra gauge theory.

7.2 Toric code

The toric code introduced in (102), is an exactly solvable lattice model, which can be understood as a gauge theory with discrete group gauge symmetry, G on a discrete spatial geometry. We will fix to the simplest situation where $G = \mathbb{Z}_2$.

Let Γ be a square lattice with k plaquettes in each direction, see Figure 7.1. We denote by E the set of edges, V the set of vertices and F the set of plaquettes. Associated to Γ is a dual graph, $\bar{\Gamma}$. The construction of $\bar{\Gamma}$ is given by replacing plaquettes with vertices and vertices with plaquettes, as indicated in Figure 7.1 with dashed lines. This serves as a discrete model of spatial surface without boundary. In fact, we will specifically impose periodic boundary conditions in both directions, making Γ a cellulation for a torus. We choose this model of space since our focus is on the ground state degeneracy and the anyon excitations in the model, however, the model can also be defined on manifolds with boundary (29; 43).

To each edge, e, we assign a qubit, denoted $\mathcal{H}_e \simeq \mathbb{C}^2$. The total Hilbert space of the model is defined by taking the tensor product of each of the Hilbert spaces on the edges of the graph

$$\mathcal{H}_{tot} = \bigotimes_{e \in E} \mathcal{H}_e. \tag{7.1}$$

On a $k \times k$ lattice this implies there are $n = 2k^2$ qubits. So the basis of $\mathcal{H}_{tot}$ contains all possible linear combinations of spin orientations on the graph. In the language of discrete gauge theory, the qubits on each edge are called link variables or a $\mathbb{Z}_2$ valued gauge potential. A full specification of the qubits over the entire graph is then considered a gauge configuration (171). We denote the Pauli operators as:

$$X = \begin{pmatrix} 0 & 1 \\ 1 & 0 \end{pmatrix}, \qquad Z = \begin{pmatrix} 1 & 0 \\ 0 & -1 \end{pmatrix}, \qquad Y = iXZ = \begin{pmatrix} 0 & -i \\ i & 0 \end{pmatrix}. \tag{7.2}$$
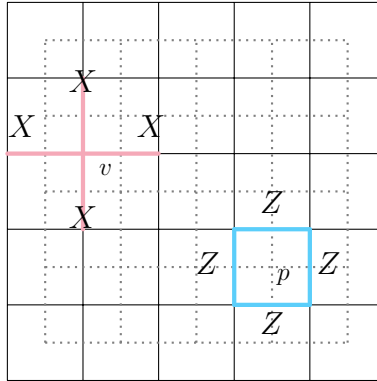

Figure 7.1: We display the graph Γ and the associated dual graph $\bar{\Gamma}$, which we indicate with dashed lines. We indicate the action of the vertex/plaquette operator by pink/blue coloured edges. We can see that the action of a plaquette operator on Γ can equivalently be viewed as a vertex operator on the dual graph.

To define the Hamiltonian we first introduce local four-body operators on the lattice.

Given $v \in V$, we define the vertex operator

$$A_v = \bigotimes_{e \in \text{star } (v)} X_e = X_{e_1} \otimes X_{e_2} \otimes X_{e_3} \otimes X_{e_4}, \qquad (7.3)$$

where star(v) indicates the edges incident to a vertex v. Given $p \in F$, we define the plaquette operator

$$B_p = \bigotimes_{e \in \partial p} Z_e = Z_{e_1} \otimes Z_{e_2} \otimes Z_{e_3} \otimes Z_{e_4} \qquad (7.4)$$

where ∂p indicates the boundary of the plaquette p. We display the action of these operators in Figure 7.1. Both the plaquette and vertex operators act as the identity operator on all other edges. Since they are constructed from Pauli operators, they are Hermitian and have eigenvalues ± 1. We could also choose to represent A_v by σ^x and B_p by σ^z; both of these choices have their own benefits. For most of the chapter, we will use the basis where B_p is diagonal, as here the connection with gauge theory is clearest. Now we will discuss the action of the local operators on the Hilbert space. We can draw again on the analogy with gauge theory.

The A_v operator implements gauge transformations since it maps from one gauge configuration to another, by flipping the orientation of the spins on the edges incident to a vertex. We note that this preserves whether there is an odd or even number of spins around a vertex oriented up or down, this is also known as the parity of the spins. The plaquette operator measures the parity of the qubits around a plaquette. In particular for $|\xi\rangle \in \mathcal{H}_{tot}$, $B_p|\xi\rangle = 1|\xi\rangle$ if $0/2/4$ of the spins are oriented up and $B_p|\xi\rangle = -1|\xi\rangle$ otherwise. This can be interpreted as measuring a $\mathbb{Z}_2$ valued flux through a plaquette.

The vertex and plaquette operators satisfy the following algebra structure (102). Let $v_1, v_2 \in V$ and $p_1, p_2 \in F$, then the vertex and plaquette operators satisfy the following relations,

$$A_{v_1} A_{v_2} = A_{v_2} A_{v_1}, \qquad B_{p_1} B_{p_2} = B_{p_2} B_{p_1}, \qquad A_v^2 = B_p^2 = \mathbb{I},$$
$$A_v B_p = B_p A_v. \qquad (7.5)$$

Firstly we note that the vertex/plaquette operators acting on separate parts of the graph commute. Furthermore, since they are both tensor products of Pauli matrices they each square to the identity under composition. If we consider acting A_{v_1} on a vertex v_1 and then acting with another vertex operator on an adjacent vertex, v_2, where $v_2 = v_1 + \hat{e}_i$, where $\hat{e}_i$, labels an edge connecting v_1 to v_2 via edge, then on that edge we would find $X_e^2 = \mathbb{I}$, hence $[A_{v_1}, A_{v_2}] = 0$, similarly for the plaquette operator.

The second line of Equation (7.5) states that the action of a plaquette operator and a vertex operator also commute, and this is true even when the plaquette p contains the vertex v. This follows from the fact that each vertex and plaquette operator if adjacent, they overlap on two edges. So, on each of the edges on which they overlap, the commutation acquires a minus sign, which cancels overall. This algebraic structure is known as a quantum double and hence the toric code is also called a quantum double model, often denoted $D(\mathbb{Z}_2)$.
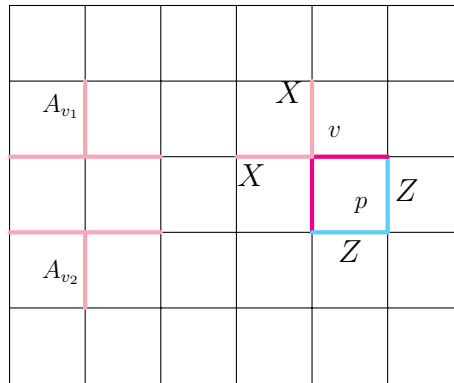

Figure 7.2: The action of A_{v_2} after the action of A_{v_1} cancels the X_e on the adjoining edge. We also show how the action of a vertex operator at v commutes with the plaquette operator at p, each overlapping edge, contributes a -1 sign, so they cancel overall. We indicate the edges where this occurs with magenta.

The vertex and plaquette operators are not all independent. In fact, they satisfy the following constraint equations

$$\prod_v A_v = \mathbb{I}, \qquad \prod_p B_p = \mathbb{I}, \tag{7.6}$$

on a closed surface, i.e. a manifold without boundary such as a torus. One way to understand this is to realise that every edge is associated with two vertex operators since each edge joins two vertices. Therefore, for a given state, i.e. configuration of the lattice spins, as we check the eigenvalues of the vertex operators on the lattice we will find we don't need to specify the eigenvalue on every edge. In fact, exactly one vertex operator will have already been specified. Similarly for the plaquette operator. This gives us $m = 2k^2 - 2$ independent operators. Now that we have analysed the operators constituting the Hamiltonian we can explicitly write it down,

$$H = -\sum_v A_v - \sum_p B_p \;, \tag{7.7}$$

where the summation is taken over all vertices $v \in V$ and $p \in F$. Since this Hamiltonian consists of mutually commuting Hermitian operators it can be solved exactly.

The ground state is defined by simultaneously satisfying all of the stabilizer conditions, which for a state $|\xi\rangle \in \mathcal{H}_{tot}$ are written as

$$A_v|\xi\rangle = |\xi\rangle, \tag{7.8}$$

$$B_p|\xi\rangle = |\xi\rangle. \tag{7.9}$$

These equations can be interpreted in discrete gauge theory in the following sense. States satisfying Equation (7.8) are said to be gauge invariant, i.e. they are invariant under the action of A_v. States satisfying Equation (7.9) are said to correspond to a gauge configuration which is flat (124; 171). By this, we mean acting with the plaquette operator on p can be interpreted as computing the holonomy around p, so if the gauge configuration satisfies (7.9), then the holonomy around p is trivial.

Let's consider states satisfying Equation (7.8) or equivalently the minimum energy states with respect to the vertex operator. The eigenvalue of B_p is -1 if there is an odd number of spins oriented down in a plaquette. To minimize the energy we must have either all spins oriented up, or states containing only an even number of spins down. Since the action of the A_v operator flips the spins at a vertex, in order to satisfy Equation(7.9), we must take all superpositions of loops. Combining both of these requirements leads to the ground state of the model being a deconfined loop gas, consisting of all superpositions of closed loops (102; 171).

The protected space or ground state manifold is defined as

$$|GS\rangle = \{\, |\xi\rangle \in \mathcal{H}_{tot} : A_v|\xi\rangle = |\xi\rangle, \; B_p|\xi\rangle = |\xi\rangle, \; \forall v \in V, \; p \in F\}. \tag{7.10}$$

The code space is identified with the space of states satisfying these constraints (102). In this sense we say the code is identified with states which are stabilised, i.e. invariant under the action of the A_v and B_p operators (38).

7.3   Excitations

Now that we have defined the Hamiltonian and defined the ground state we can analyse the excitations. This will lead us to the formalism of string operators[1]. The excitations will be denoted; e, m and ψ, which are electric, magnetic and dyonic respectively, we will discuss each of these in turn. In constructing the excitations we will find the fusion rules and R-symbols we stated in Section 2.6.1.

We suppose the system is initially in the ground state and we denote it by $|\xi\rangle$. In anyon models this would correspond to the vacuum and is denoted by 1. The excitations are defined by violating one or both of the ground state defining constraint equations (7.8) and (7.9). To be concrete we construct excitations by applying a local operator from Equation (7.2) on an edge of Γ.

---

[1]If instead of $\mathbb{Z}_2$ we chose a non-Abelian group, then it would be ribbon operators.
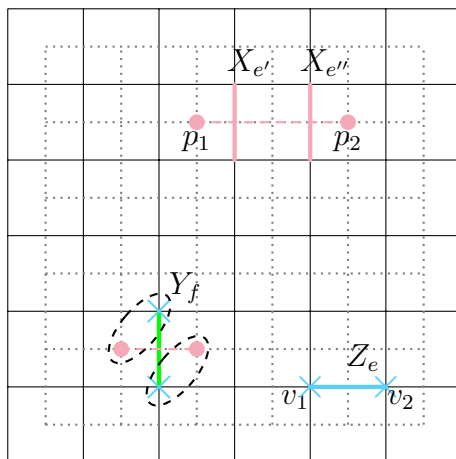
Figure 7.3: The action of local operators creates excitations. We associate the excitations at p_1 and p_2 with m particles created by the action of $X_{e'} X_{e''}$. We associate the vertex excitations at v_1 and v_2 with e particles created by the action of Z_e. The pair of dyonic excitations ψ, around an edge f are created by a Y_f operator. Each ψ excitation consists of an e and m excitation at the adjacent vertices and plaquettes respectively.

Then by considering the vertex and plaquette operators which act on that edge we will find non-trivial commutation relations and we identify the excitations accordingly. One of the implications of Equation (7.6), is that it is impossible to create a single excitation. In fact, the action of a local operator on an edge will always violate at least two vertex or plaquette operators.

Electric excitations

Consider the action of Z_e on the qubit of an edge $e \in E$. Since the plaquette operator consists of Z on each edge of the plaqutte, this action commutes with all of the plaquette operators. However, Z_e anticommutes with the vertex operators at v_1 and v_2. Thus, we identify the state $Z_e|\xi\rangle$ with the presence of electric excitations at the associated vertices. We display an example of this in Figure 7.3. Since we have violated two of the stabilizer conditions, the energy of this state is given by

$$E_e = E_{GS} + 2 \ . \tag{7.11}$$

Note, if we act again on e with Z_e, since $(Z)^2 = \mathbb{I}$, this will annihilate the electric excitation. This is encoded by the following fusion rule,

$$e \times e = 1. \tag{7.12}$$

We can see that the fusion rules of the e particles are essentially given by $\mathbb{Z}_2$. Furthermore, if we acted with Z on the edge to the left of e, then this would move the excitation at v_1 to the vertex further to the left, more generally, we could consider some string of Z operators; $S(Z)$ to move an e particle around the lattice.

Magnetic excitations

Consider the action of $X_{e'}$ on the qubit on an edge, e'. This operator will commute with the vertex operators at the edge ends of e' and anticommute with the two plaquette operators containing the edge e'. This state, $X_{e;}|\xi\rangle$ is identified with the presence of magnetic excitations, m, at the neighbouring plaquettes. See Figure 7.3 for a visual example. If we again act with X on the flipped edges we find that the excitation is annihilated, which is encoded in the following fusion rule

$$m \times m = 1 . \tag{7.13}$$

Since there are two stabilizer conditions violated, the energy of the state $X|\xi\rangle$ is given by

$$E_m = E_{GS} + 2 . \tag{7.14}$$

Since the presence of an m excitation is detected by the B_p operators, they can be interpreted as magnetic fluxes through a plaquette. We can also note that the plaquette excitations in Figure 7.3 can be viewed as vertex excitations in the dual graph, $\bar{\Gamma}$. The magnetic excitations can be separated by acting with X on a neighbouring edge, e'', as displayed in Figure 7.3. Similarly to the moving an e excitation around the lattice using, $S(Z)$, a string of Z operators, we can use, $S(X)$, a string of X operators to move m excitations around the lattice.

Dyonic excitations

The final excitation to consider is the dyon, which is given by acting with Y_f on an edge f. This operator will then anticommute with the vertex operators at the ends of the edge, but also with the plaquette operators whose boundary involves the edge. Therefore, this excitation can be considered a combination of an electric and magnetic excitation. This is expressed by the following fusion rule

$$e \times m = m \times e = \psi . \tag{7.15}$$

We indicate a dyon in Figure 7.3 by a dashed ellipse. We note, similar to the magnetic excitations and the electric excitations, that if we act again with Y on an edge hosting adjacent dyonic excitations, we will annihilate the excitations. Hence we have the following fusion rule

$$\psi \times \psi = 1 . \tag{7.16}$$

Since this excitation violates two vertex operators and two plaquette operators we can see the energy of $Y|\xi\rangle$ is given by

$$E_\psi = E_{GS} + 4 \ . \tag{7.17}$$

We can also observe further fusion processes between the excitations. If after acting with Y we act with either Z/X, this will then annihilate the corresponding electric/magnetic part of the dyon leaving only the magnetic/electric excitation. This is expressed by the following fusion rules

$$e \times \psi = m, \qquad m \times \psi = e \ . \tag{7.18}$$

In a more general sense, we can view the excitations as a local representation of $D(\mathbb{Z}_2)$. This concludes our discussion of the fusion rules of the excitations, next we will move on to the braiding of excitations.

7.4 Braiding in toric code models

In this section we will discuss the braiding of excitations in the toric code. As we discussed in the previous section, excitations are created in the toric code by the action of an operator, i.e. the action of X_e creates two m-excitations on the adjacent plaquettes. We also mentioned that the action of the same local operators on adjacent edges can be used to transport excitations around the lattice. Therefore, in order to calculate the braiding of excitations we use strings of operators to translate one excitation around another, returning the system to the initial configuration. We then consider the commutation between the operators implementing the exchange and the operators that created the excitations. This commutation will show us the effect that the braiding has on the states of the system. We shall denote the phase resulting from the exchange of an a excitation with a b excitation, which fuse to an excitation c by R_c^{ab}. The phases we will find in this section match the R-symbols we discussed in Chapter 2. Although we have imposed periodic boundaries, to calculate the braiding we focus on a local patch of Γ. This is essentially exchanging the excitations on the plane, hence the exchanges generate planar braiding statistics.

We begin with the braiding of an e particle with an e particle. We display this in Figure 7.4(a). Firstly we create four electric excitations, using two strings of Z operators. Then we use a string of Z operators, denoted $S(Z)$ to transport one e particle around another and return to the initial configuration. There will be one place where $S(Z)$ overlaps with the string of Z operators creating the other electric excitations. However, since both are strings of Z operators, these operators commute. Hence this corresponds to bosonic exchange statistics.

The braiding of an m particle with an m particle is similar. Here instead we use a string of X operators and again the braiding statistics will be bosonic. We display an example of this in Figure 7.4(b). The operator that translates an m particle around another is given by a string of σ^x. This is encoded by the following R-symbols
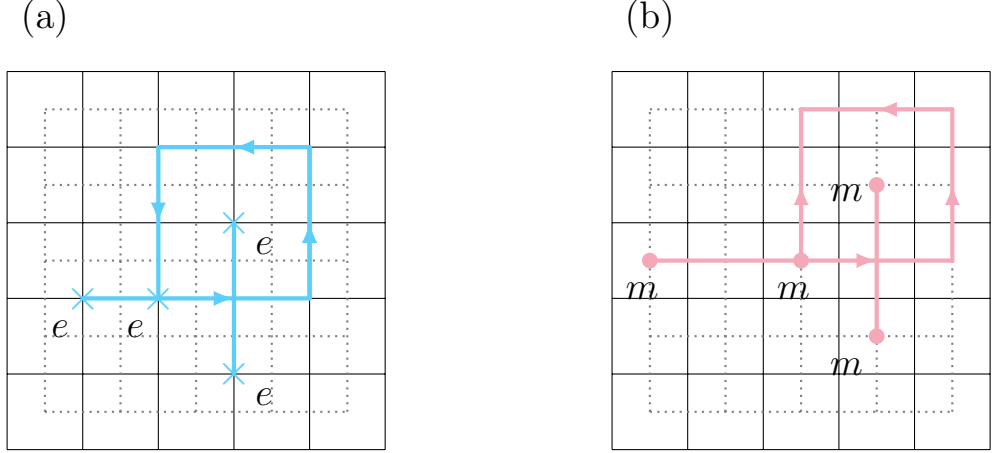
$$R_1^{e,e} = R_1^{m,m} = 1. \tag{7.19}$$

(a) (b)

Figure 7.4: In Figure (a) we display the braiding of an e particle around an e particle via a string of Z operators. In Figure (b) we display the braiding of an m particle around an m particle via a string of X operators.

Now we consider the braiding of an e particle with an m particle. In Figure 7.5 we display an example of this. We note that since the e and m particles are distinguishable from each other, we must exchange the particles twice in order to find the effect on the wave function. Here we use a string operator, $S(Z)$ to transport an e particle around an m particle and return to the initial configuration. The $S(Z)$ and the X operator creating the m particles, commute everywhere except on one edge which we colour magenta, wheras on this edge the $S(Z)$ string and the X string anticommute. Therefore we have

$$R_\psi^{e,m} R_\psi^{m,e} = -1. \tag{7.20}$$

This states that the wave function of the system acquires a -1 sign under two exchanges. We can contrast this with bosons or fermions. A wave function governing a system of either particle, under two exchanges returns to itself. Hence, the e and m particles exhibit anyonic exchange statistics. One can formally *define* a value for the exchange of the e and the m particles. For example, one can assign $R_\psi^{e,m} = R_\psi^{m,e} = \pm i$, and then the particles are called relatively semionic (159).

Now we consider the braiding of an e particle with a ψ particle. Since the dyon is a combination of an e and an m particle, braiding e around ψ corresponds to braiding e around the constituents of the dyon. We can express this in terms of the
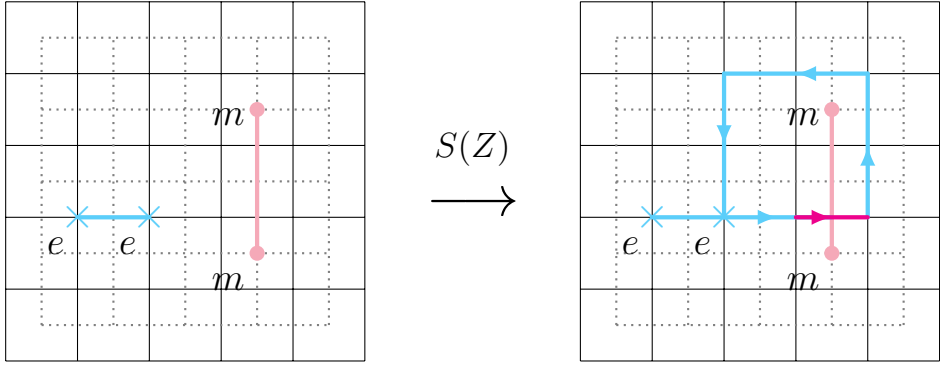
Figure 7.5: The string operator $S(Z)$, which translates the e particle around the m particle. On the magenta edge, we indicate the anticommutation between the X string, creating the magnetic excitations and the $S(Z)$ string. We use arrows on the $S(Z)$ operator to show the path taken by the e particle around the m particle.

R-symbols as

$$R_m^{e,\psi} = R_1^{e,e} R_\psi^{e,m}. \tag{7.21}$$

From this, we can conclude

$$R_m^{e,\psi} = R_\psi^{e,m}. \tag{7.22}$$

This is in the same vein as we discussed braiding commuting with fusion in Chapter 2, in particular Figure 2.8. Since $\psi = e \times m$ and we want to braid e with ψ, we can consider the individual braids in the space-time diagram. In fact, we can see that this is exactly what we would find by using the hexagon equation (2.35), with all the F-symbols equal to 1. We can use similar reasoning for the braiding of an m particle around ψ, to find

$$R_e^{m,\psi} = R_\psi^{m,e}. \tag{7.23}$$

There is one final braiding to consider: the braiding of a dyon with a dyon. As we discussed the dyons are created by the action of Y on an edge. Since the dyon is a combination of an e particle and an m particle, when exchanging two dyons we must be careful not to also rotate the dyon, as this will introduce contributions of the topological spin.
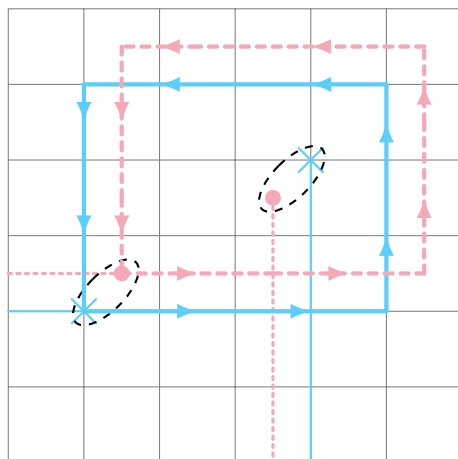
Figure 7.6: In this figure we display the string operators that implement the braiding of a dyon with a dyon. We omit the dual graph $\bar{\Gamma}$ and the creation pair for each dyon for the sake of clarity. We note there are four places where a σ^z string and a σ^x string intersect.

In Figure 7.6 we can see there are four places where a Z string intersects with a X string, so in total the monodromy is

$$(R_1^{\psi,\psi})^2 = +1, \tag{7.24}$$

from here we can see that the effect of a single exchange would be

$$R_1^{\psi,\psi} = -1, \tag{7.25}$$

so their exchange statistics are fermionic. This is an interesting feature of the model in the following sense. The degrees of freedom are qubits living on the edges of Γ. However, the dyons are collective degrees of freedom which behave as a fermion, i.e. an emergent fermion.

We note that the phase $R_1^{\psi,\psi} = -1$ due to the exchange of two dyons, is different from the phase $R_\psi^{e,m} R_\psi^{m,e} = -1$ due to the *braid* of an e particle with an m particle. In the former, we have exchanged two identical particles, hence fermionic exchange statistics, whereas in the latter we have braided two distinguishable particles and found the resulting phase factor was not trivial, hence, anyonic exchange statistics.

7.5 Topological degeneracy

Now that we have defined the ground state and the excitations, we can discuss the topological degeneracy of the toric code (99). We will show that the ground state degeneracy is related to the non-contractable cycles of the torus. This is one of the key features of the model and the crucial link between the anyonic excitations and the topology of the torus.

We start with $|\xi\rangle \in |GS\rangle$, a configuration in the ground state. We then create a pair of electric excitations by a string of Z operators. We then separate these excitations using Z operators so that they go around the entire torus and then annihilate. We denote the loop operators enacting such a configuration as

$$\mathcal{O}_{z_1} = \prod_{e \in C_{z_1}} Z_e, \qquad \mathcal{O}_{z_2} = \prod_{e \in C_{z_2}} Z_e, \qquad (7.26)$$

where we denote the closed 1-cycles on Γ by C_{z_1} and C_{z_2}.

After the action of either of these loop operators, we will be left with a closed, non-contractable loop of flipped spins. However, we can see that this state still satisfies the stabilizer conditions, as at each vertex along the non-contractable cycles there are exactly two incident spins flipped. We can also notice that if we act with a plaquette operator adjacent to the non-contractable cycle, this will deform the loop. However, this will not increase the energy of the configuration. Therefore, the energy of this configuration is exactly equal to the energy of the ground state.

We could also define this operation in the dual lattice with

$$\mathcal{O}_{x_1} = \prod_{\bar{e} \in C_{x_1}} X_{\bar{e}}, \qquad \mathcal{O}_{x_2} = \prod_{\bar{e} \in C_{x_2}} X_{\bar{e}}, \qquad (7.27)$$

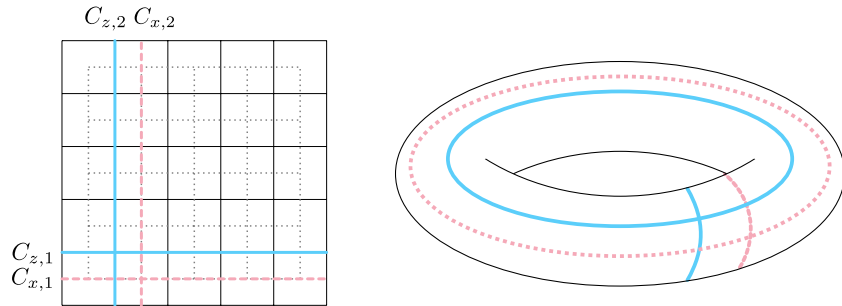We depict the action of the loop operators in Figure 7.7.

Figure 7.7: We show the non-contractable cycles on a torus. We label each cycle by the assignment of Pauli operators. We use blue lines to depict flipped spins in Γ. We could perform the same construction in $\bar{\Gamma}$, and indicate this by the pink dashed lines.

We can realise the obvious connection with homology as discussed in (102). On a two-dimensional lattice, we have 0-chains, 1-chains and 2-chains corresponding to vertices, edges and plaquettes respectively. The collection of each of these chains can be furnished with a vector space structure and is denoted $\mathcal{C}_i$, where $i = 0, 1, 2$. For example, an arbitrary element of C_1 is a collection of edges in Γ. The boundary map, d, is used to move between the chains, i.e. $d_i : \mathcal{C}_i \to \mathcal{C}_{i-1}$. There are two notable two subspaces within $\mathcal{C}_1$. The space of 1-cycles, which are 1-chains which have no boundary, i.e. $\mathcal{Z}_1 = \ker(d_1)$, and $\mathcal{B}_1 = \mathrm{Im}(d_2)$, the space of 1-chains which

are the boundary of a 2-chain. We note that $\mathcal{B}_1 \subset \mathcal{Z}_1$ since $\text{Im}(d_2) \subset \text{ker}(d_1)$. Then the first homology group is defined as

$$H_1 = \mathcal{Z}_1/\mathcal{B}_1. \tag{7.28}$$

The non-trivial elements of H_1 are 1-cycles, which are not the boundary of a 2-chain. We can readily see that the non-contractable loops of the torus are elements of H_1, since these are 1-chains which have no boundary vertices. We also note that contractable loops will be elements of $\mathcal{B}_1$, since under the action of the boundary operator, these loops will get mapped to the set of vertices that constitute the loop. We can physically interpret this. Any contractable loop can be removed by repeated action of the vertex operator and as such will not generate an independent ground state. In physics parlance, this model is sometimes called a deconfined loop gas. Since the degrees of freedom in our model are qubits, the coefficients of the homology group will be $\mathbb{Z}_2$. Therefore, the ground states of the model are generated by $H_1(T^2, \mathbb{Z}_2)$. More generally, if we consider a toric code model constructed over an Abelian group G, then the ground states of the model would be generated by $H_1(T^2, G)$. Further details on homology can be found in (89) and in the particular context of the Kitaev model see e.g. (31; 54).

Another way we can view the topological degeneracy is by considering the Euler characteristic of the graph, following (105; 159). For a genus g surface modelled as a discrete graph, the Euler characteristic is given by

$$|V| - |E| + |F| = 2 - 2g. \tag{7.29}$$

Since each edge corresponds to a two-level qubit, we know $\dim(\mathcal{H}_{tot}) = 2^{|E|}$. Equation (7.6) implies there are only $|V| - 1$ independent constraints on the vertex operators and $|F| - 1$ independent constraints on the plaquette operators. So, we subtract these from the total number of states and the dimension of the ground state manifold is given by $2^{E-V-F+2} = 2^{2g}$. If instead of $\mathbb{Z}_2$, we chose $\mathbb{Z}_N$, as we will in Chapter 8, then this analysis still holds but instead, we would find the dimension of the ground state manifold to be N^{2g}.

If we instead choose an infinite plane, then there would be no non-contractable cycles, all A_v and B_p operators would be independent and there would be a unique ground state. Hence, we can see the dimension of the ground state manifold depends on the topology of the space upon which it is placed.

Therefore, there is a four-fold degenerate ground state manifold on a torus (102). We can tabulate the states in the ground state manifold terms of the loop operators

$$|\xi_1\rangle, \qquad |\xi_2\rangle = \mathcal{O}_{z_1}|\xi_1\rangle, \qquad |\xi_3\rangle = \mathcal{O}_{z_2}|\xi_1\rangle, \qquad |\xi_4\rangle = \mathcal{O}_{z_1}\mathcal{O}_{z_2}|\xi_1\rangle. \tag{7.30}$$

These four physical states can then be used to encode two logical qubits for a

topological quantum computer. Now a natural question arises, what about errors? If we were to design a topological quantum computer based on the toric code we must understand how errors are generated and how we can minimize them.

Firstly we note, the non-contractable loops can not be removed by any local operation. As we discussed we can deform the shape of the cycle using the vertex operator but we can not remove it. In this sense, the states in the ground state manifold are protected against local errors. However, it's not hard to imagine a local error occurring and expanding to traverse one of the cycles, thereby changing the state of the system from one state in the ground state manifold to another. So how would we minimize such a process? An error is generated by local violations of the stabilizer conditions, which we identified with the quasiparticle excitations. Hence in order to find error processes in a topological quantum computer modelled on the toric code we are essentially looking for methods to detect and remove excitations. Hence, we need to frequently measure the eigenvalues of B_p and A_v. If we detect a violation, i.e. a negative eigenvalue of one of the operators, we then need to act with the local operator corresponding to the creation of the excitation, and as each of the excitations satisfies $\mathbb{Z}_2$ fusion rules, this will remove the excitation. This concludes our discussion of the $\mathbb{Z}_2$ toric code.

7.6 Quantum double models

In this chapter we focused on the $\mathbb{Z}_2$ toric code. However, the model can be defined over any group algebra, $\mathbb{C}G$ (102). This was developed in several papers see (24; 104) as examples. This is also discussed in (140) and (159).

The toric code is an example of a quantum double model, due to the algebra generated by A_v and B_p having the structure of a quantum double (102). The quantum double, $D(\mathbb{C}G)$ of a group algebra over a finite group G is a quasitriangular, semisimple finite dimensional Hopf algebra given by $D(\mathbb{C}G) = \text{Fun}(\mathbb{C}G)\tilde{\otimes}\mathbb{C}G$. The A_v operators span a subalgebra isomorphic to $\mathbb{C}G$ and the plaquette operators span a subalgebra isomorphic to $\text{Fun}(\mathbb{C}G)$, which are linear functionals on $\mathbb{C}G$. We use $\tilde{\otimes}$ to denote the "twisted" multiplication on the algebra, which on adjacent vertices and plaquettes is given by

$$A_v^g B_p^h = B_p^{g\bar{h}g} A_v^g. \tag{7.31}$$

We can see from this rule that the multiplication of functions is "twisted" by conjugation with the group element assigned to the vertex operator (96).

When G is non-Abelian, many features still carry over, but some aspects become more technical. For example, the particle content of the theory, or irreducible representations of $D(G)$ become more involved. A general particle is given by a tuple $([C_g], \text{Irr}(N_g))$, where $[C_g]$ is a conjugacy class in G with representative element g, and $\text{Irr}(N_g)$, denotes an irreducible representation of the normalizer of $[C_g]$. The

electric charges are the irreducible representations of (N_g), whereas the magentic charges are identified with the conjugacy classes of G.

When we discussed the excitations for $\mathbb{Z}_2$ we studied string operators connecting vertices or plaquettes. In the non-Abelian case, this is generalized to ribbon operators. A ribbon connects two sites, where each site consists of a vertex in Γ and an adjacent plaquette, which can be viewed as a vertex in $\bar{\Gamma}$.

In this situation, it can be more tractable to consider the representation theory of the quantum double to analyse the excitations rather than calculate the ribbon operators (20; 73). We will also use this approach in Section 8.3.3, when we consider the excitations of $D(D_3)$.

On the mathematical side, quantum doubles are also interesting objects in representation theory and more generally in category theory. In fact, toric code models have been generalised beyond group algebras to be defined with gauge symmetry given by any semisimple finite dimensional Hopf $*$-algebra (37; 92; 177). Since each quantum double is a quasitriangular Hopf algebra, the category of representation, $\text{Rep}(D(\mathbb{C}G))$ is a braided tensor category. We gave the abstract definition of a braided tensor category in Section 2.4 and discussed the connection to anyon models in Section 2.5. The monoidal product on the category of representations is given by the coproduct on $D(G)$, and the universal R matrix, $R = \sum_g A_g \otimes B_g$ gives the structure of braiding. The text Quantum Groups by Kassel (96), is a standard reference on this subject. However, the quantum double construction is older and can be attributed to V. Drinfeld, as a means to produce a quasitriangular Hopf algebra from another Hopf algebra which may not be quasitriangular (64; 65).

Previous to (102) there were already existing studies of quantum doubles or Hopf symmetry in discrete gauge theory. See (4; 5; 60; 61; 106) for some notable examples. However, the context was different, as they were not considering topological quantum computation but instead residual discrete gauge symmetry left after symmetry breaking. In recent years, an axiomatic framework of gauge theory defined over a Hopf algebra was given in (124) and the connection between this framework and Kitaev models is presented in (123).

7.7 Summary

We have devoted this chapter to discussing the toric code built from $\mathbb{Z}_2$ local degrees of freedom. Toric code models contain many of the key ingredients of topological physics. For example, anyonic excitations, which are quasiparticles whose exchange statistics can be more general than fermionic or bosonic. Another interesting feature of the model is the degenerate ground states, which *depend* on the topology of the spatial geometry. We also discussed how a quantum computer utilising anyons can be inherently fault-tolerant since the qubit is encoded in the closed cycles of the

torus. For an error to occur, stray excitations must traverse the entire manifold. It was shown in (102) that such a process is exponentially suppressed. Furthermore, since this process starts from the creation of local excitations, it can be detected by local measurements, and hence this error process can be mitigated. In fact, this exact feature led to this model becoming so ubiquitous in topological physics.

This model also provides a microscopic contextualisation of the algebraic theory of anyons discussed in Chapter 2. In particular, we discussed the solution of the hexagon equation corresponding to the Drinfeld double of $\mathbb{Z}_N$ in Section 2.6.1, the case $N = 2$ corresponds to the model we just developed in this chapter. Toric code models provide a microscopic formalism in which to understand and calculate R-symbols, see for instance Figure 7.5.

In Chapter 8, we will construct a toric code model starting from Hopf algebra gauge theory, with a quasitriangular Hopf algebra defined over $\mathbb{CZ}_N$. We will find an essentially equivalent model to the conventional $\mathbb{CZ}_N$- toric code. However, the construction from Hopf algebra gauge theory will lead to a change in the identification of the particle content. This concludes our discussion of the toric code and quantum double models.

Chapter 8

Hopf algebra gauge theory

8.1 Introduction

In this chapter, we will discuss an abstraction of the toric code introduced in Chapter 7, namely Hopf algebra gauge theory. In (124), an axiomatic formulation of a gauge theory with the gauge symmetry given by a quasitriangular semisimple finite dimensional Hopf algebra is introduced. In (123), the equivalence between toric code models based on a Hopf algebra K and Hopf algebra gauge theory based on $D(K)$, the quantum double of K is proven. In particular, an equivalence is established between the topological invariants of both frameworks, i.e. the space of gauge invariant flat connections in Hopf algebra gauge theory is equivalent to the space of protected states in Kitaev models.

In this current work, we shall closely follow the prescription in (124). We will examine the excitations in Hopf algebra gauge theory and the relation to Kitaev toric code models. Our focus will be on taking a simple class of Hopf algebras and calculating the exchange statistics, analogous to Chapter 7. We calculated the analogous quantities in Chapter 2 using category theory. In that framework they were named R-symbols, here we use the notation $\mathcal{R}$-symbols, to avoid confusion with the R-matrix on a quasitriangular Hopf algebra. In particular, our gauge theory will be given by a quasitriangular semisimple Hopf algebra constructed on $\mathbb{C}\mathbb{Z}_N$. However, on this Hopf algebra, one can introduce a non-trivial quasitriangular structure (R matrix). We will show how the choice of R matrix affects the $\mathcal{R}$-symbols in the model. In fact we will show the minimum energy electric excitations behave as if they have flux charges attached to them, this is known as flux attachment.

This chapter is based on (48) in collaboration with Domenico Pellegrino and J. K. Slingerland.

	Lattice gauge theory	Hopf algebra gauge theory
gauge object	group G	Hopf algebra K
connection	G-colouring of graph	K-colouring of graph
collections of connections	G^E	K^E
gauge transformation on connection	G-set	K^V- module structure on K^E
gauge transformation on functions	dual G set	K^V- module algebra structure on K^{*E}

Table 8.1: This table shows how many of the standard ingredients of lattice gauge theory are generalised to Hopf algebra gauge theory. E and V indicate the collection of edges and vertexes of the graph respectively. By K^E (K^V) we denote the tensor product of all of the Hopf algebras associated with each edge (vertex).

8.2 Background

A comprehensive summary of the differences caused by generalising the input gauge object from a group to K, a finite-dimensional semisimple quasitriangular Hopf algebra, can be found in (124) and we report this schematically in Table 8.1.

In this section we shall follow (124), where it is explained how to construct a Hopf algebra gauge theory on a ribbon graph from the description of the gauge theory on smaller, local constituents of the graph, called local vertex neighbourhoods. Firstly a basis for the Hilbert space in discrete group gauge theory is given by assigning group elements to the edges of the graph, often called "colouring" the graph by G. This is the basis we used Chapter 7.2, where we discussed toric code with $G = \mathbb{Z}_2$. The situation is analogous for Hopf algebra gauge theory except now the graph is coloured by elements of the Hopf algebra. As we mentioned in Section 7.6, the underlying graph must be a directed graph. In Hopf algebra gauge theory an additional structure on the graph is required, namely the graph is equipped with a cilia. A ciliated ribbon graph is used as a discrete model for space, this is a directed graph with a cyclic ordering of the edges at each vertex. The edges are enumerated anti-clockwise starting from the cilia, as we display in Figure 8.1a. The cilia are not themselves edges of the graph, but can instead be thought of as a bookkeeping device which keeps track of the ordering of edges at a vertex, so that one can associate an oriented surface with a boundary to a ribbon graph. This is done by replacing edges with ribbons, vertices with disks and glueing ribbons and disks according to the cyclic ordering defined by the cilia.
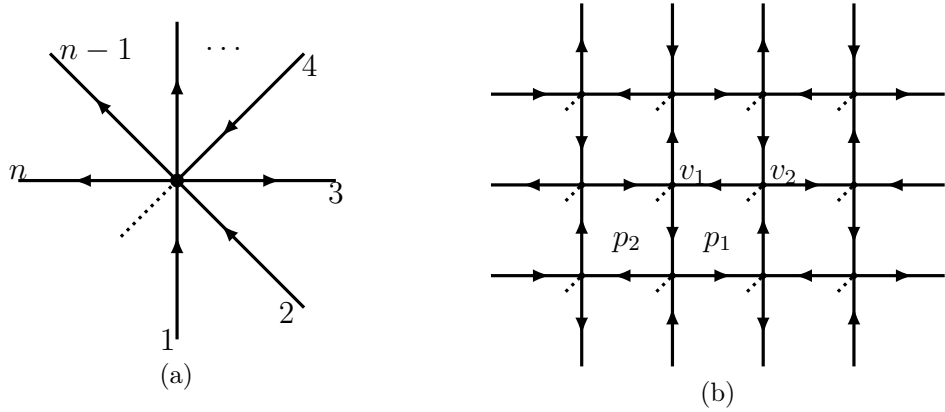
Figure 8.1: In (a) we show an example of a ciliated vertex, the edges are numbered counterclockwise starting from the cilia, which we denote by a dotted line.
In (b) we show a piece of the bulk square lattice built as a ribbon graph. In general, the lattice can be considered to have periodic boundary conditions. Note that with our choice of cilia each of the elementary plaquettes has a single cilium pointing inwards and each vertex has two incoming and two outgoing edges.

We will start with a brief outline of the main properties and definitions of a Hopf algebra that we will use throughout the chapter. Explicit actions for the canonical Hopf algebra structure on a group algebra and for the algebra of functions on a finite group can be found in Appendix E. A Hopf algebra K is an associative unital bialgebra, which consists of two compatible structures, namely an algebra and a coalgebra. The algebra structure is given by the following homomorphisms

$$\mu : K \otimes K \to K, \qquad \eta : \mathbb{C} \to K, \qquad (8.1)$$

which are the product and unit maps respectively. The map η is given by the following:

$$\eta(c) = c \, 1_K \, , \qquad (8.2)$$

where 1_K indicates the identity element of the algebra and c is an element of the field, which we take to be $\mathbb{C}$. The coalgeba structure has the following algebra homomorphisms

$$\Delta : K \to K \otimes K, \qquad \epsilon : K \to \mathbb{C}. \qquad (8.3)$$

The algebra homomorphism Δ is called the coproduct and can be considered as a sort of "reverse" of the product map. This map is used to split an element into two tensored components. The ϵ map is called counit and can be considered as the equivalent of the identity element for the coproduct. The coproduct is the structure used to define the tensor product of two representations, i.e.

$$\pi^1 \otimes \pi^2 : h \to (\pi^1 \otimes \pi^2)(\Delta(h)). \qquad (8.4)$$

This is of particular importance in toric code models as we use this structure to form

multiparticle states. For example, for determining the representation of angular momentum for two particles, the coproduct is given by

$$\Delta(j) = j \otimes 1 + 1 \otimes j .\qquad(8.5)$$

The action of Δ on an arbitrary element $h \in K$ is given by

$$\Delta(h) = \sum_i h_i' \otimes h_i'',\qquad(8.6)$$

which is a linear combination of tensor products of different elements of the algebra. However, it is common to instead use an abbreviated notation known as Sweedler notation, in which the coproduct is written:

$$\Delta(h) = \sum_{(h)} h^{(1)} \otimes h^{(2)} .\qquad(8.7)$$

The summation is often left implicit and we will follow this convention in the following. One further ingredient is necessary for the definition of a Hopf algebra, that is the antipode, $S : K \to K$, which is an algebra anti-homomorphism. This means S acts in the following way:

$$S(ab) = S(b)S(a) .\qquad(8.8)$$

The antipode must satisfy the following compatibility between the algebra and co-lagbera structures condition

$$\mu \circ (S \otimes id) \circ \Delta = m \circ (id \otimes S) \circ \Delta = \eta \circ \epsilon,\qquad(8.9)$$

where $\circ$ is composition. The coproduct and counit satisfy the following compatibility conditions with the antipode:

$$\begin{aligned}\epsilon(h^{(1)})h^{(2)} &= h^{(1)}\epsilon(h^{(2)}) = h,\\ S(h^{(1)})h^{(2)} &= h^{(1)}S(h^{(2)}) = \epsilon(h)1 .\end{aligned}\qquad(8.10)$$

There are then consistency relations amongst these maps which define the bialgebra structure, see (96), for example. The antipode is a generalisation of inverting elements of a group and for semisimple Hopf algebras, the antipode satisfies $S^2 = \text{id}$.

Note that when the Hopf algebra is obtained from a group algebra there is a canonical Hopf algebra structure given in the following form

$$\Delta(h) = h \otimes h, \qquad\qquad S(h) = h^{-1}, \qquad \epsilon(h) = 1_{\mathbb{C}} ,\qquad(8.11)$$

with the multiplication of elements given by the multiplication in the group algebra.

The final structure we require on our Hopf algebra is that it is quasitriangular, this is encoded by the existence of a special element known as an R matrix, such that

$$\Delta^{op}(h) = R \, \Delta(h) \, R^{-1} \tag{8.12}$$

where $\Delta^{op} = \tau \circ \Delta$ and τ is the flip map exchanging the tensor factors. Equation 8.12 is a weakening of cocommutativity, which is defined as $\Delta^{op} = \Delta$. We can see this is the equivalent notion of commmutativity but for a coalgebra. We represent $R \in K \otimes K$ as

$$R = \sum R' \otimes R'' \; . \tag{8.13}$$

The notation is simply meant to indicate that R can be made of sums of tensor products of elements in the algebra. An R matrix must satisfy the following properties, which express compatibility with the coproduct structure

$$
\begin{aligned}
R \, (h^{(1)} \otimes h^{(2)}) \, R^{-1} &= h^{(2)} \otimes h^{(1)} \quad \forall \, h \in K \\
(\Delta \otimes id)(R) &= R_{13} R_{23} \qquad (id \otimes \Delta)(R) = R_{13} R_{12}
\end{aligned}
\tag{8.14}
$$

where $R_{13} = R' \otimes 1 \otimes R''$, $R_{12} = R' \otimes R'' \otimes 1$ and $R_{23} = 1 \otimes R' \otimes R''$; with the summation left implicit. For a more detailed and formal discussion on this topic, we refer to the many books and articles on the subject, such as (96; 120). We will now describe aspects of Hopf algebra gauge theory that are relevant in the present context.

8.2.1 Gauge transformations

In this section, we will draw a comparison between key concepts of discrete gauge theory and the analogous ones in Hopf algebra gauge theory. For details on discrete gauge theory, we refer the reader to (60; 61; 171).

We start by recalling that for finite groups, a gauge transformation by an element h, acts at a vertex v of the graph on the elements of the group assigned to the edges incident to that vertex. This action we denote by $\tilde{A}_v^h$ and it is defined by the following rules:

$$\tilde{A}_v^h(k) = h \cdot k \qquad\qquad \tilde{A}_v^h(k) = k \cdot h^{-1} \tag{8.15}$$

for incoming and outgoing edges respectively. The tilde is to differentiate this operator from its dual counterpart, which we will introduce in the following. For Hopf algebra gauge theories, if the local vertex neighbourhood has more than one incident edge, we need to split the element h to act on each of the connected edges, in a way that is compatible with the multiplication in the algebra and linear over $\mathbb{C}$. This is where the coproduct is used. Therefore, by direct analogy, we can define the action of gauge transformations at each edge by
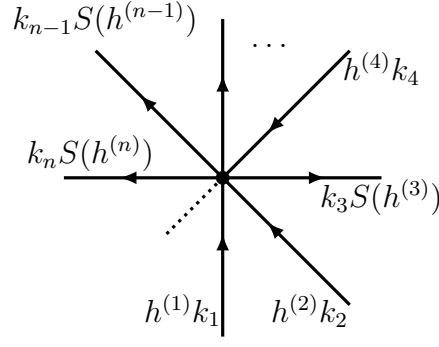
Figure 8.2: We display the gauge transformation for a local vertex neighbourhood by an element $h \in K$, the elements k_i are assigned to K^E, the Hopf algebra on the edges.

$$\tilde{A}^h_v(k_i) = h^{(i)} k_i \qquad\qquad \tilde{A}^h_v(k_i) = k_i\, S(h^{(i)}) \qquad i = 1, \ldots, n \qquad (8.16)$$

for incoming and outgoing edges respectively. For clarity, an example of this transformation is displayed in Figure 8.2. The trivial action, for edges that are not connected to the vertex v, is given by

$$\tilde{A}^h_v(k) = \epsilon(h)k \qquad \forall \ k \neq k_1,\ k_2,\ \ldots,\ k_n\ . \qquad (8.17)$$

For local vertex neighbourhoods with closed edges (loops), the action of gauge transformation can be written as

$$\tilde{A}^h_v(k) = (h^{(1)} k S(h^{(2)})) \qquad \text{or} \qquad \tilde{A}^h_v(k) = (h^{(2)} k S(h^{(1)}))\ , \qquad (8.18)$$

depending on whether the cilium is pointing inwards or outward to a counterclockwise loop. Similar relations hold for clockwise loops. We can therefore see that both the directedness and the cyclic ordering of the edges around a vertex play a role in Hopf algebra gauge theory and the above discussion should convince the reader of the necessity of the cilium in this framework.

This concludes our discussion around gauge transformation for Hopf algebra gauge theory. As shown in (124), the properties of the theory take a more appealing and simple algebraic form when working in the dual space K^*, the algebra of linear functionals over K.

For this reason, we will now describe the gauge transformations on K^*, which can be found by dualizing (8.16). This dualization is performed using two main properties, which come from the compatibility between the Hopf algebra with its dual

$$\langle \alpha, k_1 \cdot k_2 \rangle = \langle \alpha^{(1)} \otimes \alpha^{(2)}, k_1 \otimes k_2 \rangle, \qquad \langle \alpha_1 \cdot \alpha_2, k \rangle = \langle \alpha_1 \otimes \alpha_2, k^{(1)} \otimes k^{(2)} \rangle\ . \qquad (8.19)$$

Consider therefore a local vertex neighbourhood with n edges, as the one shown in Figure 8.1a, then the gauge transformation by $h \in K^v$ on $\alpha_1 \otimes \alpha_2 \cdots \otimes \alpha_n \in K^{*\otimes n}$, is given by

$$A_v^h(\alpha_1 \otimes \ldots \otimes \alpha_n) := \langle S^{\tau_1}(\alpha_1^{(1+\tau_1)}) \cdots S^{\tau_n}(\alpha_n^{(1+\tau_n)}), h \rangle (\alpha_1^{(2-\tau_1)} \otimes \ldots \otimes \alpha_n^{(2-\tau_n)}) \,, \quad (8.20)$$

where $\tau_i = 0, \ 1$ if the i'th edge is incoming to the vertex or outgoing respectively (we are assuming $S^0 = id$). Note that this constitutes a right K^V module action on $K^{*\otimes n}$, which is denoted as $(\alpha_1 \otimes \ldots \otimes \alpha_n) \triangleleft^* h$ in (124) and further details can be found there, in particular see Corollary 3.12. It can now be proved that with these definitions we have

$$A_v^{h_1} A_v^{h_2} = A_v^{h_2 h_1}, \qquad A_{v_1}^{h_1} A_{v_2}^{h_2} = A_{v_2}^{h_2} A_{v_1}^{h_1}, \qquad v_1 \neq v_2, \ \forall \ h_1, h_2 \in K \,. \qquad (8.21)$$

Analogously to what happens for discrete gauge theory we say that a function is gauge invariant at a vertex v when

$$A_v^h(\alpha_1 \otimes \ldots \otimes \alpha_n) = \epsilon(h)(\alpha_1 \otimes \ldots \otimes \alpha_n) \qquad \forall \ h \in K \,. \qquad (8.22)$$

It can be seen that given the Haar integral l of the Hopf algebra K, the projector P_v^{inv} into the space of gauge invariant functions at a vertex v is given by the gauge action

$$P_v^{\mathrm{inv}} = A_v^l \,. \qquad (8.23)$$

For a finite group G, the Haar integral is given by

$$l = \sum_{g \in G} g \qquad (8.24)$$

and by substituting this formula in Equation(8.23) the familiar projector into gauge invariant states of the toric code can be found.

8.2.2 Braided tensor product and holonomy

We can now introduce the second fundamental ingredient of Hopf algebra gauge theory, the braided tensor product, which plays an important role in the construction of the plaquette operator. As in quantum field theory, the holonomy is obtained by considering parallel transport around loops. Consider therefore a plaquette p turning counterclockwise, with all cilia at vertexes pointing outward, except for one, as shown in Figure 8.3a. The holonomy on p, for discrete gauge theory, is then the product of elements assigned along the edges of the path starting from the unique cilium pointing into the plaquette

$$\mathrm{Hol}(p) = (k_n k_{n-1} \cdots k_2 k_1)^{-1} \,. \qquad (8.25)$$

157

To simplify the discussion we have supposed that the orientation of the plaquette's edges agrees with that of a path turning counterclockwise. If the path goes against the directedness of an edge, the element assigned to that edge is first acted upon with the antipode S. When the product of the group elements around the plaquette
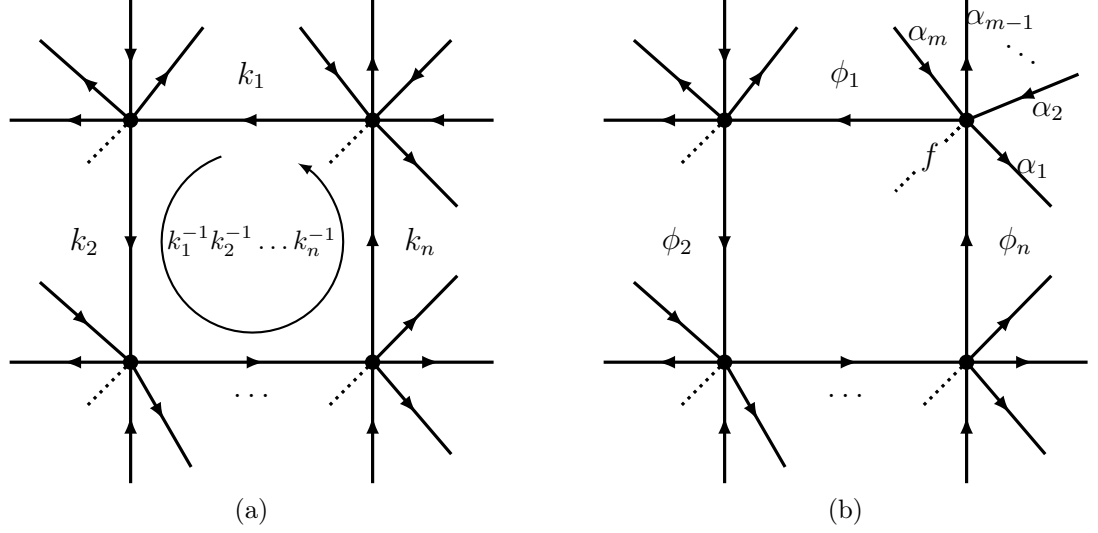

(a)   (b)

Figure 8.3: In Figure (a) we display the holonomy of elements $k_1 \ldots k_n$. In Figure (b) we display the dual holonomy on the space of functions.

is equal to the identity, we say that the connection is flat at that plaquette. The plaquette operator associated with an element f of the algebra of functions for plaquette p is then given by

$$B_p^f(k_1 \otimes k_2 \otimes \ldots k_n) = \langle f, (k_n k_{n-1} \cdots k_2 k_1)^{-1} \rangle (k_1 \otimes k_2 \otimes \ldots k_n) \qquad (8.26)$$

if in place of f we take the Haar integral $\lambda = \delta_e$ of K^*, this operator then becomes the projector into the space of flat connections on p

$$P_p^{\text{flat}} = B_p^{\delta_e} . \qquad (8.27)$$

Note that generally the plaquette operator $B_p^{\delta_a}$ is denoted by B_p^e (i.e. see (37) and (102)). The notion of holonomy can now be readily adapted to our present context. In particular, for a counterclockwise directed plaquette, we can write

$$\text{Hol}_p(k_1, k_2, \ldots, k_n) = S(k_n k_{n-1} \cdots k_2 k_1) . \qquad (8.28)$$

If now we go by analogy with discrete gauge theory, the most "obvious" extension of the plaquette operator would be

$$\tilde{B}_p^f(k_1 \otimes k_2 \otimes \ldots k_n) = \langle f, S(k_n^{(1)} k_{n-1}^{(1)} \cdots k_2^{(1)} k_1^{(1)}) \rangle (k_1^{(2)} \otimes k_2^{(2)} \otimes \ldots k_n^{(2)}) \qquad (8.29)$$

158

or similarly, in the dual space

$$B_p^f(\phi_1 \otimes \phi_2 \otimes \ldots \phi_n) = (S(f^{(1)})\phi_1 \otimes S(f^{(2)})\phi_2 \otimes \ldots \otimes S(f^{(n)})\phi_n) \ . \qquad (8.30)$$

This can also be written as

$$B_p^f(\phi_1 \otimes \phi_2 \otimes \ldots \phi_n) = \mathrm{Hol}_p^*(f) \cdot (\phi_1 \otimes \phi_2 \otimes \ldots \otimes \phi_n) \ , \qquad (8.31)$$

where $\mathrm{Hol}_p^*(f)$ is the dual holonomy:

$$\mathrm{Hol}_p^*(f) = (S(f^{(1)}) \otimes S(f^{(2)}) \otimes \ldots \otimes S(f^{(n)})) \qquad (8.32)$$

and $\cdot$ is the canonical product structure on the tensored elements [1]. Similarly to what happened before, for plaquettes whose edge orientations do not agree with a path turning counterclockwise, the antipode is employed (which would effectively remove the above antipodes as $S^2 = id$ for semisimple Hopf algebras).

It is now evident that the plaquette operator is closely related to the definition of tensor product algebra. Note however that this product is not necessarily compatible with the action of gauge transformations (17; 124). Consider a vertex with two incoming incident edges. Then if we say that $\alpha \in K^*$ is assigned to one edge and $\beta \in K^*$ to the other, the action of the vertex operator, for a general finite-dimensional Hopf algebra, is not compatible with the multiplication of functions, i.e.

$$A_v^h(\alpha \otimes \beta) = A_v^h((\alpha \otimes 1) \cdot (1 \otimes \beta)) \neq (A_v^{h^{(2)}}(\alpha \otimes 1)) \cdot (A_v^{h^{(1)}}(1 \otimes \beta)) \ . \qquad (8.33)$$

The disequality, generally, holds with an equal sign only when we are working with a group algebra or, more broadly speaking, with a cocommutative Hopf algebra. This fact poses a significant issue for the consistency of the theory, as it means that holonomies of functions on multiple edges will be changed in "unexpected" ways by gauge transformations. In particular, the set of functions with trivial holonomies will not be invariant under gauge transformations, so it won't be possible to consider the space of gauge invariant functions on flat connections, which is the topologically protected space. This is why the definition of the plaquette operator, or actually, more fundamentally, the product of the functions, needs to be modified.
When the Hopf algebra is quasitriangular and therefore admits an R-matrix, there is a natural deformation of the tensor product that allows one to recover compatibility of the tensor product algebra with gauge transformations. This product takes the

---

[1]This algebra structure is simply given by

$$(a \otimes b) \cdot (c \otimes d) = (a \cdot c \otimes b \cdot d)$$

name of the "braided tensor product". This has studied in (17; 118; 119; 121; 124). Given α, β, α', β' in the algebra of functions and the R matrix of a quasitriangular Hopf algebra around a vertex v with two edges, this product can be written as

$$(\alpha \otimes \beta) * (\alpha' \otimes \beta') = (\alpha \cdot A_v^{R'}(\alpha')) \otimes (A_v^{R''}(\beta) \cdot \beta') \qquad (8.34)$$

where $A_v^{R'}$ ($A_v^{R''}$) denotes the vertex operator acting with the first (second) tensor entry of the R matrix (e.g. see (8.13)) and we are considering the ordering of the tensored elements to agree with the ordering imposed by the cilia. More explicitly, using (8.20), this formula can be written as

$$(\alpha \otimes \beta) * (\alpha' \otimes \beta') = \langle \alpha'^{(1+\tau_1)} \otimes \beta^{(1+\tau_2)}, (S^{\tau_1} \otimes S^{\tau_2})(R) \rangle (\alpha \cdot \alpha'^{(2-\tau_1)} \otimes \beta^{(2-\tau_1)} \cdot \beta') , \quad (8.35)$$

where the above result can be regarded as a consequence of the commutation between β and α', which are sitting on edges of decreasing order (with respect to the cilia ordering).

In general, for a local vertex neighbourhood with more than two edges embedded into the lattice, the structure of the product depends not only on the relative position of the elements being multiplied but also on the edge orientations. This is to make sure that the braided tensor structure stays consistent across the lattice (124) [2]. Given two elements α and β, with i, j being their edges position as defined by the cilia, the algebra structure on a bivalent local vertex neighbourhood is given by

$$
\begin{aligned}
(\alpha)_i * (\beta)_i &= \langle \beta^{(2)} \otimes \alpha^{(2)}, R \rangle (\alpha^{(1)} \beta^{(1)})_i & \tau_i &= 1 \\
(\alpha)_i * (\beta)_i &= (\alpha\beta)_i & \tau_i &= 0 \\
(\alpha)_i * (\beta)_j &= (\alpha \otimes \beta)_{ij} & i &< j \\
(\alpha)_i * (\beta)_j &= \langle \beta^{(1+\tau_j)} \otimes \alpha^{(1+\tau_i)}, (S^{\tau_i} \otimes S^{\tau_j})(R) \rangle (\alpha^{(2-\tau_i)} \otimes \beta^{(2-\tau_j)})_{ij} & i &> j ,
\end{aligned}
\qquad (8.36)
$$

as before $\tau_i = 0$, 1 if the edge is incoming into the vertex or outgoing respectively, and the subscripts indicate which element is associated with which edge.

This local algebraic structure can be extended to the full ribbon graph by stitching together the different local vertex neighbourhood algebras. The details on this procedure can be found in (124), and we provide some description in Appendix F.

The plaquette operator for Hopf Algebra gauge theory is defined as as

$$\mathcal{B}_p^f(\phi_1 \otimes \phi_2 \otimes \ldots \phi_n) = \mathrm{Hol}^*(p) * (\phi_1 \otimes \phi_2 \otimes \ldots \phi_n) . \qquad (8.37)$$

In Appendix F, we show that this operator, when acting on a plaquette such as the

---

[2]Essentially due to the fact that an edge that is incoming for a given vertex is outgoing for a neighbouring one.

one given in Figure 8.3b, can be written as

$$\mathcal{B}_p^f(\phi_1, \ \phi_2, \ \ldots, \ \phi_{n-1}, \ \phi_n, \ \alpha_1, \ \alpha_2, \ \ldots, \ \alpha_m) =$$

$$\langle \phi_n^{(1)} \otimes f^{(1)}, R \rangle \left[\prod_{j=1}^m \langle \alpha_j^{(1+\tau_j)} \otimes f^{(j+1)}, (S^{\tau_j} \otimes id)(R) \rangle \right] \langle \phi_1^{(2)} \otimes f^{(m+2)}, R^{-1} \rangle \quad (8.38)$$

$$B_p^{f^{(m+3)}} \left(\phi_1^{(1)}, \ \phi_2, \ \ldots, \ \phi_{n-1}, \ \phi_n^{(2)}, \ \alpha_1^{(2-\tau_1)}, \ \ldots, \ \alpha_m^{(2-\tau_m)} \right) \ ,$$

with B_p^f as in (8.30). This formula may seem complicated, but it is simply saying that the most "obvious" plaquette operator and the one that is compatible with gauge transformation differ only for something that happens at the starting vertex of the plaquette. A gauge transformation acting at any combination of vertices of the lattice (i.e. some product of gauge transformations on individual vertices) cannot change the holonomy, unless it acts at the base point of the plaquette and then just in a canonical way for a gauge transformation acting on a single edge (a loop), with the group element on that edge being the monodromy of the plaquette. Note that equation (8.38) looks like an element f, placed at an extra incoming edge at the cilia, is multiplying the functions on the lattice according to equation (8.36).

With this definition, it is now possible to make sense of the concept of flat connection for Hopf algebra gauge theory. In particular, given the Haar integral λ, of the algebra of functions, the following defines a projector (see (124)) into the space of flat connections:

$$P_p^{\text{flat}} = \mathcal{B}_p^\lambda \ . \tag{8.39}$$

With this definition plaquette operators have non-trivial commutation relations, and in particular

$$\begin{aligned} \mathcal{B}_p^f \mathcal{B}_p^g &= \langle g^{(1)} \otimes f^{(2)}, R \rangle \langle g^{(3)} \otimes f^{(1)}, R^{-1} \rangle \ \mathcal{B}_p^{f^{(3)} g^{(2)}} \\ \mathcal{B}_p^f \mathcal{B}_q^g &= \mathcal{B}_q^g \mathcal{B}_p^f \qquad p \neq q \ . \end{aligned} \tag{8.40}$$

Plaquette operators and vertex operators commute when the vertex does not coincide with the plaquette cilia's vertex. However at the vertex containing the plaquette's cilia we have

$$A_v^h \mathcal{B}_p^f = \langle f^{(3)}, S(h^{(1)}) \rangle \langle f^{(1)}, h^{(2)} \rangle \mathcal{B}_p^{f^{(2)}} A_v^{h^{(3)}} \ . \tag{8.41}$$

The proofs for the above relations can be found in Appendix F. These properties can be directly compared with similar ones obtained using B_p^f (37),

$$B_p^f B_p^g = B_p^{gf} \qquad A_v^h B_p^f = \langle f^{(3)}, S(h^{(1)}) \rangle \langle f^{(1)}, h^{(3)} \rangle B_p^{f^{(2)}} A_v^{h^{(2)}} \ , \tag{8.42}$$

which is saying that plaquette and vertex operators of traditional Kitaev models form a representation of the Hopf algebra's Drinfeld double. Note that for cocommutative

Hopf algebras, Equation (8.41) agrees with Equation (8.42). In particular, this also means that the particle content of the two theories is the same, as we will see in the following.

We conclude this section by mentioning that both in the original Kitaev model and in the more general Hopf algebra gauge theory, projectors onto flat connections and onto the space of gauge invariant functions commute with each other:

$$P_{p_1}^{\text{flat}} P_{p_2}^{\text{flat}} = P_{p_2}^{\text{flat}} P_{p_1}^{\text{flat}} \qquad P_{v_1}^{\text{inv}} P_{v_2}^{\text{inv}} = P_{v_2}^{\text{inv}} P_{v_1}^{\text{inv}} \qquad \forall \, p_1, p_2, v_1, v_2$$
$$P_p^{\text{flat}} P_v^{\text{inv}} = P_v^{\text{inv}} P_p^{\text{flat}} \qquad \forall \, p, v \; . \tag{8.43}$$

These results can be proved from the properties of the Haar integrals and the relations given above. In particular, this means that we have a good set of commuting projectors to define a stabilizer code (e.g. on the torus).

8.3 Lattice Hopf algebra gauge theory for $\mathbb{C}\mathbb{Z}_N$

In this section, we will construct Hamiltonians for Hopf algebra gauge theories on a square lattice like the one shown in Figure 8.1b. We will follow Kitaev's idea and encode the space of gauge invariant functions and flat connection into the ground state of some Hamiltonian (102).

As we discussed in the previous section, we can construct local projectors in Hopf algebra gauge theory which commute with each other, hence we can define a Hamiltonian in the same vein as (102). We define the Hamiltonian as

$$H = -\sum_v P_v^{\text{inv}} - \sum_p P_p^{\text{flat}} \; , \tag{8.44}$$

where P_v^{inv} is the projector onto gauge invariant states and P_p^{flat} is the projector onto flat connections. The space of gauge invariant and flat connections is then identified with the space of ground states of this Hamiltonian. This implies that gauge invariance is now enforced by an energy penalty. We will show that excited states, i.e. states that break gauge invariance and/or flatness give rise to anyons (37; 102).

In the present context, we will consider the theory constructed over the quasitriangular Hopf algebra $\mathbb{C}\mathbb{Z}_N$, the group algebra constructed over $\mathbb{Z}_N$, the cyclic group of order N. We denote the basis of $K = \mathbb{C}\mathbb{Z}_N$ by a^p, where a is the generator of $\mathbb{Z}_N$ and a basis of characters for K^* by χ_i, with $i = 0, \ldots N-1$. The action of the characters on $\mathbb{Z}_N$ is defined as

$$\chi_i(a^p) = \omega^{ip} \qquad \omega = e^{\frac{2\pi i}{N}} \; . \tag{8.45}$$

As we have shown in Section 8.2, the novelty of this approach comes with the

introduction of a braided tensor product with a non-trivial R matrix on $K \otimes K$. We are therefore interested to see how the introduction of this non-trivial R-matrix changes the gauge theory and Kitaev model in the context where the Hopf algebra is just a group algebra. In these cases, the gauge theory with the trivial R-matrix would be exactly the conventional lattice gauge theory and the Kitaev model would be the conventional toric code. In particular, for $\mathbb{C}\mathbb{Z}_N$, there are up to N choices of quasitriangular structures. We label these by $k = 0, 1, \ldots, N - 1$ in the R matrix, which is defined by

$$R = \begin{cases} \frac{1}{N} \sum_{p,q=0}^{N-1} \omega^{-kpq} \, a^p \otimes a^q & \gcd(k, N) = 1 \\ 1 \otimes 1 & k = 0 \end{cases} \tag{8.46}$$

with ω an N'th root of unity as in (8.45). We can now start building representations of vertex and plaquette operators.

Building a matrix representation for the Hamiltonian (8.44) is equivalent to considering the regular representation of vertex operators and plaquette operator over $(\mathbb{C}\mathbb{Z}_N)^*$ and we identify

$$\chi_i \equiv |i\rangle \ . \tag{8.47}$$

Using this basis and using (8.20, 8.38), it is straightforward to find the regular representation of vertex operators and plaquette operators. In particular, these can be given in terms of the matrices

$$\sigma = \begin{pmatrix} 1 & 0 & 0 & \cdots & & 0 \\ 0 & \omega & 0 & \cdots & & 0 \\ \vdots & & \ddots & & & \vdots \\ 0 & 0 & \cdots & \omega^{N-2} & & 0 \\ 0 & 0 & \cdots & & 0 & \omega^{N-1} \end{pmatrix}, \qquad \tau = \begin{pmatrix} 0 & 1 & 0 & \cdots & 0 \\ 0 & 0 & 1 & \cdots & 0 \\ \vdots & & & \ddots & \vdots \\ 0 & 0 & \cdots & 0 & 1 \\ 1 & 0 & \cdots & 0 & 0 \end{pmatrix}, \tag{8.48}$$

which are a generalization of the Pauli matrices and reduce to the familiar σ^z, σ^x when $N = 2$. The commutation relation of the τ and σ matrices is the following:

$$\tau^m \sigma^l = \omega^{ml} \sigma^l \tau^m$$
$$\sigma^l \tau^m = \omega^{-ml} \tau^m \sigma^l \ . \tag{8.49}$$

Let's therefore start by considering the representation of a vertex operator that acts on the vertex v_1 depicted in Figure 8.4, under (8.20). It can be proved that this action, on the basis given in (8.47), corresponds to the one provided in the same
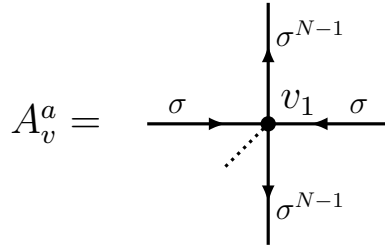
Figure 8.4: Here we display the action of the vertex operator associated with gauge transformation by $a \in \mathbb{C}\mathbb{Z}_N$ for the local vertex neighbourhood v_1. The matrix σ is assigned to incoming edges and $\sigma^{-1} = \sigma^{N-1}$ is assigned to an outgoing edge. This is the usual vertex operator for conventional $\mathbb{Z}_N$ toric code.

Figure. Using (8.20) for a general vertex v we get

$$A_v^{a^i} = (A_v^a)^i, \qquad (A_v^a)^N = 1, \qquad (A_v^a)^{N-1} = (A_v^a)^\dagger, \tag{8.50}$$

and that reversing the edge orientations corresponds to taking the Hermitian adjoint of the above operator. This means that when considering the lattice shown in Figure 8.1b, the direction of the arrows around the vertex is unimportant (note that there are two types of vertices), as the shape of the projector into gauge invariant space is independent of edge orientations at that vertex. Given the Haar integral, $l = \frac{1}{N} \sum_{i=0}^{N-1} a^i$, we have

$$P_v^{\text{inv}} = \frac{1}{N} \left(1 + (A_v^a) + (A_v^a)^2 + \ldots + (A_v^a)^{N-1} \right) . \tag{8.51}$$

We can now turn our attention to the plaquette operator. As for the vertex operator the matrix form of the plaquette operator is given by considering the representation of (8.38) on the basis (8.47). Consider therefore the plaquette shown in Figure 8.5. It is straightforward to see that the representation of the plaquette operator associated with χ_1, is then the one depicted in the same Figure, where we represent action only for those edges on which the operator acts non-trivially.

Note that given the particular choice of R matrix that we made, our plaquette operator differs from the plaquette operator of Kitaev models by an extra vertex operator attached to the vertex with the cilium. More specifically we have

$$\mathcal{B}_p^{\chi_1} = B_p^{\chi_1} A_{v_2}^{a^{\widehat{k}}} \tag{8.52}$$

where $B_p^{\chi_1}$ is the plaquette operator arising from Kitaev models for $\mathbb{C}\mathbb{Z}_N$ (24; 140), and $\widehat{k}$ is connected to the k appearing in the R matrix (8.46) in the following way

$$\widehat{k} = \begin{cases} \frac{1}{k} \bmod N & \gcd(k, N) = 1 \\ 0 & \text{otherwise .} \end{cases} \tag{8.53}$$

Similarly to the vertex operators, it can be proven that the plaquette operators

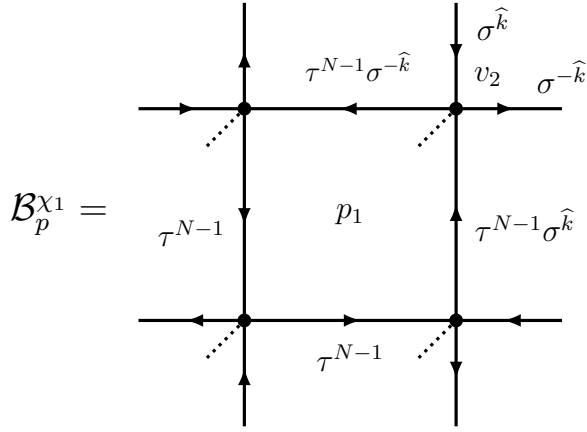Figure 8.5: We show the decomposition of $\mathrm{Hol}^*_{p_1}(\chi_1)$ for the plaquette p_1. We display the resulting matrices from the regular representation of the braided tensor product. The important observation is the presence of σ matrices at the local vertex neighbourhood with the cilia pointing inward to p_1, the power of k is related to the choice of R matrix in the braided tensor product. We can see when $k = 0$, then the plaquette operator reduces to the familiar one from the Kitaev model.

satisfy the following relations

$$\mathcal{B}^{\chi_j} = (\mathcal{B}^{\chi_1})^j \qquad (\mathcal{B}^{\chi_1})^N = 1 \qquad (\mathcal{B}^{\chi_1})^{N-1} = (\mathcal{B}^{\chi_1})^\dagger \; . \tag{8.54}$$

In light of these properties, the form of the projector onto the space of flat connections at a general plaquette p, does not depend on the orientation of that particular plaquette. Given the dual Haar integral[3] $\lambda = \frac{1}{N} \sum_{i=0}^{N-1} \chi_i$, we in fact get

$$P_p^{\mathrm{flat}} = \frac{1}{N} \left(1 + (\mathcal{B}^{\chi_1})_p + (\mathcal{B}_p^{\chi_1})^2 + \ldots + (\mathcal{B}_p^{\chi_1})^{N-1} \right) \tag{8.55}$$

which is similar to (8.51). Bear in mind, however, that the introduction of the R matrix is breaking the electro-magnetic duality given by the interchange of the vertex and plaquette operators (35; 102). In particular, the vertex operator acts on a single vertex neighbourhood in the direct lattice, while the plaquette operator does not act on a single vertex neighbourhood of the dual lattice. Given the structure we have shown for the plaquette and vertex operators, it can be shown that given any two such operators, they commute

$$\left[\mathcal{B}_p^{\chi_1}, A_v^a \right] = 0 \qquad \forall \; p, \; v \; . \tag{8.56}$$

We are now in the position to prove that the ground state of the theory coincides with the one of the original Kitaev quantum double model.

---

[3] The Haar integral on the function algebra.

Note in fact that since all the vertex and plaquette operators entering the Hamiltonian commute with each other, the ground state of the model $|GS\rangle$ is such that

$$A_v^a|GS\rangle = |GS\rangle \tag{8.57}$$

$$\mathcal{B}_p^{\chi_1}|GS\rangle = |GS\rangle \Rightarrow B_{p_1}^{\chi_1}|GS\rangle = |GS\rangle , \tag{8.58}$$

which are the exact same equations that one would obtain in the original Kitaev model. This implies that the ground states of the two theories coincide. Observe that this property should be true for any two models based on the same Hopf algebra, but differing in the choice of R-matrix on that Hopf algebra, as can be deduced more generally from (124).

This concludes the treatment of the ground state physics of the Hopf algebra gauge theory based upon $\mathbb{C}\mathbb{Z}_N$. In the next section, we will consider the states with excitations. For completeness, before undertaking this task, we will describe in some detail the braided tensor product for a local vertex neighbourhood with $\mathbb{C}\mathbb{Z}_N$, as there are some interesting aspects to it.

Consider the braided tensor product on $\boldsymbol{\chi_l}$, $\boldsymbol{\chi_r}$, two elements on a local vertex neighbourhood similar to the one shown in Figure 8.2, defined as

$$\boldsymbol{\chi_l} = \left(\chi_{l_1} \otimes \chi_{l_2} \otimes \ldots \otimes \chi_{l_n}\right) \qquad \boldsymbol{\chi_r} = \left(\chi_{r_1} \otimes \chi_{r_2} \otimes \ldots \otimes \chi_{r_n}\right) . \tag{8.59}$$

Using (8.36) it can be seen that the braided tensor product for these two general elements, is given by

$$\boldsymbol{\chi_l} * \boldsymbol{\chi_r} = \omega^{-\sum_{i=1}^n \tau_i \widehat{k}l_i r_i - \sum_{i<j}^n (-1)^{\tau_i + \tau_j} \widehat{k}l_i r_j} \left(\chi_{l_1 + r_1} \otimes \chi_{l_2 + r_2} \otimes \ldots \otimes \chi_{l_n + r_n}\right) . \tag{8.60}$$

To consider a more concrete example, let's consider vertex v_1 depicted in Figure 8.4, and let's set up

$$\begin{aligned}
(\chi_1)_1 &= \left(\chi_1 \otimes \chi_0 \otimes \chi_0 \otimes \chi_0\right) & (\chi_1)_2 &= \left(\chi_0 \otimes \chi_1 \otimes \chi_0 \otimes \chi_0\right) \\
(\chi_1)_3 &= \left(\chi_0 \otimes \chi_0 \otimes \chi_1 \otimes \chi_0\right) & (\chi_1)_4 &= \left(\chi_0 \otimes \chi_0 \otimes \chi_0 \otimes \chi_1\right) .
\end{aligned} \tag{8.61}$$

The product in (8.60) can then be summarized through the following table, where the element at row i and column j corresponds to $(\chi_1)_i * (\chi_1)_j$

$*$	$(\chi_1)_1$	$(\chi_1)_2$	$(\chi_1)_3$	$(\chi_1)_4$
$(\chi_1)_1$	$\omega^{-k}(\chi_2)_1$	$(\chi_1)_1 \cdot (\chi_1)_2$	$(\chi_1)_1 \cdot (\chi_1)_3$	$(\chi_1)_1 \cdot (\chi_1)_4$
$(\chi_1)_2$	$\omega^{k}(\chi_1)_1 \cdot (\chi_1)_2$	$(\chi_2)_2$	$(\chi_1)_2 \cdot (\chi_1)_3$	$(\chi_1)_2 \cdot (\chi_1)_4$
$(\chi_1)_3$	$\omega^{-k}(\chi_1)_1 \cdot (\chi_1)_3$	$\omega^{k}(\chi_1)_2 \cdot (\chi_1)_3$	$\omega^{-k}(\chi_2)_3$	$(\chi_1)_3 \cdot (\chi_1)_4$
$(\chi_1)_4$	$\omega^{k}(\chi_1)_1 \cdot (\chi_1)_4$	$\omega^{-k}(\chi_1)_2 \cdot (\chi_1)_4$	$\omega^{k}(\chi_1)_3 \cdot (\chi_1)_4$	$(\chi_2)_4$

As before, by $\cdot$ we are representing the canonical algebra structure on the tensor product. The products of all the other elements of the algebra can be derived from this table and we can see that they are in general non-commutative, due to the presence of the complex roots of unity. In discrete gauge theory, the product table on the same basis of functions would be similar, but without phases, and would therefore be isomorphic to the group algebra $(\mathbb{C}\mathbb{Z}_N)^{\otimes 4}$, in accordance with Pontryagin duality.

The presence of these phases now induces a very natural question, that is, are they gauge invariant or can they be gauged away by some isomorphism? This question can be addressed by studying the second cohomology group of this $\mathbb{C}\mathbb{Z}_N$-module, as non-trivial projective representations correspond to non-trivial cocycles (42; 44). It can be proved that the phases appearing in the table are 2-cocycles, which are not 2-coboundary. So, the local algebra is a twisted group algebra or, likewise, a non trivial projective representation of $(\mathbb{C}\mathbb{Z}_N)^{\otimes 4}$.

So to summarise, despite the fact that we chose a cocommutative Hopf algebra, we find that the phases introduced by the R matrix render the algebra of functions non-commutative.

8.3.1 Excitations in Hopf algebra lattice gauge theory

Now that we have constructed representations of our Hopf algebra lattice gauge theory operators, and defined the Hamiltonian, we can analyse excitations, which are created by violating the constraint equations given in Equation (8.57,8.58). This is exactly analogous to the $\mathbb{Z}_2$ toric code excitations we discussed in Section 7.3. As in Kitaev models, states above the ground state can be described by quasiparticle excitations connected by strings of operators (37; 102; 123; 177).
We will see that the fusion rules of our excitations are, in fact, the same as conventional Kitaev models, but the introduction of the braided tensor product and the non-trivial R matrix will change the braiding statistics.

We start by considering the magnetic excitations. A magnetic excitation is defined by an eigenstate of the Hamiltonian that does not satisfy the flatness constraint regarding the plaquette operators in Equation (8.58).
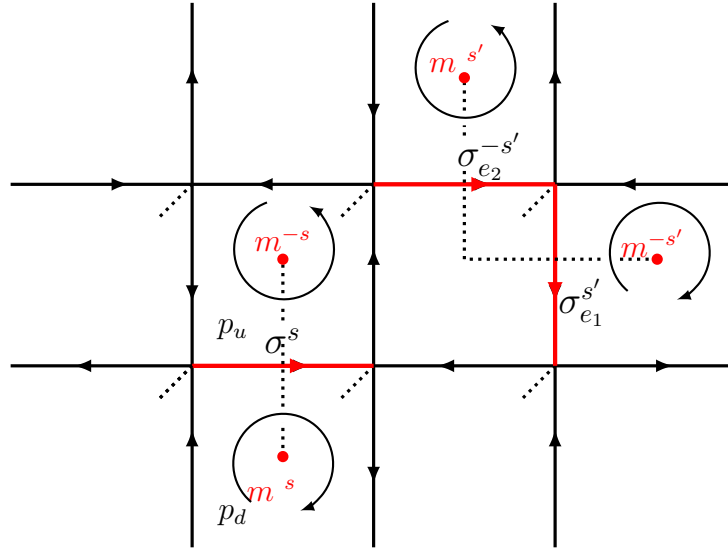
Figure 8.6: The action of σ^s on an edge generates magnetic excitations in the neighbouring plaquettes. If we initially act with $\sigma_{e_1}^{s'}$ this creates two m excitations on the adjacent plaquettes, we can then act with $\sigma_{e_2}^{-s'}$ to translate one of the excitations to another plaquette.

Consider the state obtained by applying the operator σ_e^s at a horizontal edge e for some $s \in \mathbb{Z}_N$. We name the two plaquettes adjacent this edge p_u and p_d (where u and d stand for up and down respectively), as shown in Figure 8.6. From Equation (8.52), it can be seen that

$$\mathcal{B}_{p_u}\sigma_e^s|GS\rangle = \omega^{N-s}\sigma_e^s|GS\rangle \qquad \mathcal{B}_{p_d}\sigma_e^s|GS\rangle = \omega^s\sigma_e^s|GS\rangle . \qquad (8.62)$$

Since $1 + \omega + \omega^2 + \ldots + \omega^{N-1} = 0$, this implies

$$(1 + \mathcal{B}_{p_i} + \mathcal{B}_{p_i}^2 + \ldots + \mathcal{B}_{p_i}^{N-1})\sigma_e^s|GS\rangle = 0 \quad i = u, d . \qquad (8.63)$$

Similarly, it can be seen that for all vertices v, and all plaquettes $p \neq p_u, p_d$, we get

$$A_v\sigma_e^s|GS\rangle = \sigma_e^s|GS\rangle \qquad \mathcal{B}_p\sigma_e^s|GS\rangle = \sigma_e^s|GS\rangle . \qquad (8.64)$$

These relations imply that when acting with the Hamiltonian on this state, the only non-trivial contributions come from the upper and lower adjoining plaquettes

$$H\sigma_e^s|GS\rangle =$$
$$(E_{GS} + 2)|GS\rangle - \sum_{i=u,d}(1 + \mathcal{B}_{p_i} + \mathcal{B}_{p_i}^2 + \ldots + \mathcal{B}_{p_i}^{N-1})\,\sigma_e^s|GS\rangle = \qquad (8.65)$$
$$(E_{GS} + 2)\sigma_e^s|GS\rangle ,$$

with E_{GS} the energy of the ground state. Since the energy has increased by 2 units, we can interpret this state to be obtained by creating two particles sitting on the two plaquettes. By convention, we say that the particle at plaquette p_u has magnetic
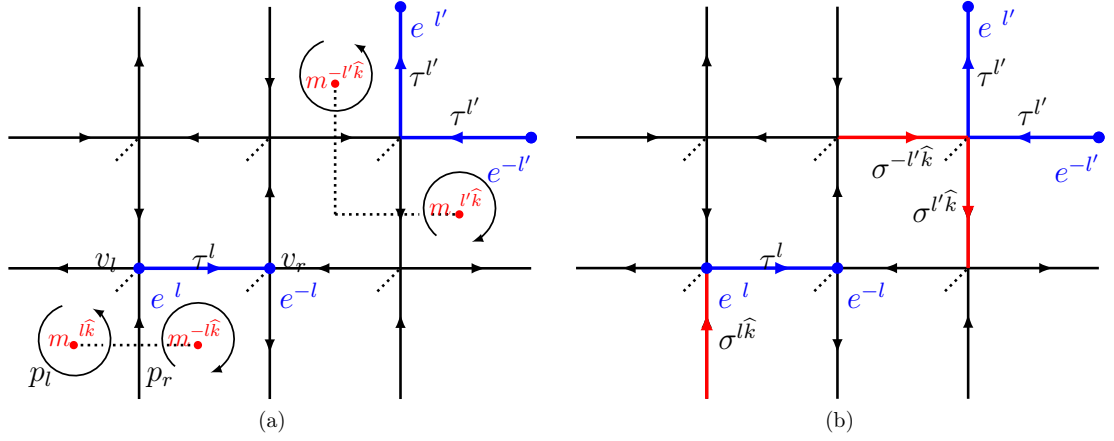
Figure 8.7: In Figure (a) we show how the action of τ^l on an edge creates electric excitations at the adjacent vertices but also magnetic excitations in the neighbouring plaquettes, given by the cilia at the adjoining vertices to the edge. In comparison to the Kitaev model, the action of τ^l creates four excitations rather than two. In Figure (b) we show that the action of $\sigma^{l\hat{k}}$ on a perpendicular edge can annihilate the additional magnetic excitations.

charge $-s$ and the one at plaquette p_d has magnetic charge s. We can separate the magnetic charges by using strings of sigma operators. For example in Figure 8.6, we create two magnetic excitations by acting with $\sigma_{e_1^{s'}}$ on a vertical edge e_1 on the graph, we then act with $\sigma_{e_2}^{-s'}$ on a perpendicular edge. This will then move $m^{s'}$ excitation upwards on the graph. The string must consist of alternating $\sigma^{s'}$ and $\sigma^{-s'}$.

We discussed this in detail in Section 7.4, in the simpler case of $\mathbb{Z}_2$ toric code.

As we can see, the magnetic excitations of our model are the same as those in the conventional toric code. The electric excitations, which we consider now, will provide some novelty. Electric excitations are defined as eigenstates that violate the gauge invariance condition (8.57). This is exactly analogous to the $\mathbb{Z}_2$ toric code excitations we discussed in Section 7.3. Similarly to the magnetic excitations, it is not possible to create isolated particles and these particles are also obtained by acting on the ground state with the appropriate operators. If we were to go by direct analogy with the Kitaev model, this type of particle would be created by the action of τ^l at some edge. For example, consider the state obtained by acting with τ^l on a horizontal edge like in Figure 8.7a and we get

$$A_{v_l}\tau_e^l|GS\rangle = \omega^l\,\tau_e^l\,|GS\rangle, \qquad A_{v_r}\tau_e^l|GS\rangle = \omega^{N-l}\,\tau_e^l\,|GS\rangle . \qquad (8.66)$$

Given these relations, we can interpret this state as the one obtained by creating two electric excitations sitting at vertices v_l and v_r, which by convention we define to have electric charges l and $-l$, respectively. Acting with τ^l creates more than these two excitations though. The presence of σ matrices attached to the edges around

the plaquette cilium, in fact, give non-trivial commutation with τ^l:

$$\mathcal{B}_{p_l}\tau_e^l\,|GS\rangle = \omega^{l\widehat{k}}\tau_e^l\,|GS\rangle \qquad \mathcal{B}_{p_r}\tau_e^l|GS\rangle = \omega^{N-l\widehat{k}}\tau_e^l|GS\rangle \ . \tag{8.67}$$

It can be checked that all the other plaquettes and vertex operators around τ^l have trivial action on this state, and this means that

$$H\,\tau_e^l\,|GS\rangle = (E_{GS} + 4)\,\tau_e^l\,|GS\rangle \ , \tag{8.68}$$

so we have extra magnetic excitations with charges $l\widehat{k}$ and $-l\widehat{k}$ at plaquettes p_l and p_r or, equivalently, we have extra flux quanta attached to each charge. This is also depicted in Figure 8.7a.

We can therefore see that, compared to Kitaev's model, the R matrix and the braided tensor product induces a change in the operators that create electric excitations and we will see that this has implications for the braiding properties of these particles. The correct creation operator for electric excitations is obtained by adding the action of an extra σ operator. In the present case, it can be checked that acting with a $\sigma^{l\widehat{k}}$ at the bottom left edge with respect to the τ^l operator does the trick[4]. Similar to the magnetic excitations we can separate electric excitations through strings of operators, as shown in 8.7b. However, these strings now have perpendicular "hairs", made of alternating $\sigma^{l\widehat{k}}$ and $\sigma^{-l\widehat{k}}$.

It is worth pointing out that in the original Kitaev model, these types of operators would create dyonic excitations rather than elementary ones. The introduction of the R matrix, therefore, is introducing a mapping between the different excitations of the original model. Since the braiding statistics of these operators on the plane are primarily independent of the Hamiltonian that was used to introduce them, we can already anticipate that these particles will have the same dyonic braiding that they have in Kitaev's model.

Following (140), non elementary excitations that are a combination of electric and magnetic charges are indicated by $\psi^{l,s}$, where l and s represent the electric and magnetic charges of the dyon. The fusion rules for the excitations are then the same as the Kitaev model

$$e^l \times e^{l'} = e^{l+l'}, \qquad m^s \times m^{s'} = m^{s+s'}, \qquad e^l \times m^s = \psi^{l,s} \ , \tag{8.69}$$

we will now consider the braiding between such excitations.

---

[4]Note that for a τ^l that acts on a vertical edge we need to act with a $\sigma^{-l\widehat{k}}$ rather than a $\sigma^{l\widehat{k}}$. This is is shown in Figure 8.7b as well.
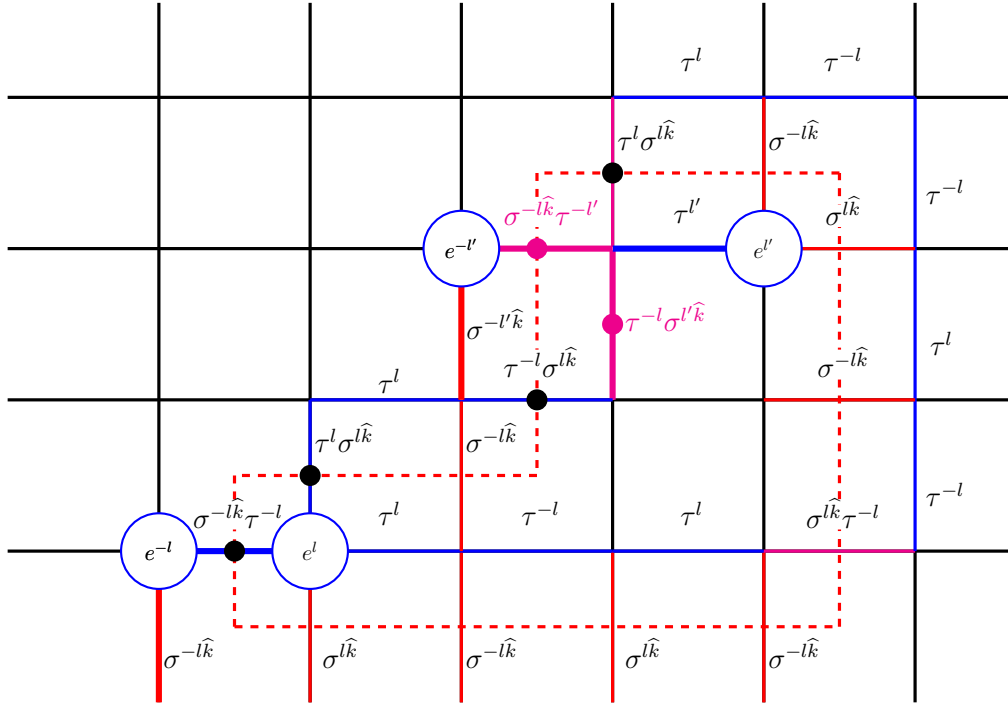
Figure 8.8: The commutation relations can be found by bringing the electric particle e^l around $e^{l'}$. When there are two operators acting on an edge, they are written in the order of occurrence acting on the ground state, from right to the left. For clarity, we have added a dashed loop where the σ's act. As the loops of electric particles are trivial when acting on the ground state, the phase difference between the initial state and the final one can be obtained by commuting the loop with the action of the l' electric particles. The non-trivial commutations enter at the meeting points between the blue loops with the red loops and similarly at the edges coloured in magenta. Note that since edge orientation and cilia have played their role in the definition of the operators, we can avoid displaying them.

8.3.2 Braiding of excitations and exchange statistics

Braiding between particles in anyon models is encoded by the $\mathcal{R}$-*symbols* (not to be confused with the R matrix), which describes the exchange statistics of two anyons (100). We discussed $\mathcal{R}$-symbols and the anyon Hilbert space in Chapter 2, and we discussed the braiding of anyons in the $\mathbb{Z}_2$ toric code in Section 7.4.

Given two anyons a, b that fuse to c, their $\mathcal{R}$-symbol is denoted $\mathcal{R}_c^{a,b}$. In conventional Kitaev quantum double models, the braiding of particles is found by considering loops between particles. In particular we can consider an electric particle e^l looping around another electric particle $e^{l'}$ as shown in Figure 8.8. It is understood that all the operators shown in the figure are acting upon the ground state. In order to find the braiding relations between particles, we need to move the blue and red loops across the particle creation operators, so that they can act on the ground state. Since the ground state is the same as the Kitaev model, and the two loops leave it unchanged, the state in which just the four particles are created is equivalent, up to a phase, to the state in which e^l encircles $e^{l'}$.

This phase difference can be found by commuting all the σ operators to the right of the τ operators. The phase difference then corresponds to the monodromy between electric particles, and it is given by

$$(\mathcal{R}^{e^l,e^{l'}}_{e^{l+l'}})^2 = \omega^{l'^2\widehat{k}-l^2\widehat{k}-2ll'\widehat{k}} = \omega^{-2ll'\widehat{k}} . \tag{8.70}$$

This implies that electric particles can have dyonic statistics, depending on the $\widehat{k}$ that comes from the R matrix. Further, they can be mapped to the dyonic excitation of Kitaev models The monodromy of electric particles has also been derived for $\mathbb{Z}_N$ gauge theory in (60). However, as already pointed out, dyonic excitations are not elementary in nature, as dyonic excitations are a combination of electric and magnetic charges that can be broken up into lower energy states. If we choose an R-matrix with $k = 0$, then the braiding reduces exactly to the familiar Kitaev model. The commutation between an electric particle e^l and a magnetic particle $m^{l'}$ is the same as usual, and the braiding statistics are given by

$$(\mathcal{R}^{e^l,m^s}_{\psi^{l,s}})^2 = \omega^{ls} , \tag{8.71}$$

while magnetic particles have bosonic statistics:

$$(\mathcal{R}^{m^s,m^{s'}}_{m^{s+s'}})^2 = 1 . \tag{8.72}$$

Note Equation (8.71) and Equation (8.72), are not affected by the $\widehat{k}$ parameter (and therefore by the R matrix). We shall succinctly display the effect of the $\widehat{k}$ dependence using the twist factors. The $\mathcal{R}$-symbols are related to the twist factors θ_a by

$$\theta_a = \sum_c \frac{d_c}{d_a} \mathcal{R}^{a,a}_c . \tag{8.73}$$

For Abelian anyons, the quantum dimensions d_c, d_a are equal to one and the summation restricts to the single fusion outcome of the two a anyons (24; 100). It is now easy to compare the twists obtained in conventional Kitaev models with what we obtained:

	θ_{m^s}	θ_{e^l}	$\theta_{\psi^{l,s}}$
Hopf algebra gauge theory	1	$\omega^{-l^2\widehat{k}}$	$\omega^{ls-l^2\widehat{k}}$
Kitaev Models	1	1	ω^{ls}

Observe how the process that we described is reminiscent of flux attachment (5; 82; 142; 172). The elementary charges behave as if they have $-\widehat{k}$ units of flux attached to them during the braiding. In a full exchange, we get just the Aharonov-Bohm phase factors for taking each charge around the flux of the other particle (see (8.70)).

To summarise, the exchange statistics are determined by the k parameter in the R matrix. The introduction of the braided tensor product (and the related R matrix) amounts to interchange particle ψ^{ls} and $\psi^{l(s-l\widehat{k})}$ with respect to conventional Kitaev model. The exchange statistics are, therefore, formally the same as the original Kitaev model, but which excitations appear as elementary, minimal energy, depends on the specific choice of the R matrix.

8.3.3 Automorphism for non-Abelian quantum double models.

This construction can be readily generalised to a non-Abelian group with an Abelian normal subgroup. As an example, one could consider a toric code model constructed over say, D_3. We discussed non-Abelian toric code models and the associated quantum double in Section 7.6. As we said many of the features of the $\mathbb{Z}_N$ toric code model generalise naturally, however the string operator structure we used to characterise excitations and their braiding becomes more involved in the non-Abelian case. As we menioned another approach is to consider representations of the quantum double abstractly. We shall follow this approach in this section. This quantum double of D_3 and the corresponding anyon model has been studied via the representation theory of the quantum double in Refs.; (20; 55; 56). Then by defining an R matrix on $\mathbb{C}\mathbb{Z}_3 \trianglelefteq \mathbb{C}D_3$, we can examine permutations of order three of the fusion algebra of $D(D_3)$. This will again lead to a mixing of the dyonic and electric sectors in the model. Therefore we can look for order three permutations in $\mathrm{Aut}(\mathrm{Rep}(\mathrm{D}(D_3)))$ which are in the electric and dyonic sectors

First, let's tabulate the conjugacy classes;

$$[C_e] := [e] \qquad [C_r] = \{r, r^2\} = [r] \qquad [C_s] = \{s, sr, sr^2\} = [s]. \tag{8.74}$$

The normalizers, i.e. $(N_g = \{h \in G, gh = hg\})$ are given by;

$$
\begin{aligned}
N_e &= D_3, & N_r = N_{r^2} &= \{e, r, r^2\} \simeq \mathbb{Z}_3, \\
N_s &= \{e, s\} \simeq \mathbb{Z}_2, & N_{sr} = \{e, sr\} \simeq \mathbb{Z}_2, & \quad N_{sr^2} = \{e, sr^2\} \simeq \mathbb{Z}_2.
\end{aligned}
\tag{8.75}
$$

Each particle in $\mathrm{Rep}(\mathrm{D}(D_3))$ is labelled by a conjugacy class and the normalizer of a representative of that class.

So we denote;

$$\mathrm{Irr}(\mathbb{Z}_2) = \{\psi_0, \psi_1\}, \qquad \mathrm{Irr}(\mathbb{Z}_3) = \{\chi_0, \chi_1, \chi_2\}, \qquad \mathrm{Irr}(D_3) = \{J_0, J_1, \alpha\}. \tag{8.76}$$

We can now tabulate the corresponding excitations

	A	B	C	D	E	E	F	G
Conjugacy class	$[e]$	$[e]$	$[e]$	$[s]$	$[s]$	$[r]$	$[r]$	$[r]$
$\mathrm{Irr}(N_g)$	J_0	J_1	α	ψ_0	ψ_1	χ_0	χ_1	χ_2
d_a	1	1	2	3	3	2	2	2

The pure electric charges, corresponding to violations of the gauge invariance constraint are $\Pi_{J_1}^{[e]}$ and $\Pi_{\alpha}^{[e]}$. The pure flux, corresponding to violations of the flatness condition are given as trivial irreps of N_g, but non-trivial conjugacy class $[C_g]$ i.e. $\Pi_{\chi_0}^{[r]}$ and $\Pi_{\psi_0}^{[s]}$.

Now to find the automorphisms of the fusion algebra we can use the quantum dimensions. Since any automorphism of the fusion algebra must preserve the quantum dimensions and the automorphism we are looking for must be of order three, we know it must act on; E, F, G. Permutations of the fusion algebra of $D(D_3)$ have already been studied in (20), and are connected to modular invariants of the category of representations.

8.4 Summary

In this chapter, we have constructed a modified $\mathbb{Z}_N$ toric code model starting from Hopf algebra gauge theory. The toric code is one of the most ubiquitous models in topological physics. As we discussed in Chapter 7, the toric code can be understood as a discrete group gauge theory, where gauge invariance is encoded by an energy penalty. This model has many features crucial for topological physics: topological ground state degeneracy, anyonic excitations and protected ground states. We studied a generalised discrete group gauge theory, namely, a gauge theory where that the gauge symmetry is given by a quasitriangular semisimple Hopf algebra. This framework has been developed in (124) and the connection with toric code models was proven in (123). In order to make gauge transformations and holonomy compatible for an arbitrary Hopf algebra, the multiplication of functions must be modified, or equivalently, twisted, by an R matrix in the gauge symmetry, which is known as the braided tensor product.

We focused on a lattice construction in the case the gauge symmetry is given by $\mathbb{C}\mathbb{Z}_N$. However, we introduced a non-trivial R matrix on this Hopf algebra. We found that the braided tensor product introduced novel features into the model. For example, we outlined in Section 8.2.2, how the braided tensor product modified the computation of holonomy in the theory. We showed explicitly how this modified the plaquette operator in Section 8.3. We found that our plaquette operator $\mathcal{B}_p$ differs from the standard $\mathbb{Z}_N$ toric code plaquette operator B_p, by the addition of a vertex operator $A^{a^{\hat{k}}}$ at the vertex where the holonomy begins, see Figure 8.5.

We then showed in Section 8.3.2 that this led to a change in the identification of the electric and dyonic sectors of the theory. Specifically, the string operators which create purely electric charges in the $\mathbb{Z}_N$ toric code can create dyonic excitations in the $\mathbb{C}\mathbb{Z}_N$ Hopf algebra gauge theory, depending on the choice of R matrix on the Hopf algebra gauge symmetry. We proposed one way to understand these novel excitations, noting that the electric excitations act like they have magnetic flux units attached. This is known as flux attachment.

In Section 8.3 we showed that a local gauge transformation can not remove this additional vertex operator. We showed this by calculating the cohomology groups of the algebra of functions. We found the second cohomology group was non-trivial. This implies that a local gauge transformation cannot remove the phase factors in the algebra of functions, which we showed in Table 8.3. This is what induces the additional vertex operator into our plaquette operator.

In Section 8.3.3 we showed one further application of our work. From the $\mathbb{C}\mathbb{Z}_N$ case, we knew that the choice of non-trivial R matrix led to a permutation between the electric and dyonic sectors. We then extended this to a non-Abelian group containing a $\mathbb{Z}_N$ normal subgroup. In particular we chose to illustrate this with D_3, the Dihedral group on 6 elements, which has a $\mathbb{Z}_3$ normal subgroup. We know that defining a non-trivial R matrix on $\mathbb{C}\mathbb{Z}_3 \trianglelefteq \mathbb{C}D_3$ will lead to an order three permutation on the fusion algebra. Then by studying the representation theory of $D(D_3)$ we found one such permutation.

Chapter 9

Conclusion

In this thesis we have studied several aspects of braiding of anyons in two-dimensional and quasi-one-dimensional systems, focusing on implications for topological quantum computation. Specifically, we studied: the braiding of anyons on graphs, error processes in Majorana-based topological qubits from non-adiabatic perturbations and finally, braiding statistics in modified toric code models.

Graph braiding of anyons

In Chapter 3, we presented the fundamental concepts of adapting anyon models to exchanges on a graph. On the physical side, this is motivated by recent proposals for engineering anyon like excitations on wire networks, which may used for fault-tolerant quantum computation. Therefore, it is important to understand what are the similarities and differences between braiding anyons on the plane and braiding anyons on a graph. It is also of academic interest. The algebraic theory of anyons is an elegant abstraction of a rich and complex area of topological physics, and therefore extending this framework to more general exchanges, such as those on graphs, would represent an exciting development. In the algebraic theory of anyons, the braiding operators, known as R-symbols are calculated by solving the hexagon equations for a given set of fusion rules and F-symbols (100; 127). We discussed some of the main features of the algebraic theory of anyons in Chapter 2. In particular, we discussed how the hexagon equations arise from braided tensor categories, see Section 2.5. We provided a brief summary of some of the main features of graph braid groups in Section 3.2 and further details can be found in Refs. (114; 116). In Section 3.3 we then derived the analogous constraint equations for exchanges at a vertex of a graph, as a model for a junction in a quantum wire network. We constructed this by mirroring the planar theory and enforcing that fusion and graph braiding should be compatible. These *graph braiding hexagon equations* are a generalisation of the planar equations. As we discussed, we recover the planar hexagon equations as a particular case.

One of the major implications of this work is supporting the notion that topological excitations on a wire network can host the same exchange statistics as anyons in the plane (8). However, there are several differences. In planar models, the set of solutions modulo gauge is finite– this is known as Ocneanu rigidity (70; 100). As we discussed, for several graph anyon models, we find continuous families of solutions. For example, for the Ising fusion category we find a two $U(1)$ parameter family of solutions, and for a fusion algebra constructed over a finite Abelian group G, we find at least $(|G| - 1)^2$ parameter family of solutions. We also find solutions for graph braiding anyon models which have no planar solution. For example, for a fusion category with $\mathbb{Z}_3$ fusion rules with a non-trivial cocycle, there is no solution to the planar hexagon equation (28), yet we find a four-parameter family of solutions, see Equation (3.28).

Another notable difference is related to whether our consistency equations are all of the necessary conditions; which is related to coherence. In the planar case, we only have to consider the fusion of four anyons and the braiding of three anyons, as guaranteed by the Mac Lane (monoidal) coherence theorem (117), and the braided coherence theorem (141), respectively. Since we did not modify the fusion rules or F-symbols, the Mac Lane (monoidal) coherence theorem also holds for our models. However, on a graph, introducing more particles leads to additional topologically inequivalent ways to exchange the particles. This requires the construction of further consistency equations beyond the hexagon equations, as we discussed in Chapter 4 and Appendix A. To gain further insight into the exchange of particles on a graph, In Section 3.6, we constructed a local hopping model of quasiparticle excitations to model our solution to the graph braiding hexagon equations when the fusion algebra is given by $\mathbb{Z}_2$. We show that by introducing an ancillary degree of freedom we can exactly model the solution. One natural further direction presents itself here. In particular a generalisation of our hopping model to non-Abelian anyons, which would then give a local hopping model for non-Abelian anyons on a junction. There is such a model for one particular non-Abelian anyon, namely Majorana bound states (8). However, it's not necessarily clear how to generalise the junction degree of freedom beyond Abelian statistics to arbitrary anyons.

In Chapter 4, we extended the formalism from Chapter 3, to include: graphs with more than one vertex, graphs containing loops, and also more particles. We first revisit the trijunction from Chapter 3, but with a focus on the greater particle number consistency equations. In particular, we discuss techniques to construct such equations, namely using fusion commuting with graph braiding and conjugating by β moves. One of the notable results here is how to *reduce* a graph braid. On a trijunction, as we increase particles, we discuss how the last "new" generator is introduced at $N = 4$ particles. Any generator involving an exchange at the level of $N > 4$ particles can be *reduced* to, at most, a graph braid generator involving

$N = 4$ particles. We develop this idea in Section 4.2 and Appendix A. This paves the way towards a graph anyon model coherence theorem, as we know how many independent generators there are in terms of the valence of the junction. The first new graph we study in Chapter 4 is the circle graph, on which we introduce a new graph braid symbol D. This corresponds to the δ graph braid generator, whose action is given by cycling the particles around the loop. Here we find a significant distinction from the graph anyon models in Chapter 3. We find that the graph anyon model on a circle is coherent at three particles. We show this by constructing a four-particle consistency equation in Section 4.4.1, which we are able to express purely in terms of the three-particle consistency equations. It should be noted that this is not a planar anyon model- for example, on a circle we find solutions to the graph hexagon equations which do not exist in the plane, e.g. $\text{TY}(\mathbb{Z}_3)$.

One of the crucial results in Chapter 4 is the proof that on a theta graph, the graph anyon model is equivalent to the planar anyon model. This result was already shown at the level of the Artin braid group, and the theta-graph braid group in (10). Here we extend the proof to include the fusion structure of anyons and also the framing, or world-ribbon structure (146). We find this necessitates the introduction of half twists of the anyon world-ribbons, as we discussed in Appendix B. We see this equivalence of the planar anyon model and the graph anyon model on a theta graph as a good consistency check for the validity of the framework. In Section 4.8 we discussed one application of our results to topological quantum computation (TQC), namely the circuit depth of a unitary gate. We discussed how on a stadium graph, consisting of two theta subgraphs decorated by four particles, the solutions for the graph braid anyon model on each theta graph generate a collection of topological gates $\mathcal{S}$ and $\mathcal{S}'$, which can be chosen independently. We chose an example of $\text{TY}(\mathbb{Z}_2 \times \mathbb{Z}_2)$ to illustrate this. This leads to the possibility of generating a bigger subgroup of $SU(4)$ than would be possible on either theta graph individually. On each of the graphs in this chapter, we considered the graph anyon model constructed over the fusion algebras; $\mathbb{Z}_N$, for some N, Fibonacci model, Ising model, $\text{Rep}(D_3)$, $\text{Rep}(D_4)$ and $\text{TY}(\mathbb{Z}_3)$.

One obvious further research direction presents itself, an adaption of the Mac Lane coherence theorem to graph anyon models. In the planar case, coherence of fusion (monoidal product) is provided by the Mac Lane coherence theorem (117). The analogous structure for 2D braiding is proved by Joyal and Street (141). To prove a similar relation in our situation, we would need to construct a full categorical treatment of graph anyon models. However, due to the structure of the graph braid group changing depending on the graph in question and the number of particles, this is a difficult challenge. However, the benefit would be that it would give an exhaustive list of consistency equations that need to be solved to fully determine the system.

This direction would lead to a "graph braided tensor category", which could generate its own interest in the mathematical community. Additionally in a proper categorical description, we would like to be able to "combine" the categories and their consistency equations. For example, consider the lollipop graph in Section 4.5, which contains two proper subgraphs: a circle and a trijunction. In a proper categorical description, we would like to view the lollipop braided category as a combination (or monoidal product) of a circle braided category and the trijunction braided category. This would then provide a recipe for constructing consistency equations on larger graphs from smaller local pieces of the graph. This would be of mathematical interest but also useful for TQC in the following two ways. For realistic implementations, one would have many wires joined into complicated networks. However, currently one would have to construct the graph braid group of the entire network and then use fusion commutes with braiding, and the procedures outlined in Chapter 3 and 4, to construct consistency equations. Currently, this must be done on a graph-by-graph basis and can be quite tedious. It would be immensely beneficial to have a recipe to understand how the consistency equations scale and change as the complexity of the graph changes.

One of the most significant results of our graph anyon framework is our proof in Section 4.7 and Section D, that the graph anyon model on a theta graph is equivalent to the planar braided tensor category. This has huge implications for topological quantum computation on networks, as this guarantees that braiding on a wire network that is at least of the same connectivity as the theta graph produces the same computational gates as a planar anyon model, since it generates the same solutions to the hexagon equations.

On the physical side, for the input data to our graph anyon models, we take a fusion algebra (or fusion category); however, we do not discuss how such models arise on a one-dimensional line. There have already been developments on one-dimensional excitations hosting fusion rules analogous to anyons, such as Majorana modes (8; 136; 154), which was also the focus of Chapters 5 and 6. A natural next step would be to adapt the local hopping model we introduced for $\mathbb{Z}_2$ anyons in Section 3.6 to non-Abelian anyons. This may provide a deeper understanding of the braiding of excitations on junctions. In particular as we discussed for the $\mathbb{Z}_2$-anyons, we needed to include an auxiliary degree of freedom in order for the graph braiding process to be non-trivial. Understanding how this model generalises to non-Abelian anyons would shed light on what other planar anyon statistics can be recovered on a nanowire junction.

Majorana modes are just one example of a zero mode, there are also generalisations known as parafermion zero modes (71). Parafermion zero modes are associated with the non-Abelian anyon in the Tambara-Yamagami braided/fusion category, see Section 2.6.2 for details on these categories. Notably, for braiding in the plane, the

Tambara-Yamagami categories are braided only when $G = (\mathbb{Z}_2)^n$, for some n. For example, this means in the case $G = \mathbb{Z}_3$, the category is only a fusion category, and there is no solution to the planar hexagon equation. However, $\mathbb{Z}_3$-zero modes can exist on "wires" consisting of interfaces between two topologically non-trivial bulk theories see e.g. (46; 90). As we proved in Appendix C, there is no solution to the graph braiding hexagon equations on a trijunction for the Tambara-Yamagami category unless $G = (\mathbb{Z}_2)^n$, for some n. Since our work does not include data from a topologically non-trivial bulk, our obstruction to a solution supports the claim that parafermion zero modes can only exist on 1D edges on the boundary of a topologically non-trivial 2D bulk.

Another obvious direction would be to consider the graph as a collection of one-dimensional defects in a topologically non-trivial two-dimensional bulk. Physically this is related to anyon condensation (43; 66). Our framework then provides a recipe to analyse the possible braiding solutions for a given set of point defects shuttling on the one-dimensional edges.

Majorana nanowires

In Chapters 5 and 6 we focused on one particular example of an anyon model, namely Majorana bound states (MBS). In Chapter 5, we examined the theoretical framework proposed to host MBS in one-dimensional systems, namely a p-wave superconductor tuned to a topologically non-trivial phase. This model has been proposed as a topological qubit due to the robust nature of the degenerate ground state manifold (99). We discussed the topological qubit in Section 5.5. Our focus with this model was to study non-adiabatic effects. This is motivated by the braiding of such a qubit to enact a gate for a topological quantum computer. This requires shuttling the Majorana around a quantum wire network (8), which is an inherently non-adiabatic process (156).

In Chapter 6 we studied the dynamical evolution of a topological qubit that consists of two p-wave superconducting wires separated by a non-topological junction. This is the minimum set-up for a topological qubit, as discussed in Chapter 5 . We studied two regimes of possibly non-adiabatic perturbations to the system: periodic driving in the boundary potentials and shuttling of the Majorana bound states. We studied two types of error in each regime: qubit loss and bit flip. Our motivation was to understand how these error processes can arise due to non-adiabatic variations of system parameters. We examined periodic driving of the boundary potentials in Section 6.3.1 as a toy model for noise in the confining potential of the topologically non-trivial phase. When one thinks of building these systems in practice, this is certainly an effect that must be considered. We fixed the total distance the wall is moved, which gives us two parameters to consider: velocity and acceleration. We found, for small values of the velocity that the qubit loss is relatively insensitive to

the acceleration. If the velocity is above the critical velocity, we found the qubit loss is substantial regardless of the acceleration, which is in agreement with earlier work in the area (95; 156). There is another feature we find noteworthy here. By examining 6.3, we observed that the rate of qubit-loss is highest when the wall oscillation frequency ω was close to the gap energy $E_{\text{gap}} = \Delta k_F$. This is a somewhat surprising result; naively one would expect at a sub-critical velocity, increasing the frequency of the oscillation would always make the qubit loss worse. However, this is not the case. This weakening of the stability of the qubit as the energy gap is increased had not been identified in this regime before. In many of the current experimental implementations there is a major drive to increase the energy gap. In fact, this is one of the main signatures that the topological phase has been produced, see e.g. (3). Our work shows that when the experiments move towards implementing braiding protocols, increasing the energy will not necessarily lead to a more stable qubit. Of course it becomes important to verify these results in the more realistic model, the proximity coupled nanowire with induced s-wave superconductivity (136).

Our analysis on secondary bit-flip errors in Section 6.4.1 showed that it is necessary that non-adiabaticity occurred in both wires, and that inter-wire tunnelling was present for this error channel to be open, we can see this in Figure 6.8. This gives an explicit mechanism for such an error to occur; non-adiabaticity in one wire creates excitations, which then tunnel into the other wire, and since it is also undergoing non-adiabatic evolution, this excitation can relax to the ground state manifold and induce an error in the topological qubit. Of course, this type of error can be reduced by keeping the barrier between the two topologically non-trivial phases as high as possible, or equivalently keeping the two topologically non-trivial phases well separated. In Section 6.4.2 we discussed another source of error prevention: introducing disorder into the middle regions of the topological phases. This can prevent the propagation of excitations via localisation. Of course, the disordered regions must be kept well separated from the MBS confining potentials as this can reduce the robustness of the qubit by reducing the gap (32; 62; 170). Moreover, this can also make the qubit more susceptible to errors under transport. It was shown in (95), that moving the confining potential (and the associated Majorana bound states) over a disordered region results in a dramatically lower critical velocity, thus severely hampering the rate at which gates can be mechanically performed.

There are several directions naturally provided by our results. Our analysis excludes errors due to interaction with an external environment, and therefore the results only incorporate a subset of possible error processes. It would be a natural question as to how the interaction of the system with an external environment modifies our results. Furthermore, and probably the most obvious direction, is to extend our results to a more realistic model of this system such as the proximity coupled nanowire with induced superconductivity (136). While the p-wave superconductor

is a perfect playground to discuss Majorana bound states, it is an idealised model. There has also been further work in this area; e.g. Ref.(51), where they included electron-electron interaction terms in the Hamiltonian. Although in an ideal physical implementation, these terms would be screened, in practice it's impossible to fully screen this effect. In addition, our results on dynamical transport have been extended in Ref.(53), where machine learning was used as a technique to study different movement protocols.

Hopf algebra gauge theory

In Chapter 8 we discussed one extension of the toric code model presented in Chapter 7. We examined the formalism of Hopf algebra gauge theory introduced in (124). This is a generalisation of discrete group lattice gauge theory, which is equivalent to the toric code model (102; 171). We chose a simple example with the gauge symmetry given by a quasitriangular Hopf algebra defined over $\mathbb{C}\mathbb{Z}_N$. Our focus was on calculating the relevant lattice quantities for toric code models, like the vertex and plaquette operators. However, the plaquette operator is modified in Hopf algebra gauge theory by the braided tensor product. This involves twisting the multiplication of functions by an R matrix, which is an element of the gauge group. This introduces several features. Firstly, a non-trivial choice of quasitriangular structure on $\mathbb{C}\mathbb{Z}_N$ breaks the explicit electric-magnetic duality of the model's stabiliser operators. In Section 8.3.2, we found the exchange statistics are modified when compared with the $\mathbb{Z}_N$ toric code. We showed that the introduction of the braided tensor product and the associated R matrix leads to a permutation on the braiding statistics of the model. In particular, in the case of $\mathbb{Z}_N$, when we considered the braiding statistics of the electric particles, due to the extra vertex operator in the plaquette operator, the local operator that creates the electric particles also created fluxes. In this case, the introduction of a nontrivial R-matrix amounts to flux attachment, permuting the excitation spectrum. In particular, this amounted to an interchange of particles ψ^{ls} and $\psi^{l(s-\widehat{lk})}$ with respect to the conventional Kitaev model. Therefore, the exchange statistics are formally the same as the original Kitaev model, but which excitations appear as elementary depends on the specific choice of R matrix.

We find this to be a rather interesting result; since we recover the familiar fusion statistics one would expect- however, the braiding statistics are modified. The most important aspect here is that the minimum stabiliser violating excitations can have fermionic or anyonic statistics, depending on the choice of R matrix, whereas in the conventional toric code the equivalent excitations have bosonic statistics. We can recover this by choosing the trivial R matrix: $R = 1 \otimes 1$. Our results show an intimate connection between automorphisms of the braiding structures of the excitations and choices of an R matrix for the braided tensor product. This connection was not known previously.

In Section 8.3.3 we showed one further application of our work. We considered the toric code model constructed over D_3, the dihedral group on six elements. We can define a non-trivial R matrix on $\mathbb{C}\mathbb{Z}_3 \trianglelefteq \mathbb{C}D_3$, we know this R matrix will be of order three, and we know from the $\mathbb{Z}_N$ case the fusion structure is unchanged. Hence to understand the implications of the R matrix, we examined automorphisms of order three on $\text{Rep}(D(D_3))$, the representations of the quantum double of D_3.

It would be interesting to generalise this work to other Hopf algebras, beyond group algebras. One notable example would be H_8, which is the unique semisimple Hopf algebra of dimension 8 and is not constructed over a group algebra (36). The representation theory of $D(H_8)$, the quantum double of H_8 has been studied in (39; 40). This Hopf algebra allows for multiple R-matrices and it would interesting to see if a similar interpretation of the permutation of the excitation spectrum is possible here. Via Tannkian duality, the corresponding anyon model is already known to be Tambara-Yamagami with $G = \mathbb{Z}_2 \times \mathbb{Z}_2$ (36; 40), so forming a lattice realisation of this anyon theory and studying how the choice of R matrix affects the exchange statistics would be interesting. Furthermore, since it is non-Abelian anyon theories that are of real use to topological quantum computation, this work could have implications for practical implementations of this theory.

Summary

In conclusion, this thesis has explored various implementations of braiding, driven by both academic curiosity and the compelling prospect of topological quantum computation. Quantum computation holds the promise to revolutionise computation. However, it suffers from inherent sensitivity to interaction with the environment. Topological quantum computation is one possible solution to this problem by encoding fault tolerance into the hardware of the machine. There are several new branches to Kitaev's original idea. One that we have devoted much of our attention to is topological quantum computation on networks of quantum wires. There are many merits to this approach. Although there are natural challenges to constructing the topologically non-trivial phase, once it is established, there are solid principles for how to implement transport of the excitations and hence, braiding. For 2D implementations, the anyons exist around magnetic flux quanta, which cause local minima or maxima in the electron fluid. This can make implementing braiding in a controlled fashion challenging. For either of these implementations, there are experimental challenges. In particular, a definitive measurement of a non-Abelian anyon is still absent in both cases. Nevertheless, substantial investments from research groups and private sector entities attest to the significant potential of this avenue.

Aside from quantum computation, anyons and their mathematical structure attract a lot of attention from the mathematics and mathematical physics community and will no doubt be pursued for many years. The fact that the anyon and category

theory communities find mutual interest is exciting and encouraging. There are constantly new topics spawning from ideas that originated in this field. In this regard, we have demonstrated an extension of the algebraic theory of anyons to braiding on wire networks. This project in particular opens the door for several mathematical developments and sheds light on topological quantum computation on networks. These graph anyon models represent a new frontier for this area which lies at the intersection of mathematical physics, category theory and quantum computation.

Appendix A

Towards coherence: increasing particle number

In this section, we will discuss how our graph anyon models change when increasing particle number. In particular, we will look into the coherence property of these anyon models – is there a particle number N_0 above which no new consistency relations appear?

Firstly, let us discuss what coherence is and why it is *a priori* not clear that our anyon models have this property. The coherence of anyon theory in the plane has been discussed e.g. in (100). In order to formulate coherence for N anyons, one considers a diagram whose nodes are all the possible N-anyon fusion trees and the edges are the F-moves between the fusion trees. The coherence theorem for F-moves (fusion coherence) states that any sequence of F-moves between a fixed pair of nodes of such a diagram results with the same morphism of the corresponding topological Hilbert spaces, provided that the pentagon equations are satisfied. In other words, solving the consistency equations for the F-moves in the case of $N = 4$ anyons implies that the entire theory is consistent for any $N > 4$. Similarly, the braided coherence theorem states that any sequence of morphisms which involves F- and R-moves between two fixed states results with the same morphism of the corresponding topological Hilbert spaces provided that the pentagon and hexagon equations are satisfied. The proof of this theorem relies on more abstract results in category theory, known as the Mac Lane monoidal (fusion) coherence theorem (117), and the braided coherence theorem, (141).

One of the first things to observe is that we *do* have the fusion coherence, since, as discussed in (50) and in Chapter 3, we do not modify the fusion rules and we use the same F-symbols as the planar anyon models. However, the braiding structure on networks is different. When considering higher numbers of anyons, more and more topologically inequivalent generators of the graph braid group are introduced (see Section 4.2, further details of which can be found in (10)). In order to faithfully represent the new generators of the graph braid group, we introduce new symbols

when increasing the number of particles from three to four, see Equation (4.2). Additionally, new consistency equations are introduced, e.g. for $N = 4$ anyons on the trijunction there are four new equations (4.4), (4.5), (4.7) and (4.10). As we explain in Section 4.7, if the graph is sufficiently highly connected, we recover planar braiding and therefore all the aforementioned coherence theorems known from the planar anyon theory. However, all the biconneted and one-connected graphs require separate treatment. For concreteness, we will next focus again on a trijunction. The entire following discussion extends in a natural way to arbitrary graphs.

As we explained in Chapter 3,our aim is to build an anyon theory which faithfully represents topologically inequivalent graph braid group generators. This is done by assigning different symbols to topologically inequivalent generators. If we solve all of the N-particle consistency equations, increasing the number of particles to $N+1$ introduces new generators and, in principle, new relations, which may be not be satisfied by solutions to the consistency equations for N particles. As we conjecture below, for every graph Γ there exists a certain number $N_0(\Gamma)$ such all the consistency relations for any $N > N_0(\Gamma)$ are readily satisfied by the solutions to the $N = N_0(\Gamma)$ consistency relations. This is what we call the *graph braided coherence conjecture*. For the trijunction, $\Gamma = \Gamma_T$, we conjecture that $N_0(\Gamma_T) = 5$. For the simplified anyon models defined in Section 4.2.2 (all the symbols having at most four labels), we conjecture that $N_0(\Gamma_T) = 4$.

Let's analyse first our symbols. In general for a σ_j graph braid we represent the action on the fusion vector space by a "symbol", with $j+1$ upper indices and j lower indices. This is because the action of a σ_j generator involves shuttling $j+1$ particles to edges of the graph and then returning them with the order of two particles exchanged. This is what we did for the P, Q symbols corresponding to the σ_2 graph braids in Equation (3.7) and the σ_3 graph braids in Equation (4.2). Intuitively, we think of this as the action of the symbol on the fusion vector space depends on the topological charges of the particles being exchanged and the charges of the particles that must be moved out of the way. In contrast, the planar R-symbols only depend on the topological charges on the particles being exchanged and their fusion outcome, see Equation (2.6). In fact, it can be shown that if all of our graph braid symbols **only** depend on the particles being exchanged and their fusion outcome, then the graph hexagon equations reduce to the planar hexagon equations, exactly. In this situation, we simply reproduce the planar braiding of anyons. Therefore, we do not faithfully represent the graph braid group on the fusion vector space. Naturally, this is not what we want. So we will now sketch three important ideas on how to generate consistency equations for graph braided anyon models.

Reducing a generator

As we displayed in Figure 4.2, often the symbol corresponding to a σ_j generator can be *reduced* to a symbol corresponding to a σ_k, $k < j$ generator. We can do this in the case of the X symbol, because the two particles closest to the junction, which are not exchanged, both go to the same edge under the action of $X = \rho(\sigma_3^{(1,1,1,2)})$. Now let's apply this to the new generators introduced going to $N = 5$ particles on a trijunction, they are written;

$$\begin{aligned}
&\sigma_4^{(1,1,1,1,2)}, \qquad \sigma_4^{(1,1,2,1,2)}, \qquad \sigma_4^{(2,1,1,1,2)}, \qquad \sigma_4^{(1,2,1,1,2)}, \\
&\sigma_4^{(2,2,2,1,2)}, \qquad \sigma_4^{(2,2,1,1,2)}, \qquad \sigma_4^{(1,2,2,1,2)}, \qquad \sigma_4^{(2,1,2,1,2)}.
\end{aligned} \tag{A.1}$$

First, we focus on the first generator. Then following the same argument as for the X symbol, there will be a square diagram, similar to Figure 4.2. This diagrams allows us to first reduce $\rho(\sigma_3^{(1,1,1,1,2)})$ to an X symbol, which we can then reduce to a P symbol. Similarly for the second generator in the first column but to a Y symbol and then to a Q symbol. So these generators are not "new". By this we mean, that if we construct some diagram which could lead to a consistency equation for such a generator, then we can join the particles going to the same edge by a fusion vertex, slide this fusion vertex through the junction and the diagram would now correspond, possibly to a constraint equation for the symbol corresponding to σ_k, $k < j$. Now let's consider the generators in the second column, we can observe under the action of these generators the two particles closest to the junction are both sent to the same edge. So again, we can use F-symbols to join these particles by a fusion vertex and then slide that vertex through the action of these generators to reduce them to an A- or B- symbol respectively. Which are then related by the pseudocommutative relation in Equation 4.6. We can do the same thing for the third column, except with the second and third particles closest to the junction point. Now all that remains are the generators in the last column. At first, it may look like we can not reduce these generators to σ_3's. However, they are related by further pseudocommutative relations. Let's focus on the first generator in the last column, then it satisfies the following relation (see Equation (1) in (116));

$$\sigma_4^{(1,2,1,1,2)} \, \sigma_1^{(1,2)} = \sigma_1^{(1,2)} \, \sigma_4^{(1,1,2,1,2)}. \tag{A.2}$$

This relation allows us to express $\sigma_4^{(1,2,1,1,2)}$ in terms of $\sigma_4^{(1,1,2,1,2)}$ conjugated by $\sigma_1^{(1,2)}$. Then we can move to a basis where the first and second particles (which go to edge 1) are joined by a fusion vertex, then slide this vertex through the junction to reduce it to $\sigma_3^{(1,2,1,2)}$ and the corresponding A- symbol. An exactly analogous procedure can be done for $\sigma_4^{(2,1,2,1,2)}$. So to summarise, going from 4 to 5 particles naively introduced 8 new generators. However, each of these new generators has repetition in the edges the particles **not** being braided are assigned. This allows us to reduce

these generators to braids involving lower numbers of particles. Hopefully, it is clear from this discussion that as we increase the number of particles beyond $N = 4$, any diagram (or equation) involving symbols of graph braid generators can be expressed in terms of the symbols for $N \leq 4$. As such, any consistency diagram involving these generators (which will discuss next), is in fact a diagram constraining symbols we already have from $N = 4$.

Intuitively the introduction of fusion vertices has changed the isotopical equivalence. Of course, it is worth pointing out, that there is nothing special about the trijunction here, on a star graph of valence d, there will be repetition in the edge assignment for any generator involving particle number $d + 1$ or higher, we chose to focus on a trijunction for ease of exposition. Additionally, one final remark on this procedure is due, the process of "reducing" a generator can be inverted. In that, we can pick any σ_j generator, then split an anyon worldline (which is not being exchanged) to allow us to construct an equation defining a σ_l with $l > j$ generator.

Fusion commutes with graph braiding.

As discussed in Chapter 3 to construct the $N = 3$ graph braiding hexagon equations we sought combinations of graph braid generators such that we could slide a fusion vertex through a graph braid. These equalities of states containing crossings are expressing the "naturality" of braiding with respect to fusion (69; 96). Examining Figure 3.9 in the bottom left of the diagram, we display the fusion commutes with braiding state from Figure 2.8. The hexagon equation is then constructed by taking two different paths (sequences of F- and graph braid symbols) and equating the resulting maps. This procedure can be lifted to greater numbers of particles. We have already displayed an example of a fusion commuting with graph braiding for four particles in Figure 4.4.

One can follow the exact same procedure, starting from the furthest right state (containing the least crossings) we resolve the graph braids to arrive at a state containing just fusion. Then from each state in the fusion commutes with graph braiding, we resolve the graph braids and use the F- symbols to arrive at a fixed fusion state. We then equate the sequences of maps to arrive at a consistency equation. We display a schematic of this idea in Figure A.1

Polygon relations coming from lifting the hexagons

Recall the P- and Q-hexagons which were derived from the following relations expressing fusion commutes with graph braiding from $N = 3$ anyons on a trijunction

$$\sigma_1^{(1_a, 2_c)} \sigma_2^{(2_c, 1_a, 2_b)} = \sigma_1^{(1_a, 2_{b \times c})}, \quad \sigma_2^{(1_b, 1_a, 2_c)} \sigma_1^{(1_b, 2_c)} = \sigma_1^{(1_{a \times b}, 2_c)}. \tag{A.3}$$
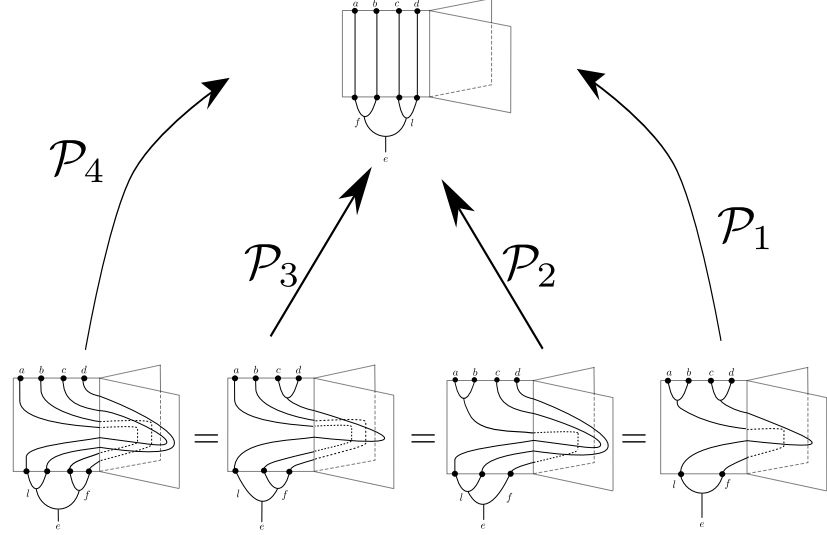
Figure A.1: A graphical representation of constructing $N > 3$ polygons starting from one example of fusion commuting with graph braiding. We schematically denote the sequence of F- and graph braid symbols to arrive at the state containing just fusion by $\mathcal{P}$.

One can lift the above relation in order to impose the commutativity of fusion and braiding for any $N > 3$ by adding a string of particles from the side of the junction. Equivalently, we can view this as embedding $B_n(\Gamma)$ can be embedded into $B_{n+1}(\Gamma)$ via conjugation by a slide move, $\beta_{(y)}$, which shuttles a particle to edge y and back.

$$\beta_1 \, \sigma_2^{(1,1,2)} \, \beta_1^{-1} = \sigma_3^{(1,1,1,2)}. \tag{A.4}$$

This has been done for $N = 4$ in Equation (4.9). In general, if the added particles have the charges $d_1, \ldots, d_M$, we obtain the analogous relations for $N = M + 3$ by appending a sequence $\overline{x} = (x(1)_{d_1}, \ldots, x(M)_{d_M})$ to each superscript in Equations (A.3). Here, $x(k) \in \{1, 2\}$ denotes the branch of the trijunction visited by the kth anyon (of the charge d_k with anyon 1_{d_1} being the closest one to the junction). The resulting lifted relations read

$$\sigma_{M+1}^{(\overline{x}, 1_a, 2_c)} \sigma_{M+2}^{(\overline{x}, 2_c, 1_a, 2_b)} = \sigma_{M+1}^{(\overline{x}, 1_a, 2_{b \times c})}, \qquad \sigma_{M+2}^{(\overline{x}, 1_b, 1_a, 2_c)} \sigma_{M+1}^{(\overline{x}, 1_b, 2_c)} = \sigma_{M+1}^{(\overline{x}, 1_{a \times b}, 2_c)}. \tag{A.5}$$

As explained in Section 4.2, the relations (A.5) show a key property of the graph-braided anyon models. Namely, the graph braiding exchange operator representing a simple braid $\sigma_i^{(\overline{x}, x(i-1), 1, 2)}$ can be expressed in terms of the graph braiding exchange operators representing the simple braid $\sigma_{i-1}^{(\overline{x}, 1, 2)}$. By repeating this argument $(i - 1)$ times, we obtain that the graph braiding exchange operator representing a simple braid $\sigma_i^{(\overline{x}, x(i-1), 1, 2)}$ can be expressed in terms of F- and R-symbols only.

Appendix B

Half-twist of the world-ribbons on junctions

In this section, we view the anyon "world-ribbons" as ribbon diagrams embedded in $\mathbb{R}^3$, see the related work by Turaev (147). The concept of half twist has been discussed in the categorical context in Refs. (93; 161).

By considering anyons' world-lines as world-ribbons, we need to introduce some extra moves which induce a half-twist (sometimes called a π-twist) of the world-ribbon. Such a half-twist can be realised in the planar theory in the way shown in Figure B.1 and will be denoted by τ.
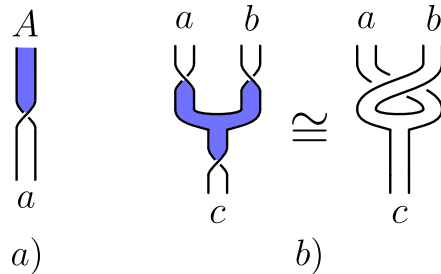
Figure B.1: Half-twists of world-ribbons in the plane. For clarity, we colour the two sides of the ribbon by white and blue. a) A world-ribbon half-twist in the plane, τ. b) Three consecutive half-twists are equivalent to the simple exchange σ_1.

In order to incorporate the half-twists as morphisms of the topological Hilbert spaces, we denote the two sides of the world-ribbon of anyon a by a (white ribbon) and A (blue ribbon) respectively. Let us start with the simplest situation of a single world-ribbon. The resulting quantum states form the following Hilbert spaces

- two one-dimensional spaces V_a and V_A for the non-twisted ribbon,

- two one-dimensional spaces for the anti-clockwise twisted ribbon denoted by V_A^a and V_a^A,

- two one-dimensional spaces for the clockwise twisted ribbon denoted by $\tilde{V}_A^a$ and $\tilde{V}_a^A$.

Note that the ribbon half-twists are not local operations, as they change the boundary conditions at the endpoints of the world-ribbon. As such, they do not have the corresponding gauge-invariant symbols. However, because a twist is a morphism between two one-dimensional Hilbert spaces, we can represent it as a complex number. Consequently, an anti-clockwise half-twist of a world-ribbon induces a morphism $\hat{\tau}$ between the one-dimensional Hilbert spaces V_A and V_a^A or V_a and V_A^a. By picking bases of the relevant one-dimensional spaces we can represent the morphism $\hat{\tau}$ by (gauge non-invariant) complex numbers T_a^A and T_A^a. Similarly, by $\bar{\tau}$ we will denote the morphism between the vector spaces V_A and $\tilde{V}_a^A$ or V_a and $\tilde{V}_A^a$ with the twist clockwise twist. The morphism $\hat{\bar{\tau}}$ will be represented by the complex number $\tilde{T}_a^A$ and $\tilde{T}_A^a$ – see Figure B.2.
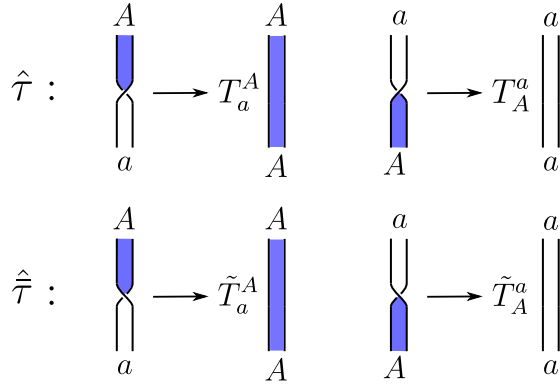
Figure B.2: The morphisms $\hat{\tau}$ and $\hat{\bar{\tau}}$ representing the anti-clockwise and clockwise half-twists respectively.

Clearly, composing an anti-clockwise half-twist with a clockwise half-twist results with a trivial move, thus we have the relations

$$T_a^A \tilde{T}_A^a = 1, \quad T_A^a \tilde{T}_a^A = 1.$$

What is more, two half-twists amount to a full twist represented by the twist factors. This gives rise to the relation

$$T_a^A T_A^a = \theta_A = \theta_a.$$

In other words, there is a canonical isomorphism between the spaces V_A^a and $\tilde{V}_A^a$ or V_a^A and $\tilde{V}_a^A$ induced the full twist and represented by the (gauge-invariant) twist factors $\theta_A = \theta_a$. Moreover, by the homotopy relation from Figure B.1b we can connect the T-symbols with the R-symbols via

$$\frac{T_c^C}{T_A^a T_B^b} = R_c^{ba}.$$

A half-twist can be realised on a trijunction in the way where the ribbon visits edge (1) of the junction, moves to edge (2) and goes back to its original position.

Such a move will be denoted by $\tau^{(1,2)}$ – see Figure B.3a. Similarly, for $N = 2$ world-ribbons we can define half-twists of the world-ribbon of the anyon which is further from the junction. Then, the first anyon needs to make space for the half-twist by first moving either to edge (1) or edge (2) of the junction. This leads to two independent ways of twisting the second anyon's world-ribbon which we denote by $\tau^{(112)}$ and $\tau^{(212)}$ respectively – see Figure B.3b and Figure B.3c.

a)   b)   c)
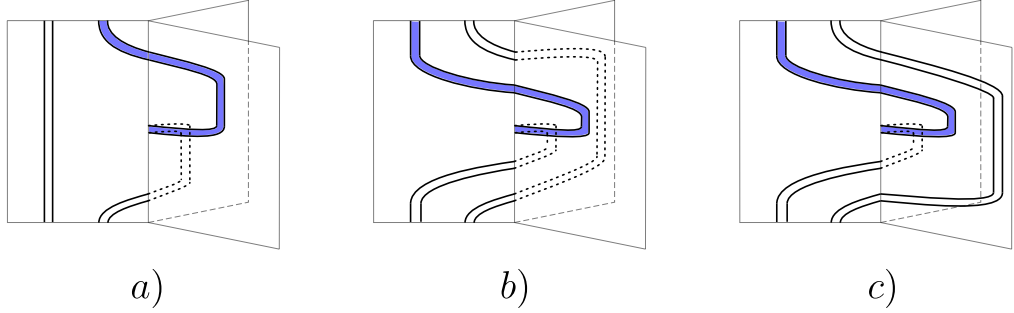
Figure B.3: Three independent world-ribbon half-twists for $N = 2$ anyons on a trijunction. For clarity, we colour the two sides of the ribbon by white and blue. a) The move $\tau^{(1,2)}$ where the world-ribbon of the anyon located closest to the junction gets the half-twist. b) and c) The moves $\tau^{(112)}$ and $\tau^{(212)}$ where the world-ribbon of the anyon located furthest from the junction gets the half-twist.

The trijunction half-twists are represented by analogous morphisms of the topological Hilbert spaces as it was in the case of the half-twists in the plane. There also exists a trijunction counterpart of the relation from Figure B.1b which reads (see also Figure B.4)

$$\tau^{(1_c,2_C)}\tau^{(2_B,2_A,1_a)}\tau^{(2_B,1_b)} = \tau^{(1_a,1_b,2_B)}\sigma_1^{(1_a,2_B)}\tau^{(2_B,1_b)}.$$
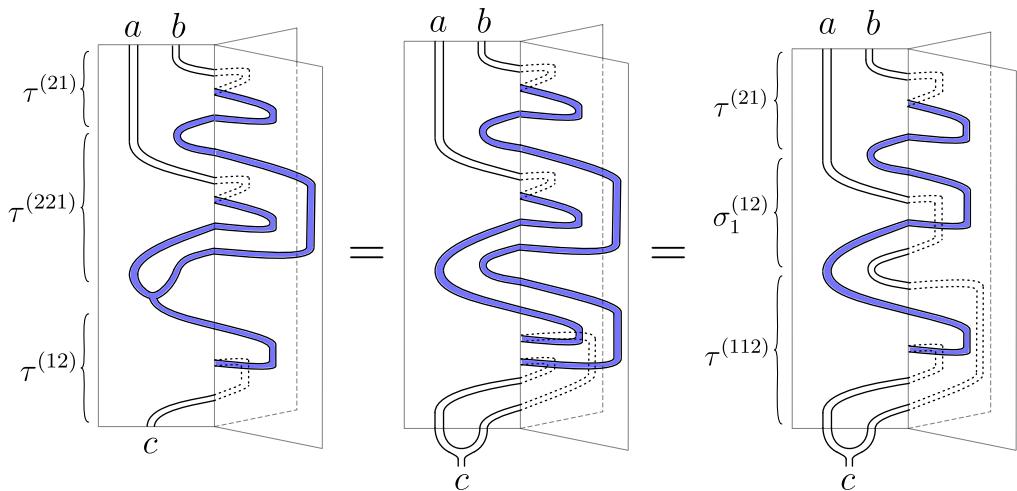
Figure B.4: A relation between half-twists on the trijunction which is a counterpart of the relation between the corresponding moves in the plane from Figure B.1b.

The moves $\tau^{(1,2)}$, $\tau^{(1,1,2)}$ and $\tau^{(2,1,2)}$ generalise to respective half-twists $\tau_v^{(1,2)}$, $\tau_v^{(1,1,2)}$

192

and $\tau_v^{(2,1,2)}$ on any tree graph in a natural way by embedding them on a local trijunction at an essential vertex v.

There is an important difference between the half-twists in the planar anyon theory and the above introduced half-twists in the anyon theory on networks. Namely, in $2D$ any spacetime diagram which involves fusion, braiding and half-twists can be resolved using local R-moves and full twists provided that all the world-ribbons that enter the diagram and leave the diagram are of the same colour (e.g. all white) (147). An example of that is shown in Figure B.1b) where three half-twists are resolved by a single R-move. However, this is no longer true for spacetime diagrams on a network. For instance, consider an analogous diagram involving three half-twists of the world-ribbons which is shown on the leftmost panel in Figure B.4. It is not possible to continuously pull the bottom half-twist in the rightmost panel in Figure B.4 through the $\sigma_1^{(1,2)}$ graph braid to cancel the top half-twist. Thus, it is not possible to resolve the spacetime diagram from the rightmost panel in Figure B.4 using an R-move.

Appendix C

Tambara Yamagami star graph obstruction

In this section we will describe the obstruction to a solution of the d valent star graph braiding hexagon equations for Tambara Yamagami over G, unless G is $\mathbb{Z}_2$ to some power. We will focus on $d = 3$, a trijunction, however, the analysis in (50), shows that this is true for any valence. We will then examine the expressions for $P_{g\sigma}^{\sigma\sigma\sigma}$ to deduce an expression that $\overline{\chi}(g_1, g_2) = \chi(g_1, g_2)$. We begin with the expression for the P-symbols from graph braiding hexagon equations starting from Equation (3.19) with $a = b = c = d = \sigma$

$$P_{g\sigma}^{\sigma\sigma\sigma} \, \nu\tau\chi^*(g, f) \, R_f^{\sigma\sigma} = \nu^2\tau^2 \sum_e \chi^*(g, e) \, R_\sigma^{\sigma e} \, \chi^*(e, f). \tag{C.1}$$

Since the values for g, f and e are group elements since they are coming from the multiplication of two σ particles, let's denote them as g_1, g_2 and g_3 respectively. Additionally since the labels that will matter for $P_{g_1\sigma}^{\sigma\sigma\sigma}$ are g_1 and the intermediate anyon label dependence on the right hand side of the equation, g_2 which we discussed previously, we shall denote, $P_{g_1\sigma}^{\sigma\sigma\sigma}(g_2) := P(g_1, g_2)$. The graph equation for P using this notation and configuration of anyons is given by

$$P(g_1, g_2) = \nu\tau\chi(g_1, g_2)(R_{g_2}^{\sigma\sigma})^* \sum_{g_3} \overline{\chi}(g_1 g_2, g_3) R_\sigma^{\sigma g_3}. \tag{C.2}$$

Now consider the following,

$$P(g_1 h, h^{-1} g_2) = \nu\tau\chi(g_1 h, h^{-1} g_2)(R_{h^{-1} g_2}^{\sigma\sigma})^* \sum_{g_3} \overline{\chi}(g_1 g_2, g_3) R_\sigma^{\sigma g_3}. \tag{C.3}$$

Since both of these expressions are non-zero complex numbers we can perform the quotient, observing they both have the same terms in the sum over g_3 to get the

following expression,

$$\frac{P(g_1, g_2)}{P(g_1, h^{-1}g_2)} = \frac{\chi(g_1, g_2)(R^{\sigma\sigma}_{g_2})^*}{\chi(g_1 h, h^{-1}g_2)(R^{\sigma\sigma}_{h^{-1}g_2})^*}. \tag{C.4}$$

Now we can we fact that χ is a symmetric bicharacter to simplify the denominator as,

$$\chi(g_1 h, h^{-1}g_2) = \chi(g_1, g_2)\chi(g, h^{-1})\chi(h, h^{-1})\chi(h, g_2). \tag{C.5}$$

Which simplifies the expression to get,

$$\frac{P(g_1, g_2)}{P(g_1 h, h^{-1}g_2)} = R^{\sigma\sigma}_{h^{-1}g_2}(R^{\sigma\sigma}_{g_2})^* \overline{\chi}(g_1 h g_2^{-1}, h^{-1}). \tag{C.6}$$

Again the right-hand side of this expression must be the same for all choices of g_2. Now since h is arbitrary, we fix it $h = g_1^{-1}$.

$$\frac{P(g_1, g_2)}{P(1, g_1 g_2)} = R^{\sigma\sigma}_{g_1 g_2}(R^{\sigma\sigma}_{g_2})^* \overline{\chi}(g_2^{-1}, g_1) \tag{C.7}$$

Now again all of these expressions are valid regardless of any choice of g_2, so we can in particular choose $g_2 = 1$, the vacuum charge then this expression simplifies to,

$$\frac{P(g_1, g_2)}{P(1, g_1 g_2)} = \frac{P(g_1, 1)}{P(1, g_1)} = R^{\sigma\sigma}_{g_1}(R^{\sigma\sigma}_1)^* \tag{C.8}$$

But again these expressions are valid for any choice of g_2, so we can equate the expressions with g_2 arbitrary to the equations with $g_2 = 1$ to get the following equation

$$R^{\sigma\sigma}_{g_1 g_2}(R^{\sigma\sigma}_{g_2})^* \overline{\chi}(g_2^{-1}, g_1) = R^{\sigma\sigma}_{g_1}(R^{\sigma\sigma}_1)^* \tag{C.9}$$

Using the fact that χ is a symmetric bicharacter, we can rearrange this equation to get

$$R^{\sigma\sigma}_{g_1 g_2} = \frac{R^{\sigma\sigma}_{g_1} R^{\sigma\sigma}_{g_2}}{R^{\sigma\sigma}_1 \chi(g_1, g_2)}. \tag{C.10}$$

Since the expressions for $Q^{\sigma\sigma\sigma}_{g_1 \sigma}$ in Equation (3.20) have inverse F-symbols, if we follow the same steps we get,

$$R^{\sigma\sigma}_{g_1 g_2} = \frac{R^{\sigma\sigma}_{g_1} R^{\sigma\sigma}_{g_2}}{R^{\sigma\sigma}_1 \overline{\chi}(g_1, g_2)}. \tag{C.11}$$

But both of these expressions must be simultaneously true so we can equate them to deduce

$$\chi(g_1, g_2) = \overline{\chi}(g_1, g_2). \tag{C.12}$$

Therefore there are only solutions for the graph braiding hexagon equations for the Tambara-Yamagami fusion category if G is a 2-group.

Appendix D

Anyon models on the Θ-graph: proving $R_e^{ba} = \tilde{R}_e^{ba}$ and $\tilde{Q}_{ed}^{bac} = \tilde{R}_e^{ba}$

In this section, we continue the proof from Section 4.7. Recall that the aim is to proove that any anyon model on the Θ-graph yields a planar anyon model provided that the circular moves δ and $\bar{\delta}$ are represented by the same D-symbols. Let us start with deriving the equality $R_e^{ba} = \tilde{R}_e^{ba}$, which means that the braiding exchange operators at v and w are the same (in contrast to the H graph in Section 4.3 where these braiding exchange operators were independent of each other).

Consider the lollipop embeddings $\Gamma_{L,v}$ and $\Gamma_{L,w}$ from Figure 4.19 and their corresponding three-anyon Δ_v- and Δ_w-moves (introduced in Section 4.5.1). We have the relations connecting the respective Δ_v- and Δ_w-moves with the simple braids $\sigma_1^{v;(1,2)}$ and $\sigma_1^{w;(1,2)}$ via the δ-move (shown in Figure D.1)

$$\delta = \sigma_1^{v;(1,2)}\Delta_v = \sigma_1^{w;(1,2)}\Delta_w$$

which imply

$$\sigma_1^{v;(1,2)}\Delta_v = \sigma_1^{w;(1,2)}\Delta_w. \tag{D.1}$$
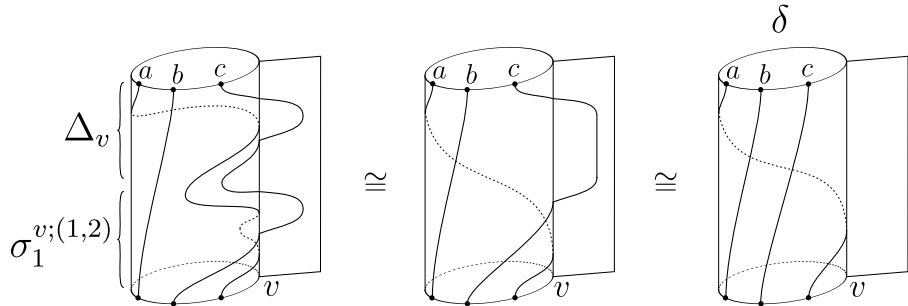
Figure D.1: The homotopy equivalence $\sigma_1^{v;(1,2)}\Delta_v = \delta$. The same reasoning holds for the relation $\sigma_1^{w;(1,2)}\Delta_w = \delta$ associated with the lollipop subgraph $\Gamma_{L,w}$.

Relation (D.1) translates to the following hexagon, where Δ_v and Δ_w are represented by the symbols G and $\tilde{G}$ respectively.
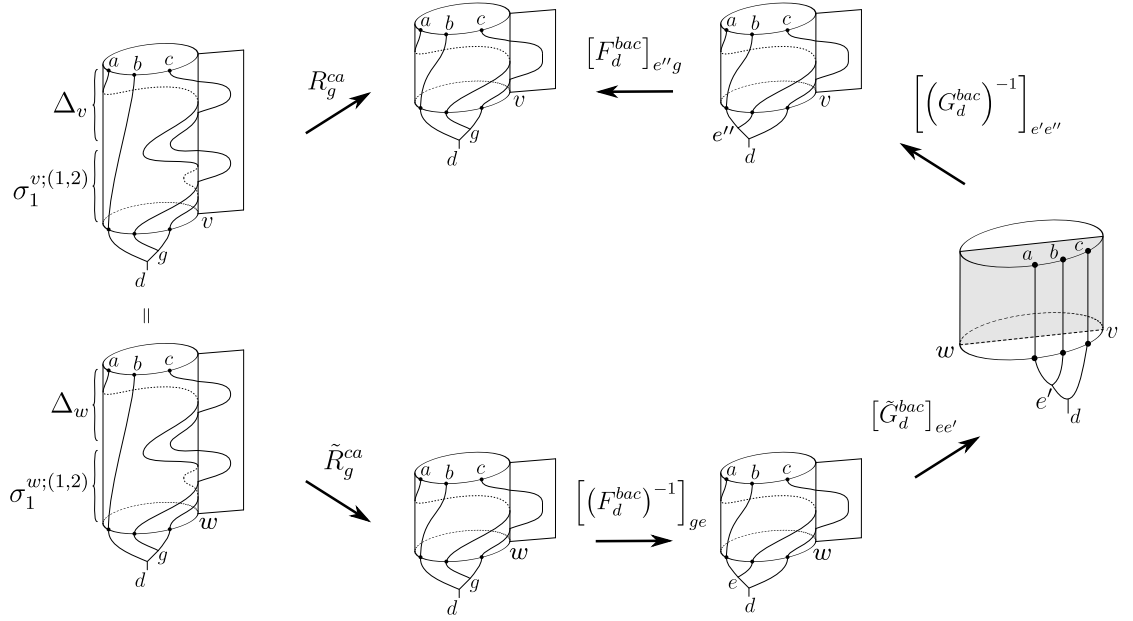
Figure D.2: The hexagon following from the relation (4.33). Note that all the states should be treated as states on the Θ-graph. For the sake of the clarity of the presentation, the diagram shows only the relevant embedded lollipops $\Gamma_{L,v}$ and $\Gamma_{L,w}$ from Figure 4.19.

$$R_g^{ca} = \tilde{R}_g^{ca} \sum_{e,e',e''} \left[\left(F_d^{bac}\right)^{-1}\right]_{ge} \left[\tilde{G}_d^{bac}\right]_{ee'} \left[\left(G_d^{bac}\right)^{-1}\right]_{e'e''} \left[F_d^{bac}\right]_{e''g}. \qquad (D.2)$$

Next, we argue that the moves Δ_v and Δ_w are in fact represented by the same G-symbols. If this is the case, then Equation (D.2) simplifies to the desired relation $R_g^{ca} = \tilde{R}_g^{ca}$. To prove the equality of the G-symbols, consider an auxiliary move γ which takes an anyon around the top loop of the Θ-graph in an anti-clockwise fashion (see the right panel in Figure D.3). The move γ can be expressed via the δ-moves and a half-twist as

$$\gamma = \bar{\delta}\delta^{-1}\tau_w^{(1,2)},$$

where $\tau_w^{(1,2)}$ is the world-ribbon half-twist at vertex w as defined at the beginning of Appendix B (Figure B.3a). This relation is proved in Figure D.3.
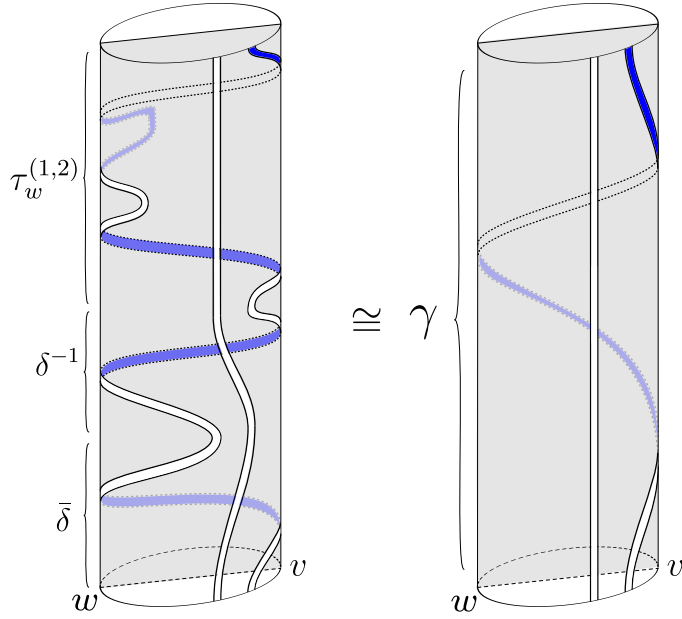
Figure D.3: A pictorial proof of the homotopy equivalence or world-ribbons $\gamma = \bar{\delta}\delta^{-1}\tau_w^{(12)}$.

The assumption that both δ and $\bar{\delta}$ moves are represented by the same set of D-symbols implies that γ induces the same morphisms of the topological Hilbert spaces as the half-twist $\tau_w^{(1,2)}$. In the remaining part of this section, we assume that the half-twist $\tau_w^{(1,2)}$ of the world-ribbon of anyon a is a morphism of one-dimensional Hilbert spaces only (i.e. it does not depend on the spacetime histories of the remaining anyons in the fusion tree). Under such an assumption, the morphism representing the half-twist $\tau_w^{(1,2)}$ can be represented as a complex number T_a. We have the relation

$$\gamma^{-1}\Delta_v\gamma = \Delta_w, \tag{D.3}$$
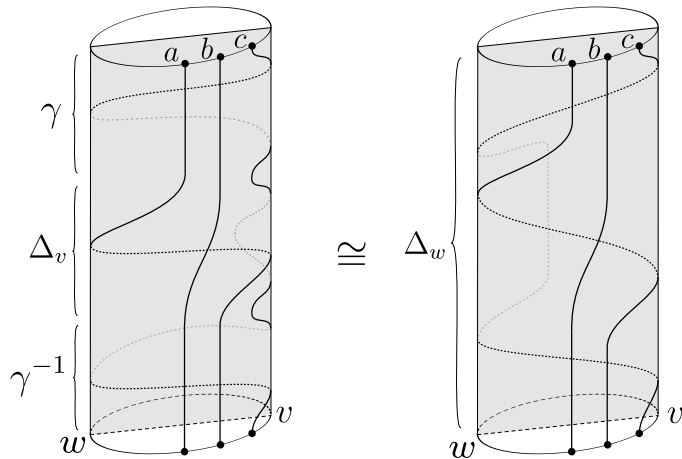
Figure D.4: The homotopy equivalence $\gamma^{-1}\Delta_v\gamma = \Delta_w$.

The relation (D.3) implies that $\hat{\Delta}_v = \hat{\Delta}_w$ ($G = \tilde{G}$ in terms of the G-symbols) – see Figure D.5.
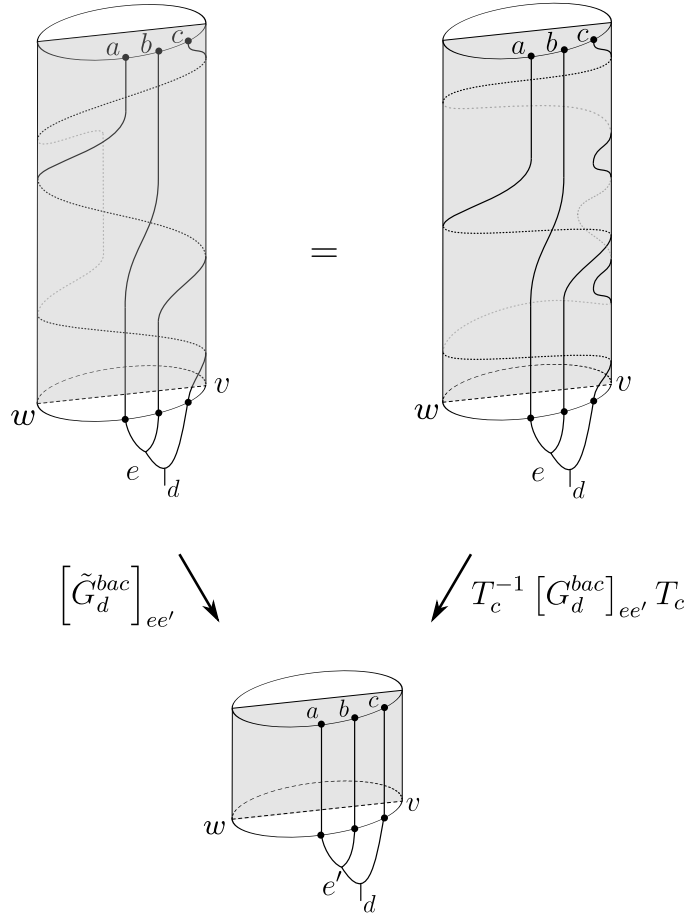
Figure D.5: The diagram following from the relation (D.3). Assuming that both circular moves δ and $\bar{\delta}$ are represented by the same D-symbols, the polygon implies $T_c^{-1} \left[G_d^{bac} \right]_{ee'} T_c = \left[\tilde{G}_d^{bac} \right]_{ee'}$, i.e. $\left[\tilde{G}_d^{bac} \right]_{ee'} = \left[G_d^{bac} \right]_{ee'}$.

Hence, using the fact that $G_d^{bac} = \tilde{G}_d^{bac}$ in (D.2), we obtain

$$R_g^{ca} = \tilde{R}_g^{ca} \sum_{e,e''} \left[\left(F_d^{bac} \right)^{-1} \right]_{ge} \delta_{ee''} \left[F_d^{bac} \right]_{e''g} = \tilde{R}_g^{ca}.$$

Finally, let us show that $\tilde{Q}_{ed}^{bac} = \tilde{R}_e^{ba}$. To this end, we use another relation involving the γ-move which reads

$$\gamma \sigma_2^{w;(2,1,2)} \gamma^{-1} = \left[\beta_{v,2}, \left(\beta_{v,1} \right)^2 \right] \sigma_1^{w;(1,2)} \left[\left(\beta_{v,1} \right)^2, \beta_{v,2} \right], \tag{D.4}$$

where β translate a particle across a vertex. A detailed exposition of the β moves can be found in (114). In order to prove relation (D.4), we first note that the LHS is homotopy equivalent to

$$\gamma \sigma_2^{w;(2,1,2)} \gamma^{-1} = \beta_{v,2} \sigma_1^{w;(1,2)} \beta_{v,2}^{-1}.$$

Next, we expand the LHS and RHS completely in terms of the corresponding β-

moves as

$$\beta_{v,2}\sigma_1^{w;(1,2)}\beta_{v,2}^{-1} = \left(\beta_{v,2}\beta_{w,1}\beta_{w,2}\right)\left(\beta_{w,1}^{-1}\beta_{w,2}^{-1}\beta_{v,2}^{-1}\right),$$

$$\left[\beta_{v,2},(\beta_{v,1})^2\right]\sigma_1^{w;(1,2)}\left[(\beta_{v,1})^2,\beta_{v,2}\right] = \left(\left[\beta_{v,2},(\beta_{v,1})^2\right]\beta_{w,1}\beta_{w,2}\beta_{v,2}\right)\times$$
$$\times\left(\beta_{v,2}^{-1}\beta_{w,1}^{-1}\beta_{w,2}^{-1}\left[(\beta_{v,1})^2,\beta_{v,2}\right]\right)$$

In Figure D.6 we prove the first "half" of the relation (D.4), i.e.

$$\beta_{v,2}\beta_{w,1}\beta_{w,2} \cong \left[\beta_{v,2},(\beta_{v,1})^2\right]\beta_{w,1}\beta_{w,2}\beta_{v,2} \tag{D.5}$$

The homotopy equivalence of the other pair of the relevant terms follows in an analogous way.
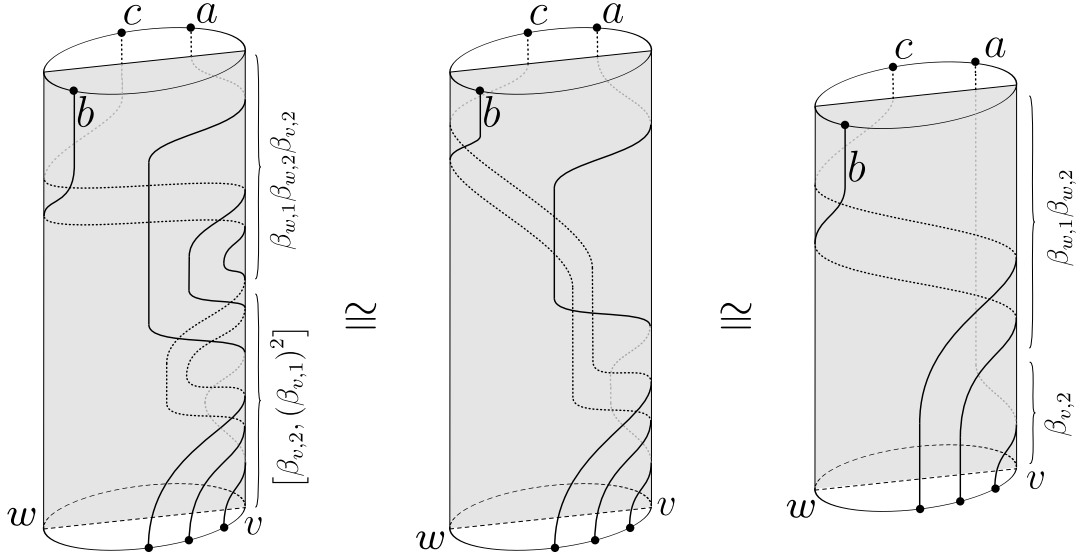
Figure D.6: A pictorial proof of the homotopy equivalence (D.5).

Let us next consider the polygon which corresponds to the relation (D.4). In the leftmost and rightmost pictures of the Figure D.6 we can see that most of the relevant moves do not split the worldlines of anyons a and b which start as the furthest ones from the vertex v. Thus, we can fuse the two anyons in the common channel $e = a \times b$ to simplify the corresponding polygon equation so that no F-moves are used (see Figure D.7).
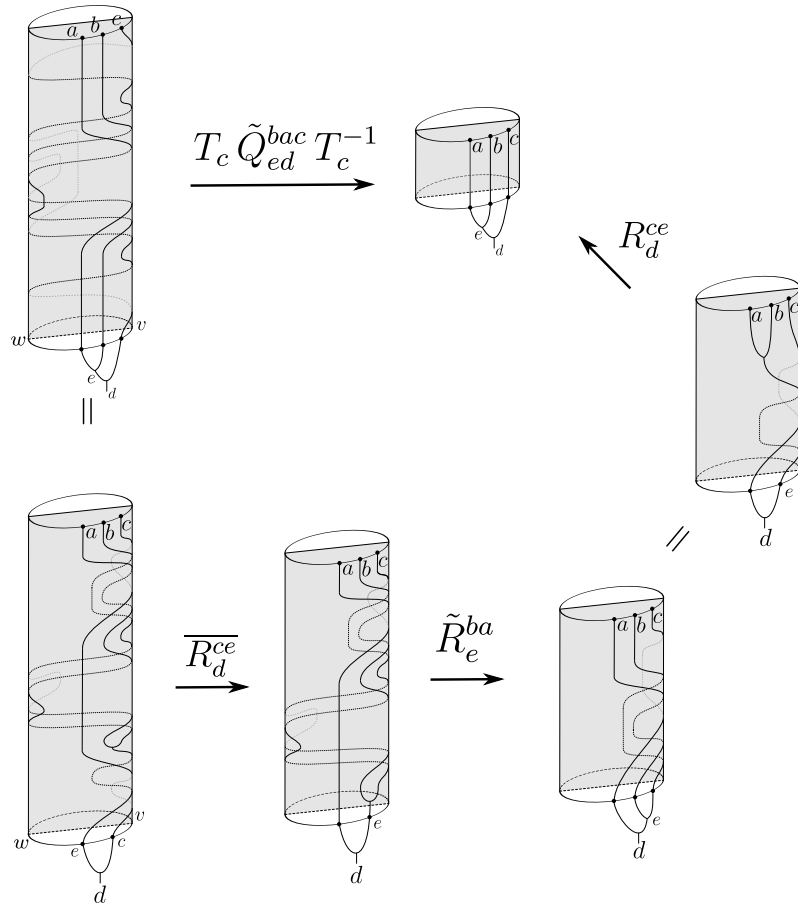
Figure D.7: The polygon following from the relation (D.4).

The polygon from Figure D.7 yields

$$T_c \, \tilde{Q}_{ed}^{bac} \, T_c^{-1} = \overline{R_d^{ce}} \, \tilde{R}_e^{ba} R_d^{ce}$$

which implies $\tilde{Q}_{ed}^{bac} = \tilde{R}_e^{ba}$.

Appendix E

Quasitrangular Hopf *-algebra from a finite group

In this section we will give a construction of a quasitriangular Hopf algebra from a finite group, this is mostly a collection of known results see (37; 58; 96; 124) and example 1.7, 1.8 in (118) for further details. Let G be a finite, not necessarily commutative group, then we can construct $\mathbb{C}G$, the free module over G, also known as a group algebra. On this space we have the following definitions of a Hopf algebra,

$$\mu(g,h) = g \cdot h \qquad \Delta(g) = g \otimes g \qquad S(g) = g^{-1} \qquad \eta(g) = 1_{\mathbb{C}} \qquad \epsilon(g) = 1_{\mathbb{C}} \quad \text{(E.1)}$$

Where all of these maps are $\mathbb{C}$ linear, a Hopf algebra constructed in this way is cocommutative. The Haar integral is given by a sum over all of the elements of the group. So for example in $\mathbb{C}\mathbb{Z}_N$ it is given by

$$l = e + a + a^2 + \ldots + a^{N-1}. \qquad \text{(E.2)}$$

Now we would like to describe the dual Hopf algebra, K^*, which is a Hopf algebra constructed on $G^* = \text{Hom}(\mathbb{C}G, \mathbb{C})$, this is a semisimple and commutative Hopf algebra. There are two standard definitions of a basis on this space which we will now describe. The basis of functions,

$$\mu(\delta_g, \delta_h) = \delta_g(h)\delta_h \qquad \Delta(\delta_g) = \sum_{uv=g} \delta_u \otimes \delta_v \qquad S(\delta_g) = \delta_{g^{-1}}$$
$$\epsilon(\delta_g) = \delta_g(e) \qquad \eta(\delta_g) = \delta_e \qquad \text{(E.3)}$$

Where $\delta_g(h)$ is equal to $1_{\mathbb{C}}$ if $g = h$ and $0_{\mathbb{C}}$ otherwise. There is also another, less commonly used basis given by matrix elements of a representation of G,

$$\mu(\pi_{ij}, \pi_{kl})(g) = \pi_{ij}(g)\pi_{kl}(g) \qquad \Delta(\pi_{ij}) \sum_k \pi_{ik} \otimes \pi_{kj} \qquad S(\pi_{ij}) = \pi_{ji}^*$$
$$\epsilon(\pi_{ij}) = \pi_{ij}(e) \qquad \eta(\pi_{ij}) = \pi_0 \qquad \text{(E.4)}$$

Where π_0 is the matrix element of the trivial reprsentation. For $(\mathbb{C}\mathbb{Z}_N)^*$ the characters are grouplike: $\Delta(\chi_i) = \chi_i \otimes \chi_i$. The Haar integral for $(\mathbb{C}\mathbb{Z}_N)^*$ is the sum over the character ring,

$$\eta = \chi_0 + \chi_1 + \ldots + \chi_{N-1}. \tag{E.5}$$

The dual Hopf algebra K^* is cocommutative if and only if the group is commutative. Both of these basis have advantages for different purposes, in particular the coproduct on the matrix element basis is familiar to anyone working in topological phases of matter as this is the structure that allows one to define the fusion rules in the theory. The definition of a quasitriangular structure of given by the R matrix, which must satisfy the following axioms

$$R\Delta(x)R^{-1} = (T \circ \Delta)(x)$$
$$(\Delta \otimes \mathrm{id})(R) = R_{13}R_{23} \tag{E.6}$$
$$(\mathrm{id} \otimes \Delta)(R) = R_{13}R_{12}$$

Where $T : K \otimes K \to K \otimes K$ is the flip map, which exchanges tensor factors. We can see that the R matrix is a weakening of cocommutativity. The R matrix satisfies the Yang Baxter equation,

$$R_{12}R_{13}R_{23} = R_{23}R_{13}R_{12}. \tag{E.7}$$

The R matrix for a finite group can be defined as follows

$$R = \frac{1}{N} \sum_{g_1, g_2} r(g_1, g_2) g_1 \otimes g_2 \tag{E.8}$$

This gives K the structure of a quasitriangular Hopf algebra if $r(g_1, g_2)$ is a g-conjugation invariant bicharacter. A bicharacter is a bilinear function, $r : G \times G \to \mathbb{C}$ satisfying the following axioms,

$$r(g_1 g_2, g_3) = r(g_1, g_3) r(g_2, g_3), \qquad r(g_1, g_3 g_4) = r(g_1, g_3) r(g_1, g_4). \tag{E.9}$$

The R matrix is a group two cocycle. The definition of a group two cocycle written multiplicatively is given by

$$r(g_1, g_2 \cdot g_3) \, r^*(g_1, g_3) \, r(g_3, g_2) \, r^*(g_1 \cdot g_3, g_2) = 1. \tag{E.10}$$

Where $\cdot$ is the product in the group and r^* is the complex conjugation of r. For example, if $G = D_N$, which has as a normal subgroup, $\mathbb{Z}_N \trianglelefteq G$. We can explicitly write the R matrix as follows,

$$R = \sum_{p,q} e^{\frac{2\pi i k}{N}} a^p \otimes a^q. \tag{E.11}$$

Where $a \in \mathbb{Z}_N$, $\omega^N = 1$ and $\gcd(k, N) = 1$. Where k labels the different projective representations of $\mathbb{Z}_N$.

In (58) it is proven that this is the most general form of quasitriangular structure on a finite dimensional cocommutative Hopf algebra. An involution can be defined on any Hopf algebra constructed over a group algebra by $* : g \rightarrow g^{-1}$ (37). A Hopf algebra constructed like this is semisimple, cosemisimple and the antipode is of order two, $S^2 = \mathrm{id}$ (37; 96; 124). In fact it is also a ribbon Hopf algebra with ribbon element 1 (68).

Appendix F

Braided tensor product and plaquette operator

In this appendix, we shall collect some proofs for the results stated in the main text. The proofs in this section are true for any quasitriangular semisimple finite dimensional Hopf algebra over an algebraically closed field. In particular, we will explain how all the different local algebra structures, as expressed in Equation (8.36), come together to form a Hopf algebra gauge theory. This procedure is explained in (124), and we refer there for a more formal approach.
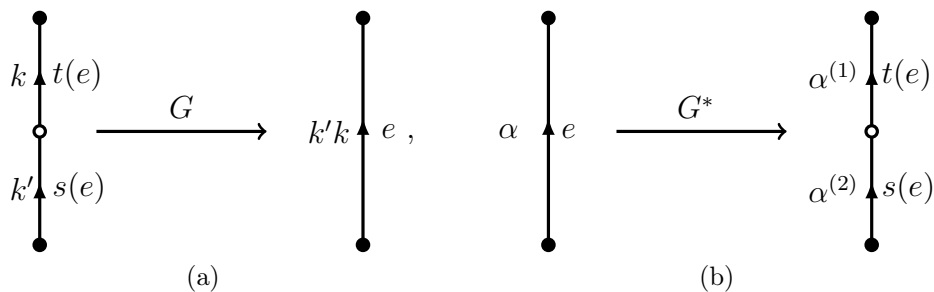
Figure F.1: Here, we display the action of the splitting map given in Equation F.1. The G map sends the two elements belonging to the edges of two local vertex neighbourhoods that correspond to the same edge ($s(e)$ and $t(e)$), to a single element on that edge. Similarly the G^* map splits a function α assigned to an edge e to functions $\alpha^{(1)}$ and $\alpha^{(2)}$ assigned to edge ends $t(e)$ and $s(e)$ respectively. We use these maps to move from the full lattice to the collection of local vertex neighbourhoods.

The procedure of stitching together all the different local algebras is related to the existence of a map that connects the elements of the algebra associated with two edges to a single one. This map needs to be linear and has to preserve the local gauge structure (K^V- module homomorphism). The most natural one, in this sense, is related to the algebra product. We will refer to this map as the G map and the corresponding dual as G^*, their action is given as

$$G : (k \otimes k')_{s(e),t(e)} \to (k'k)_e \qquad G^* : (\alpha)_e \to (\alpha^{(2)} \otimes \alpha^{(1)})_{s(e),t(e)} \ , \qquad \text{(F.1)}$$

where, here and in the following, we will call $s(e)$ $(t(e))$ the starting edge (target edge) associated with the splitting of an edge e. We show the action of G and G^* pictorially in Figure F.1. The G^* map is used to construct the braided tensor product on the whole lattice, extending it by linearity and imposing it to be a module homomorphism under the action given by the braided tensor product itself

$$G^* \left((\alpha)_{e_1} * (\beta)_{e_2} \right) = G^* \left((\alpha)_{e_1} \right) * G^* \left((\beta)_{e_2} \right) \tag{F.2}$$

for any collection of functions α, β on any collection of edges e_1, e_2.

This set up the stage for to prove the main results of this section, which are given in (8.38), (8.40) and (8.41) in the main text. Note that (8.40) is the same as Lemma 5.10 in Ref.(124) and (8.41) is essentially a refinement of the second formula in Theorem 5.7.

We can start now with the following

Proposition F.0.1. *Consider $f \in K^*$, and R the R-matrix of K, then the following is true*

$$\left\langle \phi^{(2-\tau)(1+\tau)} \otimes f^{(1)}, (S^\tau \otimes S)(R) \right\rangle \left\langle \phi^{(1+\tau)} \otimes f^{(2)}, (S^\tau \otimes id)(R) \right\rangle \phi^{(2-\tau)(2-\tau)} = \epsilon^*(f)\,\phi \tag{F.3}$$

where ϵ^* is the counit of K^*, S is the antipode of K, $\tau = 0, 1$ denotes an incoming, outgoing edge respectively and the bracketed superscripts on ϕ and f denote Sweedler indices.

Proof. Since $\tau = 0$, 1 we can just check the formula directly.

Case 1: $\tau = 0$ In this case, the left side of the formula becomes

$$\left\langle \phi^{(2)(1)} \otimes f^{(1)}, (id \otimes S)(R) \right\rangle \left\langle \phi^{(1)} \otimes f^{(2)}, R \right\rangle \phi^{(2)(2)} \,. \tag{F.4}$$

Since $(S \otimes S)(R) = R$ and dualising the action of the antipode, we get that the above function is the same as,

$$\left\langle \phi^{(2)} \otimes f^{(1)}, R^{-1} \right\rangle \left\langle \phi^{(1)} \otimes f^{(2)}, R \right\rangle \phi^{(3)} \,. \tag{F.5}$$

Using $(S \otimes id)(R) = R^{-1}$ and that $(S \otimes S)(R) = R$ we have

$$\left\langle \phi^{(1)} \otimes \phi^{(2)} \otimes f^{(1)} \otimes f^{(2)}, R_1 \otimes S(R_1) \otimes R_2 \otimes R_2 \right\rangle \phi^{(3)} = \left\langle \phi^{(1)} \otimes S(f), R^{-1}R \right\rangle \phi^{(2)} \tag{F.6}$$

since $R^{-1}R = 1$, the equality with the right-hand side follows from the properties of the counit.
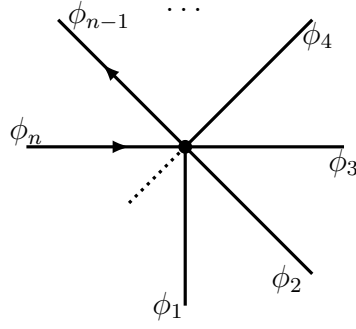
Figure F.2: Here we display an example of an n-valent local vertex neighbourhood with the last two edges having consecutive directions. All the other edges can have an arbitrary orientation, which is why we do not provide any definite direction for them.

Case 2: $\tau = 1$ In this case the left side of (F.3) becomes

$$\left\langle \phi^{(1)(2)} \otimes f^{(1)}, (S \otimes S)(R) \right\rangle \left\langle \phi^{(2)} \otimes f^{(2)}, (S \otimes id)(R) \right\rangle \phi^{(1)(1)} \qquad \text{(F.7)}$$

By collecting the coefficients and relabelling the Sweedler indices accordingly, this is equal to,

$$\left\langle \phi^{(2)} \otimes \phi^{(3)} \otimes f^{(1)} \otimes f^{(2)}, R_1 \otimes R_1 \otimes S(R_2) \otimes R_2 \right\rangle \phi^{(1)} = \left\langle \phi^{(2)} \otimes f, R^{-1}R \right\rangle \phi^{(1)} ,$$
$$= \epsilon^*(f)\phi$$
$$\text{(F.8)}$$

where we have used $R^{-1}R = 1$ and $\epsilon^*(f) = \langle f, 1 \rangle$ and $\epsilon^*(\phi^{(1)})\phi^{(2)} = \epsilon^*(\phi^{(2)})\phi^{(1)} = \phi$, so this is equal to the right-hand side of Proposition (F.3). $\qquad\square$

This proposition can be used to prove the next

Proposition F.0.2. *Consider a local vertex neighbourhood in Figure F.2 with the braided tensor product defined in 8.36. For $f \in K^*$ the following identity holds:*

$$(f^{(1)} \otimes f^{(2)})_{n-1,n} * (\phi_1 \otimes \ldots \otimes \phi_{n-1} \otimes \phi_n)_{1,2,\ldots,n} =$$
$$(\phi_1 \otimes \ldots \otimes f^{(1)} \cdot \phi_{n-1} \otimes f^{(2)} \cdot \phi_n)_{1,2,\ldots,n}$$
$$\text{(F.9)}$$

where $\cdot$ is the canonical product in K^*.

Proof. We will prove the proposition by induction over n, the number of edges around the local vertex neighbourhood.

Case $n = 3$: We can consider edge (1) to have an arbitrary direction, edge (2) to be outgoing and edge (3) to be incoming.

207

Using the braided tensor product defined in Equation 8.36 we have that

$$(f^{(1)} \otimes f^{(2)})_{2,3} * (\phi_1 \otimes \phi_2 \otimes \phi_3)_{1,2,3} =$$
$$\langle \phi_2^{(2)} \otimes f^{(2)}, R \rangle \langle \phi_1^{(2-\tau_1)(1+\tau_1)} \otimes f^{(3)}, (S^{\tau_1} \otimes S)(R) \rangle \langle \phi_1^{(1+\tau_1)} \otimes f^{(4)}, (S^{\tau_1} \otimes id)(R) \rangle$$
$$\langle \phi_2^{(3)} \otimes f^{(5)}, (S \otimes id)(R) \rangle \left(\phi_1^{(2-\tau_1)(2-\tau_1)} \otimes f^{(1)} \phi_2^{(1)} \otimes f^{(6)} \phi_3 \right) .$$

$$(\mathrm{F.10})$$

Then using the result in Proposition F.0.1 on ϕ_1, we get

$$(f^{(1)} \otimes f^{(2)})_{2,3} \cdot (\phi_1 \otimes \phi_2 \otimes \phi_3)_{1,2,3} =$$
$$\langle \phi_2^{(2)} \otimes f^{(2)}, R \rangle \langle \phi_2^{(3)} \otimes f^{(3)}, (S \otimes id)(R) \rangle \left(\phi_1 \otimes f^{(1)} \phi_2^{(1)} \otimes f^{(4)} \phi_3 \right)$$

$$(\mathrm{F.11})$$

now using that $(S \otimes id)(R) = R^{-1}$, we have

$$(f^{(1)} \otimes f^{(2)})_{2,3} \cdot (\phi_1 \otimes \phi_2 \otimes \phi_3)_{1,2,3} = \left(\phi_1 \otimes f^{(1)} \cdot \phi_2 \otimes f^{(2)} \cdot \phi_3 \right) , \qquad (\mathrm{F.12})$$

which is what we needed to prove.

Inductive step: Suppose equation (F.9) holds for a local vertex neighbourhood with $n-1$ edges (whose last edge and second last edge orientations are still the same as the ones showed in Figure F.2). With this assumption, we need now to prove the statement for a local vertex neighbourhood with n edges. From direct computation we have

$$(f^{(1)} \otimes f^{(2)})_{n-1,n} * (\phi_1 \otimes \phi_2 \otimes \ldots \otimes \phi_{n-1} \otimes \phi_n)_{1,2,\ldots,n} =$$
$$\langle \phi_1^{(2-\tau_1)(1+\tau_1)} \otimes f^{(n)}, (S^{\tau_1} \otimes S)(R) \rangle \langle \phi_2^{(2-\tau_2)(1+\tau_2)} \otimes f^{(n-1)}, (S^{\tau_2} \otimes S)(R) \rangle \ldots$$
$$\langle \phi_{n-2}^{(2-\tau_{n-2})(1+\tau_{n-2})} \otimes f^{(3)}, (S^{\tau_{n-2}} \otimes S)(R) \rangle \langle \phi_{n-1}^{(2)} \otimes f^{(2)}, R \rangle$$
$$\langle \phi_1^{(1+\tau_1)} \otimes f^{(n+1)}, (S^{\tau_1} \otimes id)(R) \rangle \langle \phi_2^{(1+\tau_2)} \otimes f^{(n+2)}, (S^{\tau_2} \otimes id)(R) \rangle \ldots$$
$$\langle \phi_{n-1}^{(3)} \otimes f^{(2n-1)}, (S \otimes id)(R) \rangle$$
$$\left(\phi_1^{(2-\tau_1)(2-\tau_1)} \otimes \ldots \otimes \phi_{n-2}^{(2-\tau_{n-2})(2-\tau_{n-2})} \otimes f^{(1)} \phi_{n-1}^{(1)} \otimes f^{(2n)} \phi_n \right)_{1,2,\ldots,n} .$$

$$(\mathrm{F.13})$$

Using Proposition F.0.1 on ϕ_1 we get

$$(f^{(1)} \otimes f^{(2)})_{n-1,n} \cdot (\phi_1 \otimes \phi_2 \otimes \ldots \otimes \phi_{n-1} \otimes \phi_n)_{1,2,\ldots,n} =$$
$$\langle \phi_2^{(2-\tau_2)(1+\tau_2)} \otimes f^{(n-1)}, (S^{\tau_2} \otimes S)(R) \rangle \ldots$$
$$\langle \phi_{n-2}^{(2-\tau_{n-2})(1+\tau_{n-2})} \otimes f^{(3)}, (S^{\tau_{n-2}} \otimes S)(R) \rangle \langle \phi_{n-1}^{(2)} \otimes f^{(2)}, R \rangle$$
$$\langle \phi_2^{(1+\tau_2)} \otimes f^{(n)}, (S^{\tau_2} \otimes id)(R) \rangle \ldots \langle \phi_{n-1}^{(3)} \otimes f^{(2n-3)}, (S \otimes id)(R) \rangle$$
$$\left(\phi_1 \otimes \phi_2^{(2-\tau_2)(2-\tau_2)} \otimes \ldots \otimes \phi_{n-2}^{(2-\tau_{n-2})(2-\tau_{n-2})} \otimes f^{(1)} \phi_{n-1}^{(1)} \otimes f^{(2n-2)} \phi_n \right)_{1,2,\ldots,n} .$$
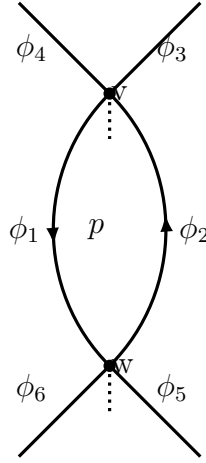
$$(\mathrm{F.14})$$

Figure F.3: Simple plaquette.

we can see that the equation above is actually equivalent to

$$(f^{(1)} \otimes f^{(2)})_{n-1,n} * (\phi_1 \otimes \phi_2 \otimes \ldots \otimes \phi_{n-1} \otimes \phi_n)_{1,2,\ldots,n} =$$
$$(\phi_1)_1 * (f^{(1)} \otimes f^{(2)})_{n-1,n} * (\phi_2 \otimes \ldots \otimes \phi_{n-1} \otimes \phi_n)_{2,3,\ldots,n} . \tag{F.15}$$

We now recognise the same product on a local vertex neighbourhood with one edge less, and because of the inductive hypothesis and associativity we have

$$(f^{(1)} \otimes f^{(2)})_{n-1,n} * (\phi_1 \otimes \phi_2 \otimes \ldots \otimes \phi_{n-1} \otimes \phi_n)_{2,3,\ldots,n} =$$
$$(\phi_1)_1 * (\phi_2 \otimes \ldots \otimes f^{(1)}\phi_{n-1} \otimes f^{(2)}\phi_n)_{2,3,\ldots,n} , \tag{F.16}$$

which is the same as (F.9). $\qquad\qquad\square$

This proposition will be used repeatedly in the following. As already explained in Section 8.2.2, the holonomy associated with a function α for an counterclockwise plaquette with edges $1, 2, \ldots n$, counting from the cilia, acts on the algebra of functions on the ciliated graph as the product by the element

$$(S(\alpha^{(1)}) \otimes S(\alpha^{(2)}) \otimes \cdots \otimes S(\alpha^{(n)}))_{1,2,\ldots,n} . \tag{F.17}$$

Proposition F.0.2 then means that all the non-trivial aspects introduced by the R matrix show up at the local vertex neighbourhood in the plaquette with the cilia pointing inwards. At all the other vertexes the holonomy simply acts with the canonical product on K^*. Because of this, when trying to find the general structure of the plaquette operator, it is sufficient to do it for the plaquette shown in Figure F.3 [1] We can now establish the following relation between the plaquette operator computed using the braided tensor product, which we denote by $\mathcal{B}_p^f$ and the plaquette operator from conventional quantum double models, denoted by B_p^f.

---

[1] Note that this is not the simplest plaquette that can be used, but this case better shows the type of calculations involved in computing plaquette operators.

Proposition F.0.3. *Consider the ribbon graph shown in Figure F.3. The plaquette operator using the braided tensor product is given by,*

$$\mathcal{B}_p^f(\phi_1,\ \phi_2,\ \phi_3,\ \phi_4,\ \phi_5,\ \phi_6) =$$
$$\langle \phi_2^{(1)} \otimes f^{(1)}, R \rangle \langle \phi_3^{(1+\tau_3)} \otimes f^{(2)}, (S^{\tau_3} \otimes id)(R) \rangle \langle \phi_4^{(1+\tau_4)} \otimes f^{(3)}, (S^{\tau_4} \otimes id)(R) \rangle \quad \text{(F.18)}$$
$$\langle \phi_1^{(2)} \otimes f^{(4)}, R^{-1} \rangle B_p^{f^{(5)}}\left(\phi_1^{(1)},\ \phi_2^{(2)},\ \phi_3^{(2-\tau_3)},\ \phi_4^{(2-\tau_4)},\ \phi_5,\ \phi_6\right)$$

where τ_i labels the directedness of the edge which has ϕ_i assigned to it.

Proof. As mentioned the plaquette operator on plaquette p for Hopf algebra gauge theory is given by

$$\mathcal{B}_p^f(\phi_1,\ \phi_2,\ \phi_3,\ \phi_4,\ \phi_5,\ \phi_6) =$$
$$\left(S(f^{(1)}) \otimes S(f^{(2)})\right)_{1,2} * (\phi_1 \otimes \phi_2 \otimes \phi_2 \otimes \phi_4 \otimes \phi_5 \otimes \phi_6)_{1,2,\dots,6} \quad \text{(F.19)}$$

where the numbering of edges is the same as the subscript labelling on the functions. In order to compute this product, we need to consider the splitting of the graph into local vertex neighbourhoods. Algebraically this translates into the use of G^* map, given in Equation F.1. This is represented pictorially in Figure F.1. We therefore need to consider two local vertex neighbourhoods associated with the vertices v and w as shown in the Figure F.4. For the vertex w, we can use Proposition F.0.2 and the product reduces to the canonical product in the algebra of functions

$$(S(f^{(3)}) \otimes S(f^{(2)}))_{w_2,w_3} * (\phi_5 \otimes \phi_2^{(2)} \otimes \phi_1^{(1)} \otimes \phi_6)_{w_1,w_2,w_3,w_4} =$$
$$(\phi_5 \otimes S(f^{(3)})\phi_2^{(2)} \otimes S(f^{(2)})\phi_1^{(1)} \otimes \phi_6)_{w_1,w_2,w_3,w_4} \ . \quad \text{(F.20)}$$

On the local vertex neighbourhood associated with v we instead have

$$(S(f^{(4)}) \otimes S(f^{(1)}))_{v_1,v_4} * (\phi_2^{(1)} \otimes \phi_3 \otimes \phi_4 \otimes \phi_1^{(2)})_{v_1,v_2,v_3,v_4} =$$
$$\langle \phi_2^{(1)(1)} \otimes S(f^{(1)})^{(2)}, R^{-1} \rangle \langle \phi_3^{(1+\tau_3)} \otimes S(f^{(1)})^{(1)(2)}, (S^{\tau_3} \otimes S)(R) \rangle$$
$$\langle \phi_4^{(1+\tau_4)} \otimes S(f^{(1)})^{(1)(1)(2)}, (S^{\tau_4} \otimes S)(R) \rangle \langle \phi_1^{(2)(2)} \otimes S(f^{(1)})^{(1)(1)(1)(2)}, R \rangle \quad \text{(F.21)}$$
$$(S(f^{(4)})\phi_2^{(1)(2)} \otimes \phi_3^{(2-\tau_3)} \otimes \phi_4^{(2-\tau_4)} \otimes S(f^{(1)})^{(1)(1)(1)(1)}\phi_1^{(2)(1)})_{v_1,v_2,v_3,v_4} \ ,$$
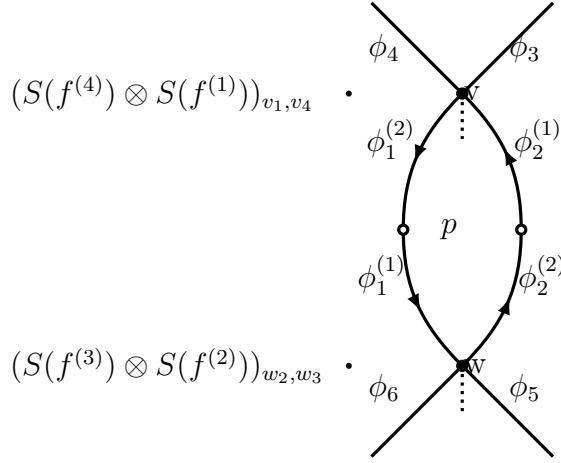
Figure F.4: Graphical representation of the product between the two local vertex neighbourhood in v and w

where we have used (8.36).

Since elements living at different local vertex neighbourhoods commute, we can see that overall the two products can be written as

$$G^* \left(S(f^{(4)}) \otimes S(f^{(3)}) \otimes S(f^{(2)}) \otimes S(f^{(1)}) \right) *$$
$$G^* \left(\phi_1^{(2)} \otimes \phi_1^{(1)} \otimes \phi_2^{(2)} \otimes \phi_2^{(1)} \otimes \phi_3 \otimes \phi_4 \otimes \phi_5 \otimes \phi_6 \right) =$$
$$\langle \phi_2^{(1)} \otimes f^{(1)}, R \rangle \langle \phi_3^{(1+\tau_3)} \otimes f^{(2)}, (S^{\tau_3} \otimes id)(R) \rangle$$
$$\langle \phi_4^{(1+\tau_4)} \otimes f^{(3)}, (S^{\tau_4} \otimes id)(R) \rangle \langle \phi_1^{(3)} \otimes f^{(4)}, R^{-1} \rangle$$
$$(S(f^{(5)})\phi_1^{(2)} \otimes S(f^{(6)})\phi_1^{(1)} \otimes S(f^{(7)})\phi_2^{(3)} \otimes (S(f^{(8)})\phi_2^{(2)} \otimes \phi_3^{(2-\tau_3)} \otimes \phi_4^{(2-\tau_4)} \otimes \phi_5 \otimes \phi_6)_{\mathbf{e}} \; .$$

where $\mathbf{e} = \{v_4, w_3, w_2, v_1, v_2, v_3, w_1, w_6\}$ and for compactness, on the first two lines, we have omitted the subscript labelling edges, since from the above discussion it should be clear which element is associated with which edge. In the last line, we can now recognise the G^* map defined in Equation (F.1) and we can therefore write

$$G^* \left(S(f^{(4)}) \otimes S(f^{(3)}) \otimes S(f^{(2)}) \otimes S(f^{(1)}) \right) *$$
$$G^* \left((\phi_1^{(2)} \otimes \phi_1^{(1)} \otimes \phi_2^{(2)} \otimes \phi_2^{(1)} \otimes \phi_3 \otimes \phi_4 \otimes \phi_5 \otimes \phi_6) \right) =$$
$$\langle \phi_2^{(1)} \otimes f^{(1)}, R \rangle \langle \phi_3^{(1+\tau_3)} \otimes f^{(2)}, (S^{\tau_3} \otimes id)(R) \rangle \qquad \text{(F.22)}$$
$$\langle \phi_4^{(1+\tau_4)} \otimes f^{(3)}, (S^{\tau_4} \otimes id)(R) \rangle \langle \phi_1^{(2)} \otimes f^{(4)}, R^{-1} \rangle$$
$$G^* \left(B_p^{f^{(3)}} \left(\phi_1^{(1)}, \; \phi_2^{(2)}, \; \phi_3^{(2-\tau_3)}, \; \phi_4^{(2-\tau_4)}, \; \phi_5, \; \phi_6 \right) \right) \; ,$$

So by linearity and from the fact that G^* is an homomorphism, we can recognise Equation (F.18) of Proposition F.0.3. $\qquad \square$

It is easy to generalise the above result for a plaquette with an arbitrary number of edges. In particular for the plaquette without any external edges, as the one shown
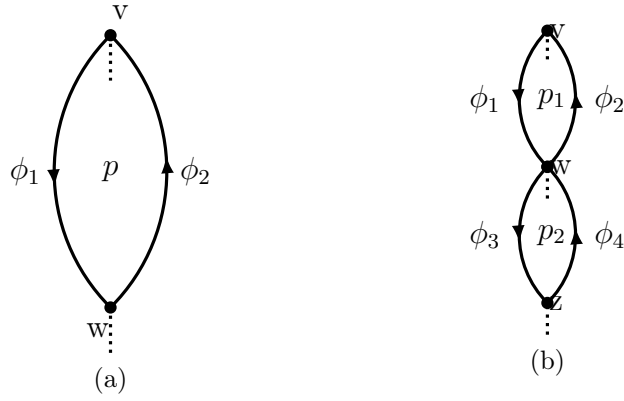
Figure F.5: In figure (a) we show a plaquette without any external edges attached. In figure (b) the relevant graph to compute the commutation between plaquette operators .

in Figure F.5a, we get

$$\mathcal{B}_p^f(\phi_1, \ \phi_2) = \langle \phi_2^{(1)} \otimes f^{(1)}, R \rangle \langle \phi_1^{(2)} \otimes f^{(2)}, R^{-1} \rangle B_p^{f^{(3)}}(\phi_1^{(1)}, \ \phi_2^{(2)}) \ . \qquad \text{(F.23)}$$

We can now start considering the commutation relations of two plaquette operators. We can distinguish between two cases, one in which the two plaquettes have coinciding starting vertices and one in which the starting vertices differ. We will consider the latter case first.

From the preceding results it is clear that the relevant graph to consider when enquiring about the commutation relation between plaquettes at different vertexes is the one given in Figure F.5b. Similarly to Kitaev models, we can see that in this case plaquette operators commute.

Proposition F.0.4. *Consider the graph shown in Figure F.5b and consider the two plaquette operators at vertexes v and w, which act with functions $f, g \in K^*$, respectively. Then we have*

$$\mathcal{B}_{p_1}^f \mathcal{B}_{p_2}^g = \mathcal{B}_{p_2}^g \mathcal{B}_{p_1}^f \qquad \text{(F.24)}$$

Proof. We start by considering the left hand of the equation (F.24) when acting on the general elements $\phi_1, \phi_2, \phi_3, \ \phi_4 \in K^*$, as given in Figure F.5b. By using (F.18) and (F.23) we have

$$\begin{aligned}
&\mathcal{B}_{p_1}^f \mathcal{B}_{p_2}^g (\phi_1, \phi_2, \phi_3, \phi_4) = \\
&\langle \phi_4^{(1)} \otimes g^{(1)}, R \rangle \langle \phi_2^{(3)} \otimes g^{(2)}, R^{-1} \rangle \langle \phi_1^{(1)} \otimes g^{(3)}, R \rangle \langle \phi_3^{(2)} \otimes g^{(4)}, R^{-1} \rangle \\
&\langle \phi_2^{(1)} \otimes f^{(1)}, R \rangle \langle \phi_1^{(3)} \otimes f^{(2)}, R^{-1} \rangle \\
&(S(f^{(3)})\phi_1^{(2)} \otimes S(f^{(4)})\phi_2^{(2)} \otimes S(g^{(5)})\phi_3^{(1)} \otimes S(g^{(6)})\phi_4^{(2)}) \ .
\end{aligned} \qquad \text{(F.25)}$$

We will now show that the right hand side of (F.24), when acting on $\phi_1, \phi_2, \phi_3, \ \phi_4 \in$

K^*, turns out to be the same as (F.25). We have in fact

$$
\begin{aligned}
\mathcal{B}^g_{p_2}&\mathcal{B}^f_{p_1}(\phi_1, \phi_2, \phi_3, \phi_4) = \\
&\langle \phi_2^{(1)} \otimes f^{(1)}, R \rangle \langle \phi_1^{(3)} \otimes f^{(2)}, R^{-1} \rangle \\
&\langle \phi_4^{(1)} \otimes g^{(1)}, R \rangle \langle S(f^{(4)})\phi_1^{(1)} \otimes g^{(3)}, R \rangle \langle S(f^{(5)})\, \phi_2^{(3)} \otimes g^{(2)}, R^{-1} \rangle \\
&\langle \phi_3^{(2)} \otimes g^{(4)}, R^{-1} \rangle (S(f^{(3)})\, \phi_1^{(2)} \otimes S(f^{(6)})\phi_2^{(2)} \otimes S(g^{(5)})\, \phi_3^{(1)} \otimes S(g^{(6)})\, \phi_4^{(2)}) \ .
\end{aligned}
\tag{F.26}
$$

Using

$$
(\Delta \otimes id)(R) = R_{13}R_{23}, \qquad (\Delta \otimes id)(R^{-1}) = (id \otimes id \otimes S)(R_{13}R_{23}), \tag{F.27}
$$

we can dualize the products in K^* into coproducts on K and have as a result

$$
\begin{aligned}
\mathcal{B}^g_{p_2}&\mathcal{B}^f_{p_1} = \\
&\langle \phi_2^{(1)} \otimes f^{(1)}, R \rangle \langle \phi_1^{(3)} \otimes f^{(2)}, R^{-1} \rangle \langle \phi_4^{(1)} \otimes g^{(1)}, R \rangle \\
&\langle S(f^{(4)}) \otimes \phi_1^{(1)} \otimes g^{(3)}, R_{13}R_{23} \rangle \langle S(f^{(5)}) \otimes \phi_2^{(3)} \otimes g^{(2)}, (id \otimes id \otimes S)(R_{13}R_{23}) \rangle \\
&\langle \phi_3^{(2)} \otimes g^{(4)}, R^{-1} \rangle (S(f^{(3)})\phi_1^{(2)} \otimes S(f^{(6)})\phi_2^{(2)} \otimes S(g^{(5)})\, \phi_3^{(1)} \otimes S(g^{(6)})\, \phi_4^{(2)}) \ .
\end{aligned}
\tag{F.28}
$$

The f's and g's can now be regrouped, and we can write

$$
\begin{aligned}
\langle f^{(4)} \otimes f^{(5)} \otimes g^{(2)} \otimes g^{(3)}, S(R'_1) \otimes S(R'_3) \otimes S(R''_4)S(R''_3) \otimes R''_1 R''_2 \rangle &= \\
\langle f^{(4)} \otimes g^{(2)}, S(R'_3 R'_1) \otimes S(R''_4)S(R''_3)R''_1 R''_2 \rangle &= \\
\langle f^{(4)} \otimes g^{(2)}, 1 \otimes S(R''_4)R''_2 \rangle = \epsilon^*(f^{(4)})\langle g^{(2)} \otimes g^{(3)}, S(R''_4) \otimes R''_2 \rangle \ ,
\end{aligned}
\tag{F.29}
$$

where the subscripts in the R matrices are used to avoid confusion between the elements of different R matrices. In the last step we have used that $(id \otimes S)(R) = R^{-1}$.

Thus, using this last result, by appropriately regrouping terms, we finally have

$$
\begin{aligned}
\mathcal{B}^g_{p_2}&\mathcal{B}^f_{p_1} = \\
&\langle \phi_2^{(1)} \otimes f^{(1)}, R \rangle \langle \phi_1^{(3)} \otimes f^{(2)}, R^{-1} \rangle \langle \phi_4^{(1)} \otimes g^{(1)}, R \rangle \langle \phi_1^{(1)} \otimes g^{(3)}, R \rangle \langle \phi_2^{(3)} \otimes g^{(2)}, R^{-1} \rangle \\
&\langle \phi_3^{(2)} \otimes g^{(4)}, R^{-1} \rangle (S(f^{(3)})\phi_1^{(2)} \otimes S(f^{(6)})\phi_2^{(2)} \otimes S(g^{(5)})\phi_3^{(1)} \otimes S(g^{(6)})\phi_4^{(2)}) \ ,
\end{aligned}
\tag{F.30}
$$

which is the same as (F.25) and therefore proves the claim on Figure F.5b. $\qquad\square$

As already mentioned the previous result holds for more general plaquettes and the proof is similar, even if more notationally involved.

Before continuing with the treatment of commutation relations between plaquettes, we need the following technical proposition:
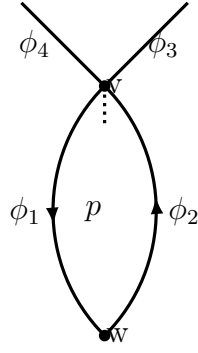
Figure F.6: Relevant plaquette used to understand the product between plaquette operators on the same plaquette with the braided tensor product.

Proposition F.0.5. *Consider f, g, $\phi \in K^*$ and the R matrix of K. Then, given $\tau = 0, 1$, the following equation holds*

$$
\begin{aligned}
&\langle \phi^{(1+\tau)} \otimes g, (S^\tau \otimes id)(R) \rangle \langle \phi^{(2-\tau)(1+\tau)} \otimes f, (S^\tau \otimes id)(R) \rangle \phi^{(2-\tau)(2-\tau)} = \\
&\langle \phi^{(1+\tau)} \otimes fg, (S^\tau \otimes id)(R) \rangle \phi^{(2-\tau)}
\end{aligned}
\tag{F.31}
$$

Proof. We can prove the formula for the two cases directly.

Case $\tau = 0$ In this instance we have

$$
\begin{aligned}
&\langle \phi^{(1)} \otimes g, R \rangle \langle \phi^{(2)(1)} \otimes f, R \rangle \phi^{(2)(2)} = \\
&\langle \phi^{(1)} \otimes \phi^{(2)} \otimes f \otimes g, R_1' \otimes R_2' \otimes R_2'' \otimes R_1'' \rangle \phi^{(3)} = \langle \phi^{(1)} \otimes f \otimes g, R_{13}R_{12} \rangle \phi^{(2)} ,
\end{aligned}
\tag{F.32}
$$

where we have used the dualisation of the coproduct. Now use $(id \otimes \Delta)(R) = R_{13}R_{12}$ to get

$$
\langle \phi^{(1)} \otimes f \otimes g, R_{13}R_{12} \rangle \phi^{(2)} = \langle \phi^{(1)} \otimes f \otimes g, (id \otimes \Delta)(R) \rangle \phi^{(2)} = \langle \phi^{(1)} \otimes fg, R \rangle \phi^{(2)} ,
\tag{F.33}
$$

which proves (F.31).

Case $\tau = 1$ In this case, we have

$$
\begin{aligned}
&\langle \phi^{(2)} \otimes g, R \rangle \langle \phi^{(1)(2)} \otimes f, (S \otimes id)(R) \rangle \phi^{(1)(1)} = \\
&\langle \phi^{(2)} \otimes \phi^{(3)} \otimes f \otimes g, R_1' \otimes R_2' \otimes R_2'' \otimes R_1'' \rangle \phi^{(1)} = \langle \phi^{(2)} \otimes f \otimes g, R_{13}R_{12} \rangle \phi^{(1)} .
\end{aligned}
\tag{F.34}
$$

As before we can use the relation $(id \otimes \Delta)(R) = R_{13}R_{12}$ to simplify the result:

$$
\langle \phi^{(2)} \otimes f \otimes g, R_{13}R_{12} \rangle \phi^{(1)} = \langle \phi^{(2)} \otimes f \otimes g, (id \otimes \Delta)(R) \rangle \phi^{(1)} = \langle \phi^{(2)} \otimes f \cdot g, R \rangle \phi^{(1)} ,
\tag{F.35}
$$

which ends our proof. $\qquad\square$

We now have everything we needed in order to prove one of the main results, that is the product between plaquette operators at coinciding starting vertexes.

Proposition F.0.6. *Consider two plaquette operators acting on the same plaquette, by functions f and g respectively. Then the following relation holds*

$$\mathcal{B}_p^f \mathcal{B}_p^g = \langle g^{(1)} \otimes f^{(2)}, R \rangle \langle g^{(3)} \otimes f^{(1)}, R^{-1} \rangle \mathcal{B}_p^{f^{(3)} g^{(2)}} \qquad \text{(F.36)}$$

Proof. To prove the relation we will consider a ribbon graph as the one given in Figure F.6. As we have seen, vertexes in the plaquette without the plaquette cilia do not play any role in the plaquette operator, so proving the formula for a plaquette with only two vertexes and without external edges at w is sufficient.

The proof of the statement comes from a direct computation. Let's therefore write

$$
\begin{aligned}
&\mathcal{B}_p^f \mathcal{B}_p^g(\phi_1, \phi_2, \phi_3, \phi_4) = \\
&\langle \phi_2^{(1)} \otimes g^{(1)}, R \rangle \langle \phi_3^{(1+\tau_3)} \otimes g^{(2)}, (S^{\tau_3} \otimes id)(R) \rangle \langle \phi_4^{(1+\tau_4)} \otimes g^{(3)}, (S^{\tau_4} \otimes id)(R) \rangle \\
&\langle \phi_1^{(3)} \otimes g^{(4)}, R^{-1} \rangle \langle S(g^{(5)}) \phi_1^{(2)} \otimes f^{(4)}, R^{-1} \rangle \langle S(g^{(8)}) \phi_2^{(2)} \otimes f^{(1)}, R \rangle \\
&\langle \phi_3^{(2-\tau_3)(1+\tau_3)} \otimes f^{(2)}, (S^{\tau_3} \otimes id)(R) \rangle \langle \phi_4^{(2-\tau_4)(1+\tau_4)} \otimes f^{(3)}, (S^{\tau_4} \otimes id)(R) \rangle \\
&(S(f^{(5)}) S(g^{(6)}) \phi_1^{(1)} \otimes S(f^{(6)}) S(g^{(7)}) \phi_2^{(3)} \otimes \phi_3^{(2-\tau_3)(2-\tau_3)} \otimes \phi_4^{(2-\tau_4)(2-\tau_4)}) \; .
\end{aligned}
\qquad \text{(F.37)}
$$

Using Proposition F.0.3 we can see that we can simplify some of the terms:

$$
\begin{aligned}
&\mathcal{B}_p^f \mathcal{B}_p^g(\phi_1, \phi_2, \phi_3, \phi_4) = \\
&\langle \phi_2^{(1)} \otimes g^{(1)}, R \rangle \langle \phi_3^{(1+\tau_3)} \otimes f^{(2)} g^{(2)}, (S^{\tau_3} \otimes id)(R) \rangle \\
&\langle \phi_4^{(1+\tau_4)} \otimes f^{(3)} g^{(3)}, (S^{\tau_4} \otimes id)(R) \rangle \langle \phi_1^{(3)} \otimes g^{(4)}, R^{-1} \rangle \\
&\langle S(g^{(5)}) \phi_1^{(2)} \otimes f^{(4)}, R^{-1} \rangle \langle S(g^{(8)}) \phi_2^{(2)} \otimes f^{(1)}, R \rangle \\
&(S(f^{(5)}) S(g^{(6)}) \phi_1^{(1)} \otimes S(f^{(6)}) S(g^{(7)}) \phi_2^{(3)} \otimes \phi_3^{(2-\tau_3)} \otimes \phi_4^{(2-\tau_4)}) \; .
\end{aligned}
\qquad \text{(F.38)}
$$

Using that $(\Delta \otimes id)(R) = R_{13} R_{23}$, we can write

$$\langle S(g^{(5)}) \phi_1^{(2)} \otimes f^{(4)}, R^{-1} \rangle = \langle S(g^{(5)}) \otimes \phi_1^{(2)} \otimes S(f^{(4)(2)}) \otimes S(f^{(4)(1)}), R' \otimes R_1' \otimes R'' \otimes R_1'' \rangle$$

and

$$\langle S(g^{(8)}) \phi_2^{(2)} \otimes f^{(1)}, R \rangle = \langle S(g^{(8)}) \otimes \phi_2^{(2)} \otimes f^{(1)(1)} \otimes f^{(1)(2)}, R' \otimes R_2' \otimes R'' \otimes R_2'' \rangle \; ,$$

where the indices 1, 2 are to keep track of the elements belonging to different R matrixes. We can now regroup some of the coproducts in (F.38)

$$\langle \phi_1^{(2)} \otimes \phi_1^{(3)} \otimes S(g^{(4)}) \otimes S(f^{(4)(1)}), R_2' \otimes R' \otimes R'' \otimes R_2'' \rangle = \langle \phi_1^{(2)} \otimes S(f^{(4)(1)} g^{(4)}), R \rangle$$

$$\langle \phi_2^{(1)} \otimes \phi_2^{(2)} \otimes f^{(1)(2)} \otimes g^{(1)}, R' \otimes R_4' \otimes R_4'' \otimes R'' \rangle = \langle \phi_2^{(1)} \otimes f^{(1)(2)} g^{(1)}, R \rangle \; ,$$

where, again, we used $(id \otimes \Delta)(R) = R_{13}R_{12}$. Therefore

$$
\begin{aligned}
\mathcal{B}_p^f \mathcal{B}_p^g (\phi_1, \phi_2, \phi_3, \phi_4) = \\
\langle g^{(5)} \otimes f^{(6)}, R \rangle \langle g^{(8)} \otimes f^{(1)}, R^{-1} \rangle \langle \phi_2^{(1)} \otimes f^{(2)} g^{(1)}, R \rangle \\
\langle \phi_3^{(1+\tau_3)} \otimes f^{(3)} g^{(2)}, (S^{\tau_3} \otimes id)(R) \rangle \langle \phi_4^{(1+\tau_4)} \otimes f^{(4)} g^{(3)}, (S^{\tau_4} \otimes id)(R) \rangle \\
\langle \phi_1^{(2)} \otimes S(f^{(5)} g^{(4)}), R \rangle (S(g^{(6)} f^{(7)}) \phi_1^{(1)} \otimes S(g^{(7)} f^{(8)}) \phi_2^{(3)} \otimes \phi_3^{(2-\tau_3)} \otimes \phi_4^{(2-\tau_4)})
\end{aligned}
\tag{F.39}
$$

Note the given two functions $\alpha,\ \beta \in K^*$ the following holds

$$
\langle \alpha^{(1)} \otimes \beta^{(1)}, R \rangle \, \alpha^{(2)} \beta^{(2)} = \langle \alpha^{(2)} \otimes \beta^{(2)}, R \rangle \, \beta^{(1)} \alpha^{(1)}
\tag{F.40}
$$

which follows from $R \cdot \Delta \cdot R = \Delta^{\mathrm{op}}$ (i.e. see Proposition 3.8 in (124)). Therefore we can write

$$
\begin{aligned}
\mathcal{B}_p^f \mathcal{B}_p^g (\phi_1, \phi_2, \phi_3, \phi_4) = \\
\langle g^{(7)} \otimes f^{(8)}, R \rangle \langle g^{(8)} \otimes f^{(1)}, R^{-1} \rangle \langle \phi_2^{(1)} \otimes f^{(2)} g^{(1)}, R \rangle \\
\langle \phi_3^{(1+\tau_3)} \otimes f^{(3)} g^{(2)}, (S^{\tau_3} \otimes id)(R) \rangle \langle \phi_4^{(1+\tau_4)} \otimes f^{(4)} g^{(3)}, (S^{\tau_4} \otimes id)(R) \rangle \\
\langle \phi_1^{(2)} \otimes S(f^{(5)} g^{(4)}), R \rangle (S(f^{(6)} g^{(5)}) \phi_1^{(1)} \otimes S(f^{(7)} g^{(6)}) \phi_2^{(3)} \otimes \phi_3^{(2-\tau_3)} \otimes \phi_4^{(2-\tau_4)})
\end{aligned}
\tag{F.41}
$$

which shows that (F.36) holds and thus concludes the proof. □

We can now analyze the relationship between plaquette operators and gauge transformations. Note, The action of gauge transformations is given by the action of the vertex operator. We will first prove that vertex operators acting at a vertex not coinciding with a plaquette's starting vertex, commute with the plaquette operator associated with that plaquette.

Proposition F.0.7. *Consider the ribbon graph in Figure F.3 then the plaquette operator at p and the gauge transformation at vertex w commute*

$$
\mathcal{B}_p^f A_w^h = A_w^h \mathcal{B}_p^f
\tag{F.42}
$$

Proof. This follows from a direct computation. From (8.20) we can write

$$
\begin{aligned}
A_w^h (\phi_1 \otimes \ldots \otimes \phi_6) = \\
\langle S^{\tau_5}(\phi_5^{(1+\tau_5)}) S(\phi_2^{(2)}) \phi_1^{(1)} S^{\tau_6}(\alpha_6^{(1+\tau_6)}), h \rangle (\phi_1^{(2)} \otimes \phi_2^{(1)} \otimes \phi_3 \otimes \phi_4 \otimes \phi_5^{(2-\tau_5)} \otimes \phi_6^{(2-\tau_6)})
\end{aligned}
\tag{F.43}
$$

and therefore, by applying the plaquette operator to this equation, we find

$$
\begin{aligned}
&\mathcal{B}_p^f A_w^h(\phi_1 \otimes \ldots \otimes \phi_6) = \\
&\langle S^{\tau_5}(\phi_5^{(1+\tau_5)})S(\phi_2^{(3)})\phi_1^{(1)}S^{\tau_6}(\phi_6^{(1+\tau_6)}), h\rangle\langle\phi_2^{(1)} \otimes f^{(1)}, R\rangle \\
&\langle\phi_3^{(1+\tau_3)} \otimes f^{(2)}, (S^{\tau_3} \otimes id)(R)\rangle\langle\phi_4^{(1+\tau_4)} \otimes f^{(3)}, (S^{\tau_4} \otimes id)(R)\rangle\langle\phi_1^{(3)} \otimes f^{(4)}, R^{-1}\rangle \\
&(S(f^{(5)})\phi_1^{(2)} \otimes S(f^{(6)})\phi_2^{(2)} \otimes \phi_3^{(2-\tau_3)} \otimes \phi_4^{(2-\tau_4)} \otimes \phi_5^{(2-\tau_5)} \otimes \phi_6^{(2-\tau_6)}) \; .
\end{aligned}
$$

$$(\text{F.44})$$

On the other hand we have

$$
\begin{aligned}
&A_w^h \mathcal{B}_p^f(\phi_1 \otimes \ldots \otimes \phi_6) = \\
&\langle S^{\tau_5}(\phi_5^{(1+\tau_5)})S(\phi_2^{(3)})S(f^{(6)}S(f^{(7)}))\phi_1^{(1)}S^{\tau_6}(\phi_6^{(1+\tau_6)}), h\rangle\langle\phi_2^{(1)} \otimes f^{(1)}, R\rangle \\
&\langle\phi_3^{(1+\tau_3)} \otimes f^{(2)}, (S^{\tau_3} \otimes id)(R)\rangle\langle\phi_4^{(1+\tau_4)} \otimes f^{(3)}, (S^{\tau_4} \otimes id)(R)\rangle\langle\phi_1^{(2)} \otimes f^{(4)}, R^{-1}\rangle \\
&(S(f^{(5)})\phi_1^{(2)} \otimes S(f^{(8)})\phi_2^{(2)} \otimes \phi_3^{(2-\tau_3)} \otimes \phi_4^{(2-\tau_4)} \otimes \phi_5^{(2-\tau_5)} \otimes \phi_6^{(2-\tau_6)}) \; ,
\end{aligned}
$$

$$(\text{F.45})$$

which is the same as (F.44) once we note that $f^{(6)}S(f^{(7)}) = \epsilon^*(f^{(6)})$. This completes the proof. Note that the general case, with an arbitrary number of edges at vertex w, is essentially the same as the current case since the plaquette's edges are always adjacent with respect to the ordering imposed by the cilia. $\qquad\square$

We can now consider the commutation relation between plaquette and vertexes at the same vertex. Before undertaking this task, we need to prove the one last auxiliary proposition

Proposition F.0.8. *Consider ϕ, $f \in K^*$, then for $\tau = 0$, 1, the following equation holds*

$$
\begin{aligned}
&\langle\phi^{(1+\tau)} \otimes f^{(1)}, (S^{\tau} \otimes id)(R)\rangle S^{\tau}(\phi^{(2-\tau)(1+\tau)})f^{(2)} = \\
&\langle\phi^{(2-\tau)(1+\tau)} \otimes f^{(2)}, (S^{\tau} \otimes id)(R)\rangle f^{(1)}S^{\tau}(\phi^{(1+\tau)})
\end{aligned}
$$

$$(\text{F.46})$$

Proof. The above equation follows from the identity

$$
\langle\alpha^{(1)} \otimes \beta^{(1)}, R\rangle\alpha^{(2)}\beta^{(2)} = \langle\alpha^{(2)} \otimes \beta^{(2)}, R\rangle\beta^{(1)}\alpha^{(1)} \; ,
$$

$$(\text{F.47})$$

which holds for every α, $\beta \in K^*$, as a result of $R\Delta(h) = \Delta(h)R$. We can prove the statement directly for the two cases $\tau = 0$, 1.

Case 1: $\tau = 0$

$$
\begin{aligned}
&\langle\phi^{(1)} \otimes f^{(1)}, R\rangle\phi^{(2)(1)}f^{(2)} = \langle\phi^{(1)(1)} \otimes f^{(1)}, R\rangle\phi^{(1)(2)}f^{(2)} = \\
&\langle\phi^{(1)(2)} \otimes f^{(2)}, R\rangle f^{(2)}\phi^{(1)(1)}
\end{aligned}
$$

$$(\text{F.48})$$

which proves the first of the two equations.

Case 2: $\tau = 1$

$$\langle \phi^{(2)} \otimes f^{(1)}, (S \otimes id)(R)\rangle S(\phi^{(1)(2)})f^{(2)} = \langle S(\phi^{(2)})^{(1)} \otimes f^{(1)}, R\rangle S(\phi^{(2)})^{(2)}f^{(2)} =$$
$$\langle S(\phi^{(2)})^{(2)} \otimes f^{(2)}, R\rangle f^{(2)}S(\phi^{(2)})^{(1)} \; ,$$

(F.49)

that ends our proof. $\qquad\square$

With this technical proposition, we are finally in a position to prove the following

Proposition F.0.9. *Consider the ribbon graph in Figure F.6, then we have*

$$A_v^h \mathcal{B}_p^f = \langle f^{(3)}, S(h^{(1)})\rangle \langle f^{(1)}, h^{(2)}\rangle \mathcal{B}^{f^{(2)}} A_v^{h^{(3)}}$$

(F.50)

Proof. We will prove the statement by direct computation. Firstly we can see that

$$\mathcal{B}_p^f A_v^h(\phi_1 \otimes \phi_2 \otimes \phi_3 \otimes \phi_4) =$$
$$\langle \phi_2^{(1)} S^{\tau_3}(\phi_3^{(1+\tau_3)})S^{\tau_4}(\phi_4^{(1+\tau_4)})S(\phi_1^{(3)}), h\rangle \langle \phi_2^{(2)} \otimes f^{(1)}, R\rangle$$
$$\langle \phi_3^{(2-\tau_3)(1+\tau_3)} \otimes f^{(2)}, (S^{\tau_3} \otimes id)(R)\rangle \langle \phi_4^{(2-\tau_4)(1+\tau_4)} \otimes f^{(4)}, (S^{\tau_4} \otimes id)(R)\rangle$$
$$\langle \phi_1^{(2)} \otimes f^{(4)}, R^{-1}\rangle (S(f^{(5)})\phi_1^{(1)} \otimes S(f^{(6)})\phi_2^{(3)} \otimes \phi_3^{(2-\tau_3)(2-\tau_3)} \otimes \phi_4^{(2-\tau_4)(2-\tau_4)}) \; .$$

(F.51)

For the product on the right hand side of (F.50), we instead have

$$A_v^h \mathcal{B}_p^f(\phi_1 \otimes \phi_2 \otimes \phi_3 \otimes \phi_4) =$$
$$\langle S(f^{(8)})\phi_2^{(2)} S^{\tau_3}(\phi_3^{(2-\tau_3)(1+\tau_3)})S^{\tau_4}(\phi_4^{(2-\tau_3)(1+\tau_4)})S(\phi_1^{(2)})f^{(5)}, h\rangle \langle \phi_2^{(1)} \otimes f^{(1)}, R\rangle$$
$$\langle \phi_3^{(1+\tau_3)} \otimes f^{(2)}, (S^{\tau_3} \otimes id)(R)\rangle \langle \phi_4^{(1+\tau_4)} \otimes f^{(3)}, (S^{\tau_4} \otimes id)(R)\rangle \langle \phi_1^{(3)} \otimes f^{(4)}, R^{-1}\rangle$$
$$(S(f^{(6)})\phi_1^{(1)} \otimes S(f^{(7)})\phi_2^{(3)} \otimes \phi_3^{(2-\tau_3)(2-\tau_3)} \otimes \phi_4^{(2-\tau_4)(2-\tau_4)}).$$

(F.52)

Now note that

$$\langle \phi_1^{(3)} \otimes f^{(4)}, R^{-1}\rangle S(\phi_1^{(2)})f^{(5)} = \langle \phi_1^{(2)} \otimes f^{(5)}, R^{-1}\rangle f^{(4)}S(\phi_1^{(3)})$$

(F.53)

and therefore

$$A_v^h \mathcal{B}_p^f(\phi_1 \otimes \phi_2 \otimes \phi_3 \otimes \phi_4) =$$
$$\langle S(f^{(8)})\phi_2^{(2)} S^{\tau_3}(\phi_3^{(2-\tau_3)(1+\tau_3)})S^{\tau_4}(\phi_4^{(2-\tau_3)(1+\tau_4)})f^{(4)}S(\phi_1^{(3)}), h\rangle \langle \phi_2^{(1)} \otimes f^{(1)}, R\rangle$$
$$\langle \phi_3^{(1+\tau_3)} \otimes f^{(2)}, (S^{\tau_3} \otimes id)(R)\rangle \langle \phi_4^{(1+\tau_4)} \otimes f^{(3)}, (S^{\tau_4} \otimes id)(R)\rangle \langle \phi_1^{(2)} \otimes f^{(5)}, R^{-1}\rangle$$
$$(S(f^{(6)})\phi_1^{(1)} \otimes S(f^{(7)})\phi_2^{(3)} \otimes \phi_3^{(2-\tau_3)(2-\tau_3)} \otimes \phi_4^{(2-\tau_4)(2-\tau_4)}) \; .$$

(F.54)

We can now repeatedly apply Proposition F.0.8, to get

$$
\begin{aligned}
A_v^h \mathcal{B}_p^f(\phi_1 \otimes \phi_2 \otimes \phi_3 \otimes \phi_4) = \\
\langle S(f^{(8)})\phi_2^{(2)} f^{(2)} S^{\tau_3}(\phi_3^{(1+\tau_3)}) S^{\tau_4}(\phi_4^{(1+\tau_4)}) S(\phi_1^{(3)}), h\rangle \langle \phi_2^{(1)} \otimes f^{(1)}, R\rangle \\
\langle \phi_3^{(2-\tau_3)(1+\tau_3)} \otimes f^{(3)}, (S^{\tau_3} \otimes id)(R)\rangle \langle \phi_4^{(2-\tau_3)(1+\tau_4))} \otimes f^{(4)}, (S^{\tau_4} \otimes id)(R)\rangle \\
\langle \phi_1^{(2)} \otimes f^{(5)}, R^{-1}\rangle (S(f^{(6)})\phi_1^{(1)} \otimes S(f^{(7)})\phi_2^{(3)} \otimes \phi_3^{(2-\tau_3)(2-\tau_3)} \otimes \phi_4^{(2-\tau_4)(2-\tau_4)}) \; .
\end{aligned} \tag{F.55}
$$

Finally, since $\langle \phi_2^{(1)} \otimes f^{(1)}, R\rangle \phi_2^{(2)} f^{(2)} = \langle \phi_2^{(2)} \otimes f^{(2)}, R\rangle f^{(1)}\phi_2^{(1)}$, we can write

$$
\begin{aligned}
A_v^h \mathcal{B}_p^f(\phi_1 \otimes \phi_2 \otimes \phi_3 \otimes \phi_4) = \\
\langle S(f^{(8)}), h^{(1)}\rangle \langle f^{(1)}, h^{(2)}\rangle \langle \phi_2^{(1)} S^{\tau_3}(\phi_3^{(1+\tau_3)}) S^{\tau_4}(\phi_4^{(1+\tau_4)}) S(\phi_1^{(3)}), h^{(3)}\rangle \langle \phi_2^{(2)} \otimes f^{(2)}, R\rangle \\
\langle \phi_3^{(2-\tau_3)(1+\tau_3)} \otimes f^{(3)}, (S^{\tau_3} \otimes id)(R)\rangle \langle \phi_4^{(2-\tau_3)(1+\tau_4))} \otimes f^{(4)}, (S^{\tau_4} \otimes id)(R)\rangle \\
\langle \phi_1^{(2)} \otimes f^{(5)}, R^{-1}\rangle (S(f^{(6)})\phi_1^{(1)} \otimes S(f^{(7)})\phi_2^{(3)} \otimes \phi_3^{(2-\tau_3)(2-\tau_3)} \otimes \phi_4^{(2-\tau_4)(2-\tau_4)})
\end{aligned} \tag{F.56}
$$

where (F.50) can be recognised. Note that as for the other propositions of this appendix, this property can be easily generalised to ribbon graphs with an arbitrary number of edges at vertex v. $\qquad\square$

Appendix G

Bogoliubov-de Gennes formalism

In this section, we will describe one particular framework, which we make extensive use of when analysing p-wave superconductors in Chapter 6, namely, the Bogoliubov-de Gennes formalism (BdG). Accordingly, we shall focus again on the Kitaev chain from Section 5.2. However, this procedure is easily applied to more general free fermion models such as an s-wave superconductor and also models in spatial dimensions greater than one. For a more detailed account of the BdG formalism we refer the reader to (21; 163), as well in the appendix of (138). We start with a tight binding Hamiltonian which has nearest neighbouring pairing for free spinless fermions in one spatial dimension,

$$H = \sum_i c_i^\dagger h_{ij} c_j + \frac{1}{2} c_i^\dagger \Delta_{ij} c_j^\dagger + \frac{1}{2} c_i (\Delta_{ij})^\dagger c_j. \tag{G.1}$$

By h_{ij} we abbreviate both the chemical potential $(i = j)$ and hopping terms in a Hamiltonian such as Equation 5.1 and $i \neq j$ labels neighbouring lattice sites in a wire. In order for the Hamiltonian to be Hermitian we must require that $\Delta_{ij} = (\Delta_{ji})^\dagger$. We introduce a change of basis,

$$c^\dagger := (c_1^\dagger, \dots, c_N^\dagger), \qquad c := (c_1, \dots, c_N). \tag{G.2}$$

Using this basis we can rewrite the Hamiltonian in the following form;

$$H = \frac{1}{2} \left(c^\dagger c \right) \mathcal{H}_{\mathrm{BdG}} \begin{pmatrix} c \\ c^\dagger \end{pmatrix} + \frac{1}{2} \mathrm{Tr}(h_{ij}) \tag{G.3}$$

where,

$$\mathcal{H}_{\mathrm{BdG}} = \begin{pmatrix} h_{ij} & \Delta \\ -\Delta^* & -h_{ij}^* \end{pmatrix} \tag{G.4}$$

$\mathcal{H}_{\mathrm{BdG}}$ is called the BdG Hamiltonian, which is a $2N \times 2N$ Hermitian matrix.

Before we proceed, it's worth pointing out some features. Firstly, by rewriting the Hamiltonian in the form of Equation(G.3) we have essentially "doubled" the degrees of freedom (21). By this, we mean the same state is represented in hole space and in particle space. However, these two spaces are related by particle-hole "symmetry" [1] . This is given by conjugating the Hamiltonian by $\mathcal{U} = \sigma^x K$, where K implements complex conjugation:

$$\mathcal{U}\mathcal{H}^*(k)\mathcal{U}^{-1} = -\mathcal{H}(-k). \tag{G.5}$$

We now seek a convenient basis to diagonalise $\mathcal{H}$. Following (138), we can introduce a unitary matrix, W;

$$W = \begin{pmatrix} U & V^* \\ V & U^* \end{pmatrix}, \tag{G.6}$$

which is defined such that the first row consists of eigenfunctions of positive energy eigenvalue of $\mathcal{H}$ and the second row corresponds to negative energy eigenvalues. The basis transformation is given as

$$\begin{pmatrix} \beta \\ \beta^\dagger \end{pmatrix} = \begin{pmatrix} U & V^* \\ V & U^* \end{pmatrix} \begin{pmatrix} c \\ c^\dagger \end{pmatrix}. \tag{G.7}$$

This matrix equation defines the Bogoliubov quasi-particle operators, which in components are given by

$$\begin{aligned} \beta_n &= \sum_j U_{j,n} c_j + V^*_{j,n} c^\dagger_j, \\ \beta^\dagger_n &= \sum_j U^*_{j,n} c^\dagger_j + V_{j,n} c_j, \end{aligned} \tag{G.8}$$

where $U_{j,n}$, $V_{j,n}$ are the coefficients of the unitary matrix that diagonalizes $\mathcal{H}_{\text{BdG}}$ and the index j labels positions along the lattice. The U and V satisfy the following relations:

$$\begin{aligned} UU^\dagger + V^*V^T = 1, && U^\dagger U + V^\dagger V = 1, \\ U^T V + V^T U = 0, && UV^\dagger + V^*U^T = 0. \end{aligned} \tag{G.9}$$

---

[1]We use inverted commas since the Hamiltonian does not come back to the same form, however, it is quite commonplace to use the word symmetry to describe this redundancy.

We have the following actions

$$\mathcal{H}_{\text{BdG}} \begin{pmatrix} U_n \\ V_n \end{pmatrix} = \epsilon_n \begin{pmatrix} U_n \\ V_n \end{pmatrix}, \qquad \mathcal{H}_{\text{BdG}} \begin{pmatrix} U_n^* \\ V_n^* \end{pmatrix} = -\epsilon_n \begin{pmatrix} U_n^* \\ V_n^* \end{pmatrix}. \tag{G.10}$$

The β operators satisfy the canonical anticommutation algebra, which follows from the relations in Equation (G.9), and therefore they correspond to fermionic quasiparticles, i.e.,

$$\{\beta_n^\dagger, \beta_m\} = \delta_{nm}, \qquad \{\beta_n^\dagger, \beta_m^\dagger\} = \{\beta_n, \beta_m\} = 0. \tag{G.11}$$

Written this way we can see

$$W^\dagger \mathcal{H}_{\text{BdG}} W = \text{diag}(\epsilon_0, \dots, \epsilon_{N-1}, -\epsilon_0, \dots, -\epsilon_{N-1}). \tag{G.12}$$

We can see the doubling clearly here in the eigenvalues of the diagonalised $\mathcal{H}_{\text{BdG}}$, as each value for the quasi particle energy appears with a $+$ sign and $-$ sign. In this basis, the Hamiltonian is,

$$H(t) = \sum_{n=1}^{N} \epsilon_n (\beta_n^\dagger \beta_n - 1/2). \tag{G.13}$$

The quasiparticle ground state, $|\Psi_0\rangle$ is then defined through

$$\beta_j |\Phi_0\rangle = 0, \qquad \forall j = 1, 2, \dots, N, \tag{G.14}$$

i.e. this is the vacuum for the ordered configuration of $(\beta_1, \beta_2, \dots, \beta_N)$. The definition of the BdG ground state is such that all negative energy states are filled. We can make a few observations on these quasiparticle operators. Firstly if we consider states created by $\beta^\dagger$ operators with $U_{j,n} \approx 0$ and $V_{j,n} \approx 1$, then these excitations are hole like. Since they will be just summations of c_j operators. Similarly we can consider states created by β operators with $U_{j,n} \approx 1$ and $V_{j,n} \approx 0$, then we create excitations which are electron like. So to create Majorana excitations from these quasiparticle operators, one of the necessary criteria is that they are equal superpositions of electrons and holes, i.e. $|U| = |V|$, as we discussed in the introduction to Chapter 5.

One of the advantages of this formalism is that we can compute quasiparticle excitations in terms of these β operators and the W matrix in the following way. Let's consider the state given by

$$|\Phi_1\rangle = \beta_1^\dagger |\Phi_0\rangle, \tag{G.15}$$

this is the first excited state above the quasiparticle ground state. This state is

annihilated by all β_j, where $j = 2, \ldots, N$ and it is also annihilated by $\beta_1^\dagger$, since the β operators satisfy the canonical anticommutation algebra. As such we can view $|\Phi_1\rangle$ as the vacuum for $(\beta_1^\dagger, \beta_2, \ldots, \beta_N)$. We can encode this in a matrix similar to W in Equation (G.6) except with the first column (corresponding to β_1) switched with the N'th column (corresponding to $\beta_1^\dagger$). This gives us a useful description of excitations. If we exchange β_n with $\beta_n^\dagger$, this corresponds to swapping the n'th column of W with the $N + n'th$, which expressed in terms of the coefficients are given as

$$U_{l,n} \Leftrightarrow V_{l,n}^*, \qquad V_{l,n} \Leftrightarrow U_{l,n}^*, \tag{G.16}$$

where l is the site index. In this quasiparticle basis, we denote the Majorana bound states as the lowest energy mode operators. To be explicit, if we consider a p-wave wire with two topologically non-trivial regions ($-2w < \tilde{\mu} < 2w$) separated by a non-topological region, then the four Majorana modes will be given in this notation by $\beta_0, \beta_1, \beta_2$ and β_3. This concludes our discussion of the BdG formalism and excitations. We make frequent use of this methodology in Chapter 6.

Bibliography

[1] M. N. Vyalyi A. Yu. Kitaev, A. H. Shen. *Classical and Quantum Computation*, volume 47 of *Graduate Studies in Mathematics*. AMS, 2002. `doi:10.1090/gsm/047`.

[2] David Aasen and et al. Milestones toward Majorana-based quantum computing. *Phys. Rev. X*, 6:031016, Aug 2016. `doi:10.1103/PhysRevX.6.031016`.

[3] Aghaee, Morteza and et al. InAs-Al hybrid devices passing the topological gap protocol. *Phys. Rev. B*, 107:245423, Jun 2023. `doi:10.1103/PhysRevB.107.245423`.

[4] F. Alexander Bais, Peter van Driel, and Mark de Wild Propitius. Quantum symmetries in discrete gauge theories. *Physics Letters B*, 280(1-2):63–70, April 1992. `doi:10.1016/0370-2693(92)90773-W`.

[5] F. Alexander Bais, Peter van Driel, and Mark de Wild Propitius. Anyons in discrete gauge theories with Chern-Simons terms. *Nuclear Physics B*, 393(3):547–570, March 1993. `doi:10.1016/0550-3213(93)90073-X`.

[6] Jason Alicea. Majorana fermions in a tunable semiconductor device. *Phys. Rev. B*, 81:125318, Mar 2010. `doi:10.1103/PhysRevB.81.125318`.

[7] Jason Alicea. New directions in the pursuit of Majorana fermions in solid state systems. *Reports on Progress in Physics*, 75(7):076501, July 2012. `doi:10.1088/0034-4885/75/7/076501`.

[8] Jason Alicea, Yuval Oreg, Gil Refael, Felix von Oppen, and Matthew P. A. Fisher. Non-Abelian statistics and topological quantum information processing in 1d wire networks. *Nature Physics*, 7(5):412–417, 2011. `doi:10.1038/nphys1915`.

[9] Alexander Altland and Martin R. Zirnbauer. Non-standard symmetry classes in mesoscopic normal-superconducting hybrid structures. *Phys. Rev. B*, 55:1142–1161, Jan 1997. `doi:10.1103/PhysRevB.55.1142`.

[10] Byung Hee An and Tomasz Maciazek. Geometric presentations of braid groups for particles on a graph. *Communications in Mathematical Physics*, 384(2):1109–1140, 2021. `doi:10.1007/s00220-021-04095-x`.

[11] P. W. Anderson. Local moments and localized states. *Rev. Mod. Phys.*, 50:191–201, Apr 1978. `doi:10.1103/RevModPhys.50.191`.

[12] Eddy Ardonne and Joost Slingerland. Clebsch-Gordan and 6j-coefficients for rank 2 quantum groups. *Journal of Physics A Mathematical General*, 43(39):395205, October 2010. `doi:10.1088/1751-8113/43/39/395205`.

[13] Emil Artin. Theorie der Zöpfe. *Abhandlungen aus dem Mathematischen Seminar der Universität Hamburg*, 4(1):47–72, 1925. `doi:10.1007/BF02950718`.

[14] Pavel P. Aseev, Jelena Klinovaja, and Daniel Loss. Lifetime of Majorana qubits in Rashba nanowires with nonuniform chemical potential. *Phys. Rev. B*, 98:155414, Oct 2018. `doi:10.1103/PhysRevB.98.155414`.

[15] Pavel P. Aseev, Pasquale Marra, Peter Stano, Jelena Klinovaja, and Daniel Loss. Degeneracy lifting of Majorana bound states due to electron-phonon interactions. *Phys. Rev. B*, 99:205435, May 2019. `doi:10.1103/PhysRevB.99.205435`.

[16] Benjamin Balsam and Jr Kirillov, Alexander. Kitaev's lattice model and Turaev-Viro TQFTs, June 2012.

[17] W. K. Baskerville and S. Majid. The braided Heisenberg group. *Journal of Mathematical Physics*, 34(8):3588–3606, August 1993. `doi:10.1063/1.530047`.

[18] Bela Bauer, Torsten Karzig, Ryan V. Mishmash, Andrey E. Antipov, and Jason Alicea. Dynamics of Majorana-based qubits operated with an array of tunable gates. *SciPost Phys.*, 5:4, 2018. `doi:10.21468/SciPostPhys.5.1.004`.

[19] R. J. Baxter. *Exactly solved models in statistical mechanics*. Academic Press, 1982. URL: `https://physics.anu.edu.au/research/ftp/mpg/baxter_book.php`.

[20] Salman Beigi, Peter W. Shor, and Daniel Whalen. The quantum double model with boundary: Condensations and symmetries. *Communications in Mathematical Physics*, 306(3):663–694, September 2011. `doi:10.1007/s00220-011-1294-x`.

[21] B. Andrei Bernevig and Taylor L. Hughes. *Topological Insulators and Topological Superconductors*. Princeton University Press, 2013. URL: http://www.jstor.org/stable/j.ctt19cc2gc.

[22] M. V. Berry. Quantum phase corrections from adiabatic iteration. *Proceedings of the Royal Society of London. Series A, Mathematical and Physical Sciences*, 414(1846), 1987.

[23] A. T. Bolukbasi and J. Vala. Rigorous calculations of non-Abelian statistics in the Kitaev honeycomb model. *New Journal of Physics*, 14(4):045007, apr 2012. doi:10.1088/1367-2630/14/4/045007.

[24] H. Bombin and M. A. Martin-Delgado. Family of non-Abelian Kitaev models on a lattice: Topological condensation and confinement. *prb*, 78(11):115421, September 2008. doi:10.1103/PhysRevB.78.115421.

[25] Parsa Bonderson. Measuring topological order. *Physical Review Research*, 3(3):033110, August 2021. doi:10.1103/PhysRevResearch.3.033110.

[26] Parsa Bonderson, David J. Clarke, Chetan Nayak, and Kirill Shtengel. Implementing arbitrary phase gates with Ising anyons. *PRL*, 104(18):180505, May 2010. doi:10.1103/PhysRevLett.104.180505.

[27] Parsa Bonderson, Colleen Delaney, César Galindo, Eric C. Rowell, Alan Tran, and Zhenghan Wang. On invariants of modular categories beyond modular data. *Journal of Pure and Applied Algebra*, 223(9):4065–4088, 2019. doi:10.1016/j.jpaa.2018.12.017.

[28] Parsa Bonderson, Kirill Shtengel, and J.K. Slingerland. Interferometry of non-Abelian anyons. *Annals of Physics*, 323(11):2709–2755, 2008. doi:10.1016/j.aop.2008.01.012.

[29] S. B. Bravyi and A. Yu. Kitaev. Quantum codes on a lattice with boundary. *arXiv e-prints*, pages quant–ph/9811052, November 1998.

[30] Sergey Bravyi. Universal quantum computation with the $\nu=5/2$ fractional quantum Hall state. *PRA*, 73(4):042313, April 2006. doi:10.1103/PhysRevA.73.042313.

[31] John Brennan. *The Kitaev Model on Surfaces with Lattice Defects and of Higher Genus*. PhD thesis, National University of Ireland Maynooth, 2018. URL: https://mural.maynoothuniversity.ie/10252/.

[32] P. W. Brouwer, M. Duckheim, A. Romito, and F. von Oppen. Probability distribution of Majorana end-state energies in disordered wires. *Physical Review Letters*, 107(19):196804, November 2011. doi:10.1103/PhysRevLett.107.196804.

[33] Piet Brouwer, Klaus Ensslin, David Goldhaber-Gordon, and Patrick Lee. Nature paper "Quantized Majorana conductance", report from independent experts, March 2021. `doi:10.5281/zenodo.4545812`.

[34] Paul Bruillard, Siu-Hung Ng, Eric C. Rowell, and Zhenghan Wang. Rank-finiteness for modular categories. *Journal of the American Mathematical Society*, 29(3):857–881, 2016. URL: `https://www.jstor.org/stable/jamermathsoci.29.3.857`.

[35] Oliver Buerschaper, Matthias Christandl, Liang Kong, and Miguel Aguado. Electric–magnetic duality of lattice systems with topological order. *Nuclear Physics B*, 876(2):619–636, 2013. `doi:10.1016/j.nuclphysb.2013.08.014`.

[36] Oliver Buerschaper, Juan Martín Mombelli, Matthias Christand l, and Miguel Aguado. A hierarchy of topological tensor network states, July 2010. `arXiv:1007.5284v1`.

[37] Oliver Buerschaper, Juan Martín Mombelli, Matthias Christandl, and Miguel Aguado. A hierarchy of topological tensor network states. *Journal of Mathematical Physics*, 54(1):012201, 01 2013. `doi:10.1063/1.4773316`.

[38] Stephen S. Bullock and Gavin K. Brennen. Qudit surface codes and gauge theory with finite cyclic groups. *Journal of Physics A Mathematical General*, 40(13):3481–3505, March 2007. `doi:10.1088/1751-8113/40/13/013`.

[39] S. Burciu. On some representations of the Drinfeld double. *Journal of Algebra*, 296(2):480–504, 2006. `doi:10.1016/j.jalgebra.2005.09.004`.

[40] Sebastian Burciu. Representations and conjugacy classes of semisimple quasitriangular Hopf algebras. *SIGMA*, 16:039, May 2020. `doi:10.3842/SIGMA.2020.039`.

[41] Earl T. Campbell. Decoherence in open Majorana systems. *arXiv e-prints*, page arXiv:1502.05626, February 2015. `arXiv:1502.05626`.

[42] R. Casalbuoni. Projective group algebras. *International Journal of Modern Physics A*, 14(1):129–146, January 1999. `doi:10.1142/S0217751X99000063`.

[43] Yevheniia Cheipesh, Lorenzo Cevolani, and Stefan Kehrein. Exact description of the boundary theory of the Kitaev toric code with open boundary conditions. *PRB*, 99(2):024422, January 2019. `doi:10.1103/PhysRevB.99.024422`.

[44] Chuangxun Cheng. A character theory for projective representations of finite groups. *Linear Algebra and its Applications*, 469:230 – 242, 2015. `doi:10.1016/j.laa.2014.11.027`.

[45] Meng Cheng, Victor Galitski, and S. Das Sarma. Non-adiabatic effects in the braiding of non-Abelian anyons in topological superconductors. *PRB*, 84(10):104529, September 2011. `doi:10.1103/PhysRevB.84.104529`.

[46] David J. Clarke, Jason Alicea, and Kirill Shtengel. Exotic circuit elements from zero-modes in hybrid superconductor–quantum-Hall systems. *Nature Physics*, 10(11):877–882, 2014. `doi:10.1038/nphys3114`.

[47] David J. Clarke, Jay D. Sau, and Sumanta Tewari. Majorana fermion exchange in quasi-one-dimensional networks. *Phys. Rev. B*, 84:035120, Jul 2011. `doi:10.1103/PhysRevB.84.035120`.

[48] A Conlon, D Pellegrino, and J K Slingerland. Modified toric code models with flux attachment from Hopf algebra gauge theory. *Journal of Physics A: Mathematical and Theoretical*, 56(29):295302, jun 2023. `doi:10.1088/1751-8121/acdf9a`.

[49] A. Conlon, D. Pellegrino, J. K. Slingerland, S. Dooley, and G. Kells. Error generation and propagation in majorana-based topological qubits. *Phys. Rev. B*, 100:134307, Oct 2019. `doi:10.1103/PhysRevB.100.134307`.

[50] A. Conlon and J. K. Slingerland. Compatibility of braiding and fusion on wire networks. *Phys. Rev. B*, 108:035150, Jul 2023. `doi:10.1103/PhysRevB.108.035150`.

[51] L. Coopmans, S. Dooley, I. Jubb, K. Kavanagh, and G. Kells. Dynamical phase error in interacting topological quantum memories. *Phys. Rev. Research*, 3:033105, Jul 2021. `doi:10.1103/PhysRevResearch.3.033105`.

[52] Luuk Coopmans. *On the control of quantum many-body systems*. PhD thesis, Trinity College Dublin, 2022. URL: `http://hdl.handle.net/2262/97982`.

[53] Luuk Coopmans, Di Luo, Graham Kells, Bryan K. Clark, and Juan Carrasquilla. Protocol discovery for the quantum control of Majoranas by differentiable programming and natural evolution strategies. *PRX Quantum*, 2:020332, Jun 2021. `doi:10.1103/PRXQuantum.2.020332`.

[54] Shawn X. Cui. Topological quantum computation, 2018. URL: `https://www.math.purdue.edu/~cui177/Lecture_Combined.pdf`.

[55] Shawn X. Cui, Seung-Moon Hong, and Zhenghan Wang. Universal quantum computation with weakly integral anyons. *Quantum Information Processing*, 14(8):2687–2727, 2015. `doi:10.1007/s11128-015-1016-y`.

[56] K. A. Dancer, P. S. Isac, and J. Links. Representations of the quantum doubles of finite group algebras and spectral parameter dependent solutions of

the Yang-Baxter equation. *Journal of Mathematical Physics*, 47(10):103511–103511, October 2006. `doi:10.1063/1.2359575`.

[57] Sankar Das Sarma, Michael Freedman, and Chetan Nayak. Topologically protected qubits from a possible non-Abelian fractional quantum Hall state. *Phys. Rev. Lett.*, 94:166802, Apr 2005. `doi:10.1103/PhysRevLett.94.166802`.

[58] A. A. Davydov. Quasitriangular structures on cocommutative Hopf algebras, June 1997. `arXiv:q-alg/9706007`.

[59] Christopher M. Dawson and Michael A. Nielsen. The Solovay-Kitaev algorithm, 2005. `doi:10.48550/ARXIV.QUANT-PH/0505030`.

[60] Mark de Wild Propitius. *Topological interactions in broken gauge theories*. PhD thesis, University of Amsterdam, November 1995. URL: `https://arxiv.org/abs/hep-th/9511195v1`.

[61] Mark de Wild Propitius and F. Alexander Bais. Discrete gauge theories, November 1995. `arXiv:hep-th/9511201`.

[62] Wade DeGottardi, Diptiman Sen, and Smitha Vishveshwara. Majorana fermions in superconducting 1d systems having periodic, quasiperiodic, and disordered potentials. *Physical Review Letters*, 110:146404, April 2013. `doi:10.1103/PhysRevLett.110.146404`.

[63] Colleen Delaney, Eric C. Rowell, and Zhenghan Wang. Local unitary representations of the braid group and their applications to quantum computing, April 2016. `arXiv:1604.06429`.

[64] V.G. Drinfeld. Quantum groups. *Proceedings of the international congress of mathematicans*, 1986.

[65] V.G. Drinfeld. Problems of modern quantum field theory. *Proceedings of the Conference, Alushta*, 1989.

[66] I. S. Eliëns, J. C. Romers, and F. A. Bais. Diagrammatics for Bose condensation in anyon theories. *prb*, 90(19):195130, November 2014. `doi:10.1103/PhysRevB.90.195130`.

[67] H. Bartolomei et al. Fractional statistics in anyon collisions. *Science*, 368(6487):173–177, 2020. `doi:10.1126/science.aaz5601`.

[68] Pavel Etingof and Shlomo Gelaki. Some properties of finite-dimensional semisimple Hopf algebras. *Mathematical Research Letters*, 5(2):191–197, 1998. `doi:10.4310/MRL.1998.v5.n2.a5`.

[69] Pavel Etingof, Shlomo Gelaki, Dmitri Nikshych, and Victor Ostrik. *Tensor Categories*. American Mathematical Society, 2016. URL: https://bookstore.ams.org/surv-205.

[70] Pavel Etingof, Dmitri Nikshych, and Viktor Ostrik. On fusion categories. *Annals of Mathematics*, pages 581–642, 2005.

[71] Paul Fendley. Parafermionic edge zero modes in Zn-invariant spin chains. *Journal of Statistical Mechanics: Theory and Experiment*, 2012(11):P11020, Nov 2012.

[72] Bernard Field and Tapio Simula. Introduction to topological quantum computation with non-Abelian anyons. *Quantum Science and Technology*, 3(4):045004, October 2018. doi:10.1088/2058-9565/aacad2.

[73] Peter E. Finch and Holger Frahm. The $D(D_3)$-anyon chain: integrable boundary conditions and excitation spectra. *New Journal of Physics*, 15(5):053035, May 2013. doi:10.1088/1367-2630/15/5/053035.

[74] K. Fredenhagen, K.-H. Rehren, and B. Schroer. Superselection sectors with braid group statistics and exchange algebras. I. General theory. *Communications in Mathematical Physics*, 125(2):201 – 226, 1989. doi:cmp/1104179464.

[75] M.H. Freedman, A. Kitaev, M.J. Larsen, and Z. Wang. Topological quantum computation. *Bull.Am.Math. Soc*, 40:31–38, 2003. doi:10.1090/S0273-0979-02-00964-3.

[76] Michael H. Freedman, Michael Larsen, and Zhenghan Wang. A modular functor which is universal for quantum computation. *Communications in Mathematical Physics*, 227(3):605–622, 2002. doi:10.1007/s002200200645.

[77] Michael H. Freedman, Michael J. Larsen, and Zhenghan Wang. The two-eigenvalue problem and density of Jones representation of braid groups. *Communications in Mathematical Physics*, 228(1):177–199, January 2002. arXiv:math/0103200, doi:10.1007/s002200200636.

[78] J. Fröhlich and F. Gabbiani. Braid statistics in local quantum theory. *Reviews in Mathematical Physics*, 02(03):251–353, 1990. doi:10.1142/S0129055X90000107.

[79] Liang Fu and C. L. Kane. Superconducting proximity effect and Majorana Fermions at the surface of a topological insulator. *Phys. Rev. Lett.*, 100:096407, Mar 2008. doi:10.1103/PhysRevLett.100.096407.

[80] Wen X. G. Topological order in rigid states. *International Journal of Modern Physics B*, 04(02):239–271, 1990. doi:10.1142/S0217979290000139.

[81] César Galindo and Nicolás Jaramillo Torres. Solutions of the hexagon equation for Abelian anyons, 2016. `arXiv:1606.01414`.

[82] Alfred S. Goldhaber. Connection of spin and statistics for charge-monopole composites. *Phys. Rev. Lett.*, 36:1122–1125, May 1976. `doi:10.1103/PhysRevLett.36.1122`.

[83] V. J. Goldman and B. Su. Resonant tunneling in the quantum Hall regime: Measurement of fractional charge. *Science*, 267(5200):1010–1012, 1995. `doi:10.1126/science.267.5200.1010`.

[84] D. Guéry-Odelin, A. Ruschhaupt, A. Kiely, E. Torrontegui, S. Martínez-Garaot, and J. G. Muga. Shortcuts to adiabaticity: Concepts, methods, and applications. *Rev. Mod. Phys.*, 91:045001, Oct 2019. `doi:10.1103/RevModPhys.91.045001`.

[85] Bertrand I. Halperin, Yuval Oreg, Ady Stern, Gil Refael, Jason Alicea, and Felix von Oppen. Adiabatic manipulations of Majorana fermions in a three-dimensional network of quantum wires. *PRB*, 85(14):144501, April 2012. `doi:10.1103/PhysRevB.85.144501`.

[86] J. M. Harrison, J. P. Keating, J. M. Robbins, and A. Sawicki. n-particle quantum statistics on graphs. *Communications in Mathematical Physics*, 330(3):1293–1326, 2014. `doi:10.1007/s00220-014-2091-0`.

[87] M. Z. Hasan and C. L. Kane. Colloquium: Topological insulators. *Rev. Mod. Phys.*, 82:3045–3067, Nov 2010. `doi:10.1103/RevModPhys.82.3045`.

[88] Fabian Hassler. Majorana qubits, April 2014. `arXiv:1404.0897`.

[89] Allen Hatcher. *Algebraic topology*. Cambridge Univ. Press, Cambridge, 2000. URL: `https://cds.cern.ch/record/478079`.

[90] Adrian Hutter and Daniel Loss. Quantum computing with parafermions. *Phys. Rev. B*, 93:125105, Mar 2016. `doi:10.1103/PhysRevB.93.125105`.

[91] D. A. Ivanov. Non-Abelian statistics of half-quantum vortices in p-wave super-conductors. *PRL*, 86(2):268–271, January 2001. `doi:10.1103/PhysRevLett.86.268`.

[92] Zhian Jia, Dagomir Kaszlikowski, and Sheng Tan. Boundary and domain wall theories of 2d generalized quantum double model. *Journal of High Energy Physics*, 2023(7):160, 2023. `doi:10.1007/JHEP07(2023)160`.

[93] Egger. J.M. On involutive monoidal categories. *Theory and Applications of Categories*, 25:368–393, 2011.

[94] Torsten Karzig, Armin Rahmani, Felix von Oppen, and Gil Refael. Optimal control of Majorana zero modes. *PRB*, 91(20):201404, May 2015. `doi:10.1103/PhysRevB.91.201404`.

[95] Torsten Karzig, Gil Refael, and Felix von Oppen. Boosting Majorana zero modes. *Physical Review X*, 3:041017, November 2013. `doi:10.1103/PhysRevX.3.041017`.

[96] Christian Kassel. *Quantum Groups*. Graduate Texts in Mathematics. Springer Publishing Company, 2012. `doi:10.1007/978-1-4612-0783-2`.

[97] G. Kells, D. Meidan, and P. W. Brouwer. Near-zero-energy end states in topologically trivial spin-orbit coupled superconducting nanowires with a smooth confinement. *Phys. Rev. B*, 86:100503, Sep 2012. `doi:10.1103/PhysRevB.86.100503`.

[98] Udit Khanna, Moshe Goldstein, and Yuval Gefen. Parafermions in a multi-legged geometry: Towards a scalable parafermionic network. *Phys. Rev. B*, 105:L161101, Apr 2022. `doi:10.1103/PhysRevB.105.L161101`.

[99] A. Y. Kitaev. Unpaired Majorana fermions in quantum wires. *Phys. Usp.*, 44:131, October 2001. `doi:10.1070/1063-7869/44/10S/S29`.

[100] Alexei Kitaev. Anyons in an exactly solved model and beyond. *Annals of Physics*, 321(1):2–111, 2006. January Special Issue. `doi:10.1016/j.aop.2005.10.005`.

[101] Alexei Kitaev. Periodic table for topological insulators and superconductors. In Vladimir Lebedev and Mikhail Feigel'Man, editors, *Advances in Theoretical Physics: Landau Memorial Conference*, volume 1134 of *American Institute of Physics Conference Series*, pages 22–30, May 2009. `doi:10.1063/1.3149495`.

[102] A.Yu. Kitaev. Fault-tolerant quantum computation by anyons. *Annals of Physics*, 303(1):2–30, 2003. `doi:10.1016/S0003-4916(02)00018-0`.

[103] Robert Koenig, Greg Kuperberg, and Ben W. Reichardt. Quantum computation with Turaev-Viro codes. *Annals of Physics*, 325(12):2707–2749, December 2010. `arXiv:1002.2816`, `doi:10.1016/j.aop.2010.08.001`.

[104] Anna Kómár and Olivier Landon-Cardinal. Anyons are not energy eigenspaces of quantum double Hamiltonians. *PRB*, 96(19):195150, November 2017. `doi:10.1103/PhysRevB.96.195150`.

[105] Liang Kong and Zhi-Hao Zhang. An invitation to topological orders and category theory, May 2022. `arXiv:2205.05565`.

[106] Lawrence M. Krauss and Frank Wilczek. Discrete gauge symmetry in continuum theories. *Phys. Rev. Lett.*, 62:1221–1223, Mar 1989. `doi:10.1103/PhysRevLett.62.1221`.

[107] Ethan Lake and Yong-Shi Wu. Signatures of broken parity and time-reversal symmetry in generalized string-net models. *PRB*, 94(11):115139, September 2016. `doi:10.1103/PhysRevB.94.115139`.

[108] Saunders Mac Lane. *Categories for the Working Mathematican*. Springer-Verlag New York, 1978. `doi:10.1007/978-1-4757-4721-8`.

[109] Nicolai Lang and Hans Peter Buchler. Minimal instances for toric code ground states. *pra*, 86(2):022336, August 2012. `doi:10.1103/PhysRevA.86.022336`.

[110] Dominique Laroche, Daniël Bouman, David J. van Woerkom, Alex Proutski, Chaitanya Murthy, Dmitry I. Pikulin, Chetan Nayak, Ruben J. J. van Gulik, Jesper Nygård, Peter Krogstrup, Leo P. Kouwenhoven, and Attila Geresdi. Observation of the 4π-periodic Josephson effect in Indium Arsenide nanowires. *Nature Communications*, 10(1):245, 2019. `doi:10.1038/s41467-018-08161-2`.

[111] J. M. Leinaas and J. Myrheim. On the theory of identical particles. *Il Nuovo Cimento B (1971-1996)*, 37(1):1–23, 1977. `doi:10.1007/BF02727953`.

[112] Chun-Xiao Liu, Jay D. Sau, and S. Das Sarma. Distinguishing topological Majorana bound states from trivial Andreev bound states: Proposed tests through differential tunneling conductance spectroscopy. *Phys. Rev. B*, 97:214502, Jun 2018. `doi:10.1103/PhysRevB.97.214502`.

[113] Roman M. Lutchyn, Jay D. Sau, and S. Das Sarma. Majorana fermions and a topological phase transition in semiconductor-superconductor heterostructures. *Phys. Rev. Lett.*, 105:077001, Aug 2010. `doi:10.1103/PhysRevLett.105.077001`.

[114] Tomasz Maciazek, Aaron Conlon, Gert Vercleyen, and J. K. Slingerland. Extending the planar theory of anyons to quantum wire networks, 2023. `doi:10.48550/ARXIV.2301.06590`.

[115] Tomasz Maciążek and Adam Sawicki. Non-Abelian quantum statistics on graphs. *Communications in Mathematical Physics*, 371(3):921–973, 2019. `doi:10.1007/s00220-019-03583-5`.

[116] Tomasz Maciążek and Byung Hee An. Universal properties of anyon braiding on one-dimensional wire networks. *Phys. Rev. B*, 102:201407, Nov 2020. `doi:10.1103/PhysRevB.102.201407`.

[117] Saunders MacLane. Natural associativity and commutativity. *Rice Institute Pamphlet-Rice University Studies*, 49(4), 1963.

[118] S. Majid. Algebras and Hopf algebras in braided categories, September 1995. arXiv:q-alg/9509023.

[119] Shahn Majid. Braided groups. *Les rencontres physiciens-mathématiciens de Strasbourg -RCP25*, 43, 1992. talk:7. URL: http://www.numdam.org/item/RCP25_1992__43__107_0/.

[120] Shahn Majid. *Foundations of Quantum Group Theory*. Cambridge University Press, 1995. doi:10.1017/CBO9780511613104.

[121] Shahn Majid. *A Quantum Groups Primer*. London Mathematical Society Lecture Note Series. Cambridge University Press, 2002. doi:10.1017/CBO9780511549892.

[122] Ettore Majorana. Teoria simmetrica dell'elettrone e del positrone. *Il Nuovo Cimento (1924-1942)*, 14(4):171, 2008. doi:10.1007/BF02961314.

[123] Catherine Meusburger. Kitaev lattice models as a hopf algebra gauge theory. *Communications in Mathematical Physics*, 353(1):413–468, 2017. doi:10.1007/s00220-017-2860-7.

[124] Catherine Meusburger and Derek K. Wise. Hopf algebra gauge theory on a ribbon graph. *Reviews in Mathematical Physics*, 33(05):2150016, 2021. doi:10.1142/S0129055X21500161.

[125] Michaël Mignard and Peter Schauenburg. Modular categories are not determined by their modular data. *Letters in Mathematical Physics*, 111(3):60, 2021. doi:10.1007/s11005-021-01395-0.

[126] Gregory Moore and Nicholas Read. Nonabelions in the fractional quantum Hall effect. *Nuclear Physics B*, 360(2):362–396, 1991. doi:10.1016/0550-3213(91)90407-O.

[127] Gregory Moore and Nathan Seiberg. Polynomial equations for rational conformal field theories. *Physics Letters B*, 212(4):451–460, 1988. doi:10.1016/0370-2693(88)91796-0.

[128] Gregory Moore and Nathan Seiberg. Classical and quantum conformal field theory. *Communications in Mathematical Physics*, 123(2):177–254, 1989. doi:10.1007/BF01238857.

[129] V. Mourik, K. Zuo, S. M. Frolov, S. R. Plissard, E. P. A. M. Bakkers, and L. P. Kouwenhoven. Signatures of Majorana fermions in hybrid superconductor-semiconductor nanowire devices. *Science*, 336(6084):1003–1007, 2012. `doi:10.1126/science.1222360`.

[130] Deepak Naidu and Eric C. Rowell. A finiteness property for braided fusion categories. *Algebras and Representation Theory*, 14(5):837–855, 2011. `doi:10.1007/s10468-010-9219-5`.

[131] Chetan Nayak, Steven H. Simon, Ady Stern, Michael Freedman, and Sankar Das Sarma. Non-Abelian anyons and topological quantum computation. *Rev. Mod. Phys.*, 80:1083–1159, Sep 2008. URL: `https://link.aps.org/doi/10.1103/RevModPhys.80.1083`.

[132] Chetan Nayak and Frank Wilczek. 2n quasihole states realize 2n-1 dimensional spinor braiding statistics in paired quantum Hall states. *Nuclear Physics B*, 479(3):529–553, 1996. `doi:10.1016/0550-3213(96)00430-0`.

[133] Michael A. Nielsen and Isaac L. Chuang. *Quantum Computation and Quantum Information: 10th Anniversary Edition*. Cambridge University Press, 2010. `doi:10.1017/CBO9780511976667`.

[134] Naoki Onishi and Shiro Yoshida. Generator coordinate method applied to nuclei in the transition region. *Nuclear Physics*, 80(2):367 – 376, 1966.

[135] Felix von Oppen, Yang Peng, and Falko Pientka. Topological superconducting phases in one dimension. In *Topological Aspects of Condensed Matter Physics: Lecture Notes of the Les Houches Summer School: Volume 103, August 2014*. Oxford University Press, 01 2017. `doi:10.1093/acprof:oso/9780198785781.003.0009`.

[136] Yuval Oreg, Gil Refael, and Felix von Oppen. Helical liquids and Majorana bound states in quantum wires. *Phys. Rev. Lett.*, 105:177002, Oct 2010. `doi:10.1103/PhysRevLett.105.177002`.

[137] Masaki Oshikawa, Yong Baek Kim, Kirill Shtengel, Chetan Nayak, and Sumanta Tewari. Topological degeneracy of non-Abelian states for dummies. *Annals of Physics*, 322(6):1477–1498, 2007. `doi:10.1016/j.aop.2006.08.001`.

[138] P. Schuck P. Ring. *The Nuclear Many-Body Problem*. Springler-Verlag, 2004.

[139] J K Pachos, W Wieczorek, C Schmid, N Kiesel, R Pohlner, and H Weinfurter. Revealing anyonic features in a toric code quantum simulation. *New Journal of Physics*, 11(8):083010, aug 2009. `doi:10.1088/1367-2630/11/8/083010`.

[140] Jiannis K. Pachos. *Introduction to Topological Quantum Computation*. Cambridge University Press, 2012. doi:10.1017/CBO9780511792908.

[141] A. Joyal R. Street. Braided monoidal categories. *Macquarie Mathematics Reports*, No. 860081, 1986.

[142] Djordje Radicevic. Confinement and flux attachment, October 2021. arXiv:2110.10169.

[143] Diego Rainis and Daniel Loss. Majorana qubit decoherence by quasiparticle poisoning. *PRB*, 85(17):174533, May 2012. doi:10.1103/PhysRevB.85.174533.

[144] N. Read and Dmitry Green. Paired states of fermions in two dimensions with breaking of parity and time-reversal symmetries and the fractional quantum Hall effect. *Phys. Rev. B*, 61:10267–10297, Apr 2000. doi:10.1103/PhysRevB.61.10267.

[145] N. Read and E. Rezayi. Beyond paired quantum hall states: Parafermions and incompressible states in the first excited Landau level. *Phys. Rev. B*, 59:8084–8092, Mar 1999. doi:10.1103/PhysRevB.59.8084.

[146] N. Reshetikhin and V. G. Turaev. Invariants of 3-manifolds via link polynomials and quantum groups. *Inventiones mathematicae*, 103(1):547–597, 1991. doi:10.1007/BF01239527.

[147] N. Y. Reshetikhin and V. G. Turaev. Ribbon graphs and their invaraints derived from quantum groups. *Communications in Mathematical Physics*, 127(1):1–26, 1990. doi:10.1007/BF02096491.

[148] Andrew Resnick. Topological aspects of condensed matter physics: lecture notes of the Les Houches summer school: Volume 103, august 2014. *Contemporary Physics*, 59(3):320–321, 2018. doi:10.1080/00107514.2018.1464518.

[149] Heinz J Rothe. *Lattice Gauge Theories*. World Scientific Publishing Company, 2012. doi:10.1142/8229.

[150] Eric C. Rowell and Zhenghan Wang. Mathematics of topological quantum computing, May 2017. arXiv:1705.06206.

[151] L. Saminadayar, D. C. Glattli, Y. Jin, and B. Etienne. Observation of the $e/3$ fractionally charged Laughlin quasiparticle. *Phys. Rev. Lett.*, 79:2526–2529, Sep 1997. doi:10.1103/PhysRevLett.79.2526.

[152] Masatoshi Sato and Satoshi Fujimoto. Majorana fermions and topology in superconductors. *Journal of the Physical Society of Japan*, 85(7):072001, 2016. doi:10.7566/JPSJ.85.072001.

[153] K. J. et al. Satzinger. Realizing topologically ordered states on a quantum processor. *Science*, 374(6572):1237–1241, December 2021. `doi:10.1126/science.abi8378`.

[154] Jay D. Sau, Sumanta Tewari, and S. Das Sarma. Universal quantum computation in a semiconductor quantum wire network. *Phys. Rev. A*, 82:052322, Nov 2010. `doi:10.1103/PhysRevA.82.052322`.

[155] J. A. Sauls. Andreev bound states and their signatures. *Philosophical Transactions of the Royal Society of London Series A*, 376(2125):20180140, August 2018. `doi:10.1098/rsta.2018.0140`.

[156] M. S. Scheurer and A. Shnirman. Non-adiabatic processes in Majorana qubit systems. *Physical Review B*, 88:064515, August 2013. `doi:10.1103/PhysRevB.88.064515`.

[157] Manuel J. Schmidt, Diego Rainis, and Daniel Loss. Decoherence of Majorana qubits by noisy gates. *Phys. Rev. B*, 86:085414, Aug 2012. `doi:10.1103/PhysRevB.86.085414`.

[158] Jacob Siehler. Near-group categories, September 2002. `arXiv:math/0209073`.

[159] Steve Simon. *Topological Quantum: Lecture Notes and Proto-Book*. Oxford University Press, 2017. URL: `http://www-thphys.physics.ox.ac.uk/people/SteveSimon/topological2021/TopoBook-Sep28-2021.pdf`.

[160] Steven H. Simon and Joost K. Slingerland. Straightening Out the Frobenius-Schur Indicator, August 2022. `arXiv:2208.14500`.

[161] Noah Snyder and Peter Tingley. The half-twist for $U_q(\mathrm{g})$ representations, October 2008. `arXiv:0810.0084`.

[162] Chao Song, Da Xu, Pengfei Zhang, Jianwen Wang, Qiujiang Guo, Wuxin Liu, Kai Xu, Hui Deng, Keqiang Huang, Dongning Zheng, Shi-Biao Zheng, H. Wang, Xiaobo Zhu, Chao-Yang Lu, and Jian-Wei Pan. Demonstration of topological robustness of anyonic braiding statistics with a superconducting quantum circuit. *Phys. Rev. Lett.*, 121:030502, Jul 2018. `doi:10.1103/PhysRevLett.121.030502`.

[163] D. Stanescu, Tudor. *Topological Quantum Matter & Quantum Computation*. CRC Press, 2016. `doi:10.1201/9781315181509`.

[164] Daisuke Tambara and Shigeru Yamagami. Tensor categories with fusion rules of self-duality for finite Abelian groups. *Journal of Algebra*, 209(2):692 – 707, 1998. `doi:10.1006/jabr.1998.7558`.

[165] Michael. Tinkham. *Introduction to superconductivity*. McGraw Hill, New York, 1996. URL: http://books.google.com/books?id=XP_uAAAAMAAJ.

[166] Simon Trebst, Matthias Troyer, Zhenghan Wang, and Andreas WW Ludwig. A short introduction to Fibonacci anyon models. *Progress of Theoretical Physics Supplement*, 176:384–407, 2008. URL: https://doi.org/10.48550/arXiv.0902.3275.

[167] D. C. Tsui, H. L. Stormer, and A. C. Gossard. Two-dimensional magneto-transport in the extreme quantum limit. *Phys. Rev. Lett.*, 48:1559–1562, May 1982. doi:10.1103/PhysRevLett.48.1559.

[168] Cumrun Vafa. Toward classification of conformal theories. *Phys. Lett. B*, 206:421–426, 1988. doi:10.1016/0370-2693(88)91603-6.

[169] G. E. Volovik. Fermion zero modes on vortices in chiral superconductors. *Journal of Experimental and Theoretical Physics Letters*, 70(9):609–614, 1999. doi:10.1134/1.568223.

[170] Piet W. Brouwer, Mathias Duckheim, Alessandro Romito, and Felix von Oppen. Topological superconducting phases in disordered quantum wires with strong spin-orbit coupling. *Physical Review B*, 84(14):144526, October 2011.

[171] Xiao-Gang Wen. *Quantum Field Theory of Many-Body Systems: From the Origin of Sound to an Origin of Light and Electrons*. Oxford University Press, 09 2007. doi:10.1093/acprof:oso/9780199227259.001.0001.

[172] Frank Wilczek. Magnetic flux, angular momentum, and statistics. *Phys. Rev. Lett.*, 48:1144–1146, Apr 1982. doi:10.1103/PhysRevLett.48.1144.

[173] Frank Wilczek. Quantum mechanics of fractional-spin particles. *Phys. Rev. Lett.*, 49:957–959, Oct 1982. doi:10.1103/PhysRevLett.49.957.

[174] Frank Wilczek and A. Zee. Appearance of gauge structure in simple dynamical systems. *Phys. Rev. Lett.*, 52:2111–2114, Jun 1984. doi:10.1103/PhysRevLett.52.2111.

[175] Edward Witten. Topological quantum field theory. *Commun. Math. Phys.*, 117:353, 1988. doi:10.1007/BF01223371.

[176] James R. Wootton, Ville Lahtinen, and Jiannis K. Pachos. Universal quantum computation with a non-Abelian topological memory, June 2009. arXiv:0906.2748.

[177] Bowen Yan, Penghua Chen, and Shawn X Cui. Ribbon operators in the generalized Kitaev quantum double model based on Hopf algebras. *Journal of Physics A: Mathematical and Theoretical*, 55(18):185201, apr 2022. doi:10.1088/1751-8121/ac552c.

[178] Zhi-Cheng Yang, Dmitry Green, Hongji Yu, and Claudio Chamon. Z$_3$ quantum double in a superconducting wire array. *PRX Quantum*, 2(3):030327, August 2021. doi:10.1103/PRXQuantum.2.030327.